Radio spectroscopy and space science with VLBI radio telescopes for Solar System research

Guifré Molera Calvés

Radio spectroscopy and space science with VLBI radio telescopes for Solar System research

Guifré Molera Calvés

Doctoral dissertation for the degree of Doctor of Science in Technology to be presented with due permission of the School of Electrical Engineering for public examination and debate in Auditorium S1 at the Aalto University School of Electrical Engineering (Espoo, Finland) on the 27th of April 2012 at 12 noon.

Supervisor
Professor Martti Hallikainen

Instructor
Doctor Sergei Pogrebenko, JIVE, the Netherlands

Preliminary examiners
Doctor Kaj Wiik, Tuorla Observatory, University of Turku, Finland
Doctor Alan R. Whitney, MIT/Haystack radio observatory, USA

Opponent
Doctor Franco Mantovani, Istituto di RadioAstronomia, Italy

NORDIC ECOLABEL

441   697
Printed matter

Abstract

Only a tiny fraction of the universe has been studied even though the possibilities are unlimited given the current technologies, the resources and the time. To optimize the use of resources, the Metsähovi antenna and the existing VLBI processing hardware were exploited to study a broad variety of space phenomena.

The research began with radio spectroscopy of the celestial bodies of our Solar System. Every object emits certain spectral signatures at several radio frequencies depending on its chemical molecules. Earth-based observations of the emitted radio spectral signal help to determine the composition of the structure and atmosphere of the planets. A unique method for processing the data captured by VLBI radio telescopes for radio spectroscopy purposes was developed during this work.

Although the initial research focused on planetary bodies, it later shifted to the spacecraft motion. This new aim included studying ground support to planetary and deep-space mission spacecraft with VLBI radio telescopes, which opened up possibilities for collaboration between space agencies and radio astronomers. In addition, with VLBI phase-referencing, a high accuracy estimation of the spacecraft state vectors could be obtained. These new tools provide an opportunity for studying a broad variety of physical processes, including the dynamics of planetary atmospheres, geodynamical diagnostics of the interior of planets, fundamental physics effects of spacecraft motion and solar wind characterization. For instance, we organised a VLBI tracking session of Venus Express that involved 10 antennae and it estimated the spacecraft position with a precision of few hundred metres.

The most interesting physical process for further investigation was the characterisation of the solar wind along the propagation path. The phase fluctuations on the signal allowed us to study essential parameters of the interplanetary scintillations, such as the phase scintillation index, bandwidth of scintillations or spectral broadening and their dependence on the solar elongation, distance to the target, celestial position of the spacecraft and radio telescopes. A scintillation and electron density model as a function of solar elongation was developed based on the data collected during two years. This model is powerful for improving the accurate determination of the spacecraft state vectors.

Preface

I have been working as a post-graduate student at the Metsähovi radio observatory since spring 2006. Because of my incorporation with the VLBI group, I have been collaborating with several international projects in the field of the space science and radio astronomy using VLBI telescopes.

First, I want to express my deep gratitude to the thesis advisor and mentor, Dr. Sergei Pogrebenko, who has provided support, guidance and interesting opportunities over the years. I would like to thank my colleagues at Metsähovi for offering a good working environment, strong collaboration and support. I would like to acknowledge the CASPER group at UC Berkeley who welcomed me to their group and provided a place for writing the dissertation. I would like to express my appreciation for the supervisor Prof. Martti Hallikainen, the director of Metsähovi Prof. Merja Tornikoski and the two pre-examiners that supervised this dissertation, Dr. Kaj Wiik and Dr. Alan R. Whitney. I'm also grateful to Megan, Giuseppe, Sergei, Leonid, Neville and Anna for the language help and everyone who have contributed directly or indirectly on this thesis.

I wish to thank my parents Roser and Angel, and my brother Guillem for all the love and support they have given me. I also want to thank all my friends for the relaxing times after the work. Last but not least, I want to thank my wife Anna for the innumerable hours helping with the thesis and for being the most awesome thing in my life.

Helsinki, March 28, 2012,

Contents

Contents

List of Figures

List of Tables

List of Symbols

a	Solar radius
æ	Spatial wave number
b	Distance of baselines
BW	Bandwidth
c	Speed of light
c_n	Structural coefficient of plasma irregularity
D	Size of a dish antenna
E_x	Energy state of a molecule
f	Frequency
h	Planck constant
k	Wavenumber
L	Distance Earth-spacecraft
m	Kolmogorov spectrum slope
N_{df}	Degrees of freedom
$N_e(l)$	Electron content density
p	Impact point
P_x	Transmitted or Received Power
R	Angular resolution
R_f	Fresnel scale
r	Distance to the Sun
u	Impact parameter rate
V_{ij}	Visibilities coefficients
V_{range}	Velocity range
V_w	Smoothing velocity width
Y	Attenuation of a radio wave

α	Spatial spectrum index of plasma irregularities
β	Kurtosis momenta
γ	Coefficient absorption
$\delta\phi$	Undetermined phase fluctuations
ΔF	Frequency shift
Δt	Time elapsed
λ	Wavelength of the signal
Λ	Scales of large plasma irregularities
μ	Mean
σ_φ	RMS variance of the phase scintillation
σ_{Sc}	RMS variance of power scintillation
τ_g	Delay between signals
υ	Frequency of radiation
ϕ	Phase fluctuations
Φ	Spatial spectrum of refractive index of irregularities

List of Abbreviations

ADC   Analogue-to-Digital Converter
AU   Astronomical Unit
BBC   Base Band Converter
BW   Frequency bandwidth
COTS   Commercial-Off-The-Shelves
CRF   Celestial Reference Frame
CT   Celestial Time
CTRF   Celestial Terrestrial Reference Frame
DAS   Data Acquisition System
dBBC   Digital Base Band Converter
DBE   Digital Back End
Dec   Declination
DFT   Direct Fourier Transform
ESA   European Space Agency
EVN   European VLBI Network
FS   Field System
FWHP   Full Width at Half Peak
Gbps   Gigabits per second
GSFC   Goddard Space Flight Centre
ICRF   International Celestial Reference Frame
IF   Intermediate Frequency
INAF   Istituto Nazionale di AstroFisica
I/O   Input/Output
IPS   Interplanetary Scintillations
IRA   Isituto di Radioastronomia
JAXA   Japan Aerospace Exploration Agency
JIVE   Joint Institute for VLBI in Europe
LCP   Left Circular Polarization
Ma   Matera
maser   Microwave Amplification Stimulated Emission of Radiation
Mc   Medicina
MEX   Mars Express
Mh   Metsähovi
NASA   National Aeronautics and Space Administration
NRAO   National Radio Astronomy Observatory
Nt   Noto
On   Onsala
PCal   Phase Calibration tone
PLL   Phase Locked Loop

PMP	Port Multiplier Port
pps	pulse per second
PRIDE	Planetary Radio Interferometry and Doppler Experiment
RA	Right Ascension
RAID	Redundant Array of Independent Disks
RCP	Right Circular Polarization
RF	Radio Frequency
RMS	Root Mean Square
RX	Reception
SATA	Serial Advanced Technology Attachment
S/C	Spacecraft
SEFD	System Equivalent Flux Density
SK	Spectral Kurtosis
SNR	Signal to Noise Rate
SOT	Sun-Observer-Target
TDB	Barycentric Dynamical Time
TEC	Total Electron Content
tecu	Total Electron Content Unit
T_{sys}	System temperature
TX	Transmission
UDP	User Datagram Protocol
USO	Ultra Stable Oscillator
VDIF	VLBI Data Interchange Format
VEX	Venus Express
VLBA	Very Long Baseline Array
VLBI	Very Long Baseline Interferometry
VSI	VLBI Standard Interface
WLMS	Weighted Least Mean Square
WOLA	Windowed-Overlapped Add
Wz	Wettzell
Ys	Yebes

1. Introduction

1.1 Background

Very Long Baseline Interferometry (VLBI) is a technique that combines the radio signals captured simultaneously by several radio telescopes, which are distributed worldwide, to emulate a virtual antenna as large as their baselines. This technique is being used at Metsähovi Radio Observatory, which has a 14-metre dish that is connected to the European VLBI Network (EVN). The radio telescope belongs to the Aalto University and has been involved in the joint VLBI observations since the 1990's. This radio telescope is extremely valuable for the VLBI community due to its northern location and its wide range of radio frequency receivers.

VLBI observations allow image reconstruction and provide higher accuracy on distant cosmic radio sources that are only detectable with radio interferometry techniques. To achieve this, data captured by the telescopes are digitised and stored on hard disks for the signal correlation. Data are interleaved with timestamps, provided by a local atomic clock, to give precise information of the captured time of the incoming signal. In addition, VLBI observations record the whole limited bandwidth of the radio signal, known as raw data. Unlike VLBI, conventional radio astronomy observations measure the brightness temperature or the power spectra of the radio sources. Although capturing raw data requires a large amount of storage capacity, its benefit is the ability to post-process the data infinite times and consequently to achieve the desired precision. Furthermore, e-VLBI will replace the current data acquisitions systems in the near future. In e-VLBI, the data are streamed on fly to the correlator core, instead of being recorded into disk, and processed in real-time.

The use of the radio telescope with the specific VLBI data acquisition system can be extended to single-dish operations for radio astronomy purposes within our Solar System. The goal of the research presented in this dissertation is to utilise the existent hardware of Metsähovi and from other similar observatories to investigate extraordinary physical phenomena that take place in our neighbouring planets.

1.2 Technical development

As an EVN member, the Metsähovi VLBI group has been actively involved in developing new hardware and software tools for e-VLBI. In 2002, a PCI-based computer board was purposely developed as a conventional VLBI data acquisition system. This system was used to record astronomical data with regular Linux machines and standard RAID disk-arrays. Then, in 2006, an aggressive network transfer UDP protocol was improved to allow real-time recording and streaming from the radio telescope to the correlator. The first tests demonstrated unprecedented ultra rapid transfers in long haul connections in 1 Gbps link. A year later, a new high capacity storage recording system prototype that handles 4 Gbps data streams was built.

In 2008, several designs of digital back ends were implemented based on FPGA boards and 10 GbE links. The models ran in the popular iBOB boards for radio astronomy, designed by the group in the University of California, Berkeley. These digital back ends and recording systems were extensively studied and used for our observations. A year later, a software tool that handles the formatted VLBI data and measures the spectral signature of the radio waves was programmed. This software was developed at Metsähovi in coordination with JIVE and it is used in this dissertation to process the data of the projects presented.

Finally in 2010, the software auto correlator was complemented with the on-purpose spacecraft tracking software. The software detects the narrow band tone of the spacecraft, provides high accuracy measurements of the Doppler frequency and estimates the power and relative phase information of the tone.
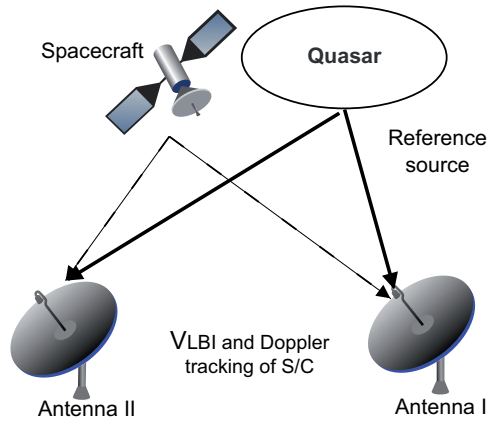
Figure 1.1. Scheme of VLBI and Doppler tracking of planetary spacecraft.

1.3 Scientific purpose

Planetary observations searching for radio spectral emissions opened up the first opportunity to utilise the new digital back ends and the software spectrometer. This astronomy technique is known as radio spectroscopy. The VLBI radio telescope captures the radio signal at a specific wavelength and divides its bandwidth into several frequency channels. The spectral lines are then analysed individually per each channel looking for prominent detections. The goal was to explore indices of water plumes emitted by any of the elements of the Saturnian system. The results of water search sessions were successful and motivated us to extend our goals to study other planets and other physical processes: including C_2S molecule emission in Venus and electric discharges in the Mars atmosphere.

The work progressed towards artificial radio signal emitted by planetary spacecraft orbiting near-by planets. Using spacecraft as targets of radio astronomy provide new tools for studying a wide range of physical processes. These phenomena include the dynamics of extra-terrestrial atmospheres, geodynamical diagnostics of the interior of planets and outer ring structures, fundamental physics effects of spacecraft motion and solar corona and solar wind characterization. Many of these applications require an extremely high angular resolution coupled with very high spectral resolution, which is only achievable with VLBI technique. The VLBI and Doppler tracking of spacecraft is adopted by a number of prospective planetary science missions as part of their scientific suite. Several

attempts of tracking spacecraft have been made since 2009 yielding excellent results.

The phase analysis of the spacecraft carrier line demonstrated a high level of fluctuations caused during the propagation within the Solar System. The primary contributions for the phase variations are from the Earth's ionosphere, the system noise temperature and the interplanetary plasma. A campaign observing the phase fluctuations of the ESA Venus Express (VEX) spacecraft signal at several solar elongations and different distances to the target started in 2009. The sessions tracked the spacecraft orbiting in Venus at X-band (8.4 GHz) using several EVN radio telescopes.

1.4 Outline of the thesis

- Chapter 2 gives a theoretical introduction to familiar concepts in the radio astronomy field: radio spectroscopy, radio interferometry techniques and space radio science.

- Chapter 3 introduces technical details of the data acquisition systems of the radio telescopes and presents the hardware and software developed for the VLBI systems at Metsähovi.

- Chapter 4 describes the benefit of using VLBI radio telescopes for radio spectroscopy purposes in the Solar System. Three principal scientific projects with diverse results are discussed.

- Chapter 5 extends the use of radio spectroscopy to Doppler measurements of the signal transmitted by the planetary spacecraft. The whole chapter is a walk-through from the software developed for data processing to the results obtained using several VLBI radio telescopes.

- Chapter 6 includes the data analysis of the spacecraft signal phase during the last two years. The phase fluctuations have served to characterise the interplanetary plasma scintillations caused by the solar wind.

1.5 Contribution of the author

The author was involved in the process of designing, building and developing the recording software, as well as testing the new VLBI data acquisition systems presented in Chapter 3. Furthermore, the author

programmed several FPGA firmware for digital back ends. Part of this work was completed while visiting the University of California, Berkeley in 2010-11.

The radio spectroscopy observations introduced in Chapter 4 were conducted at Metsähovi by the author. The observations involved arranging the observing time, preparing the relevant schedules, conducting the observations at the corresponding epoch, processing the data and finally analysing the results. For the observations conducted at the radio telescope of Robledo, the author performed all the same tasks, except for conducting the observations.

The author was responsible for conducting the spacecraft tracking observations explained in Chapter 5. For all the sessions observed at Metsähovi, the author arranged the observing time, created the schedules, conducted the sessions, processed the spacecraft signal and finally performed the post-processing of the signal. When the sessions were observed with another VLBI antenna, the author arranged the observing time, prepared the schedules, transferred the data from the station to Metsähovi, processed the data and analysed the phase and Doppler detections of the spacecraft signal. The author also developed the post-analysis of the spacecraft signal software and improved significantly the spacecraft multi-tone software. In VLBI and Doppler tracking, which involves the correlation of the signal with a correlator, the author was responsible for the narrow-band detection of the spacecraft. The rest of broadband correlation and phase-referencing was conducted at JIVE by my thesis advisor.

The author conducted the observations for characterising the interplanetary scintillations in Chapter 6. That work included selecting the proper epochs to observe, creating the schedules, processing the spacecraft signal with the spacecraft multi-tone software, analysing the phase fluctuations per each session and finally compiling all the results together to project the phase scintillations at several solar elongations and different distance to the target. The author also developed the Matlab code to analyse the phase fluctuations and estimate the Kolmogorov spectrum.

2. Fundamentals of radio spectroscopy and VLBI

2.1 Microwave spectroscopy

2.1.1 Interstellar microwave spectroscopy

Microwave spectroscopy became an identifiable branch of experimental physics in the field of radio astronomy in the middle of the last century. Karl Jansky was the first man to discover emissions in the sky of natural radio sources back in 1930. He reported undetermined radio signals originated in near-by galaxies at $20\,\mathrm{MHz}$ frequency. Until two decades later, the radio astronomers did not continue the path initiated by Jansky and started unveiling several molecular spectra lines, quasars, pulsars and the cosmic microwave background. Hence, radio astronomy is considered as a relatively new technique compared to the classic optical observations.

Optical observations primarily target to the surface of planets and stars; the high temperatures of the stars bring the thermal radiation into the visible range. X-ray astronomy addresses to hotter regions, where the temperatures are of the order of several million Kelvins, such as ionized gas found in the solar corona or in the centre of galaxies clusters. Infrared observations deal with cooler regions, where the thermal radiation from dust in the interstellar medium is a prominent feature, or with warmer regions, originated by star-forming areas with a strong thermal radiation. The radio astronomers study a broad range of thermal radiation phenomena caused by a wide variety of molecular lines at several different wavelengths. The energy flux of the electromagnetic radiation spectrum visible from the Earth is illustrated in Figure 2.1.

As seen in the illustration, the optical window is relatively narrow be-
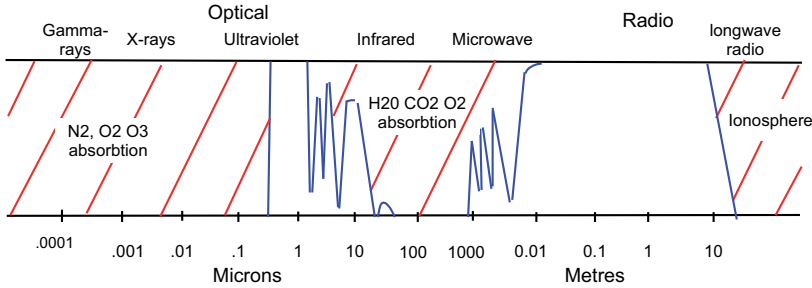
Figure 2.1. Electromagnetic spectrum from long wave radio to γ-rays visible from the Earth. The radio signals captured from antennas on Earth are limited by the ionosphere and atmosphere absorption of certain wavelengths.

tween the infrared and ultraviolet. The ozone layer absorbs the ultraviolet rays while the water vapour and carbon dioxides the infrared waves. Furthermore, the X- and γ-rays are completely blocked by the atmosphere. Thus, the observations at this frequency range need to be carried out using telescopes in space. Several radio spectral lines are absorbed by the atmosphere, but the majority of large wavelengths can be observed from ground stations on the Earth. The radio wave window shown above is still fragmented into several frequency bands and wavelengths: HF (below $30\,\mathrm{MHz}$), VHF (30-$300\,\mathrm{MHz}$), UHF (300-$1000\,\mathrm{MHz}$), microwaves (1-$30\,\mathrm{GHz}$), millimetre-wave and sub-millimetre-wave (30-$300\,\mathrm{GHz}$). In addition to this division, the microwave band is also characterised as: L-band ($20\,\mathrm{cm}$ / $1\,\mathrm{GHz}$), S-band ($10\,\mathrm{cm}$ / $2\,\mathrm{GHz}$), X-band ($3\,\mathrm{cm}$ / $8\,\mathrm{GHz}$), Ku-band ($2\,\mathrm{cm}$ / $12\,\mathrm{GHz}$), and K-band ($1\,\mathrm{cm}$ / $22\,\mathrm{GHz}$).

Two different kind of emissions of the wide radio spectrum are detected using Earth-based radio telescopes. The radio emission from hot sources, such as the Sun, is understood as a **thermal process**. In this case, the radiation is generated by electron-ion collisions, also known as free-free emission. The heat emitted in this thermal process implies that the medium is in near-equilibrium state. On the other hand, the outburst of very powerful radiation, like the explosions of supernova, cannot be associated with a process in equilibrium. In this case, the radiation from these sources is called a **non-thermal process**.

2.1.2 Radio spectral line

Spectral lines are caused by the interaction between the quantum systems. In the radio range, these systems are usually molecules or single

photons. Any photon, which reaches a certain level of energy, provokes a change in the energy state of the system. The photon ends being absorbed by the molecule and, consequently, spontaneously re-emitted, either with similar frequency or in cascade. The sum of the energy emitted by these photons is equal to the energy of the one absorbed.

Depending on the nature of the molecule these changes in the quantum system can either cause an **emission line** or an **absorption line**. The emission lines are one of the main targets of radio astronomy. Meanwhile, the absorption lines are one of the major problems for radio observations, since the atmosphere absorbs several spectral lines. A basic scheme for a quantum system is shown in Figure 2.2.
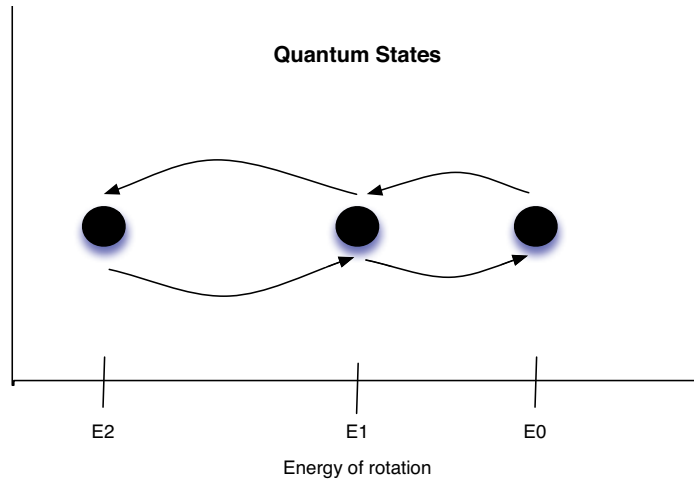
Figure 2.2. Notational energies of a simple diatomic molecule. Collisions with other molecules in the gas cause a molecule to change its quantum state. A collision can either speed up the rotation or slow it down.

The frequency of emission by a molecule and a proton was first announced by Bohr [1] in the quantum relation given by:

$$hv = E_1 - E_2 \tag{2.1}$$

where E_1 and E_2 are the energy levels of two different quantum states, h is the Planck constant ($h = 6.626 \cdot 10^{-34} \, \text{m}^2\text{kg/s}$) and v the frequency of rotation.

Radio spectroscopy investigates all possible spectral lines, radiated from any interesting celestial body, that are detectable in the electromagnetic spectrum. Spectroscopy is mostly used to determine physical characteristics of the distant stars, quasar or galaxies. However, it is also suitable

for the search of the spectral emissions of the Solar System planets or for calculating the motion of elements, planets or spacecraft, by means of Doppler shift measurements. The spectrometers measure the density flux of the entire instantaneous bandwidth of the receiver to determine the broad continuum spectrum of the radio source. This frequency bandwidth is usually divided into several smaller frequencies, also known as frequency channels. The receivers are band pass limited enabling the measurement of few spectral lines in each frequency band. Systems with a large number of narrow channels are limited by their poor efficiency. Since, they require require a high hardware complexity and usually the resolution achieved is lower than desired. The design of a spectrometer is usually based on demand and requirements. Hence, several examples of how hardware spectrometers have been built can be found in the literature [2].

The analysis of spectral lines can have another approach. It consists of recording the temporal evolution of the electromagnetic signal captured by the wide band receiver and then calculate the spectrum, as described in [3]. This implementation allows aiming for higher resolution when increasing the post-processing latency. This technique is also compatible with the VLBI hardware systems. The work by the author concentrates mainly on recording the temporal signal to disk and calculating the frequency spectra with the newly developed software spectrometer. This auto correlator software is described in detail in Chapters 4 and 5.

2.1.3 Masers

Many molecular clouds and the mass outflow from giant stars emit strong radio signals known as **maser** (Microwave Amplification by the Stimulated Emission of Radiation). They originate when the energy levels of a molecular combination are populated in a non-Boltzmann distribution [4]. The exchange of energy within the molecular combination is small, typically in the order of $0.1\,\mathrm{K}$. The molecular clouds contain material and radiation at different temperatures and a population inversion (a negative state temperature) may be caused by **radiation** or **collisions**. The typical emissions from the masers are originated by several types of molecules, the strongest and the most commonly observed are OH, H_2O and SiO masers. Maser emission requires a pump to maintain the population of the upper energy level above the equilibrium thermal level. This

pump may be caused by a source of radiation or by a mechanism of collision. In both cases, the equivalent temperature of the pumping process is higher than the temperature corresponding to the energy difference of the energy-level pair that serves as the maser [4].

Weaver reported the first evidence of a maser structure in 1965 [5], when he noticed an intense line seen at the $1665\,$MHz frequency. The emission line was originally attributed to an unknown interstellar origin, since the intensity was too great to be generated by a thermal source. Later studies confirmed that the spectral line belonged to the hydroxyl emission at $18\,$cm wavelength. Several masers were discovered in multiple molecular clouds in the following years. In 1982, the discovery of emission from an extra-galactic source with luminosity about million times larger than earlier detections started a new era in the study of masers. These powerful masers were denominated as **megamasers**. Several examples of megamasers have been found ever since.

The origin of the masers can be separated in two types: the circumstellar masers, which are originated in outflow, and interstellar masers, where the material is condensed to form new stars. Both astrophysical masers are of great interest to understand unknown conditions in the space: number density, magnetic field, temperature or velocity from stellar birth and death or the galactic nucleus.

The H_2O masers usually appear far from the central star, at distances between 6 and 30 solar radius. They are also found in regions of active star formation. Several powerful megamasers are found in certain external galaxies as NGC 5128. The most prominent line for detection is characterised at $22\,$GHz and is the transition between rotational states designated 6_{16}-5_{23}. The excitation of the states in the water masers is produced by collisions with molecules, requiring a temperature of at least $225\,$K, consistent with the location further away from the star. The total energy output of these water masers, concentrated in few kHz band, can carry more energy than the total bolometric output of the Sun. Masers vary their intensity by orders of magnitude over periods of months or years.

2.2 Space radio science

Radio scientists take benefit of the data communications links between spacecraft and ground stations to examine very small variations that oc-

cur in the power amplitude, phase, frequency and/or polarization of the radio signals to investigate a broad range of physical phenomena in the Solar System. These phenomena are mainly related to propagation effects of the radio waves through the atmospheres of planets and the solar corona. Radio science experiments include a broad range of interesting fields, such as: atmospheric temperature-pressure profiles and ionospheric composition of planets and satellites, structure of planetary rings, planetary gravitational fields, shapes and masses of the bodies, characteristics of the planetary surfaces, atmospheric wind profiles, magnetic fields, deviation on the ephemerides of the planets, total electron content and scintillation in the solar corona, mass flux and particle distribution of comets, search for gravitational radiation, gravitational red-shift, and relativistic time-delay experiments. The basic scheme of a radio science experiment is shown in Figure 2.3
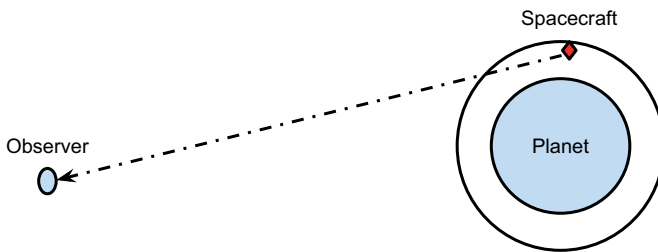
Figure 2.3. Typical scheme of radio science experiments, where the radio telescope detects and processes the signal transmitted by a spacecraft.

Radio science mainly studies the temporal evolution and frequency variations of the radio signal transmitted by the spacecraft due to the propagation of the waves in a non-homogeneous media. The signal is monitored for a long continuous time range. The results improve if the spacecraft is equipped with dual-frequency transmitting channels or the observations are repeated during consecutive epochs.

The technique of **radio occultation** is convenient for studying the atmosphere of the planets and their gravity fields. The method consists on tracking the spacecraft radio signal, when it disappears behind a planet and then reappears from the other site. During these events the radio waves pass through regions of the planetary atmosphere.

The sensitivity of the end-to-end radio science experiments depends on

several key elements. Among them, the most important are the stability of the frequency and amplitude of the signal transmitted, the Signal-to-Noise Ratio (SNR), the accuracy in reconstructing the navigation trajectories or the optimal characterisation of the propagation effects of the media. A complete summary of the radio data communications system on a spacecraft is described in Section 5.1.3.

2.2.1 Radio wave propagation

We assume that the propagation of a radio signal travelling from the spacecraft to the radio telescope on the Earth may be considered as in free space. In principle the waves crossing the Solar System do not experience a strong degradation by the medium. Therefore, the propagation of a free radio wave can be simplified as shown in [6]:

$$P_R = \frac{P_T A_R A_T}{L^2 \lambda^2} \tag{2.2}$$

where P_R and P_T are the received and transmitted power, the A_R and A_T are the receiving and transmitting antennas effective area, L is the distance between spacecraft and ground-station and λ is the wavelength of the signal.

The relation shown in Equation 2.2 is only applicable to radio waves moving in free space. Unfortunately, the spacecraft communications signals are affected by the propagation through the troposphere and ionosphere of the Earth, the atmosphere of the planet or the satellite, in which they orbit, and from the solar corona. In this situation, the amplitude and phase of the signal may vary due to the absorption and fluctuation produced on the propagation media. The frequency and polarization of the radio waves may slightly drift from its original value. Moreover, the radio waves may be refracted in the propagation media causing the ray path to deviate from its expected. Lastly the travel time for the signal may increase from the estimated.

The effect of the ionosphere is not distributed equally along the globe. The **power fluctuations** are more accentuated in the northern pole area than in the middle or equatorial latitudes. The incidence is relatively similar to all the signals and independent of the wavelength. The ionospheric fluctuations have been well-studied during the last years and specially the dependence of the fluctuation amplitude on the wavelength and geometric parameters for the ray path [7, 8]. However, the irregular and

turbulent nature of the ionospheric plasma obstructs the measure of the depth of these fluctuations.

The propagation of radio waves in the centi- and millimetre range in the troposphere is limited by their absorption by water vapour and oxygen. These gases cause a strong attenuation of the waves intensity depending on the depth of the tropospheric layer. The attenuation of radio waves is defined by the term Y, as the ratio between the emitted and received power [9].

$$Y = \frac{P_R}{P_T} = \exp\left(-\int \gamma_1 dl\right) \tag{2.3}$$

The attenuation is also expressed as the integral of the absorption coefficient (γ) in the path section of the troposphere (ΔL) assuming a homogeneous medium. Once again, the troposphere is not a homogeneous medium and the attenuation should be integrated along the path, taking into account any kind of water and oxygen bubbles. However, for a first approximation we can reduce the attenuation as:

$$Y = \exp\left(-\gamma_1 \Delta L\right) \tag{2.4}$$

where the absorption coefficient is basically the contribution of two absorbing gases: water vapour and oxygen ($\gamma_1 = \gamma_w + \gamma_o$).

The distance between the spacecraft and the receiving antenna is estimated by the time elapsed (Δt) between the transmission and reception multiplied by the speed of an electromagnetic wave propagating on vacuum:

$$L = \Delta t \cdot c \tag{2.5}$$

The troposphere and ionosphere of the Earth introduce a significant error in the **ranging** or **time delay** of the signal, since the speed of a wave propagating for the media differs from c, and rays are bent. The estimated measure of L is slightly higher than the theoretical value. The effect of the different atmosphere layers on the ranging has to be taken into account when it is necessary to determine precisely the position of a planetary spacecraft or terrestrial location using global positioning satellites. In the case of geodesy, more complex models of the atmosphere are used to determine more accurately the magnitude of L [10].

Several references in the literature demonstrate how to calculate the path delay in the troposphere and ionosphere [9, 11]. One theoretical approach that suits the VLBI spacecraft tracking consists on using multiple frequency channels. In this case, the real distance between observer and spacecraft is calculated using two separated frequency channels and with only one antenna:

$$L_0 = \frac{m^2 L_2 - L_1}{m^2 - 1} \tag{2.6}$$

where m depends on the frequencies f_1 and f_2 and follows the relation $f_2 = m \cdot f_1$. This dual-frequency method let us to calculate the value of L_0 accurately. This method assumes that the refraction of the ray is similar in both radio wavelengths. This statement is valid in decimetre radio waves, however, in metre wavelengths it is not necessarily true. The refractive index of a charged media depends on the radio wave frequency f as $(1 - a/f^2)$, hence, the propagation path of waves with different frequencies may differ considerable at lower frequencies (below $\sim 500\,\mathrm{MHz}$).

The propagation of the radio waves through the atmosphere is also accompanied from irregular **phase fluctuations**. These phase variations will condition the performance of the antenna and of the data correlation. Indeed, instability of the phase detected may lead to wrong estimates of spacecraft state vectors in orbit determination. In principle, the phase fluctuation of a signal propagating in the atmosphere is estimated as:

$$\phi \;=\; \phi_0 + \phi_1 + \delta\phi \tag{2.7}$$

where ϕ_0 is the phase of radio wave travelling in vacuum and basically depend on ($\phi_0 = 2\pi\lambda^{-1}L$). ϕ_1 is the phase shift of the radio wave in the atmosphere ($\phi_1 = 2\phi\lambda^{-1}\Delta L$) and finally the term $\delta\phi$ that takes into account undetermined phase fluctuations.

The troposphere and ionosphere also insert small variations in the carrier frequency of the signal emitted by the spacecraft. This frequency variation caused in the atmosphere of the Earth is a small contribution to the **Doppler shift**. These anomalies on the signal described for the Earth should be considered for the planet where the spacecraft orbits as well. Of course, depending on the nature of the planet (specially the characteristics of its atmosphere) and the orbit position at the time of observations the incidence on the radio waves may be lower or higher.

2.2.2 Propagation in the interplanetary plasma

The interplanetary and circumsolar plasma affects as well the propagation of the radio wave transmitted by a spacecraft. The plasma generated by the Sun is ejected towards the solar corona and travels at high velocity into interplanetary space. This stream of plasma into the space is called **solar wind**. It originates in the solar photosphere, accelerates to supersonic velocities, crosses the Solar System and finally diffuses into interstellar space. The concentration of the plasma depends on the solar activity level and the distance to the Sun as well. Approximately, about one million tons of matter per second are emitted into outer space. For instance, up to five plasma particles per cubic centimetre can be detected at a distance from the Sun equivalent to the position of the Earth [12].

The solar wind distorts the radio waves in a similar way like the planetary atmosphere does. These effects include the time delay on the signal, rotation of the polarization, ray refraction, amplitude and phase variations, frequency drift, and the spectral line broadening.

The first studies investigating the relationship between the time delay on a radio wave and the electron content density used optical measurements of the Sun itself [13]. New techniques of detecting accurately the arrival time of a distant pulsar at different frequencies introduced a new method to calculate the relation between both terms [14, 15]. Other opportunities to estimate the electron density were offered by studying the propagation of the radio signal through the solar plasma. The spacecraft data communications path towards the Earth propagating through the Solar System is illustrated in Figure 2.4.

Where a is the solar radius, r is the distance of any point along the path with respect to the Sun, p is the impact point (closest point between the path trajectory and the Sun) and L is the path length. When the radio wave travels through the solar corona, the measurement of the trajectory leads to apparent larger distance. Determining the integral electron density I as a function of the impact parameter p is possible from the measured values of ΔT, as demonstrated by Muhleman et al. [16]. In the paper, the study of the radio communications of several spacecraft missions leaded to an approximated time delay of:

$$\Delta T = \frac{\gamma}{c \cdot f^2} \int_0^L N(l)\delta l \qquad (2.8)$$

Figure 2.4. Spacecraft data link scheme. The signal propagates through the interplanetary plasma (L is the distance) toward the Earth. The amplitude and phase of the signal fluctuates due to the solar wind (at velocity V).

where l is measured along the direct-line path between the spacecraft and the Earth, the constant γ is equal to $40.4 \, \mathrm{m}^{-3} \, \mathrm{kHz}^{-3}$ and $N(l)$ is the density profile of any point in the path with respect to the Sun. The time delay and deviation of the path length directly depends on the total electron density for the line of sight. The deviation of path length is:

$$\Delta S = \frac{\gamma}{f^2} \int_0^L \Delta N(l) \delta l \tag{2.9}$$

For the electron density profile in the solar wind we use the approach described in [16, 17]. This approach is valid when the distance respect the Sun is 3 times bigger than its radius ($r \geq 3a$):

$$N_e = \left[2.21 \cdot 10^8 \left(\frac{a}{r} \right)^6 + 1.55 \cdot 10^6 \left(\frac{a}{r} \right)^{2.3} \right] \quad cm^{-3} \tag{2.10}$$

where a is $6.96 \cdot 10^{05}$ km and r is the distance of any point with respect to the Sun. The first term dominates the waves nearer the Sun and the second term defines the solar wind at farther distances with a slower radial attenuation.

The radial decrease of the electron density in the circumsolar plasma may cause the radio waves to refract. This effect is also known as **ray path bending**. The most direct effect of the path bending is the increase on the propagation distance, but also the transmitted frequency

of the signal experiences Doppler shift. This Doppler noise can be evaluated either using two rays at different frequencies or two rays with the same frequency captured by two antennas simultaneously. The refractive frequency shift ΔF depends on the refraction angle ξ and the relation between the impact point and the solar radius (p/a). The refractive frequency shift can be derived from the Equations 2.8 and 2.10. The estimation of ΔF was extracted from the work of Yakovlev [9] and the derivation will not be explicitly described here:

$$\Delta F = \frac{\gamma u}{cf} \left[1.3 \cdot 10^9 \left(\frac{a}{p} \right)^6 + 5.3 \cdot 10^6 \left(\frac{a}{p} \right)^{2.3} \right] \tag{2.11}$$

where u is the rate of impact parameter changes.

Studies of the radio waves fluctuations and the spectral broadening are relevant for determining the plasma heterogeneity. The interplanetary plasma is considered as a randomly inhomogeneous medium with a wide range of scales. The plasma inhomogeneity can range from tens to thousand of kilometres [18, 19]. The motion of the plasma irregularities directly provokes the phase and amplitude fluctuations of the signal and broadening of its power spectrum. The magnitude of the fluctuations is reduced inversely proportional with the distance respect to the Sun ($1/r^2$).

Several studies have compared the interplanetary plasma irregularities with the turbulence presence on the ionized gases [9, 20]. The spatial spectrum of the refractive index fluctuations can be calculated as:

$$\Phi_n(\textit{æ}) = 0.033 c_n^2 \left(\textit{æ}^2 + \textit{æ}_0^2 \right)^{-\alpha/2} exp \left(-\frac{\textit{æ}^2}{\textit{æ}_m^2} \right) \tag{2.12}$$

where Φ_n is the spatial spectrum of refractive index of irregularities of radio wave phase, $\textit{æ}$ is the spatial wave number with $\textit{æ} = 2\pi/\Lambda$, where Λ determines the characteristic scales of large plasma irregularities crossed by the signal, $\textit{æ}_m$ and $\textit{æ}_0$ are the spatial wave numbers in the outer and inner scales of the refractive index irregularities respectively, c_n is the structural coefficient of plasma irregularity and α is the spatial spectrum index of plasma irregularities. If we assume that the refractive index $\textit{æ}$ is within the interval [$\textit{æ}_0$,$\textit{æ}_m$] the Equation 2.12 can be simplified to [9]:

$$\Phi_n(\textit{æ}) = 0.033 c_n^2 \textit{æ}^{-\alpha/2} \tag{2.13}$$

Typical values in the interplanetary and circumsolar plasma for these parameters are $\Lambda_0 \approx 10^{06}$ km, size of the plasma irregularities ≈ 10 km

and the coefficient of plasma irregularity $\alpha \approx 11/3$. The dependency of the radio wave fluctuations is proportional to the spatial spectrum index of plasma irregularities.

The variance of the phase fluctuations is defined by the coefficient σ_φ^2. The fluctuations suffered by a radio wave are generally more intense in phase than in amplitude ($\sigma_\varphi^2 \gg \sigma_{Sc}^2$). The variance can be calculated as [9]:

$$\alpha_\varphi^2 = (2\pi k)^2 \int_0^L \int_0^{\ae_0} \Phi_n(\ae)\ae\, d\ae\, dx \tag{2.14}$$

where k is the wavenumber of a wave propagating in vacuum, the integration is done with respect to the path spacecraft-Earth and the wave number of the plasma inhomogeneity spectrum ($\ae$), from 0 to $\ae= 2\pi\Lambda_0^{-1}$. The whole derivation can be seen in the work developed by Coles et al. and Woo et al. [21, 22]. In both cases, the variance of the phase fluctuation leads to:

$$\alpha_\varphi^2 = 0.018k^2\Lambda_0^{5/3}c_0^2\, a^2\, p^{-2}\, L \tag{2.15}$$

where p is the impact point, a is the solar radius, and L is the distance to the spacecraft. These formulas are valid when the observation of the signal is long enough, usually like $\Delta T > \Lambda_0/V$. The optimal recording time for (ΔT) is above 3 hours, since typically the $\Delta_0 = 3 \cdot 10^6$ km and V is approximately $400\,\mathrm{km\ s^{-1}}$.

Finally, we consider that the spectrum of the phase fluctuations ϕ_φ is proportional to the power function ω^{-m} with the parameter m given by:

$$m = \alpha - 1 \tag{2.16}$$

This relation basically indicates that the index α of the spatial spectrum of plasma irregularities is estimated from the index m of the power-law spectrum of the phase fluctuations.

We have found several studies in the literature that report how to calculate the index m using spacecraft missions. The first results reported accounted an m equal to 2.6 [23], 2.68 ± 0.3 [24] and 2.65 ± 0.2 [25]. The phase fluctuation spectra of the Viking spacecraft radio signal presented on [24] are illustrated in Figure 2.5.

The curves 1, 2 and 3 correspond to the impact parameters p/a equal to 2.17, 10.5 and 30.5 respectively within the interval $[20 < p/a < 200]$;
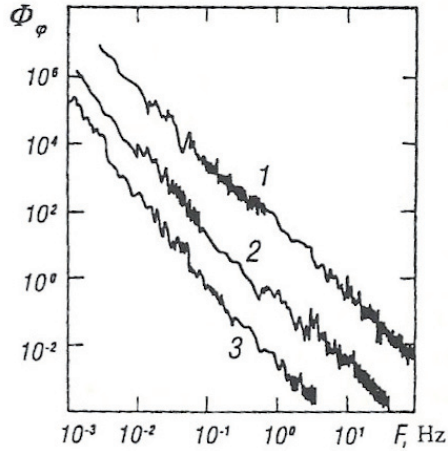
Figure 2.5. Representative spectra of phase fluctuation presented in the paper Woo et al. 1979. The curves 1, 2 and 3 correspond to the impact parameters p/a equal to 2.17, 10.5 and 30.5 respectively. The variance of phase fluctuations varies according to the law $\sigma_\varphi \sim p^{-2.45}$.

the variance of the phase fluctuations varies according to the law $\sigma_\varphi \sim p^{-2.45}$. The spectral components of phase scintillations take the range of $1\,\mathrm{mHz}$ to $10\,\mathrm{Hz}$, which corresponds to the size of plasma irregularities ranging from 40 to $4\cdot10^{05}\,\mathrm{km}$. The plasma irregularities also move on time and therefore cause random variations in the radio signal frequency and induce the broadening of its spectral line.

2.3 Radio interferometer

2.3.1 Radio interferometer system

The capacity of the radio astronomers to distinguish finer details in the sky, known as **angular resolution**, is limited by the wavelength of the signal and the size of the radio telescope. It is possible to achieve higher angular resolution, and therefore improve the antenna sensitivity, simply by building a radio telescope with a bigger dish. However, the **slewing speed**, defined as the capacity to track at certain speed any sky object, becomes a handicap. Needless to say, bigger dishes have also a serious impact on the cost of building the new antenna.

Radio interferometry allows combining the signal captured simultaneously by two or more elements with the benefit of improving the angular

resolution of the individual antenna. The elements of a radio interferometer array can be either physically connected to each other or not. More details about these two types are seen in Section 2.3.3. The angular resolution for a single-dish (R) is defined as in [6].

$$R = \frac{\lambda}{D} \tag{2.17}$$

where λ is the wavelength of the observations and D the diameter of the dish. The angular resolution for a radio interferometer system is similar to the resolution for single-dish [6].

$$R = \frac{\lambda}{b} \tag{2.18}$$

where b is the longitude of the physical separation between the elements of the system, also known as **baseline**. From this equation we can easily prove that the highest resolution achievable by a radio interferometer on-Earth is limited by the diameter of the globe. Two antennas with a baseline as long as the diameter of the Earth synthesize a dish telescope as large as the planet itself.

The radio telescope captures the upcoming radio signal from a compact source, down-converts it to baseband frequency and records its total power as a function of time. In radio interferometry, the same radio signals are received by two or more antennas, down-converted by their radio receivers and combined in the post-processing. A diagram of a two-element interferometer is shown in Figure 2.6.

The signals detected by the elements of the interferometer are mixture of cosmic background noise, noise generated in the receivers and Earth-based radio interferences. The two antennas are separated by the baseline b_λ, expressed in terms of wavelength, and both are pointing into the direction of the radio source, specified by the vector s. The geometric time delay between the signal arriving at antenna A and antenna B is given by:

$$\tau_g = \frac{b \cdot s}{c} \tag{2.19}$$

where $b = \lambda \cdot b_\lambda$ and s is the direction vector to the source. One of the antennas is always designated as the reference antenna.

Radio interferometry also lets us to create multi-pixel maps of the radio sources at any frequency band using multiple baselines. The **Earth**
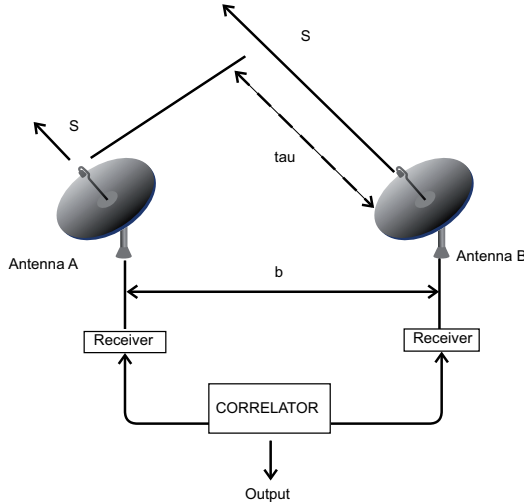
Figure 2.6. Geometry of the two-element interferometer. The difference in the arriving time of the signal at each telescope is known as the path delay (τ_g). The correlator measures and compensated this delay.

Rotation synthesis, first introduced by Ryle [26], takes the advantage of the Earth rotation to model the shape of the source as the orientation of the baselines and elements on the interferometer shift with respect to the source. The source image and its surroundings is formed indirectly from the complex visibilities according to the geometry of the interferometer baselines. Briefly, the image reconstruction consists of three main steps as reported by Cornwell [27]. First, an initial dirty image is formed from the visibility data via Fourier inversion. Secondly, the deconvolution correction is applied for the Fourier plane sampling effects. Finally, the atmospheric and instrumental errors are corrected, causing phase and amplitude fluctuations in the visibility measurements.

The interferometry theory can be found in several examples of the literature [28, 29]. Primarily two basic approaches for the correlation of the data are used: in time-domain and in frequency-domain. The approach for correlation based on the time-domain, found on the books mentioned above, is briefly described here. The radio signal received at the antennas can be considered as a monochromatic signal, with frequency ν, since it simplifies the analysis. For the same reason, the instrumental delay τ_i at each of the stations is considered null. Considering the detected signal at the antenna A as $V(t) = \upsilon_A \cos 2\pi\nu(t - \tau_g)$, the cross-correlation defined as:

$$R(\tau) = \langle x(t) \cdot y(t - \tau) \rangle \qquad (2.20)$$

being $x(t)$ a sinusoidal signal with a certain amplitude. The product of both signals is:

$$r(t) = A(s)S \cdot \cos\left(2\pi\nu\tau_g\right) = A(s)S \cdot \cos\left(2\pi b_\lambda \cdot s\right) \qquad (2.21)$$

where the power amplitude of the signal is proportional to the effective antenna area $A(s)$ and the density flux of the source S. From a physical point of view the output of the cross-correlation is an average of the power energy of the source, modulated by a quasi-sinusoidal oscillation. This quasi-sinusoidal modulation is called in VLBI terms as the **fringe pattern**. The alternately constructive and destructive interference of the signals from both antennas originates this fringe modulation. An alternative to the time domain analysis of the cross-correlation is to handle it in the frequency domain. Instead of calculating the cross-correlation product, the product of the Fourier transform of both signals are calculated. Either way, the primarily task in order to correlate the input signals is to search for the optimal fringe time, or **fringe frequency**, that constructs correctly the sum of them.

The **fringe visibility** (V_M) is considered as the relative amplitude of the fringes. The complex visibility (V_{ij}) introduced by Bracewell in 1958 [30], is a measure of the coherence of the radio sky brightness distribution, between to antennas i and j and takes into account the fringe phase. The complex visibility for two antennas i and j is:

$$V_{ij} = \int A(\sigma)B_\nu(\sigma)\exp\left(i2\pi b_{ij,\lambda}\sigma\right)d\omega^2 \qquad (2.22)$$

Once the complex visibility for a baseline is calculated, it is time to generate the radio sky image of its brightness distribution. To express the visibility and the sky brightness of a source in a more valid coordinate system, we substitute the current axis to ones based on the baseline vector of the two antennas $b_{ij,\lambda}$ (u, v, w). The axis w is defined by the unit vector s_0, and in the perpendicular plane, the directions u and v are projected to celestial east and north respectively. This perpendicular plane to the source is known as uv-plane. The natural units for the visibility plane are expressed in wavelengths of the observed frequency. So the previous expression in Equation 2.22 can now be expressed in uv-plane as:

$$V(u, v) = \int B(x, y) \exp\left(i2\pi\left(u(x)v(y)\right)\right) dx\, dy \qquad (2.23)$$

The visibility evaluates the Fourier transform of any source brightness distribution at a particular wavelength projected onto the respective uv-plane and by a specific baseline vector. A single observation by an interferometer provides the brightness value of one point, but complete observations determine the Fourier transform of the source brightness distribution.

The sensitivity of a single-dish radio telescope is known as the System Equivalent Flux Density (SEFD). The SEFD is the flux density that produces an amount of power equal to the off-source noise measured by the antenna expressed in Janskys and it is a measure of the performance of the antenna and the receiving equipment. The SEFD for a radio interferometer improves as well by adding multiple baselines. Having the antennas i and j, the RMS noise ΔS of the baseline in a radio interferometer system according to Wrobel and Walker [31] is:

$$\Delta S_{ij} = \frac{1}{\eta_s} \cdot \sqrt{\frac{SEFD_i \cdot SEFD_j}{2BW\tau_{int}}} \qquad (2.24)$$

where τ_{int} is the integration time, BW the total bandwidth of observations and η_S the system efficiency of the data recording and correlator. Therefore, the image sensitivity ΔI_m for an array of identical elements is calculated as the standard deviation of L-sample mean $\Delta I_m = \Delta S/L$. The image sensitivity is now the standard deviation of the mean:

$$\Delta I_m = \frac{1}{\nu_s} \cdot \frac{SEFD_{ar}}{\sqrt{N\,(N-1)BW\tau_{int}}} \qquad (2.25)$$

where N is the number of antennae in the array and $L = 1/2 \cdot N \cdot (N-1)$. The SEFD for an array with identical kind of antennas is basically the sum all SEFD over each possible baseline:

$$SEFD_{ar} = \frac{1}{\eta_S} \frac{SEFD_i}{\sqrt{N\,(N-1)/2}} \qquad (2.26)$$

2.3.2 Very Long Baseline Interferometry

VLBI is a technique where radio telescopes that are not physically connected can be used as a radio interferometer array. The distances between

the elements of the array can be separated by thousands of kilometres. The interferometry of telescopes is conducted by inserting accurate timestamps into the data, which is recorded into disks at each of the stations. The precise time information is provided by a stable atomic frequency oscillator. One of the principal requirements for a VLBI station is to have a standard hydrogen maser oscillator that generates a master signal and which is inserted into the VLBI data. In the correlator centre, all the data from each station are played back and the timestamps are synchronised to align the radio signal. The instability of each independent local maser is solved with the use of global accurate timing information. GPS gives precise information of the offset between the GPS timing and the frequency oscillator of the radio telescopes. For instance, at Metsähovi we record these offsets every second and they are available via FTP for the correlation centre.

The concept in VLBI is similar to a connected-element interferometer, although some differences exist. In the VLBI systems and in general in most of the radio telescopes, the radio frequency (RF) signal is down-converted to intermediate frequencies (IF) several times. The cost and complexity decreases when data is handled in lower frequency bands. First, the signal is down converted in the receiver to an IF around $1\,$GHz. Then again down converted into multiple channels (baseband frequency). These frequency channels are usually limited to a bandwidth of 2, 4, 8 or $16\,$MHz. The bandwidth of the channels and the amount of channels is currently limited (among others) for the VLBI hardware system and the capacity to record the digital data into disks. Typical scheme of a VLBI system is shown in Figure 2.7

The highest angular resolution at any frequency band in radio astronomy is only achievable using VLBI techniques. The longer the antenna baselines are, the larger the synthesized radio telescope is. Therefore more distant and weaker radio sources can be observed.

Another direct benefit of the VLBI observations is the cancellation of most of the radio frequency interferences (RFI) on the observations. Almost all the RFI present at the telescopes are independent and particular for each station. The interference signals are not correlated between them, unlike the signal that arrives from the radio source. Therefore all undesired interferences are eliminated at the output of the correlator. Furthermore, signals arriving from directions with an offset from the observed radio source by more than an angular-resolution scale are dis-
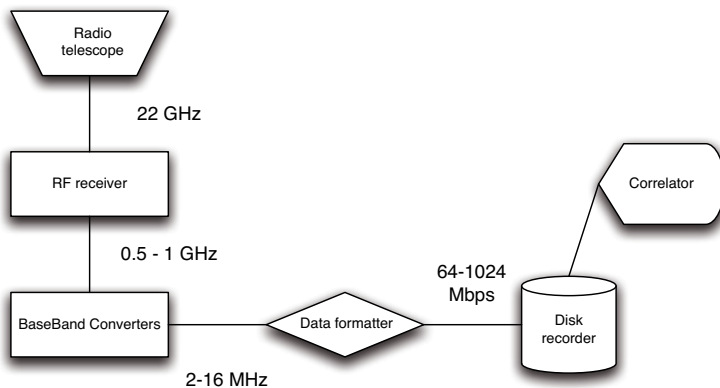
Figure 2.7. Typical configuration of a VLBI radio telescope.

persed or washed out in the interferometer instrumentation [32].

In the old times the VLBI observations used to be recorded on thick magnetic tapes. The magnetic tape recorders were substituted by conventional computers and disk packs in the beginning of the new millennium. The Mark5 disk pack modules consisted of a rugged enclosure with 8 hard disks [33]. They are inserted inside the Mark5A unit to record the observations. Once the observations are completed the disks are shipped by regular courier service to the correlator centre. Metsähovi developed an alternative recording system aiming for simpler design and based on regular computer components [34]. The PC-EVN stored the data in standard Linux RAID systems. Shipping disks using regular post service delays the data correlation for several weeks. From 2005 and on-wards, in most of the observations conducted at Metsähovi the data are recorded to disks and then transferred via a high-speed network connection after the experiment. More detailed information about digital back ends and VLBI systems is explained in Chapter 3.

In e-VLBI data is no longer recorded to disks, but instead the digitized data is transferred directly to the correlator via Internet or dedicated lightpaths. The e-VLBI takes advantage of the last improvement in fibre-connection and the advance educational fibre networks available along all the Europe to perform routine interferometric observations ranging from 512 Mbit/s up to Gbit/s. We demonstrate successful experiments of e-VLBI data transfers up to 8 Gbit/s in a single baseline [35].

2.3.3 Current radio interferometers

For several years new radio interferometer arrays have emerged world wide and the perspective for new systems is prominent. Compromise in radio interferometers must be made between big or fast. The sensitivity and accuracy are higher in dishes with bigger size, although tracking and switching between sources is slower. Hence, the trend is to replace those big antenna by multiple smaller ones. The current main connected-element interferometers are:

- **Merlin** the six antenna forms an array, with dishes of several sizes, spread around England. A coming upgrade will link the telescopes with fibre-optic (e-Merlin).

- **Westerbrok Synthesis Radio Telescope** is a 16-antenna array, each dish with 25-metre diameter, located in the Netherlands.

- **Very Large Array** (VLA) is 27-antenna array, 25-metre diameter each, located in the desert of New Mexico, USA.

- **Atacama Large Millimetre Array** (ALMA) is on-going project that aims to install about 50 small dish antennas (12-m) to observe a wide frequency range 30-850 GHz, in Chile.

Thanks to the high-speed networks and the possibility to include almost any telescope in the world in the same array the Very Long Baseline Interferometers are becoming more fashionable. Some of them are:

- **European VLBI Network** (EVN), a network of 20 radio telescopes from Europe and other location around the globe coordinated by the Joint Institute for VLBI in Europe, the Netherlands.

- **Very Long Baseline Array** (VLBA) consists of 10 antenna located along the United States.

- **Australian Large Baseline Array** (LBA) consists of up to 9 antennas along the Australian land with the expectation that New Zealand joins the array.

- **VLBI Exploration of Radio Astrometry** (VERA) consists of a VLBI array of several antennas distributed along the Japanese islands.

- China, Korea and India are the latest countries to construct their own VLBI radio telescopes and soon we could see a new Asian array.

The future of the radio astronomy leads to the development of completely new radio interferometer arrays with larger bandwidth and multiple frequency bands. These arrays include the Low Frequency Array (LOFAR), the Atacama Large Millimetre and Sub-millimetre Array (ALMA) or the Square Kilometre Array (SKA). For instance, SKA aims to combine the signal received from thousands of small antennae spread over large areas. The array will cover broad frequency coverage from $70\,\mathrm{MHz}$ up to $10\,\mathrm{GHz}$. The project is still in development and estimated to be in operation by 2020.

3. Digital Back Ends

3.1 Introduction

The Metsähovi radio observatory has been an active member of the VLBI community since early 1990. Metsähovi is equipped with a 14-meter diameter high-accuracy parabolic dish and a Cassegrain type feed. The radio telescope is utilised for VLBI astronomical and geodetic observations. The ranges of available frequency bands are S/X-band (2 and 8 GHz with a total bandwidth of 384 MHz), K-band (22 GHz, 0.5 GHz), Q-band (43 GHz, 0.5 GHz) and W-band (80-115 GHz, 0.5 GHz)[1]. The Metsähovi VLBI group has developed new hardware equipment and software applications for VLBI purposes during the last years. These developments were in the framework of the EXPReS [36] and NEXPReS [37] projects.

The primary goal of the **Express Production Real-Time e-VLBI Service** (EXPReS[2]) was to connect up to 16 radio telescopes on the six continents to the central data processor of the European VLBI Network (EVN) at the Joint Institute for VLBI in Europe (JIVE), in the Netherlands. The specific activities to be developed at the radio telescopes involved guaranteeing the last-mile connections to a fast network, upgrading existing connections to the telescopes, updating the correlator to process up to 16 data streams at 1 Gbps each in real time and research possibilities for distributed computing to replace the centralized data processor. The European EXPReS project concluded successfully in summer 2009 achieving all the goals initially proposed [36].

---

[1] Detailed receiver specifications: http://www.metsahovi.fi/en/receiver/

[2] EXPReS was an Integrated Infrastructure Initiative (I3), funded under the European Commission's Sixth Framework Programme (FP6), contract number 026642, from March 2006 through August 2009.

During autumn 2010, there was the continuation of the EXPReS project with the goal to further develop e-VLBI services around Europe. The **Novel Explorations Pushing Robust e-VLBI Services** (NEXPReS[3]) is a 3-year project aimed at further developing e-VLBI services of the EVN, with the goal of incorporating e-VLBI into every astronomical observation conducted by the EVN. NEXPReS is a collaboration project between 15 astronomical institutes and the National Research and Education Network (NREN) providers. The NEXPReS objective is to offer enhanced scientific performance for all the users of the EVN and its partners. The proposed activities will introduce the e-VLBI as standard observation mode to every experiment, aiming for improved robustness, flexibility and higher sensitivity. This will boost the scientific capability of EVN and offer better quality and more rapid radio sky images to the radio astronomers [37].

NEXPReS continues to work on several activities such as providing real-time grid computation, offering dynamic bandwidth or network resources on demand, developing software that manages and process all the complexities in a shared infrastructure and providing high-speed recording hardware and high-capacity network storage. The development of new instrumentation and software for the EVN improves the collaboration between the European institutes. Furthermore, the performance of the stations benefit from close interactivity with the other institutes and possible errors during observations or correlation decrease.

e-VLBI observations became a new challenge to demonstrate the capabilities of the stations to conduct joint real-time VLBI sessions in 2008. Metsähovi participated in several e-VLBI sessions in conjunction with other radio telescopes around the globe. The author was actively involved in preparing and conducting these sessions. **Ultra-rapid dUT1 measurements** on Japan-Fennoscandian baselines initiated during 2007 [38, 39]. The time correction dUT1 is estimated as the difference between the Universal Time (UT), defined by the rotation of the Earth, and the Coordinated Universal Time (UTC), measured by a network of high precision clocks [40]. The radio observatories of Metsähovi, Onsala (Sweden) and Tsukuba (Japan) simultaneously observed cosmic radio sources for determining the dUT1 in real-time. The data were correlated almost in

---

[3]NEXPReS is an Integrated Infrastructure Initiative (I3), funded under the European Community's Seventh Framework Programme (FP7/2007-2013) under grant agreement n° RI-261525, NEXPReS.

real-time at the correlator centre in Tsukuba. Measurements of the differential time were obtained several hours after the session was completed[4].

EVN and EXPReS held a demonstration during the ceremony of the **International Year of Astronomy** in Paris on 15th January 2009 at the UNESCO headquarters [41]. During the 24-hour session the VLBI radio telescopes observed several cosmic sources and data were streamed in real-time to the correlator at JIVE. The Metsähovi observatory was one of the stations amongst other 20 that participated in the largest e-VLBI experiment ever undertaken at that time. Later, Metsähovi also took part in the 100 **hours of Astronomy** event in April 2009 [42]. The e-VLBI session observed continuously several radio sources over 100 hours using telescopes located worldwide. Data were correlated at Washington correlator (WaCo).

To improve the sensitivity and frequency bandwidth of the radio telescopes the current VLBI hardware of the stations requires a major upgrade. New VLBI high data-rate acquisition systems have been designed and developed by the Metsähovi group. The new hardware implementations are presented in Section 3.2.

All the VLBI geodesy sessions conducted since 2009 have relied on the data transfer over the network, either in real-time or once the session had completed. The transfers are performed with several software tools developed at Metsähovi that will be introduced in Section 3.3.

Finally, new prototypes of digital back ends based on FPGA boards were developed for VLBI radio telescopes applications. They enable high computational signal processing tasks for radio astronomical projects. These developments are presented in Section 3.4.

3.2 Implementation of VLBI hardware

The radio telescopes capture the incoming cosmic radio source signal at any frequency band. The Radio Frequency (RF) receiver filters the signal at the specific frequency band and down-converts it to an Intermediate Frequency (IF). The VLBI Data Acquisition System (DAS) filters the signal to multiple baseband channels, samples them and stores the digital data into any compliant VLBI digital recording system. Nowadays, the

---

[4]The dUT1 experiments were partially funded by the Academy of Finland project "From ultra-rapid data transfer into science - a near real-time VLBI application"

current VLBI equipment at the radio telescopes limits the sensitivity and performance of the VLBI observations. The original hardware was developed 15-20 years ago. Most of the components and its spare parts are old and obsolete. The ability to obtain high quality scientific data is limited by the capabilities of the existing hardware. The latest developments in radio communications, network bandwidth and computer technologies provide a path forward improvement in the old DAS.
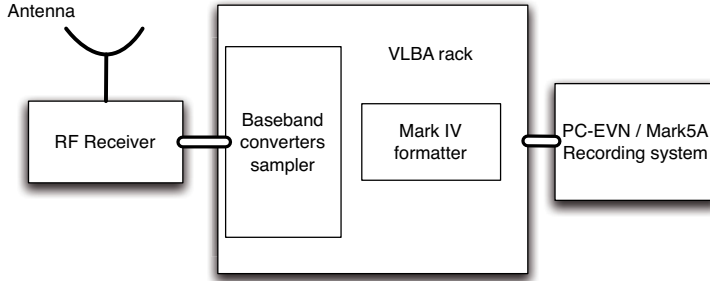
Figure 3.1. Simplified block diagram of a VLBI radio telescope. Antenna captures the radio signal, RF receiver down-converts it to IF signal, the VLBA rack filters, samples and formats the digital data to store into disk.

The development of new DAS copes with requirement of flexibility and scalability. The system needs to be flexible to work in the broad scenario: variable input bandwidth, bit codification, time sampling or frequency channelization. It also need to be scalable to increase the computational performance of the system by adding an additional hardware layer, for instance, additional FPGA boards. Several groups in the VLBI community are currently working in designing the future **Digital Back End** (DBE) for radio astronomy: the modularized digital Baseband Converters (dBBC) developed by the Istituto di Radioastronomia (Italy) [43, 44], the ROACH Digital back end (RDBE) developed by MIT/Haystack and NRAO [45] or the K5/VSI (ADS3000 series) 4 Gbps VLBI DAS developed by the Japanese VLBI group [46, 47].

All these models are designed to sample the data, down-convert the IF signal, filter it and transmit via network connection to the recording unit. They are all easily reconfigurable in terms of the IF centre frequency, number of IF bands, pass band bandwidth, cut-off steepness and band overlap. Whilst, currently the analogue equipment provide still better signal quality but are lacking in reconfigurability and as a result they require much higher level of design. Further improvements of digital tech-

nology are expected soon. Less expensive competing designs are based on the networked computing FPGA boards. There is already a large community of people developing tools and offering a brilliant alternatives for DAS. More on FPGA implementations for VLBI is presented in Section 3.4.

First VLBI systems, back in the 1980's, recorded the cosmic signal to magnetic tapes. Those tapes were replaced at the beginning of the new century with digital hard disks. The evolution of the systems and data format standards have conserved the compatibility after each new version. Hence, the current data formats still maintain the legacy from the magnetic tape era. Even now, data are encapsulated in a similar way to that previously used in magnetic tapes. This results in an extremely inefficient data format, which is difficult to read, and the need for dedicated software programs to extract the channel information.

The old VLBI Simple Interface Hardware (VSI-H) [48] connectivity is also becoming obsolete in favour of generic $10\,$Gbps connectors. It seems natural to replace the old data format by newer standards that are more orientated to a computational networking environment. New data formats, which include the network protocol embedded in the headers, allow transmitting data to most devices without any additional work. The new standard data format, the VLBI Data Interchange Format (VDIF), [49], benefits from global compatibility in different scenarios. Standard network packets can be simultaneously streamed in real-time to the correlator, recorded into large storage grid-server, locally pre-processed using CPU or GPU's software, etc. These new formats essentially contain small header with embedded information of time-stamped samples, channel information, additional metadata and the payload with the astronomical data.

The sensitivity of the VLBI observations depends on many factors, such as the size of the radio telescopes, number of antennas in the array, geometrical distribution on the uv-plane, observational time, bit quantification or the observational bandwidth. By increasing any of these parameters we immediately benefit by better sensitivity, which increases the possibility of detecting even weaker radio sources. However, some of these parameters cannot be easily modified. One of the simplest way to improve the sensitivity on a wide range of observation is to augment the observing bandwidth. Most of the VLBI observations in 2010 were scheduled with a sampling data-rate of 256 or $512\,$Mbps (8 channels$\times 2$

bits×2 side bands×8 or 16 MHz per channel). New wide band receivers and 10 Gbps network connections will achieve observational bandwidth up to 2 GHz. The brightness temperature (T_B) sensitivity and image RMS noise at X-band (8.4 GHz) depending on the sampling data-rate is shown in Table 3.1. The results were extracted from the work made by Phillips with the Australian VLBI array (LBA) [50].

Table 3.1. T_B sensitivity and the image RMS noise at the X-band (8.4 GHz) depending on the recording data-rate, data simulated from an array as the LBA.

Rate	Brightness Temperature	RMS noise
128 Mbps	$8 \cdot 10^4$ K	30μJy/beam
1 Gbps	$3 \cdot 10^4$ K	10μJy/beam
4 Gbps	$1 \cdot 10^4$ K	5.2μJy/beam
8 Gbps	$9 \cdot 10^3$ K	3.7μJy/beam
16 Gbps	$7 \cdot 10^3$ K	2.6μJy/beam

The table qualitatively demonstrates how the sensitivity improves VLBI observations when the data-rate is increased. Higher data-rates reduce the image noise and allow weaker radio sources to be resolved.

3.2.1 New VLBI Data Acquisition System

The primary objective of the EXPReS project was to create a production-level e-VLBI service in which the EVN radio telescopes are reliably connected via high-speed optical-fibre connections to the correlator centre. Each radio telescope should be able to support a data flow of up to 4 Gbps. The task for the Metsähovi VLBI group was to provide a new prototype of a network-connected multi-Gigabit DAS with real-time data transfer and high-speed storage capabilities [51].

The design of a high data-rate acquisition and real-time streaming system was a challenge for:

- Testing the limitations of Commercial-Off-The-Shelf (COTS) hardware components.

- Benchmarking the latest 10 GbE boards and devices: routers/switches, CX4/SFP+/SMF Ethernet card or networked FPGA-based devices.

- Evaluated the high-speed data transfers and long-haul baselines over Internet using different network protocols.

- Compared the performance of SATA hard disks, RAID-disk controllers and Port Multipliers (PMP).

- Developing and improving UDP-based data transfer protocols: Tsunami UDP [52], VDIF UDP or VSIB multicast [53].

During the 2-year project, several top-range COTS were evaluated to build the new prototype. We implemented the use of two different 4 Gbps recording prototypes that comply with the standard VLBI recording systems [54]. The author was involved in selecting the components, building the systems, developing the pertinent software and thoroughly testing these prototypes. The first design was a 2-dual core AMD processor, with 12 integrated on-board SATA disk controller ports and a Chelsio 10 GbE board. The second prototype was a Pentium Quad-core, with 6 integrated on-board SATA ports, a PCI-Express SATA external disk controller and a Myrinet 10 GbE board. The list of hardware components tested for both 4 Gbps recording systems is shown in Tables 3.2 and 3.3.

Table 3.2. Hardware components used to build the two high data-rate recording systems. Both units are capable of recording to disks and streaming to network over 4 Gbps streams.

Components	System A	System B
Motherboard	Asus L1N-SLI WS	Asus Rampage Extreme II
Processors	Two dual-core AMD	Pentium Quad-core
RAM memory	DDR-2 4 GB	DDR-3 4 GB
SATA controller	Native ports	HighPoint RocketRaid 2522
10 *Gbps card*	Chelsio 10 Gbps	Myrinet 10 Gbps
HDD disks	Samsung F1 1TB	Samsung F1 1TB
Max capacity	24 TB (12 disks)	40 TB (20 disks)

Table 3.3. Additional PCI-E RAID controllers, motherboard and port multipliers from different manufacturers tested during the 2009/10.

PCI-E RAID controller	Motherboards	Port Multiplier
HighPoint RocketRaid 2522	Asus L1N-SLI WS	ADSAPM
Hewlett-Packard SC44Ge	Asus Rampage II	AD5SAMP-E
Addonics ADSA3GPx8-4	Asus Striker II	
	Asus P5Q Pro	

These two new 4 Gbps DAS were also extensively used in a wide range of

radio astronomy applications. The author used these computers as VLBI recorders and processing units for: radio spectroscopy of planetary bodies and tracking of planetary spacecraft. Two images of these systems are shown in Figure 3.2. In the left image there is the system A with the 12 SATA disks integrated in the same enclosure. In the right the system B with the external disk pack with 20 disks.

Figure 3.2. left: COTS computer with 12 SATA disks using all the SATA ports integrated on the motherboard. right: New disk pack with a capacity for 20 SATA disks and 4 PMP connected via an Infiniband cable to the DAS. A cooling tray is used to keep optimal hard disks temperatures.

The testing and performance benchmarking of both systems were conducted using **Tsunami-UDP** [52] and **wr/VSIB** [55] tools. The software is fully described in Section 3.3.

We demonstrated that sustained data recording over 4 Gbps to COTS systems was achievable with the current technology available in 2009. Initially, the specifications and benchmarks of the latest motherboards, PCI-Express SATA disk controllers and hard disks promised extraordinarily stand-alone performance. However, the initial expectations were not achieved when all the components were assembled as a single working unit. The performance of large storage computers is constrained by several factors: the real writing-reading throughput of the SATA hard disks, the performance of the Linux file system [56], the handling of the data in non-parallel mode by the RAID disk controllers [57], the efficiency of the 10 GbE boards and the overload of the processor core when several CPU-intensive tasks run simultaneously on the computer.

We considered whether to use the SATA on-board chip set or the external PCI-Express based disk controllers. The on-board ports proved to be faster than any external controller when configured in RAID mode. However, these chip sets do not usually provide support for external Port Multipliers (PMP) boards. The PMP electronic board allows to concate-

nate multiple hard disks or additionally PMP boards to a single SATA port. Virtually, the capacity of any SATA port increases infinitesimally. The native number of ports mainly limits the storage capacity of this type of a recording system. On the other hand, external RAID disk controllers based on PCI-Express cards offer easy scalability due to the PMP support, high data-rate write performance and computational processing reduction of the CPU load. The writing throughput to a RAID-0 system, with different amount of disks and recording mode is shown in Figure 3.3.
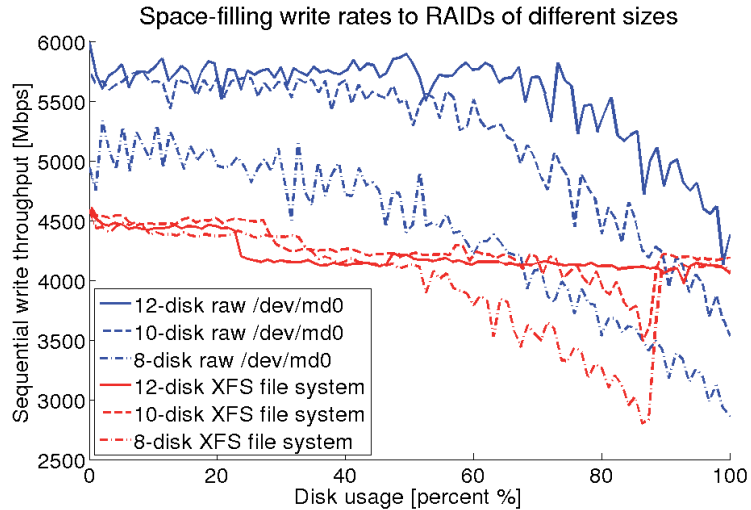
Figure 3.3. Writing data-rate to RAID-0 system with 8, 10 and 12 SATA disks. The data were written directly to raw disk (in blue) and to XFS file system (in red).

The data were recorded to the RAID-0 disk system using raw disks (blue line) and XFS file system format for Linux (red line). These results rapidly discarded that formatted disks might not affect the writing performance. The tests with other Linux file systems demonstrated even worse performances. Using a file system and the poor implementation of Linux paging tools, like **pdflush**, increase the usage of the processor resources. The performance of the system from raw to formatted disks decreased by 25 %. Despite this, data recording at over 4 Gbps using XFS file system is feasible. Although we worked within a narrow margin that did not guarantee trouble-free data recording.

The disk recording tests were reinforced by long haul and backbone network link attempts. We demonstrated that 8 Gbps continuous streaming over the Internet via NREN without data-recording was possible [35]. We found no errors or packet losses on the optical-fibre link during the

Shanghai demonstration. The Finnish and Swedish local NRENs (Funet[5] and SUNET[6]) played an active role in testing the capacity and VLBI usability of their international links. These tests led to recognition in the Finnish press [58] for all involved parties. The standard Internet protocols and northern NRENs demonstrated to support all the requirements and constraints for e-VLBI with no disruption to the rest of Internet traffic. Considering the even higher trunk capacity and lower load of Central European backbones and NRENs, extrapolating from our experience with Funet, SUNET and GÉANT2[7], we recommend a simple connection to the correlator without Quality of Service (QoS), Bandwidth on Demand (BOD) or other services for all the EVN radio telescopes. The configuration is suitable for connecting the stations to a central or distributed correlator - for classic single-site, cloud or grid correlation, respectively, without traffic routing limitations. An example of 4 Gbps file transfer of a 20 GB files over Internet using Tsunami UDP software is shown in Figure 3.4.
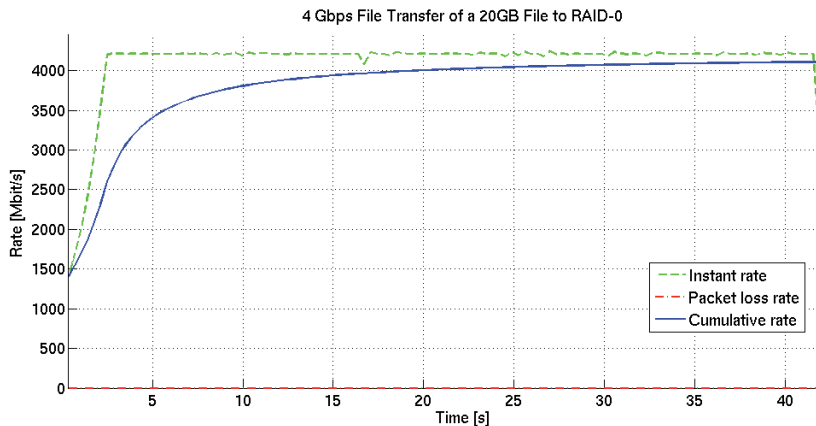
Figure 3.4. 20 GB data file transfer using Tsunami-UDP protocol with a 4.3 Gbps transfer data-rate target. There were not packets loss during the 40 seconds transfer.

Server micro bursting of large data packets combined with small buffer memory in some low-end switches and routers is a problem that requires closer inspection for smoother streaming over the Internet. Thus, the next generation of DAS based on FPGA designs that do not exhibit micro bursting may contribute to a direct reduction in e-VLBI transfer loss. The FPGA can ensure a fixed inter-packet delay for which the user has full control. When streaming is implemented on standard PC's, even if

---

[5] http://www.csc.fi

[6] http://www.sunet.se

[7] http://www.geant.net/pages/home.aspx

the user sets a fixed inter-packet delay in software, the generated traffic can still be transmitted as microbursts. The user does not have easy control over certain low levels of the computer architecture such as the PCI Express bus, Ethernet board or some drivers. The network layer and driver can re-group packets regardless of user-land settings. Disabling interrupt coalescing to reduce microbursts is effective only to a certain limit. With current hardware the modifications come at the cost of either reduced throughput or increased system load.

The network and disk recording results proved that it was possible already in 2009 to record network data with a single Linux computer at a sustained $4\,$Gbps sampling rate using consumer hardware. The constant development of the computer components reduces the costs and improves the performance. Metsähovi designed and shared expertise of low-cost, low-power and high-speed storage solutions to the research community. These systems are useful as temporary VLBI station data storage, high bandwidth data acquisition systems with file capture and network streaming including file transfer for VLBI, at unprecedented data-rates.

Moreover, we studied and shared how to integrate the disk pack into the existing VLBI recording system. Most of the radio telescopes are equipped with at least one unit of the Mark5A/B. During a major upgrade of the Metsähovi Mark5A, the unit was retrofitted with $4\,$Gbps + RAID capabilities by adding a 10 Gigabit card and an additional PCI-E disk controller. The system was capable to operate as a standard VLBI DAS or as the new $4\,$Gbps DAS prototype. The upgrade is shown in Figure 3.5.

The future aim is to expand the $4\,$Gbps limit towards $8\,$Gbps and beyond. The latest SATA III hard disks and Solid State Disks (SSD), the better performance of the PCI-E disk controllers, greater amount of PCI-E buses integrated on motherboards and the fact that new computer hardware is on average 2-3 years newer provides larger margins for improvement. This stand-alone system is the main objective of the Metsähovi group for the NEXPReS project.

3.3   VLBI software applications

We basically utilised two software programs developed in house at Metsähovi to test and benchmark the performance of new DAS', the Tsunami-UDP [52] network protocol and the wr/VSIB [55] tools:
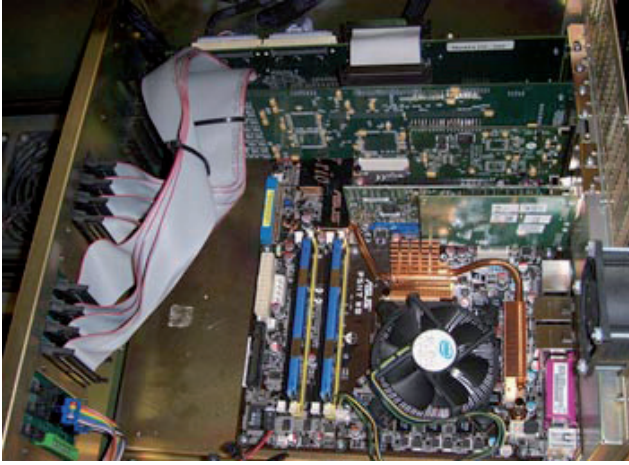
Figure 3.5. Possible configuration for the Mark5A units with the existing Conduant boards, a new 10 GbE card and a RAID disk controller. This unit could run both Mark5A and the new Metsähovi-designed system.

- **wr** software was developed to read data from a VSIB board used in the VLBI observations and record onto the PC-EVN [59]. The **wr-nexgen** performs sequential RAID I/O benchmarks with versatile settings, such as raw and formatted disk writing modes or multi-thread and parallel writing capabilities. The tool-kit was improved in 2009 with real-time priority, CPU affinity and similar optimizing load processing features.

- **Tsunami-UDP** is a fast aggressive FTP, which can also be used as a data transmission protocol. Tsunami was developed at Pervasive Technology Labs Research Centre at the University of Indiana and currently is maintained completely at Metsähovi. Data chunks are transmitted as UDP/IP packets at a significantly higher transfer rate than that of TCP, especially over long distances. The basic idea behind Tsunami-UDP is that the transmission data are chopped into large packets of equal size and the server tolerates a long delay of the acknowledge packets from the client site.

The next generation of VLBI digital recorders will most probably use 10 GbE interfaces to get the recorded data directly from the wide band digital samplers. Right now, both dBBC and RDBE allow streaming UDP data for their 10 Gbps connectors. The current VSI-H data interface will therefore be obsolete in the next few years. The new connection interface will guarantee recording data-rates of 4 Gbps and beyond and will simplify the

implementation of the system.

We also designed a simple software package[8] in Python to control and manage the new implementation of Mark5C style data recorders [60]. The software, known as **Mark5Cemulator**, allows communication between the Field System, which controls the antenna schedule, and the DAS. The Mark5C commands are similar implemented to the existing DAS. The communications between the Field System and the recording system is sustained via a TCP port. The software includes the major features to run a simple session. For instance, it allows to start/stop the recording, request disk pack information or listing the files list. However, it does not yet include several implementations available in the current Mark5A. The development of the software is in halt before evaluating whether all the features are really necessary for the next generation of digital recorders.

3.4   iBOB designs/firmware

Metsähovi acquired 3 digital signal-processing boards based on FPGA chips and three Analogue-to-Digital Converters (ADC) on 2009. The Interconnect Break-Out Board (iBOB) was designed at the Centre for Astronomy Signal Processing and Electronics Research (CASPER[9]) and the Berkeley Wireless Research Center (BWRC) of the University of California (UC), at Berkeley. The iBOB adopted the powerful FPGA Xilinx chip for digital signal processing tasks orientated to radio astronomy projects. The iBOB became extremely popular in the astronomy community and was used in several relevant projects worldwide. The iBOB has many advantages with respect to other alternatives available in the market. It offers high calculations performance at a relative moderate cost. The designing and programming environment is based on Simulink and VHDL and simple models can be built in few hours. The development of the different models and blocks is open source. The CASPER group has a great impact on providing tools support for the development of specific projects.

The initial idea behind a board like iBOB was to develop a simple interface to capture the analogue signal, convert to a digital format and send the data over the XAUI/10GbE connector. Soon the computational capacity of the iBOB was pushed beyond the limits and projects aimed

---

[8]Available at http://www.metsahovi.fi/en/vlbi/

[9]http://casper.berkeley.edu

for down-conversion, signal filtering, FFT operations, multi-beam correlation, etc.

The iBOB board allows a variety of I/O cards to be connected via two Z-DOK+ connectors. We selected an interleaved ADC (iADC) card, based on Atmel's AT84AD001B 8-bit ADC conversion chip. It accepts two analogue IF inputs, sampling clock and 1 pulse per second (pps) sync signal. The board operated at 512-1024 MHz sampling clock, generated from an external stable 5 MHz H-maser clock references using a National LMX3521-based frequency synthesizer board [61]. The iADC is capable of digitizing one IF frequency channel input at 2 Gsample/s or two at 1 Gsample/s. Furthermore iBOB is equipped with a Xilinx Virtex-II Pro 2VP50 FPGA, one 100 Mbps Ethernet port for control operations, two copper CX4 10 GbE data port connectors and one VSI connector for VLBI purposes. Basic schematic model for iBOBs is shown in Figure 3.6.
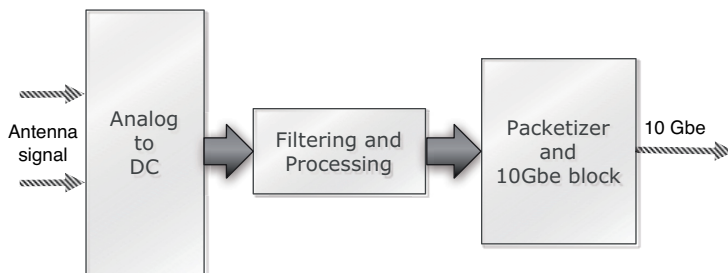
Figure 3.6. Basic concept behind most of the designs implemented on FPGA-based boards, like iBOBs. The analogue data is sampled, pre-processed and finally sent via the network.

A replacement of the iBOBs was necessary after the huge demand of boards and need of higher computational performance. Hence, the Reconfigurable Open Architecture Computing Hardware boards (ROACH and ROACH-02) [62] were developed between the UC and the South African group for radio astronomy MeerKAT [63]. The ROACH boards are basically an upgrade of the iBOB with newer and more powerful Xilinx chips, higher I/O bandwidth/capacity DRAM memory and standalone usage. The design is a standalone board with a faster Xilinx Virtex 5 FPGA chip (either the LX110T for logic-intensive applications or the SX95T for DSP-slice-intensive applications). The board is also equipped with 2 Z-DOK+ connectors, which accept 3 or 6 Gsample/s ADC boards, two quad data rate (QDR) SRAMs, which can provide high-speed and medium capacity memory, and 1 DDR2 DIMM that provides high-capacity buffer

memory for the FPGA. Four CX4 connectors provide a total of 40 Gbits/sec bandwidth output for connecting several ROACH boards together, or connecting them to other XAUI/10GbE-capable devices. Furthermore, a PowerPC allows booting Linux/BORPH and provides faster configuration of the FPGA chip.
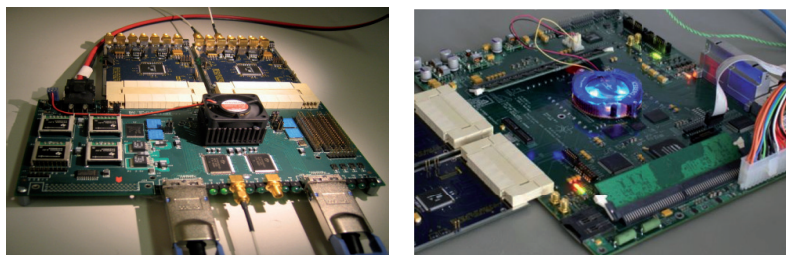
Figure 3.7. left: iBOB device, with the two respective ADC boards and CX4 connectors. right: ROACH board, with 2 ADC cards and four CX4 connectors.

When the iBOBs were purchased, the EXPReS project did not require Metsähovi to design a new VLBI DAS or DBE. Hence, the outcome is the style of the future correlator for radio astronomy with the requirements for DBE that we envisioned. Our implementations were based on distributed, cloud software or hybrid FPGA-GPU correlator. We also intended to use the iBOBs as a substitute in some projects of our existing VLBI system. All implementations allowed easy selection of several channels, operating at multiple bandwidths, reconfigurable bit resolution or generic data packet generators. The boards were able to transfer data via UDP to a local recording system or via Internet to the correlator centre, no matter where it was physically located.

The Metsähovi VLBI group has been involved in developing or taking benefit of several models since the arrival of the boards. These firmware were used for a wide range of projects orientated to future VLBI applications [64]:

- **IF spectrometer** [65] takes one or two frequency band channels, with a tunable input bandwidth, and calculates the time-spectra for a short integration time. The spectra are sent via the 10 GbE port to the user computer. Data are read and plotted in real-time with the Python matplotlibs [10] tools.

- **Kurtosis spectrometer** [66] designed at the Korean Solar Radio Burst

---

[10]http://matplotlib.sourceforge.net/

Locator (KSRBL) takes one IF channel with a fixed input bandwidth of $500\,$MHz and calculates the **spectral kurtosis** (SK) from the data set. The SK estimator is used for real-time detection of the RFI on the signal. The power and the power-square data is plotted using LabView graphical libraries.

- **Random packet generator** [67] was used to generate random data and sent the UDP packets at any tunable data-rate via the 10 GbE connector. This model was primarily designed to benchmark the capabilities of the $4\,$Gbps recording system.

- **IF-to-Ethernet** [68] digitizes two or four $500\,$MHz bandwidth channels; it performs a down-conversion, puts the data into VDIF packets and sent them via the $10\,$Gbps link. This design was used to stream $8\,$Gbps data from Metsähovi to Onsala during the Shanghai demonstration [58].

Two other implementations have contributed in the scientific research presented in this dissertation. These designs are:

A **real-time spectrometer** was built by the author to provide parallel support to the radio spectroscopy experiments. The spectrometer is used to preview the spectral signature of the calibrator sources during the experiments. The preview of the calibrator can prevent common errors occurring during the sessions. Several masers were used as a calibrators in the quest for water and other chemical elements during searches of the planets of the Solar System. The results of the radio spectroscopy sessions are described in Chapter 4.

The radio signal was filtered to a baseband frequency using the standard VLBA converter. Then, the iBOB sampled the analogue signal from two of baseband converters. Two frequency channels, LCP and RCP, with a bandwidth of 8 or $16\,$MHz are sampled by the ADC at $32\,$Msample/s per channel and 8-bit encoding. The total data aggregate handled in the FPGA is $512\,$Mbps. Each channel is processed with a Polyphase Filter Bank (PFB) and a FFT block. The spectral resolution is variable and can be adjusted either to 1 or $2\,$kHz. The spectra is packed in UDP blocks and sent via the $10\,$Gbps link. The UDP packets can be recorded to disk or displayed in real-time using Python matplotlib tools.

The second firmware was designed for **spacecraft tracking** purposes by Jan Wagner at Metsähovi. The concept behind the model was relatively simple. The two channels (RCP and LCP) with a bandwidth of 8 or

$16\,\mathrm{MHz}$ are filtered by the analogue baseband converters and then sampled by the 2 ADC. The clock of the ADC was oversampled and therefore data had to be decimated before building the Internet packets. The time-stamped packetizer basically builds the packet interleaving the data from both channels and adding the specific VDIF packet header. Packets were finally sent at $512\,\mathrm{Mbps}$ via the $10\,\mathrm{GbE}$ connector with 8-bit resolution. A snapshot of the model is seen in Figure 3.8.

3.5 Conclusions

The current aim of the Metsähovi VLBI team is to build a COTS data acquisition system capable of recording, buffering and streaming of the data up to $8\,\mathrm{Gbps}$. The first tests have been very satisfactory and the stand-alone system will be completed within the deadlines for the NEXPReS project.

The iBOBs are being replaced by the ROACH and the newest ROACH-02. The prototype of the latter was released on summer 2011 by the MeerKAT (South Africa) institute. ROACH-02 has a similar configuration to its predecessor but has been upgraded with a Xilinx Virtex-6 SX475T FPGA, supporting up to 8×10 GbE with CX4 or SFP+ interface. We have anticipated their arrival by requesting 3 Virtex-6 chips using a university contracts with DigiCOM. The possibilities of the new board are multiple: DBE for VLBI radio telescopes, small scale correlator for several VLBI radio telescopes or Doppler tracking of spacecraft in real-time. The Metsähovi VLBI group expects to work with the firsts boards in the summer 2012.
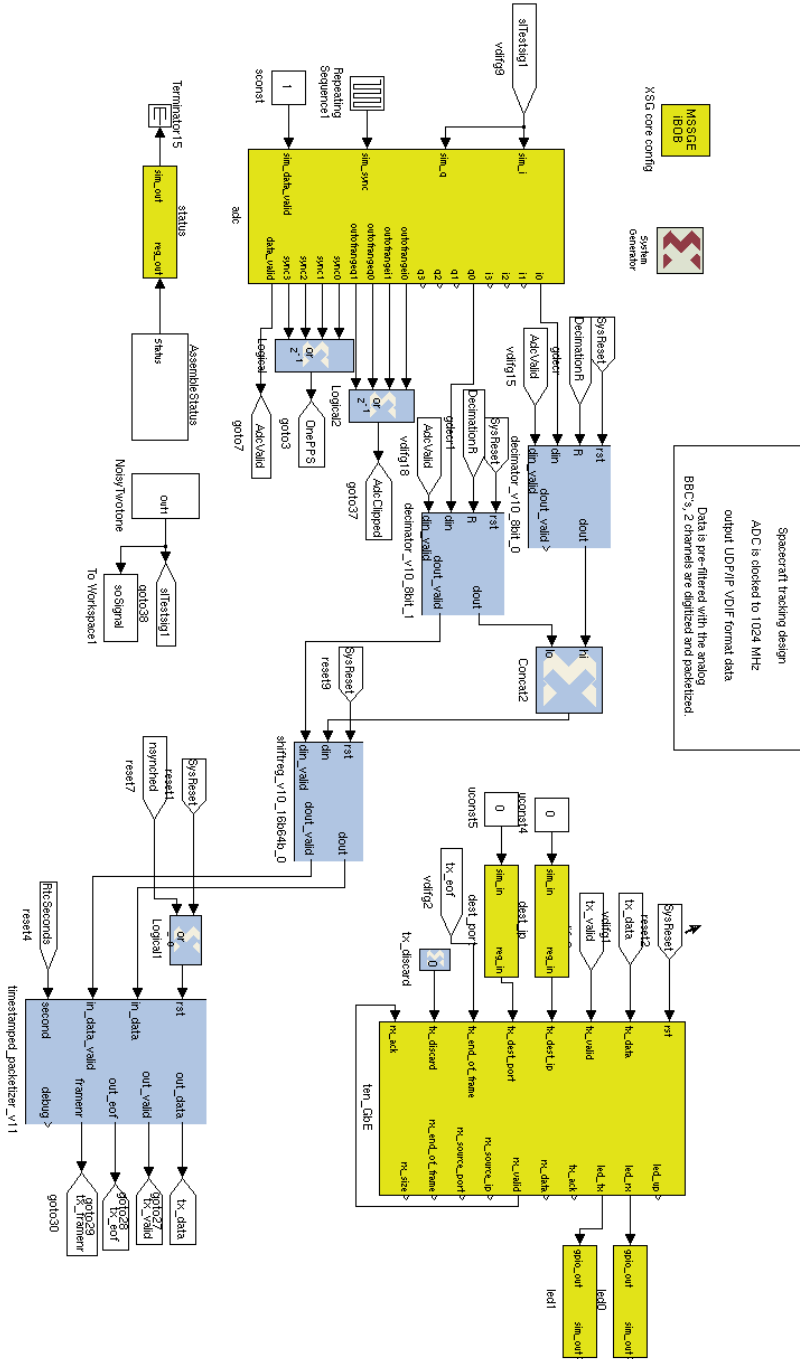
Figure 3.8. iBOB design for spacecraft tracking purposes. The design digitizes two ana-
logue channels with 8 or 16 MHz bandwidth, decimates the data, packetizes
the data with a VDIF compliant format and sends the packets via the 10 GbE
link.

4. Radio spectroscopy in the Solar System

4.1 Introduction

Radio telescopes are commonly used to observe distant objects on the sky. Combining these radio telescopes with radio interferometry techniques allows us to detect even weaker and more distant astronomical sources. On the other hand, optical telescopes were the main resource to investigate and research events located on sources closer to Earth. Nowadays, the planets in our Solar System are widely studied with in-situ spacecraft and unmanned robot craft. Several missions, striving to reveal the mysteries of Venus, Mars, Jupiter, Saturn, etc., are already fully operating or in the preparation stage. The measurements performed by these planetary spacecraft provide unprecedented information on the origin and evolution of our neighbouring planets. Earth-based measurement of the emitted radio spectral signal of these bodies cannot compete with the highly accurate systems on-board spacecraft. However, these observations at radio wave frequencies with VLBI antennas are a valuable complement to in-situ detections and can enhance the significance of the results.

The radio spectral components of any celestial body are obtained using specific-built spectrometers. These systems capture the radio signal at a specific wavelength and divide its bandwidth into several frequency channels. The spectral lines are then analysed individually per channel looking for prominent detections. The approach followed in this research consisted of re-using the existing VLBI recording systems for radio spectroscopy purposes. As explained in Section 3.2, the radio signals, at centimetre wavelengths, are captured by the antenna, filtered, digitised and finally stored into disks. A software that reads the formatted VLBI data and processes it looking for possible emissions of spectral lines was devel-

oped. This software is introduced in Section 4.2.3.

Three main projects have benefited from this software spectrometer. All of them have focussed on exciting physical phenomena in a different planetary body within our Solar System.

- The Cassini spacecraft detected traces of water vapour near the south pole of one of Saturn's moon back in 2006. Observations of Saturn and its planetary system, also known as **Kronian system**, were initiated soon after the discovery. The sessions were conducted with VLBI radio telescopes at K-band ($22\,$GHz). We attempted to prove similar evidence of water emission by analysing the spectral signatures using Earth-based radio telescopes. The campaign lasted for almost four years. It included several observations conducted at the radio telescopes of Medicina, Metsähovi and Robledo and the development of the new processing software. Indeed, traces of water plumes were found at several of the Kronian moons. The results of this work were published by Pogrebenko et al. [69], in which the author actively collaborated, in 2009. A thorough analysis of the results obtained with the Finnish antenna and the work conducted after the publication of this paper are described in Section 4.2.

- The discovery of water traces in Saturn prompted us to look for evidence of similar spectral lines produced by other chemical components. We initiated regular observations of Saturn, Venus and Jupiter searching for carbon-chain molecules. More specifically the observations focussed on emissions of dicarbon sulphide (C_2S) that has several spectral lines around 22-23$\,$GHz region. For this study, more than 15 hours of observations, including planets and calibrator sources, were conducted. These results are presented in Section 4.3.

- The work striving for the discover of electric discharges in the Martian dust storms using ground-based instrumentation was published by Ruf et al. [70] in 2009. The possibility of detecting lightning on Mars using standard radio telescopes motivated us and several other research groups to conduct observations of the red planet. We observed Mars several times in March 2010, coinciding with the high season of dust storms. The sessions were in conjunction with the regular spacecraft detections of Mars Express (MEX) [71] and were observed at X-band ($8\,$GHz). These tests were meant to detect the signal transmitted by the spacecraft. However, the rest of the frequency band was available to

perform additional spectral analysis. The idea was to analyse the **spectral kurtosis** (SK) of the data and discriminate between the **thermal** and **non-thermal** noise radiation originating at the planet [72]. Detection of spectral kurtosis over a certain sigma (σ) can be associated with non-thermal noise and, therefore, possibly caused by electric discharges. The data processing and the results of these observations are described in Section 4.4.

4.2   Water search in the Solar System

4.2.1   Introduction

Saturn is the second largest planet in the Solar System at an average distance of 9.5 Astronomical Units[1] (AU) from the Sun. The orbital period of the planet is 29.5 Earth years with an average orbital speed equal to 9.69 km/s [73]. Saturn is one of the four gas giants in the Solar System and is composed primarily of a thick atmosphere (hydrogen and helium) and a dense molten core. Seven rings around the equatorial plane and up to 30 known satellites defines the Kronian system. The Cassini spacecraft, a joint effort by NASA/ESA/ASI, has provided relevant scientific revelations of the planet for the last ten years.

The discovery by Cassini's spacecraft of a water plume near the south pole of Enceladus [74] motivated the radio observations at 22 GHz of the planetary system searching for water evidence. The Cassini probe was equipped, among other instruments, with an ultra-violet imaging spectrograph that searched for any interesting chemical spectral signature. Spectral observations of stellar occultations during two consecutive flybys of Enceladus confirmed the existence of a water vapour plume in the southern polar region of the Saturnian moon. This plume provides an adequate amount of water to resupply losses from Saturn's E-ring and to be the dominant source of the neutral OH and atomic oxygen that the Saturnian system mainly consists of. The level of the plume observed by Cassini anticipated possible detections of such events with Earth ground-based radio telescopes.

---

[1]1 AU = distance from Earth to Sun.

The first attempts began in 2006 using the VLBI 32-metre dish radio telescope of Medicina (INAF-IRA[2], Italy) by Pogrebenko et al. [69]. The first tests observing the Kronian system were conducted during the spring season. Data were recorded with the Mark5A disk based VLBI recording system [33] and processed with the software correlator-spectrometer developed for the Huygens probe VLBI tracking experiment [75]. Systematic observations at Medicina started in December 2006 with the on-line direct-FFT spectrometer *MSPEC0*, developed by Montebugnoli [3]. The Medicina radio telescope observed more than 280 hours of Kronian data during the two-year period.

The 14-metre radio telescope of Metsähovi performed few test observations at the end of 2006, officially joining the project. The availability of the antenna and the K-band receiver for Kronian observations was constrained by the amount of EVN sessions at this frequency. We could only observe when the receiver was installed for regular VLBI sessions and, therefore, the observing opportunities were reduced to two or three times per year. There were no sessions in K-band during the whole of 2007. That is why, two years elapsed (2006-2008) before we could continue again with the Kronian observations. During the last two years of the project we scheduled 17 sessions accumulating up to 150 hours of data. Data were recorded on the PC-EVN data acquisition system [34] and processed with the software spectrometer [76]-[77].

Several observations of the Saturnian system demonstrated significant detections of the spectral water line during the period from 2006 to 2008. Most of these were achieved with the observations conducted with the Medicina radio telescope. These results were published by Pogrebenko et al. [69] in collaboration with the author in 2009. The results from the Metsähovi radio telescope also revealed evidence of water content in Atlas, one of the Saturn's moons. The Kronian observations continued until mid 2010.

During this period, we were also able to observe on a couple of occasions with the 70-metre dish telescope of Robledo, in Madrid. More than 20 hours of Kronian data were acquired with the high accuracy radio telescope. Unfortunately, no additional spectral evidences of the water line were found in the following attempts.

The scheduling of the observations and the methodology for the data

---

[2]National Institute for Astrophysics-Radioastronomy Institute

processing are presented in Sections 4.2.2 and 4.2.3. The detection of water in Atlas, the results obtained with the Metsähovi and Robledo radio telescopes, and the spectral analysis of several well-known water masers are presented in Section 4.2.4. This chapter emphasises the observations and the analysis conducted by the author at Metsähovi and Robledo.

4.2.2 Materials and methods

The Metsähovi radio telescope conducted 17 sessions observing Saturn and its moons during the period 2006-09. In fact, most of the sessions were observed during the last year and a half of the project, from spring 2008 to fall 2009. The visibility of Saturn allowed observations of the system for an average of seven to nine hours per session. We gathered more than 150 hours of data, while Medicina observed twice as much. The list of Kronian observations conducted with the Metsähovi radio telescope at 22 GHz is shown in Table 4.1.

Observations were performed recording alternating scans targeting to the source and few degrees away. This technique of observations is known as the **on-off source** method. It measures the difference between the radio noise originating at the Kronian system, called **on-source**, and the radio noise from few degrees away, the **off-source** position [78]. This technique enables us to compensate for the effect of the background noise on the targeted source. The optimal nodding cycle, with a $50\,\%$ duty cycle, varies depending on the sensitivity of the radio telescope. More sensitive radio telescopes require a shorter observing time than smaller dishes. Indeed, the optimal nodding cycles for observing the Kronian system were 80 seconds for Medicina and 275 for Metsähovi. As the sensitivity of the Metsähovi dish is lower than at Medicina, we selected a longer integration time in order to obtain a similar level of detections in both stations. For the Finnish antenna, we used a frame time of $600\,$s, during which the antenna pointed to the on-source for $275\,$s, measured the system temperature and calibrated for $25\,$s, then pointed to the off-source for $275\,$s more and the last $25\,$s for re-pointing and calibration again.

These sessions alternate observations targeting the Kronian system and reference sources as calibrators. We used for that several well-known water masers that were relatively close to Saturn in angular terms. The possible emission of the water line in the Kronian system was weak. We tried to not observe strong masers and, thus, avoid the saturation of the

Table 4.1. Kronian system observations conducted at $22\,$GHz with the Metsähovi radio telescope. More than $150\,$hours of data were recorded from the period 2006 to 2009.

Session	Epoch	Start (UTC)	End (UTC)	Duration (h)
s1612	2006.12.16	$00:00$	$07:00$	7
s1712	2006.12.17	$00:00$	$07:00$	7
s1812	2006.12.18	$00:00$	$07:00$	7
s0603	2008.03.06	$17:30$	$02:30$	9
s0703	2008.03.07	$17:30$	$02:30$	9
s0803	2008.03.08	$17:30$	$02:30$	9
s0903	2008.03.09	$17:30$	$02:30$	9
s2905	2008.05.29	$14:00$	$21:00$	7
s0206	2008.06.02	$08:30$	$21:30$	13
s0306	2008.06.03	$11:30$	$21:00$	9.5
s0406	2008.06.04	$11:30$	$21:00$	9.5
s2905	2008.05.29	$14:00$	$21:00$	7
s2602	2009.02.26	$21:00$	$01:30$	4.5
s2702	2009.02.27	$21:00$	$01:30$	4.5
s0906	2009.06.09	$10:00$	$21:30$	11.5
s0407	2009.07.04	$13:00$	$18:00$	5
s2410	2009.11.24	$06:00$	$16:00$	10
s2510	2009.11.25	$05:30$	$13:00$	7.5

input signal. Furthermore, in order to simplify the re-pointing operations of the antenna between the targets, it was preferable to use calibrator sources angularly close to Saturn. We tried to not observe strong masers and, thus, avoid the saturation of the input signal. The best candidate for our observations was the W75N water maser. We also observed few times stronger masers such as W3OH and W49N, when we were limited by the visibility of the radio telescope. The calibrator sources were analysed using the on-off source method.

The whole process of capturing the signal with the radio telescope, filtering it to the desired frequency band, storing the digital data to disk and processing the raw data with the spectrometer is illustrated in the schema of Figure 4.1.

The observations were performed using the MarkIV formatter (VLBA BBC rack) connected directly to both Mark5A and PC-EVN recording sys-
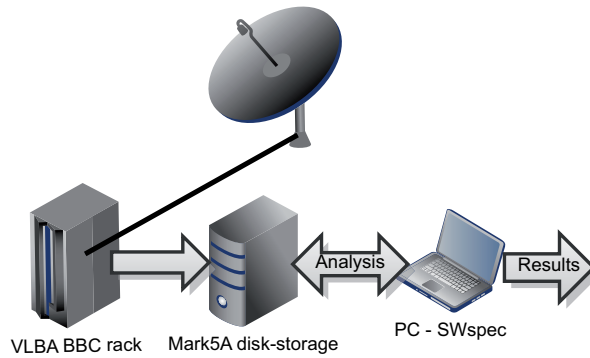
Figure 4.1. The radio signal is acquired by the telescope, down-converted to preserve the spectral water line, stored to Mark5A disk or PC-EVN system and processed with SWspec.

tems. Generally, data were recorded redundantly with both systems to prevent possible session failures. Data were acquired for the two circular polarizations, LCP and RCP, with a bandwidth of 8 or 16 MHz, 2-bit encoding and centred on the 22235.08 MHz water line. The observed spectra were Doppler corrected in the frequency domain in accordance with the predicted radial velocity [78] of Saturn (calculated by the NASA JPL Horizons software [79]). An average of 100 scans were recorded during each Kronian session.

The Metsähovi 14-metre dish gives a primary beam, Full Width at Half Peak (FWHP), of 4 arc minutes at 22 GHz. So, when targeting Saturn, the antenna beam also encompasses all the inner Saturnian rings, part of the F-ring, all the inner satellites and Dione at certain orbital phases. The Saturnian system seen by the antenna beam of the Metsähovi telescope on 2009.02.27 is shown in Figure 4.2. The image is courtesy of the SIMBAD database[3] [80].

Typical values for the VLBI 22 GHz receiver system noise temperature (T_{sys}) varies between 90 and 130 K. The T_{sys} is mostly affected by the atmospheric conditions during the sessions. Doubtlessly, the heavy clouds and rain present during few of the sessions conducted resulted in the poor results obtained on several occasions. The expectations of detection for these days were really low. The nominal gain for the Metsähovi antenna at 22 GHz in good atmospheric conditions is 0.04 K/Jy.

In addition to the observations conducted at Metsähovi, we also ar-

[3]http://simbad.u-strasbg.fr/simbad/

Saturn view from Metsahovi station - Feb 2009
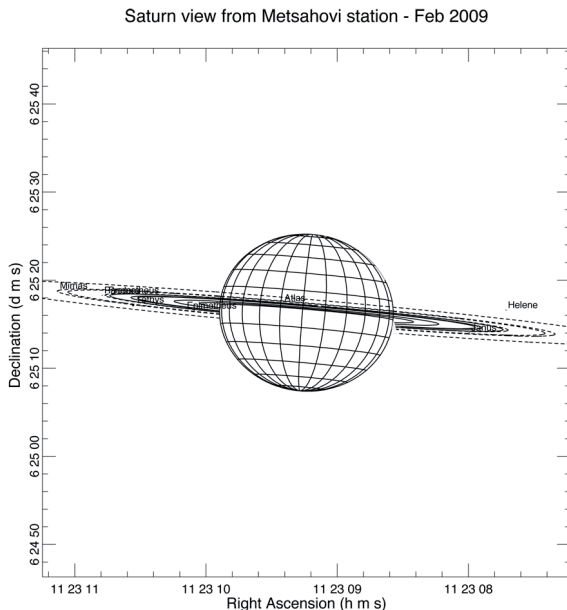
Figure 4.2. Field of view seen with the 14-metre at Mh on the Kronian system on 2009.02.27. The 4 arc minutes FWHP encompassed all the inner Saturnian rings, part of the F- and G-rings and several inner satellites.

ranged observing time with the NASA's Deep Space Network station at Robledo, Madrid. Three DSN stations, located in California, Australia and Spain, enable continuous observation and suitable overlap for capturing the transmitted radio link of any NASA spacecraft. When the antenna is not busy with these projects, the DSN telescopes can be used for radio astronomy purposes. The 70-meter dish is one of the largest and most sensitive radio telescopes available for radio astronomy. The surface of the telescope remains accurate within a fraction of the signal wavelength, meaning that the precision across the 3850-square-meter surface is maintained within one centimetre at K-band. The main characteristics (dish size, SEFD and nominal gain (Degree Per Flux Unit DPFU)) of these telescopes at K-band is shown Table 4.2.

Table 4.2. Specifications of the Metsähovi, Robledo and Medicina radio telescopes[4].

Antenna	Country	Dish size	SEFD	DPFU
Metsähovi	14 m	FI	2608	0.029 K/Jy
Medicina	32 m	IT	700	0.11 K/Jy
Robledo	70 m	SP	83	0.90 K/Jy

The Spanish DSN station offers a chance for native radio astronomers to conduct scientific observations with their radio telescopes. The proposal, under the code D63-115, was submitted as host country radio astronomers to the Madrid Deep Space Communication Complex (MDSCC). 20 hours of antenna time were granted for the search of water maser evidence in the Kronian system. The observations were conducted during the weekend of 2010.03.12-13 and lasted for 10 hours. We observed Saturn and several of its moons Titan, Enceladus, Dione and Hyperion, among others. We used the water masers W75N and W3OH as calibrator sources. The list of sources, their coordinates and the observed time are listed in Table 4.3.

Table 4.3. Saturnian sources observed during the two-day session on 2010.03.12-13 with the 70-metre radio telescope at Robledo (J2000 coordinates system).

Source	RA	Dec	Total scans	Duration
Saturn	12h10m34.1s	01d38'38"	21	210 min
Titan	12h10m37.4s	01d38'35"	9	90 min
Enceladus	12h10m34.0s	01d38'39"	6	60 min
Dione	12h10m35.3s	01d38'59"	6	60 min
Hyperion	12h10m17.1s	01d38'32"	9	90 min
W3OH	02h25m40.7s	62d05'52"	3	30 min
W75N	20h38m36.4s	42d37'35"	3	30 min

The 2 circular polarizations were acquired using a bandwidth of 8 MHz and four channels using the standard MarkIV video-band converters. The digital data were stored into Mark5A disk modules unit and then shipped with regular consumer hard disks to Metsähovi for the processing. Only the two channels around the water spectral line were analysed. The T_{sys} of the receiver was 70 K. The atmospheric conditions during the two nights were good. In addition to the standard VLBI recording system, the JPL Water Vapour Spectral Radiometer (WVSR) [81] was used in parallel. The radiometer was configured with 2 channels, bandwidth of 16 MHz and 8-bit encoding. Unfortunately, some calibration problems using the WVSR corrupted the spectral data and ,therefore, the results were not useful for the experiment.

4.2.3   Data processing and analysis

The analysis of the Kronian system and the reference sources was performed using the high-resolution software spectrometer **SWspec**[5] [82, 83] developed by J. Wagner in coordination with JIVE. The software is based on the software correlator developed for data processing of the Huygens and Smart-1 experiments [84]. For more detailed information about SWspec, a short user guide is introduced in Section 5.2.1. I will briefly describe some of its main functionalities here.

SWspec extracts any selected frequency channel from the raw data input data file. It performs an accurate windowed-overlapped Discrete Fourier Transform (DFT) per each iteration and calculates the time-integrated spectrum. A Hann window is used to calculate the DFT. The user can select any specific number of DFT points and the integration time to increase or decrease the resolution of the detection. The software allows reading of most of the multi-bit and multi-channel formatted data co-existing in the VLBI community. To process the data with SWspec an integration time equal to the entire length of the scan, 290 seconds, is used with 16 or 32 thousand points.

For the data analysis, a statistical weighting was applied to the on-off source difference spectra per each of the nodding cycles. The statistical weight was based on antenna gain (as a function of target elevation), system temperature of the receiver and angular distance between the target and antenna-pointing centre. The resultant spectra were accumulated with a long integration time, accounting for the Doppler shifts of Saturn and the variety of known Saturnian satellites. The Doppler tracking was performed for each element group as shown in Table 4.4

Table 4.4. Doppler tracking velocities for the different elements in the Kronian system.

Elements	Doppler tracking
Saturn's central spot and polar regions	$0 \, \text{km s}^{-1}$
Equatorial belt	$\pm 9 \, \text{km s}^{-1}$
Ring system	$\pm 20\text{-}25 \, \text{km s}^{-1}$

The average spectra with a velocity range of $V_{range} = 50\text{-}80 \, \text{km s}^{-1}$ is smoothed with a Gaussian kernel and equivalent width of $V_w = 1 \, \text{km s}^{-1}$.

---

[5] http://cellspe-tasklib.cvs.sourceforge.net

Therefore, the resulting spectra had:

$$N_{df} = V_{range}/V_w \tag{4.1}$$

N_{df} degrees of freedom. After the data were filtered, we constructed a polynomial fit of order N_p and extracted it from the observed spectra. Consequently, the number of degrees of freedom was reduced to:

$$N_{df,1} = N_{df} - N_p \tag{4.2}$$

We searched in the resultant spectra for any significant feature in the $2.8 \, \text{km s}^{-1}$ window centred on $0 \, \text{km s}^{-1}$. The statistical significance was estimated by inflating the RMS of the residual baseline-ripple-corrected spectra by a factor of:

$$N_{df,1} = \sqrt{\frac{Ndf}{Ndf - Np}} \tag{4.3}$$

accounting for the degrees of freedom removed by polynomial fitting and subtraction. We inflate the measured RMS by a certain factor corresponding to the degrees of freedom removed.

Data processing was conducted for several Saturnian satellites, in their different 16 orbital phases, and Saturn itself. All different orbital phases take into account all possible geometries of the beamed maser emission. Combining data from both stations (Metsähovi and Medicina), it was possible to accumulate over 4 hours of observations per phase. For this amount of collected spectra, the detection of a spectral feature at the level of $\sim 4\sigma$ is indicative rather than definitive, while higher levels of detections should be seen as statistically significant.

Our approach of Doppler tracking on the bodies does not cover all possibilities of maser emissions: the velocity resolution and line width of $\sim 1 \, \text{km s}^{-1}$ allows us to relate the water emission of a certain body with a given Saturnian satellite with an accuracy of $1000 \, \text{km}$.

4.2.4 Kronian results

We selected five candidates out of the total 20 objects in the Saturnian system for further analysis. The candidates were selected based on the discovery of the water plume made by the Cassini's sensors and the SNR

of the potential detections. The five candidates were: Titan, Hyperion, Atlas, Dione and Enceladus. We divided the location and orientation of the satellites in 16 possible orbital phases. The sessions were intended to monitor the five satellites in all their 16 orbital phases.

Saturn and several of its moon were observed per separate and recorded into 290-seconds scans. The inner satellites were observed when they were within the antenna beam. The scans were then accumulated in groups of three and evaluated per each orbital phase.

An example of non-detection spectra is shown in Figure 4.3. The session was observed with the Robledo radio telescope on 2010.03.12.
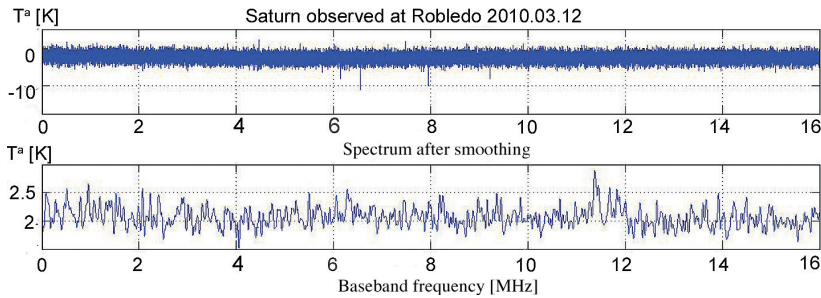
Figure 4.3. Dispersion of the 3 scans on-off scans before (top) and after (bottom) smoothing the data with 100 Hanning window. No significant detection ($\geq 3\sigma$) was seen in the data recorded at Robledo on 2010.03.12.

The antenna temperature, expressed in Kelvins, of the dispersion from the three on-off sources difference scans is shown in the upper plot. The dispersion after smoothing the difference 100 times using a Hanning window function is shown in the lower plot. From the ten hours of data observed on 2010.03.12-13 at the Robledo radio telescope, we did not obtain any significant detection ($\geq 3\sigma$).

Several bodies exhibited significant detections at the expected water maser frequency from the combined observations of Medicina and Metsähovi. The typical detections were at the level of $20\,\text{mK}$, which is equivalent to $0.3\,\text{Jy}$ using the nominal antenna gains of the telescope. Several of the bodies showed detection levels exceeding 3.5σ. At this level the detection can be circumstantial but not definitive in confirming a water spectral line. Furthermore, an additional 20-30 % due to instrumental and propagation fluctuations might be added on the threshold level of σ.

The observations of Enceladus conducted on 2010.05.29 at Metsähovi demonstrated a prominent feature at the water spectral line above 4σ. The

orbit properties and satellite phases are shown in Figure 4.4.
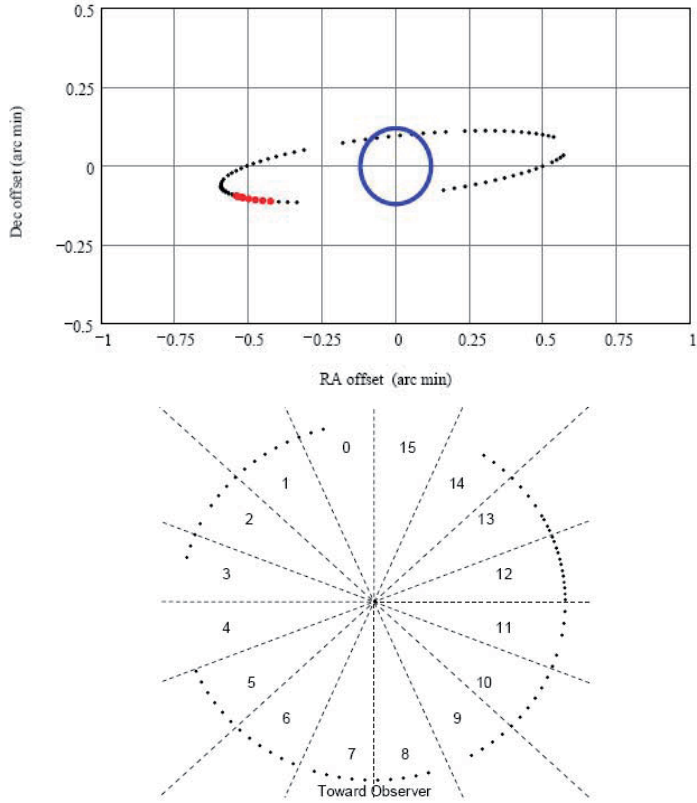
Figure 4.4. top: Enceladus track on its 31.2-hour orbit around Saturn on 2010.05.02 and 2010.06.02-04 observed at Mh. Black dots indicate the satellite position and in bold those observed in May, from which the spectral signature was at 4σ. bottom: Sampled orbital phases, projected onto the target's orbit plane.

The Enceladus track around Saturn observed by Metsähovi is shown in the upper plot. The antenna observed the Kronian system with Enceladus in the antenna's beam on 2010.05.29 and on 2010.06.02-04. The black dots indicate the position of the satellite at our acquisition time. Each dot represents single 10 minutes on-source observation. The black bold dots indicate the satellite position on 2010.05.29 ($18:00$-$20:00$ UTC), from which the spectral signature at 4σ level was detected. No other Enceladus orbital phases/time slots of the same duration showed detection levels above 2.6σ.

The sampled orbital phases, projected onto the target's orbit plane are shown in the lower plot. The coverage of Enceladus trajectory was almost complete using only Metsähovi observations.

The evidence of a water plume on 2010.05.29 was the only proof reported by Metsähovi. The spectral signature of that event is shown in top of Figure 4.5. The spectrum is averaged over seven scans of 10 minutes on-source and 10 minutes off-source nodding cycles. The spectra were corrected by applying the Doppler velocity correction according the orbit of Enceladus. The water evidence is present around the velocity offset $0\,\mathrm{km}$ s^{-1}. The post-smoothing velocity resolution is $1\,\mathrm{km}\ \mathrm{s}^{-1}$. In the graph, the red line represents a raw spectrum. The blue line represents the corrected 8th order polynomial fit of the baseline ripple.
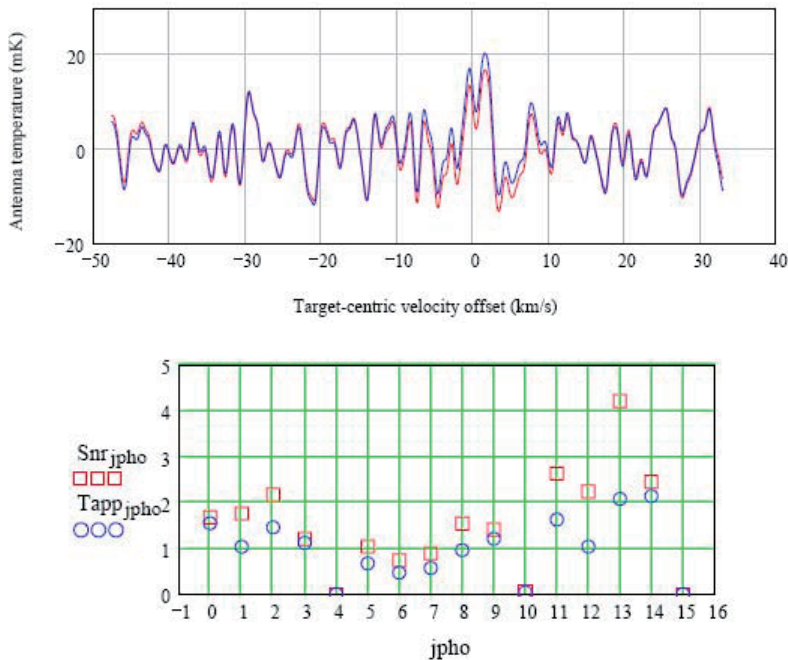
Figure 4.5. top: Spectrum averaged over 7 *on-off* nodding cycles. Doppler velocity correction applied. Post-smoothing velocity resolution is 1 km s^{-1}. Red line represents a raw spectrum, blue line - corrected for the 8th-order polynomial fit. bottom: Antenna temperature (rel. units) - blue circles, and SNR - red boxes for sampled orbital phases of Enceladus.

The lower plot of Figure 4.5 shows the Metsähovi antenna's temperature, expressed in relative units, and represented by blue circles. The red boxes represent the SNR for the sampled orbital phases of Enceladus.

Although only one of the multiple observations reported evidence of water in one of the satellites of the Kronian system, the results obtained by the Metsähovi and Robledo supplemented all the previous work done at Medicina. The total amount of data observed by the three radio telescopes

was large enough to make definitive conclusions. Significant detections at the water spectral line were exhibited by several of the Saturnian moons. Among those were Titan, Atlas and Hyperion. In the paper published by Pogrebenko et al. [69], there is the description of the work performed and the overall results of the project. This chapter focussed on the spectral analysis of the data set, the results provided by the radio telescopes of Metsähovi and Robledo, and the detection of evidence of water in Enceladus.

4.2.5 W75N maser results

We used several well-known water masers to calibrate the data during the Kronian observations. It was mainly used the W75N, but also W7S, W3OH and W49N. Due to the angular proximity to Saturn at most of the epochs, the wide range of visibility hours and the level of the flux emitted, W75N was the perfect candidate for the observations. The flux density of W75N is optimal for detecting it with the 14-metre antenna of Metsähovi and the signal is no too strong to saturate the data calibration.

The sky coordinates of the water maser W75N are RA=20h38m36.4s and DEC=42d37'35" (J2000). The W75N sky map is shown in Figure 4.6 [80].
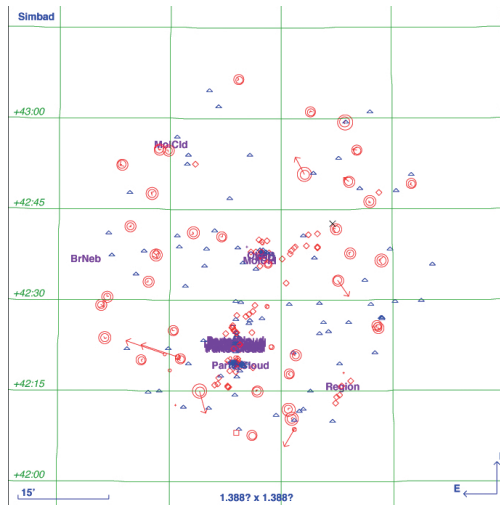
Figure 4.6. Sky map of the water maser W75N. The star-forming region is a molecular cloud that emits a strong spectral line at $22.235\,\mathrm{GHz}$. Map courtesy of the SIMBAD database.

W75N is a star-forming region in which dense parts of molecular clouds collapse into a ball of plasma to form a star. The appearance of astro-

physical masers in the form of molecular clouds is common in such regions. Various pumping schemes, combining radiation, collision and combination, result in the maser emission of multiple transitions of many species [4, 85]. In this case, the radio telescope captures the presence of a strong stimulated spectral line at 22.2358 GHz, coinciding with the H_2O spectral line.

The spectral line emitted by the W75N region is shown in Figure 4.7. The water maser was observed on $2009.02.27 - 28$ with the Metsähovi radio telescope. The antenna temperatures of the detections were in the order of 10 K. Four pairs of on-off scans were observed during the weekend. The apparent topocentric velocity of the maser was 10 km s^{-1}.
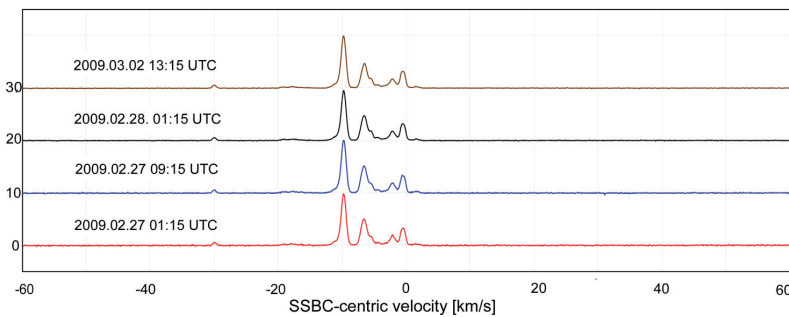
Figure 4.7. Spectra observed on $2009.02.27 - 28$ of the W75N region at Mh. The density fluxes for 4 different scans have been added $+10$ K to improve readability. The W75N water maser has been used widely as a calibrator in the Kronian sessions.

Our last chance to observe of the Kronian system was on 2010.03.12-13. The observations were conducted with the 70-m telescope at Robledo. Although W75N was located far from Saturn, we observed the water maser a couple of times for comparing results. The spectral line detected from the W75N region is shown in Figure 4.8.

The level of the detections with the 70-metre dish yielded an antenna temperature detection of 700 K. This is 70 times higher than previous results with Metsähovi. We note that the spectral peak of the maser shifts toward the centre from the previous session.

Several observations of W75 were accumulated from the Kronian sessions. An interesting exercise was to compare the level of detection of the maser using several data acquisition systems with the same antenna. For the comparison we used the common VLBI Mark5A and PC-EVN (2-bit
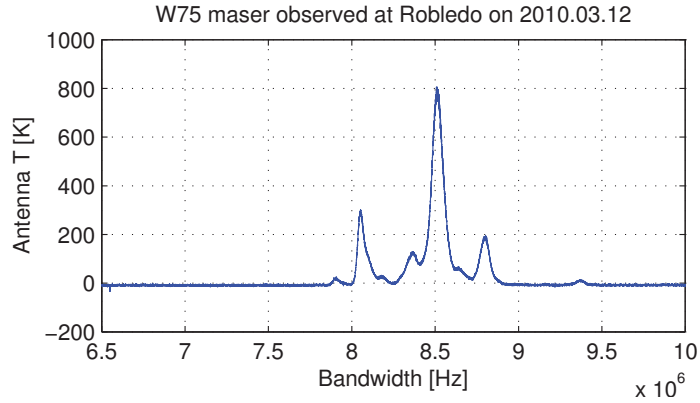
Figure 4.8. W75N spectra observed on 2010.03.12-13 at Robledo. The x-axis shows the baseband frequency of the channel centred at the 22.235 GHz. The level of the detection is in the order of 700 K.

encoding), the iBOB board (8-bit) and the ADC MAX board (12 or 16-bit) [6]. The comparison of the systems is shown in Figure 4.9.
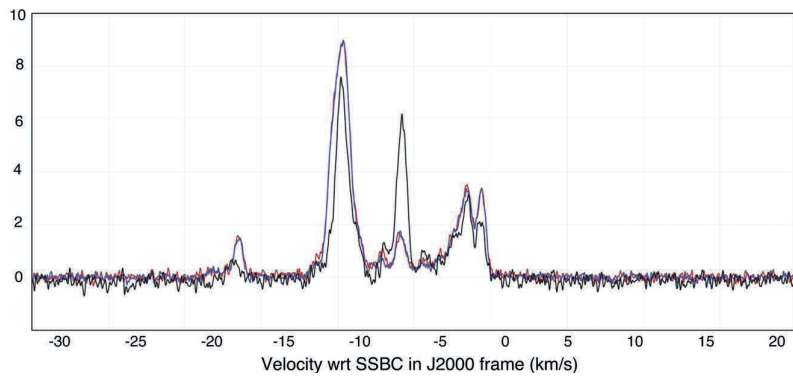
Figure 4.9. Water maser emission spectra of W75N observed at Mh using several DAS. The experiments were conducted on 2008.03.06 13:40 UTC (black line), 2008.06.02 08 : 30 (red) and 2008.06.04 10 : 00 UTC (blue). Months-time scale changes in component's brightness and velocity is clearly seen.

The experiments were carried out on 2008.03.06 using the PC-EVN (in black), on 2008.06.02 using iBOB (in red) and on 2008.06.04 using Maxim (in blue). For the analysis we used a DFT resolution of 1 kHz (16K points) or 13 m s^{-1} for a SNR (at 1 kHz) for the brightest component of $60 \sim 70$ (2008.06), a DFT resolution of 2 kHz (8K points) or 26 m s^{-1} for a SNR (at 2 Hz) for the brightest component of 30 (2008.03).

The differences in the apparent topocentric velocities between the data from March and June were ~ 12 km s^{-1} and 85 m s^{-1}. The apparent ve-

___

[6]http://www.metsahovi.fi/en/vlbi/misc-hardware/Maxim1217EVKIT/

locity was reduced to Solar System Barycenter (SSBC) using NASA-JPL SSDG Horizons state vectors of Metsähovi station in SSBC/J2000 frame.

4.3 Dicarbon sulphide search in the Solar System

The search of chemical spectral lines in stars and molecular clouds has been a target of radio astronomy for the last half century. Radio astronomers constantly scanned the sky looking for some evidence of strong molecular emissions. Water masers are an example of such emissions from molecular clouds, as previously seen in Section 4.2. Another case worthy of investigation is the possible emission caused by carbon-chain molecules.

The goal of our research was to detect the presence of sulphur-containing carbon-chain molecules in the planetary atmospheres of our Solar System. Our search mainly concentrated on two planets: Saturn and Venus. The decision was based on the characteristics of the atmospheres of these planets and their visibility at the time of observations. The sessions were performed in conjunction with the water search campaign. The dicarbon sulphide (C_2S) chain has a prominent spectral line at a frequency of 22.344 GHz. Hence, for the observations two of the frequency channels were centred at water spectral line and the other two at the carbon-chain spectral line.

Venus is the closest planet to the Earth and the second brightest planetary body after the moon. Venus is the most similar planet to Earth with respect to the structure of the core, body size and gravity field. The atmosphere is thick and dense with carbon dioxide and sulphuric acid clouds [86]. Thus, several space missions seek to understand further the composition of its atmosphere. Venus orbits the Sun at an average distance of 0.72 AU and has a sidereal period of 225 Earth days.

Taurus Molecular Cloud-1 (TMC-1) was used as a reference source, since the molecular cloud is abundant with carbon molecules and has strong emission at several frequency lines [87]. TMC-1 is a giant cold dark cloud located around 140 pc away. Several studies of the cloud have shown evidence of carbon-chain molecules in a gaseous state: HC_xN, C_xH, C_xH_2, C_xN, C_xO and C_xS [88].

The molecular cloud TMC-1 emits an intense spectral line due to C_2S molecules; the peak antenna temperature at the spectral line frequency

was $2.2\,\mathrm{K}$ [88]. The sky map of TMC-1 is shown in Figure 4.10.
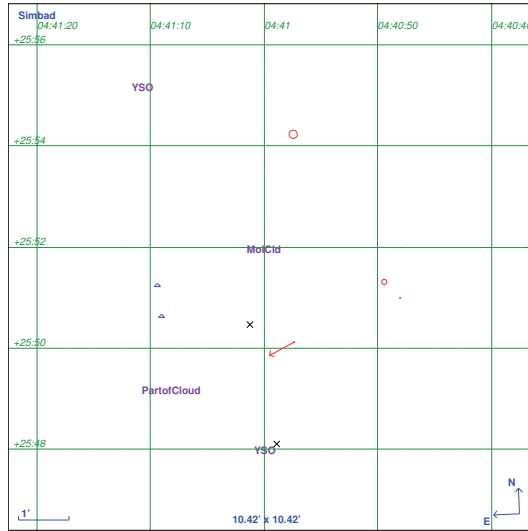
Figure 4.10. Sky map of the Taurus Molecular Cloud-1 (TMC-1), the blue triangles show the maser radio emission and the red arrow is the star. Map courtesy of the SIMBAD database.

We observed Saturn, Venus and TMC-1 on several occasions during the year 2009. The observations are summarised in Table 4.5.

Table 4.5. Observations conducted looking for carbon-chain evidence in Saturn and Venus.

Source	Station	Epoch	Hours	Scans
Saturn	Mh	2009.02.26	6	60
	Mh	2009.02.27	6	60
Venus	Mh	2009.02.27	2	24
	Mh	2009.02.28	2	24
	Mh	2009.06.09	3	30
TMC-1	Mh	2009.02.27	2	24
	Mh	2009.02.28	2	24
	Mh	2009.06.09	2	24

The reference source and the planets were observed during a span of several hours. In total, we accumulated 7 hours of Venus data and around 6 hours from the molecular cloud. The methodology of the data processing is similar to what was statistically applied to the Kronian observations. We separated LCP and RCP for the analysis. All the scans observed dur-

ing the same epoch were averaged. The background cosmic noise was subtracted from the planetary radio signal using the on-off source scans. The 8th-grade polynomial fit was removed from the original data and we searched for prominent features in the dispersion data after correcting the Doppler velocity of the elements. The procedure was explained in detail in Section 4.2.

The spectral average of the 24 scans on and off observed on 2009.02.28 is shown in Figure 4.11.
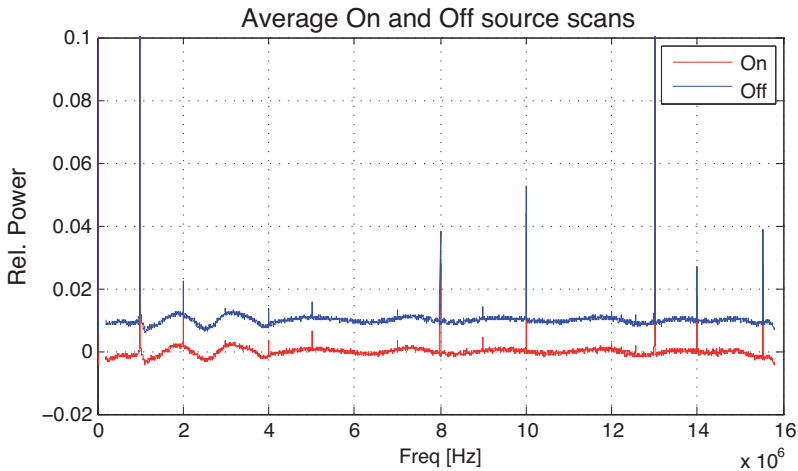
Figure 4.11. *On* and *off* scans average of 24 scans observed over Venus on 2009.02.28. The frequency is centred to 22.344 GHz. Only the RCP channel is shown here.

The difference in noise level of the spectra between high and low frequencies of the bandwidth is due to an incorrect filtering of the baseband converter. The peaks in Figure 4.11 are simply RFI. For the analysis, the regions with high level of RFI in the spectra were masked. Then the spectra were smoothed with multiple Hanning windows. The data were processed in both polarizations and they gave similar results. The non-detection of any prominent spectra line on Venus is shown in Figure 4.12.

We did not detect any spectral feature at the C_2S in any of the planetary observations. A similar analysis was performed to the TMC-1 data, which yielded better results. The characteristic size of emitting regions in TMC-1 is about 1 arcmin, while Venus is about 10 arcsec. The beam-filling factor is about 30 times lower. This difference may explain the non-detection of the gases in the atmosphere of Venus. Furthermore, Venus' atmosphere is rich with carbon and sulphur oxides, the chemical chain to produce C_2S
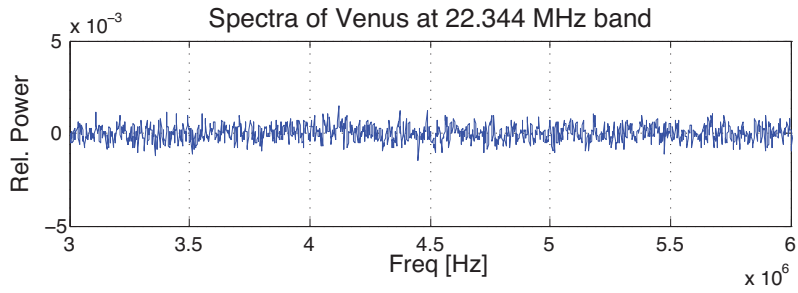
Figure 4.12. Non-detection of any spectral line at $22.344\,\mathrm{GHz}$ with the Mh telescope on 2009.02.27. The results were similar for the other epochs.

at Venus can also differ from emitted at TMC-1.

We were able to detect the spectral line of C_2S in two of the three epochs. The power of the spectral line detected was weak compared to the RFI and drastically different from the powerful emissions from water masers. The dicarbon sulphide emission line of TMC-1 was detected in Figure 4.13.
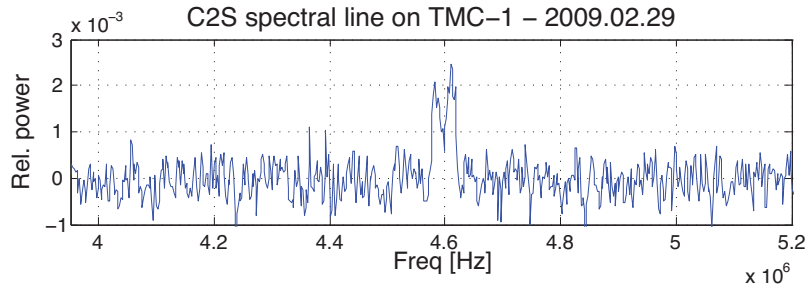
Figure 4.13. Detection of the disulphide carbon emission line of TMC-1 observed at Mh on 2010.02.28.

Due to the discouraging results of Venus search for the C_2S, we were happily surprised by the detection of dicarbon sulphide chains in TMC-1. The non-detection of the spectral lines over the planet can be attributed to several factors: high system temperature of the receiver, poor sensitivity of the antenna, the spectral line emissions were not favourable to be detected from Earth-based antennas or simply it is not possible to achieve such detections.

4.4 Lightning discharges on Mars

Mars is the fourth planet from the Sun at an average distance of 1.6 AU. The orbital period is 687 Earth days and has a synodic period of 780 Earth days [73]. A rock core, considered similar to the moon, composes the structure of the planet. Phobos and Deimos are two small satellites that orbit the red planet. The atmosphere is thinner than of the Earth and the Sun's radiation is just barely absorbed.

The tenuous atmosphere of Mars reacts to the solar heating by leading strong winds across the day-night line [86]. These strong winds are known as **thermal tide winds**. When these winds achieve speeds over 50 to 100 m s^{-1}, they may originate local dust storms. These storms can be classified by **saltation** and **dust devils**; in the first, the grains hop over the surface, while in the second the dust grains are raised up. The dust acts as catalyst for the tidal winds so that within just a few weeks, the dust storms may grow so large that they cover the entire planet. During the dust devils, the small dust particles rub against larger particles causing the dust particles to collide and the saltation of the triboelectric charges. In this process negative charges are transferred from large to small particles during collisions. Two natural phenomena may occur: strong electric field generated by the storms and electric discharges caused by the charge separation producing **non-thermal radiation** [89, 90].

Motivated by the recent discoveries of Earth-based detections of Martian lightning reported by Ruf et al. [70] we planned to observe Mars, in conjunction with the spacecraft sessions that focussed on tracking the ESA Mars Express [71] signal. To process the data and discriminate the non-thermal from the thermal noise radiation of the planet, we modified the software spectrometer to calculate the SK [82].

The concept of the non-thermal detections is based in the power of the signal and its kurtosis momentum [91]. The kurtosis momentum is a measure of the "peakedness" of the probability distribution of data series. The fourth standardized momentum can be defined as the ratio of the fourth central moment of a curve to the second moment squared, see Equation 4.4 [92]. If the value of the kurtosis is high, the variance is caused by infrequent extreme deviations.

$$\beta_2 = \frac{\mu_4}{\sigma_4} \qquad (4.4)$$

where μ_4 is the fourth moment of the mean and σ is the standard deviation. The kurtosis momentum is extremely sensitive to the presence of non-thermal radiation, but is insensitive to variations in the intensity of the thermal radiation. Hence, it is possible to detect non-thermal radiation of much lower amplitude than ordinary thermal radiation [93] by using kurtosis. Kurtosis values around 3σ indicate a Gaussian distribution. For instance, the cosmic background noise observed with radio telescopes is normally distributed. The cosmic background is an example of thermal microwave emission. Higher values of the kurtosis momenta will mean that is not normally distributed, and in fact, the origin of the microwave emissions is non-thermal.

4.4.1   Observations

We conducted an observation on 2010.03.04 of the Mars Express Phobos flyby [71]. The event was observed with three EVN radio telescopes: Metsähovi, Yebes and Wettzell. The observations included 3 hours observing the spacecraft signal and accurate measurements of the Doppler frequency. More information about this event is provided in detail in Chapter 5. Mars was in the same beam as the spacecraft, and therefore the observations could be reused for any other radio spectroscopy purpose as well. In total we conducted 3 sessions: on 2010.03.01-04 we used only the Metsähovi telescope and on 2010.03.03 with all three antennas. The sessions coincided with a period of high activity of dust storms in the Martian atmosphere. The angular resolution of the antenna at this frequency was $200\,\text{arcsec}$, and the full Mars disk fills approximately $0.04\,\%$ of the solid angle of the antenna beam.

Radiometric measurements were made using the narrow-band geodetic S/X receiver. The observations mode alternated between the usage of 4 or 8 sub band channels with a channel bandwidth of 8-$16\,\text{MHz}$. For instance, for the longest session on 2010.03.03, eight frequency sub bands were used with a bandwidth of 16 MHz. Four of the adjacent channels observed at X-band [8412 to $8466\,\text{MHz}$] and the other 4 at S-band [2288 to $2348\,\text{MHz}$]. In the other two cases, the observations were performed only in X-band. The S-band data were discarded due to their high level of RFI, since the S/C detection was too low to be correctly detected. The signal was split into eight $16\,\text{MHz}$-frequency channels with a total bandwidth of $96\,\text{MHz}$ from 8412 to $8506\,\text{MHz}$. Data were recorded with the standard MkIV VLBI data acquisition systems with 2-bit coding for a data-rate of $512\,\text{Mbps}$.

4.4.2   Results

Observational data were recorded into PC-EVN and immediately trans-
ferred to Metsähovi for the data analysis. A slight modification of the
SWSpec was programmed in order to calculate the SK and the windowed-
overlapped DFT in parallel. The real-time SK estimates via sub-channe-
lization and histogramming of the power magnitudes still in the frequency
domain between 8470 and 8490 MHz. This spectrum was divided into 8
adjacent, 2.5 MHz wide, sub bands prior calculating the kurtosis. The
spectral kurtosis using a time span of 250 ms and 10 ms are shown in Fig-
ure 4.14.
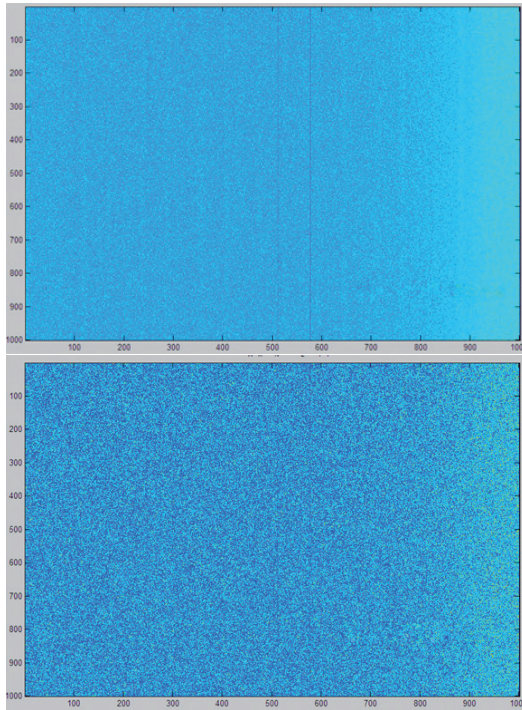
Figure 4.14. top: SK using a time resolution of 250 ms. bottom: using a time resolution
of 10 ms. We did not find any indication of possible detection of lightning
discharges in Mars on $2010.03.04$ at Mh. Frequency (x-axis) and Time (y-
axis).

We did not detect any indication of non-thermal processes during any of
the observations performed with the VLBI antennas. The next high sea-
son of electrical storms in Mars is expected to occur during spring 2012.
The team will try to arrange new proposals for observing the red planet
and searching for non-thermal emissions originating in the dust storms.

5. VLBI and Doppler tracking of spacecraft

5.1 Introduction

Planetary and deep-space science mission spacecraft as targets of radio astronomy offer new tools for studying a broad variety of physical processes. These physical processes include the dynamics of extra-terrestrial atmospheres, geodynamic diagnostics of the interior of planets and satellite ring structures, fundamental physics effects of spacecraft motion and solar corona, and solar wind characterization. Many of these applications require an extremely high angular resolution coupled with very high spectral resolution, only achievable with VLBI. The spacecraft VLBI tracking technique has already been demonstrated to be successful in several experiments. The most outstanding examples include the ground-based radio tracking of VEGA balloons for determination of Venus winds in 1985 [94], the VLBI tracking of the descent and landing of Huygens probe in the atmosphere of Titan in 2004 [95, 96], the VLBI tracking of the landing of Smart-1 probe on the surface of the moon with EVN radio telescopes in 2006 [75], the Very Long Baseline Array astrometric observations of the Cassini spacecraft at Saturn in 2010 [97] and VLBI tracking of the solar sail mission IKAROS with Japanese radio telescopes in 2011 [98].

The **Planetary Radio Interferometry and Doppler Experiment** is the latest development in the spacecraft radio science based on VLBI tracking. PRIDE is adopted by a number of prospective planetary science missions as a part of their scientific suite. These missions include:

- The Phobos-Soil mission, also known by its original denomination in Russian Phobos-Grunt, launched in November 2011. Phobos-Soil aimed

to land a robot craft on the surface of Phobos. Unfortunately, the mission failed minutes after its launching.

- The BepiColombo/MMO (Mercury Magnetospheric Orbiter) commissioned by JAXA and to be launched by ESA in 2014. BepiColombo focuses on studying the structure of the magnetosphere, the magnetic field and the geological composition of Mercury.

- The international ExoMars mission to be launched in 2016. The ExoMars targets to land a scientific robot on the surface of Mars in order to search for signs of past and present life, investigate the presence of water, existing geochemical processes and trace of gases on the atmosphere.

- Furthermore, PRIDE has been included into prospective space missions proposals as the Jupiter Icy Satellites Explorer (JUICE), Titan Saturn System Mission (TSSM), MarcoPolo-R and European Venus Explorer (EVE), which all aim for launch from the year 2020 on-wards.

As a preparatory stage for future space missions, mainly the ESA Venus Express (VEX), but also the Mars Express (MEX) spacecraft, have been used as a test bench for spacecraft tracking with VLBI antennas [99]. The spacecraft detection and data processing can be conducted in almost real-time and ensures the success in scientific research areas with the current technologies. These valuable research fields ranges from:

- Ultra-precise measurements of the celestial mechanics of the planetary elements and possible estimation of tidal deformation of the satellites.

- Study of geodynamic processes, composition and structure of the interior of planets and their respective satellites.

- Characterisation of the shape and strength of gravitational field of satellites by conducting several flybys.

- Analysis of the internal structure, topography and gravity field of planets by estimating the relative position of the orbiters and penetrators.

- Measurements of anomalous accelerations of deep space probes and other fundamentals physics effects.

- Measurements of the electric properties and the plasma media in environments of certain satellites by using spacecraft occultation.

- Direct-to-Earth telemetry from probes and rovers missions on the surface of the planets.

Spacecraft tracking experiments conducted before 2006 required significant amount of computational tasks and long latency before the first results were obtained. A software package that could drastically reduce the time for the data processing and a fast method to transfer the data from the antenna to the analysis centre were the two primarily concerns at the beginning of the project. VLBI spacecraft tracking combines the narrow band analysis of the spacecraft signal and VLBI phase-referencing to estimate the state vectors of the object. The new software simplifies previous methods developed by other groups and systematises the data processing pipeline. The current implementation of the tracking software is described in detail in Section 5.2. The software is available to the public under GNU license and is scalable to a wide range of scenarios and targets.

Other objectives were to standardize the session scheduling and configuration regardless of the telescope and data acquisition system. VLBI has a wide research community and most of the radio telescopes have different instrumentation. Thus, the constraints to observe vary at each station and the data processing is not homogenised, increasing the complexity of the processing. In order to properly schedule the observations and process the data, the existing VLBI data acquisition systems had to be tested. It is impossible to prepare a spacecraft session without knowing beforehand the available DAS at the radio telescopes. The observation modes, the characteristics of the radio telescopes and the different DAS are described in Section 5.3.

Results from previous spacecraft tracking endeavours with VLBI radio telescopes [75] were obtained after several months of work. First, data from each station were recorded into the disk pack modules. Then these modules were shipped to the correlation centre using regular post service. It could take up to one month before the data arrived to the analysis centre and similar amount of time before data were finally correlated. The last developments in fibre optics, last mile connections to the radio telescopes, real-time e-VLBI transfers, fast computational processors and the implementation of new software correlator can reduce the time delay to a matter of hours. A thorough study of this data processing latency is described in Section 5.3.2.

The new technical developments and the results of the tests have demonstrated that the VLBI radio telescopes are a potential tool for radio science scenario. The spacecraft Doppler tracking results using single-dish and VLBI antennas are presented in Section 5.4.

5.1.1 Radiometric tracking techniques

Tracking of any spacecraft or vehicle in the Solar System is accomplished using different radio and optical techniques. Both have been successfully demonstrated in various deep space missions. Radiometric tracking with ground-based support are typically used during the cruise phase of a mission and the insertion of the module into planetary orbits. Optical images are mostly used in the approaching phase, since better precision of the spacecraft position relative to the target is provided. Both techniques are complementary, improving the accuracy of the detection and reducing the uncertainty in the target-body ephemeris. Better sensitivity of the radio telescopes and new methods for radio spacecraft tracking enables more challenging navigation performance and complementary information in unexpected situations during the approach phase. The various radio techniques are well described in the literature [9, 100] and summarised below:

Ranging consists of a precise measurement of the round-trip transit time of a ranging signal transmitted from a ground station to the spacecraft. The transit time of the signal allows measuring the distance between the observer and the target. The ranging signal is a sequence of sinusoidal tones derived from the station frequency standard and is phase modulated onto the transmitted carrier signal. The spacecraft receiver detects and demodulates the transmitted ranging signal using a Phase-Locked Loop (PLL). Then, the ranging signal is phase modulated again onto the downlink carrier, the signal is coherent with the uplink signal but with an offset in frequency. A PLL at the ground station is in charge of detecting and demodulating the downlink signal. The round trip transit time is obtained by comparing the received and emitted range codes.

Doppler consists of measuring the frequency difference between the reference signal frequency received and emitted. The frequency transmitted from the ground station to spacecraft and from the spacecraft back to Earth is stable and well-known. The Doppler measurements provide information about the spacecraft topocentric range rate. The expression for the received frequency received at Earth is approximated as:

$$f_r = \left(1 - \frac{\dot{\rho}}{c}\right) \cdot f_t \qquad (5.1)$$

where f_t is the frequency transmitted by the spacecraft, $\dot{\rho}$ is the space-craft instantaneous **slant range rate**. Therefore, the term $(\dot{\rho}/c) \cdot f_t$ is associated to the Doppler shift. The slant range, or distance to the target, is:

$$\rho = \tau_g \cdot c \qquad (5.2)$$

where τ_g is the measured transit time between spacecraft and ground station Earth. Thus, the slant range rate can be approximated to [100]:

$$\dot{\rho}(t) = \dot{r}(t) + \omega_e r_s \cos \delta \sin(\omega_e t + \phi + \lambda_s - \alpha) \qquad (5.3)$$

where $\dot{r}$ is the geocentric range data, ω_e is the average rotation of Earth, r_s is the distance from Earth spin axis to the tracking station, λ_s is the longitude of the tracking station, α and δ are the coefficients for the right ascension and declination of the spacecraft and ϕ the phase angle depending on the epoch.

The most accurate ranging and Doppler measurements are obtained using the two-way tracking mode, in which the signal transmitted starts and finishes at the same ground station. In a generic one-way tracking, the spacecraft is the one that generates a downlink signal from an on-board oscillator and transmits it to the ground station. Furthermore, the three-way mode is possible as well. The Doppler 3-way occurs when the signal is transmitted by one radio telescope and recorded by another. Using VLBI radio telescopes for spacecraft tracking is not the two-way mode, as there is no access to the original signal emitted by the ground station. Hence, the data captured by the VLBI antennas is a mixture of one-way and 3-way modes.

Delta Differential One-way Range (ΔDOR) is a technique that uses two radio telescopes widely separated from each other to simultaneously track the radio signal and calculate the difference in the arrival time of the signals at each station, the **delay time**. The unambiguous delay obtained from spacecraft measurements is referred as **Differential One-way Range** (DOR) and the several tones and sub-harmonics transmitted by the spacecraft are referred as the DOR tones.

The measurement of the delay time can be affected by the propagation through the interplanetary plasma, Earth's troposphere and ionosphere and clock instabilities at the ground station. These errors can be corrected when using a known radio cosmic source as a reference for calibration. The observations alternate between the radio signal from the spacecraft and from the reference source. The differential delay between the spacecraft and the quasar is defined as ΔDOR. The delay time obtained by the classical correlation of the quasar is used to calculate the relative time and Doppler values. ΔDOR yields highly accurate measurement of the spacecraft angular position in the radio source frame.

Delta Very Long Baseline Interferometry (ΔVLBI) takes advantage of the radio interferometry techniques used in VLBI in order to determine the geocentric angular position and the velocity of deep space probes. The concept for the ΔVLBI is similar to ΔDOR, the one-way Doppler is obtained by simultaneously recording the broadcast signal with several radio telescopes. By alternatively observing the spacecraft and a quasar near-by, in angular terms, the ΔVLBI technique allows to estimate the state vectors and velocity of the target and correct the major error sources common to each separate downlink. The scenario for tracking spacecraft with VLBI technique developed by PRIDE is extensively described in Section 5.1.2.

5.1.2 Scenario for VLBI spacecraft tracking

The two-way data communications link between the planetary spacecraft and the ground-based station is observed for radio science and spacecraft tracking purposes. The approach presented here analyses the impact of detecting the transmitted signal from the spacecraft using VLBI radio telescopes. The basic scenario in VLBI spacecraft tracking observations is shown in Figure 5.1.

Several VLBI antennas located around the globe observe simultaneously the data communications between the mission support ground stations and the spacecraft. Data are transferred, either in real-time or after the experiment completes, to the computational centre for the data processing, correlation and analysis. The radio telescopes alternate observing the spacecraft and a near-by radio cosmic source. It is recommended to use a well-characterised quasar, which in terms of angular distance is relatively close to the target. The radio telescopes records the temporal
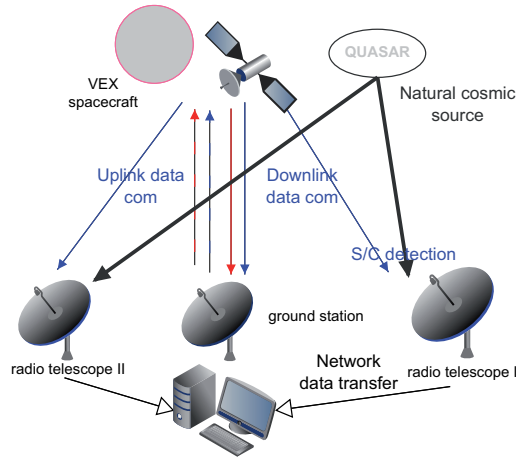
Figure 5.1. Typical set-up for spacecraft tracking observations. The S/C and a nearby quasar are observed simultaneously with several VLBI radio telescopes. Data can be transferred in real-time to the processing centre.

evolution of the radio signal emitted by both sources. A local H-maser clock is used as a reference to provide precise time information of the arrival time of the signals. This time precision is needed for correlation of the signals captured by the two separate elements of any interferometer array. The quasars provide a reference method for amplitude and phase calibration using the well-known Celestial Reference Frame (CRF). The broadband correlation of the several baselines is used for VLBI phase-referencing [101]. The VLBI tracking scenario is based on three major tasks: processing the narrow band spacecraft data, correlation of the cosmic radio broadband source and applying the phase-referencing.

Three kind of sessions were carried out regularly during the last two years with VLBI radio telescopes:

- **Single-dish:** Detection of the spacecraft with a single antenna. No reference source was observed for phase-referencing.

- **Multi-antenna:** Detections of the spacecraft with two or more radio telescopes simultaneously. The use of reference source for calibration and measure of time delay difference was optional.

- **VLBI tracking:** Detections of the spacecraft with several radio telescopes. The observations alternate between the spacecraft signal and the quasar. VLBI phase-referencing was used to estimate the state vectors of the spacecraft.

Details of the configurations and the significance of these scenarios for tracking planetary probes are detailed in Section 5.4. The full data flow for VLBI and Doppler tracking of planetary spacecraft is illustrated in Figure 5.2.
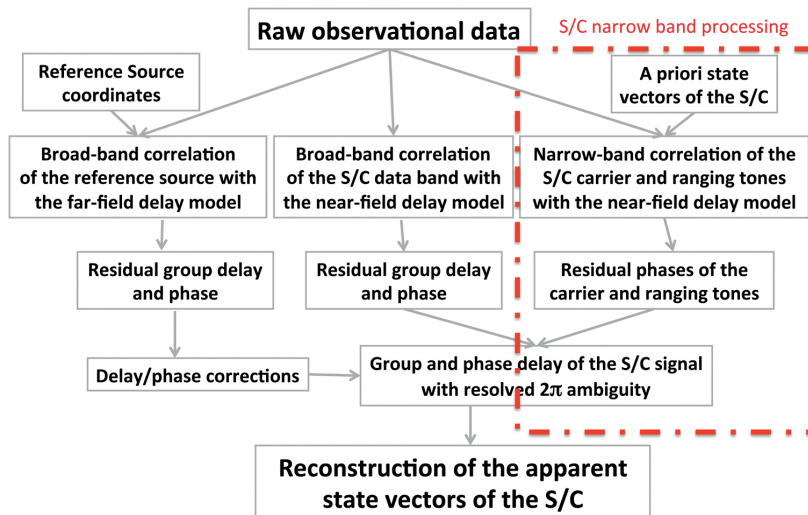
Figure 5.2. Block diagram with the full data flow for VLBI and Doppler tracking of spacecraft. The red box includes the modules this author have been working and that are presented in this chapter.

Tracking and positioning spacecraft in the near-field orbits is a complex procedure that involves several independent processes: far-field broadband correlation, near-field broadband correlation and spacecraft narrow band processing. The red box indicates the modules that the author contributes in the project and which are extensively presented in this chapter.

5.1.3   Solar System planetary spacecraft

During the last two years we have used several spacecraft for our tracking experiments. Any satellite equipped with a transponder, which can operate at UHF, S-, L- and X-bands, has an Ultra Stable Oscillator (USO), and a data communication link between spacecraft and ground station, is a candidate to be tracked. We have performed several experiments to detect the following spacecraft:

- **ESA Venus Express** (VEX) was launched in 2005. It is acquiring valuable data since 2006 and is expected to operate until the end of 2012

(latest official prediction). It contributes with long-term observations of the Venusian atmosphere, with the goal to better understand atmospheric dynamics.

- **ESA Mars Express** (MEX) was launched in 2003. It is sending data since 2004 and is expected to be operative until the end of 2012 (latest official prediction). It was intended for studying the interior, surface and atmosphere of Mars, in addition to the two moons orbiting the planet.

- **Akatsuki** & **Ikaros** were launched in the summer 2010 by JAXA (Japanese space agency). Akatsuki was originally designed to explore Venus, but unfortunately the entrance attempt failed. Ikaros is the first spacecraft to successfully demonstrate solar-sail technology in interplanetary space.

- **Ulysses** was launched in 1990 aiming to study the Sun at any latitude. This required a major orbital plan shift and, thus, the maximum distance Earth to spacecraft was larger than the distance to Jupiter. The spacecraft mission was officially shut down on 2009. Before the last operational day, we conducted a couple of trials to detect the signal. Unfortunately, the spacecraft signal was not detected.

- **Stereo A** & **B** The Solar Terrestrial Relations Observatory is a pair of spacecraft that were launched in 2006 by NASA. The spacecraft are identical and orbit respectively farther ahead and behind of the Earth. They enable stereoscopic imaging of the Sun and solar phenomena, such as coronal mass ejections. Several observations of both spacecraft have been conducted with the Metsähovi radio telescope.

- **Mars Exploration Rover** (MER) is an on-going robotic space mission that involves two rovers exploring the planet Mars. The rovers were sent to Mars on 2003 and, since then, they have been exploring the surface and geology of the planet. Only one of them is still working after 6 years of operation. The rovers used a transmission channel in the UHF-band. We could not detect its downlink signal either.

Most of the spacecraft are equipped with transponders capable of working simultaneously at S- and X-bands. For instance, the VEX communications are performed via redundant dual band transponders, which contain two duplicate receiver/transmit chains, each with X-band TX (8419 MHz) - RX (7166 MHz) and S-band TX (2296 MHz) - RX (2100 MHz). The sys-

tem uses a 1.3-meter high gain S- and X-band antenna, a smaller secondary high-gain X-band antenna, and two low-gain omnidirectional S-band antennas. The possible bit rates vary from at least 10.6 bps up to 262.14 Mbps. Other missions may have similar configuration. The gain and the size of the transmission antenna depends directly on the distance and the budget of the mission. Typical transmission bands are shown in Table 5.1 [100]

Table 5.1. Up- and downlink frequency channels commonly used in NASA deep-space communications.

Band	Uplink Frequency (MHz)	Downlink Frequency (MHz)
UHF	$395 - 405$	$395 - 405$
S	$2110 - 2120$	$2290 - 2300$
X	$7145 - 7190$	$8400 - 8450$
Ka	$34200 - 34700$	$31800 - 32300$

In radio science experiments, it is essential to have very stable one-way data links and precise phase control. Consequently, all spacecraft are equipped with an USO that provides a high quality on-board reference frequency source. The frequency stability of the one-way link typically is limited by the performance of the USO.

There are few constraints in order to select the appropriate USO for each mission: they should be light and relative small in size so that the weight of the payload will not increase drastically, and they should have an optimal budget-cost. Two main types of USO, based on quartz and rubidium oscillators, are available [102]. The quartz-based clock provides high stability with longer warm-up period and less stringent long-term stability, but consumes more power. The rubidium-based clock offers higher accuracy on measurement of the frequency but the output is statistically nosier. Summing up, over short periods a rubidium oscillator is nosier but more accurate, while a quartz oscillator is less accurate but more precise over a longer time period. A recurring question is the criterion for a choice between which crystal oscillators to use in the planetary probes. Venus Express is equipped with an USO based on quartz crystal (SiO_2). The Allan deviance ($\sigma_y(\tau)$) is used to estimate the frequency stability of oscillators due to noise processes [103].

$$\sigma_y(\tau) = \sqrt{\frac{1}{2(n-1)} \sum_{i=0}^{n} (y_{i+1} - y_i)^2} \tag{5.4}$$

where y is the number of samples analysed. The Allan deviation ($\sigma_y(\tau)$) for the USO mounted in the VEX spacecraft is about about 10^{-13} Hz s in 100 s.

5.2 Theory and calculations

A software packages for spacecraft tracking, based on the original software correlator developed by S.V. Pogrebenko, were developed at Metsähovi. The core of the software was initially designed for the data processing of Huygens and Smart-1 experiments [84]. The software is segmented in three modules. The first two modules were written entirely in C++ by J. Wagner. They perform the initial data processing by extracting the frequency channels from the raw VLBI data, calculating the time-integrated spectra of the broadband channel, narrowing the band around the spacecraft tone and extracting the spacecraft carrier signal relative to the local reference clock. The last module is written in Matlab by the author and performs the post-processing with high-precision and the post-analysis of the phase. The block diagram with the principal modules for tracking spacecraft is illustrated in Figure 5.3.

This software handles the spacecraft data recorded in one-way mode. The broadband correlation of the reference source is performed using classic VLBI correlators. Although the spacecraft signal is extremely narrow and is present only one frequency channel, the data are stored using standard broadband VLBI data format and several frequency channels. Using VLBI formatted data simplifies the recording with existing systems and allows correlating the radio cosmic sources. The software modules are described in the next sections.

5.2.1 Software spectrometer

The initial detection of the spacecraft carrier and sub-ranging tones is performed using the high-resolution software spectrometer **SWspec** [82, 83]. The program was developed by J. Wagner and can be download from the Source Forge web site[1]. The code is written mostly in C++ with a graphical

---

[1]http://cellspe-tasklib.sourceforge.net/
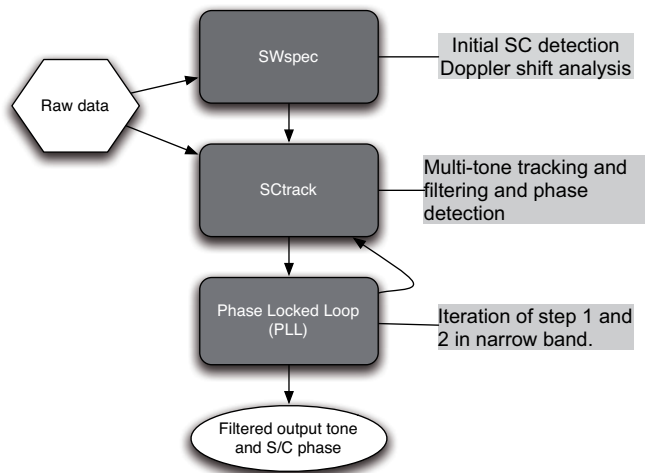
Figure 5.3. Principal modules for narrow band spacecraft analysis. SWspec performs the initial signal detection, SCtracker performs the multi-tone tracking and filtering, and the digital PLL the post-processing in narrow band with high precision.

interface based on Python PyQt4 GUI, which allows fast reconfiguration for new tasks and easy selection of the settings and parameters. SWSpec supports several input file formats, both formatted and raw data, which are broadly distributed in the VLBI research group. The software is compatible with the formatted data generated by the Mark5A/B/C (developed by Haystack/MIT) [33], the PC-EVN (developed by Metsähovi/Aalto) [59] and the newest attempt of standardized data format, the VLBI Data Interchange Format (VDIF) [104]. The support to Mark5A/B data format is possible thanks to the NRAO Mark5 access library developed by Walter Brisken [105]. The libraries have been included into the release of SWspec.

SWspec also supports several multi-channels and multi-bit raw data formats. These raw data can be generated by reconfigurable FPGA boards with 10 GbE interface like iBOB or ROACH at 8-bit, the MAXIM ADC board with 12-bit precision developed at Metsähovi[2], the Metsähovi VSIB board [34] and any other data acquisition systems not subject to a specific data format.

The initial design intended to run the SWspec on Cell platform, like the one offered by the Playstation 3. Hence, all the development was optimised for Cell Synergistic Processes Elements (SPE). Immediately, the

---

[2]http://www.metsahovi.fi/en/vlbi/misc-hardware/Maxim1217EVKIT/

code was ported to other generic platforms. Intel platform offered the best performance according to our internal tests. More information about computational tests performance is seen in Section 5.3.2.

The initial settings for SWspec are totally configurable by the user. They can be adjusted to cope with the specific set-up used during the observation. The configurable parameters are listed in Table 5.2.

Table 5.2. List of initialization parameters for the software spectrometer (SWspec). The parameters are stored in a text format file.

Label	Definition
FFTpoints	Number of DFT's to perform
SourceFormat	Format of the input data
SourceChannels	Number of frequency channels
BitsPerSample	Bits per sample
BandwidthHz	Bandwidth of the frequency channel
SourceSkipSeconds	Skip seconds to skip from the scan
UseFile1Channel	First channel source selected
UseFile2Channel	Second channel source selected
ChannelOrderIncreasing	Choose between MSB and LSB
PlotProgress	Plot the spectrum in real-time
DoCrossPolarization	Perform a cross-correlation of channels
FFTIntegrationTime	Integration time of the FFT's
MaxSourceBufferMB	Maximum of the buffer size
NumCPUCores	Number of CPU cores in multi-task
SinkFormat	Data output format
PCalOffsetHz	Offset of the PCal tone respect to MHz
ExtractPCal	Whether to extract the PCal tone
BaseFilename1	Input file name 1
BaseFilename2	Optional input file name 2

The SWspec module extracts any selected frequency channel from the raw data input file. It performs an accurate windowed-overlapped Discrete Fourier Transform (DFT) per each iteration and spectrum time-integration. The number of DFT's and integration time are the key parameters for the data processing. By default, SWspec uses a Hann window function to calculate the DFT [106]:

$$w(n) = 0.5 \left(1 - \cos \left(\frac{2\pi n}{N-1} \right) \right) \tag{5.5}$$

where n is the number of sample and N is the total number of DFT's per spectrum.

An additional feature of the SWspec allows extracting the phase of the Phase Calibration (PCal) frequency from the data [107]. PCal is a well-known frequency signal injected into the analogue receiver chain at the telescope to determine instrumental phase drift from. This is widely used in most of the VLBI stations as a checking utility to detect errors and problems in the receiver chain. Most of the old baseband receiver hardware are getting unreliable (VLBA rack BBC units) and is necessary to discriminate errors before the correlation. However, PCal extraction has no direct application with the processing of spacecraft data.

Finally, the time-integrated spectra along the entire scan with 32-bit precision are iteratively written to disk for the next iteration.

5.2.2 Phase-stop polynomial fit

The time-integrated spectra generated by SWspec are analysed using a Matlab script that determines the frequency drift of the spacecraft detections along the series of spectrum. The first version was developed at JIVE using MathCAD. The newest version was developed in Matlab m-code by the author, based on the previous version. The results obtained by both methods have been extensively tested and lead to similar results.

The idea behind the **phase-stop polynomial fit** is to extract the moving phase of spacecraft carrier tone signal from the series of time-integrated spectra. The process is almost automated and does not usually require extra tuning by the user. The spacecraft detection is expected to lie within certain boundaries. These limits are selected from previous experiences. When the SNR detection is low or the frequency of the carrier is not known before hand, a visual inspection is required for picking the correct tone. The spacecraft tones can be distinguished from the typical RFI, since the carrier tone frequencies varies along the integrated spectra with a known Doppler-defined pattern. The pattern drift depends on the spacecraft instant speed and distance. For VEX the drift is usually about 5 to 10 Hz per spectrum.

The series of frequency detections f of the spacecraft signal through the all time-integrated spectra are fitted to a M-order phase stopping polynomial. The polynomial grade is usually in the order of 4 to 7. The phase polynomial is calculated as:

$$P(t) = 0 + \hat{C}_{pp}(1) \cdot t^1 + \hat{C}_{pp}(2) \cdot t^2 + .. + \hat{C}_{pp}(M-1) \cdot t^{M-1} \qquad (5.6)$$

where $P(t)$ is the phase polynomial function, C_{pp} are the phase polynomial coefficients and t is the time from the beginning of the scan. The polynomial fit is built using a Weighted Least Mean Square (WLMS) method depending on the level of the SNR detection and nearby RFI consideration. At higher frequency resolution (1-10 Hz) and integration times (5-10 seconds), the spectrum of the carrier line appears smeared by the Doppler change. We estimate the position of the line in spectral domain as the centre of gravity over 5 frequency bins centred at the location of the maximum. Thus, we can achieve the sub-bin determination of the line position. The SNR weighted window follows:

$$\left(T^T W_{SNR} T\right) \hat{C}_{pp} = T^T W_{SNR} F \qquad (5.7)$$

where the time, the frequency and the weighted SNR are represented by matrices along the entire integrated spectra. The calculated polynomial coefficients C_{pp} are stored to disk for the next iteration.

5.2.3   Spacecraft multi-tone tracking

The spacecraft multi-tone tracking **SCtracker** [108] software is the core for detecting and tracking the spacecraft. The SCtracker was developed and maintained at Metsähovi by J. Wagner. It is written entirely in C++ with a Python Q4 GUI script for the graphic interface. The code is open source too, but obtaining the code is upon request. The SCtracker is in charge of tracking any desired tone, filtering the signal, extracting the narrow band data around the tones and detecting their relative phases. The list of input files required by the SCtracker is shown in Table 5.3.

The initial settings files for SCtracker and SWspec have similar format. SCtracker reads the text file and fills in the parameters to the software. The initial settings are listed in Table 5.4.

Table 5.3. List of the input files required to run spacecraft tracking software.

Files	Files description
Input data	Input data recorded with the radio telescope.
Tones list	List of spacecraft tone frequencies relative to carrier line.
	To track the carrier line the offset tones are set to 0.
C_{pp} list	Pre-calculated M-order phase stopping polynomial coefs.
Ini file	File with the initial settings for the tracking software.

The block diagram in Figure 5.4 illustrates the combined tasks between the SCtracker and the PLL. SCtracker corrects the Doppler shift based on the initial phase polynomial fit and then tracks, filters and extracts the selected tone. This process is repeated in the next iteration of PLL that performs the same mathematical concept in a narrow band.
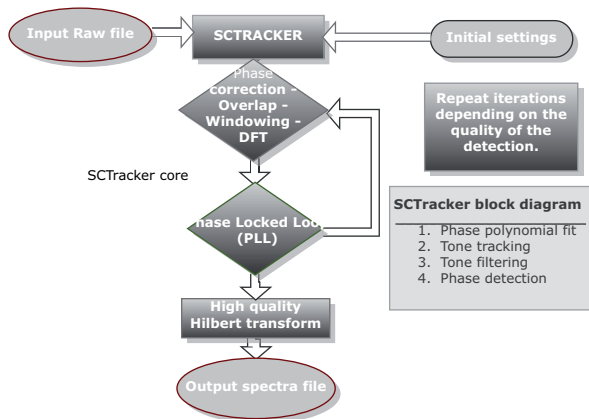
Figure 5.4. Block diagram for the main processes running on the SCtracker: First detection of the carrier signal, phase-polynomial fit, tone detection, filtering and finally extraction of the signal's phase.

Initially, the double-precision polynomial evaluation is applied to the baseband sample sequence $x[n]$ to stop the carrier tone phase. The mathematical approach to stop the spectra is:

$$\hat{x}[n] = x[n] \exp \left(\pm i \sum_{k=1}^{M-1} C_{pp}(k) \cdot (T_n)^k \right) \qquad (5.8)$$

where the $\hat{x}[n]$ are the new samples, the $x[n]$ is the original raw samples and T_n are the time samples of the spectrum. The new time-integrated

Table 5.4. List of initialization parameters for the spacecraft multi-tone tracking (SC-tracker).

Parameter	Description of the parameters
InputSource	Input File
TonesOffsetFile	Input file of the tones offset
SourceFormat	Format of the input data
SinkFormat	Data output format
DoSpacecraftTracking	Perform the tone spacecraft tracking
WriteDoublePrecision	Output the data file in float 64 bits
SourceChannels	Number of frequency channels
BitsPerSample	Bits per sample
BandwidthHz	Bandwidth of the frequency channel
SourceSkipSeconds	Skip seconds to skip from the scan
UseChannel	First channel source selected
FFTpoints	Number of DFT points
FFTIntegrationTime	Integration time of the DFT
FFToverlapFactor	Overlap factor of the DFT
PaddingFactor	Padding factor to calculate the DFT
WindowType	Window type for the DFT
WindowOutType	Output window type of the DFT
FilterBandwidthHz	Output filter bandwidth in Hz
PhasePolySign	Sign of the phase polynomials coefs $(+1/-1)$
PhasePolyCoeffType	Phase polynomial coefficients types
PhasePolyOrder	Phase polynomial order
PhasePolyCpmFile	File with the C_{pp} coefficients
PhasePolyCppFile	File with the C_{pp} coefficients
PhaseLockSpectra	Parameter for the statistics log file
NumCores	Number of CPU cores in multi-task
MaxRawBufSize	Maximum of the buffer size
BaseFilename	Output file name
ToneOutPattern	Output labels for the extracted tones

windowed-overlapped spectra of the stopped baseband signal are written again to disk. The new resultant spectra are the same spectra output as obtained with the SWspec but with the compensated Doppler shift. Therefore, the spacecraft carrier signal appears as a single narrow tone along all the series of spectra. The new time-integrated spectra are useful to verify the quality of the phase stop.

A narrow band around each tone is selected to track them at higher precision. The typically band is decimated in the range of $1{:}4000$ decimation ratios that is equivalent to $2\,\text{kHz}$ output. These narrow bands are extracted from the stopped baseband signal around each specified tone frequency. Each extracted tone is associated with a number. The number 0 refers to the carrier line and from number 1 on-wards refers to the sub-sequent ranging tones. The numbering is sorted according to their proximity in respect to the carrier tone. The current implementation of the software allows a practically unlimited number of narrow bands to be filtered and down-converted, with arbitrary distribution of them in the input band. The extracted bands (with the tones in the centre) are filtered out into continuous complex time-domain signals with $\leq 4\,\text{kHz}$ bandwidth using a 2nd order Window-Overlap-Add (WOLA) DFT-based algorithm of the Hilbert transform approximation. The extracted signals in temporal domain are written to complex floating-point output files for further post-processing. All data are stored with complex floating-point precision to avoid to loose resolution between the different iterations.

Furthermore, SCtracker calculates also the relative phase of the main carrier tone at the end of each spectrum. The phase at this relative wide bandwidth, $2\,\text{kHz}$, is not useful for data post-analysis and the values are not used as input for the PLL. The output files of SCtracker are listed in Table 5.5:

5.2.4 Phase-Locked Loop (PLL)

The last iteration of the data processing is performed using the digital **PLL**. The software has been written in Matlab m-code by the author as an add-on to the post-processing tools developed at Metsähovi. The software is based on the previous implementation developed by Pogrebenko. The software runs high precision reiterations of the steps in Equation 5.6- 5.8 on the filtered low-rate signals as showed in Figure 5.4.

Table 5.5. List of output files provided by the spacecraft tracking software.

Files	Files description
Output data	Output spectra after phase stopping
Tone files	Temporal signal around the tone selected
Phase files	Phase values of the main carrier line
StartTiming	Timing information of the beginning of the scan
Log file	Log file with the SCtracker processing
ToneBinning	Frequency information of each tone

The PLL calculates the new time-integrated overlapped spectra, calculates a second set of phase polynomial fit and finally performs the phase stopping of the time-integrated spectra of the narrow band signal. The output of the PLL provides a new filtered and down-converted signal and its residual phase. This residual phase in a stopped band is determined with respect to both subsequent frequency/phase polynomials initially applied for the phase stopping. The nature of the code allows us to down-convert and filter the output of the carrier tone as many times as desired. The decimation ratio between the iterations is variable and depends on the SNR of the signal. By default, the decimation ratio used is $1{:}100$.

The number of times to run the PLL depends on the frequency precision and on the required phase detection. Indeed, for the interplanetary scintillations studies a narrow band around the carrier line of $20\,\mathrm{Hz}$ is required. The precision at $20\,\mathrm{Hz}$ band is good enough to detect the relative phase of the signal. Two iteration of the digital PLL is needed to achieve a band output of $20\,\mathrm{Hz}$. On the other hand, spacecraft tracking and estimation of the state-vectors requires higher resolution. Thus, data are filtered and down-converted up to 5 or $1\,\mathrm{Hz}$. The frequency detections at the $1\,\mathrm{Hz}$ range have a resolution in the mHz order.

5.2.5 Default set-up for the tracking software

The typical parameters and frequency resolution used during the tracking software are shown in Table 5.6.

The default settings for the SWspec are optimised to detect the VEX spacecraft signal. Using 3.2 million DFT points, in a recording bandwidth of $8\,\mathrm{MHz}$ and $5\,\mathrm{s}$ of integration time provides a frequency resolution of

Table 5.6. Spectral resolution of the spacecraft tracking software. For the digital PLL the frequency resolution is not longer important and, instead, the phase and frequency noise are significant.

Software	BW	DFT points	Integration	Resolution
SWspec	$8\,\text{MHz}$	$3.2 \cdot 10^{06}$	$5\,\text{s}$	$5\,\text{Hz}$
SCtracker	$8\,\text{MHz}$	$3.2 \cdot 10^{06}$	$5\,\text{s}$	$5\,\text{Hz}$
PLL	$2\,\text{kHz}$	$20 \cdot 10^{03}$	$10\,\text{s}$	$0.2\,\text{Hz}$

$5\,\text{Hz}$ ($1\,\text{Hz}$ per $1\,\text{s}$). This frequency resolution is chosen coherently with the Doppler variation along the time-integrated spectra for VEX. The Doppler shift on VEX is about 1-$2\,\text{kHz}$ during the 20 minutes scans, or what is the same, 1-$2\,\text{Hz}$ per second. In a good detection, where the SNR is approximately several thousands of units, the Doppler detection at $5\,\text{s}$ is at the level of $30\,\text{mHz}$. The resolution of the detection after the SWspec is basically limited by the frequency change on the Fourier Transform, rather than the level of SNR. That is mainly because the spectra is smeared by higher spectral resolution and finite integration, so the frequency detections are not as accurate as they could be.

Similar settings are parsed to initialize the SCtracker. It uses 3.2 million DFT points, bandwidth of $8\,\text{MHz}$ and integration time of $5\,\text{s}$. The initial wide band signal is filtered down to any desired narrow band. The user can select the final output bandwidth. For the VEX signal we use an output bandwidth of $2\,\text{kHz}$. The decimation ratio in this case is 1:4000. If the initial channel bandwidth was $16\,\text{MHz}$ then the output band is usually $4\,\text{kHz}$. After processing the data with SCtracker the frequency detection change rate is below $0.5\,\text{Hz}$ during an entire 19-minute scan. These variation rate can also be expressed in terms of $1.6\,\text{mHz}$ at $5\,\text{s}$.

The filtered narrow band signal obtained with SCtracker is then processed with the PLL. Firstly, PLL calculates the time-integrated spectra using the $2\,\text{kHz}$ bandwidth signal, 20 thousands FFT points and $10\,\text{s}$ integration time. Thus, the new frequency resolution of the spectra is $0.2\,\text{Hz}$. At this point, the frequency detection noise may vary from 1-$2\,\text{mHz}$, when the SNR is of the order of several thousands of units, to 3-$5\,\text{mHz}$ when SNR is several hundreds of units. PLL calculates a second set of polynomial coefficients to compensate the Doppler at higher resolution. After stopping the spectra, the output signal is narrowed down and filtered to a default bandwidth of $100\,\text{Hz}$. To avoid introducing excessive noise we use

a decimation ratio of $1{:}200$. Successive iterations of PLL continue filtering the signal to the bandwidth desired.

For instance, a $5\,\mathrm{Hz}$ bandwidth is used in Doppler tracking for previewing the signal. After that, the data are processed again with the PLL to finally achieve the bandwidth of 1 or $0.5\,\mathrm{Hz}$. Using the bandwidth of $0.5\,\mathrm{Hz}$ we are able to remove most of the system noise. The frequency detection noise at this point is about $3\text{-}5\,\mathrm{mHz}$ in $1\,\mathrm{s}$. The main limitation for improving the frequency detection noise is caused by the interplanetary scintillations and LO phase noise of the receiver. Most of the improvements on this detection can be made in the telescope domain: improving the performance of the system temperature, increasing the phase LO stability and enlarging the collecting area.

5.2.6 Software FX Correlator

The broadband data from the radio cosmic sources are correlated using the classical VLBI hardware correlator. More information about operations in a correlator is available in Section 2.3. Nowadays, there is a wide range of possibilities to correlate the different experiments: hardware, FPGA-based and software correlators. The **Software FX Correlator** (SFXC) [109, 110] VLBI software correlator is being developed at JIVE to replace the old Mark IV hardware correlator and is currently used as a production correlator for astronomical observations with the EVN. SFXC is based on the original design of the VLBI tracking of the Huygens probe and is capable of supporting both the far field and near field models (see Section 5.2.7).

Several VLBI spacecraft tracking observations were correlated with the SFXC at JIVE using the near field theoretical delay model. SFXC can be used to correlate both the far field phase-referencing calibrators and near field spacecraft signals. The plan for 2012 includes integrating narrow band spacecraft software with the current Software FX Correlator in order to improve the performance and reduce the processing latency.

5.2.7 Far and near field model

The correlation of the calibrator provides the phase and time delay solutions per each of the baselines. These results are then combined with the results from the spacecraft signal obtained with the spacecraft tracking software. Since the nature of the sources is different, two different

delay models are required. For the reference sources, located at millions of light years from the Earth, the **far field** model [111] is used. This model, also known as the Consensus model, is broadly used for analysis and reduction of VLBI observations for distant objects. For spacecraft observations, a relativistic delay model for Earth-based VLBI observation of sources at finite distances is used. The **near field** model, developed by Sekido-Fukushima [112], implements a VLBI delay model, in the scale of terrestrial time, for radio sources at finite distances.

A new slightly modified version, written in Matlab m-code by Duev [10], of the near field delay model is integrated into the SFXC operational environment. The integration between the far field and near field is simpler and faster compared to using conventional models. The Sekido-Fukushima model calculates the delay of a near-field object according to the algorithm shown in Figure 5.5.
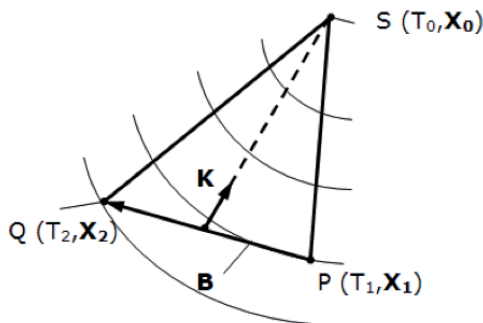
Figure 5.5. VLBI observation configuration for a radio source at a finite distance. The signal emitted from the radio source S arrives at the observational station 1 and 2 at (T_1, X_1) and (T_2, X_2), respectively.

The topocentric measurements of the frequency and phase provided by the spacecraft signal at each station are reduced to the common phase centre, known as **geocenter**. The model computes the geometrical part of the delay, in the general relativity metric sense, by introducing a pseudo vector to compensate the effect of the curved wave front and by using Halley's method up to the second-order to correct the variation of the baseline vector due to differences in the arrival time. The pseudo direction vector K is defined by [112, 10]:

$$K = \frac{\mathbf{R}_1(T_1) + \mathbf{R}_2(T_1)}{R_1(T_1) + R_2(T_1)} \tag{5.9}$$

and the vector from the geocenter R_i is equal to:

$$R_i = X_0(T_0) - X_1(T_1) = X_0(T_0) - X_E(T_1) - R_{iE}(T_1) \qquad (5.10)$$

where $R_{iE}(T_1)$ is the vector from the geocenter (T_1, X_E) to the station of the baseline in Barycentric Dynamic Time (TDB). The coordinate time T_0, time of the signal departure from the radio source, is obtained by solving the light-time equation using Newton-Raphson iterative method [113]:

$$T_0 = T_1 - \frac{|X_0(T_0) - X_1(T_1)|}{c} - \Delta T_{g,01} \qquad (5.11)$$

where $\Delta T_{g,01}$ is the gravitational effect on the ray path from the radio source S to the station 1 [10]:

$$\Delta T_{g,01} = 2 \sum_j \frac{GM_j}{c^2} \ln \left(\frac{R_{1j} + R_{0j} + R_{01}}{R_{1j} + R_{0j} - R_{01}} \right) \qquad (5.12)$$

The position of the gravitating body is evaluated at the epoch of closest approach of the photon to that body. The spacecraft position and velocity at each iteration step is interpolated to the T_0 using the initial ephemeris. The results from this new method for near field delay model were compared to the results produced by VTD far/near field delay model software, which was used for Huygens VLBI tracking experiment [95]. The differences were not significant.

Tropospheric and ionospheric signal delay

Different approaches are used for calculating the signal delay caused by the Earth's troposphere and ionosphere. Most widely used are models based on the standard atmosphere, which use the surface meteorological parameter values (temperature, pressure and relative humidity) at the observational site, and models based on the use of global Numerical Weather Models (NWM) that calculates tropospheric zenith delays and mapping functions.

The Vienna Mapping Functions [114] are used to model the tropospheric and ionospheric delay. This model is based on the direct ray tracing through the NWM and provides zenith delays and mapping functions calculated for the majority of VLBI stations around the world with a time resolution of 6 hours[3].

A Matlab script, which automatically calculates the azimuth and elevation of the spacecraft (based on its geocentric ephemeris), downloads the

[3]http://ggosatm.hg.tuwien.ac.at/DELAY/SITE/VLBI/

necessary files with zenith delays and mapping functions and calculates full tropospheric delays for each epoch of the observation at each VLBI site was written. The tropospheric signal delay model for radio astronomical observation research conducted by Duev [10] is used for the spacecraft VLBI tracking post-analysis.

5.3 Materials and methods

5.3.1 Methodology of the observations

The data communication link between the VEX and the mission support ground station (ESTRACK) operates daily during a six hours time frame. We limited the sessions to 2 or 3 hours due to the large amount of data collected. The data easily fill the disk capacity of the processing servers, increases the duration of the network transfer and the complexity of the data processing. Consequently, longer sessions demand additional user-time for the processing. Moreover, the available time for the observations is extremely limited. Indeed, the observations at Metsähovi of other astronomical radio sources consume most of the antenna time and the spacecraft sessions need to be squeezed between the geodesy sessions. The time to swap from one receiver to another is about 6 hours for two operators. So, a single session requires up to three days of antenna time, so one-day session are not efficient.

The scheduling of the spacecraft observations with VLBI radio telescopes is generated by **SCHED**[4] [115]. The program is broadly used among the astronomy VLBI community to prepare the sessions. The schedules for these observations are generated at Metsähovi or JIVE several days before the epoch. These schedules contain information about the sky pointing coordinates for the antenna and specific start/stop times for the recording of the scans, among others. The schedules, once created, are sent to the operator of each station. The operator compiles the file on the VLBI Field System (FS) [116] and checks the integrity of the session. The FS is a specific computer designed to control all the operations in VLBI stations. The FS sends the commands to control and manoeuvre the antenna, sets up the configuration of the analogue BBC and manages the data recording times with the Mark5A. The FS runs in standard Debian

[4]http://www.aoc.nrao.edu/~cwalker/sched/.

Linux OS with additional customised software packages directed for astronomical purposes. The FS is developed and maintained by Ed Himwich from the NASA Goddard Space Flight Centre (GSFC). The configuration of VLBI equipment has been shown in Figure 3.1.

The observing sessions were prepared depending on their purpose. The interplanetary scintillations study aimed to analyse the behaviour of the spacecraft phase. Therefore, the recorded scans had to be long enough (19 minutes) to characterise the temporal evolution of the phase. On the other hand, the VLBI tracking of spacecraft intends to estimate the state vectors of the target as accurate as possible using phase-referencing. Thus, these scans were shorter, about 5 minutes. The phase-referencing implies that the antenna alternated observing the reference source and the spacecraft. For a better characterisation of the plasma scintillations, the epoch of the sessions were ideally planned to run once per week. Unfortunately, due to the high demand of antenna time for other purposes we were not able to observe as much as intended.

The observations use the existing VLBI equipment at the radio telescopes. The astronomical data are captured using the standard VLBI MkIV-VLBA data acquisition rack systems with four or eight frequency channels. Each channel has fully configurable bandwidth of 4, 8 or 16 MHz with 2-bit Nyquist sampling mode. The total aggregate recording data rate varies from 128 to 512 Mbps, generating over hundred of Gigabytes per each session. Data are recorded to disks using the Mark5A or PC-EVN VLBI recording systems. When the session is conducted abroad, the data are transferred over the network from the remote station to Metsähovi once the session is done. In real-time sessions, data are not stored to the local disks of the radio telescopes; instead, data are streamed in real-time to the servers at Metsähovi. The Tsunami-UDP transfer protocol is used for real-time streaming and recording over network. If the sessions included observation of reference sources then the data has to be correlated at the JIVE VLBI correlator. In that case, data are recorded to disk pack modules and then shipped using a courier mail service to the correlator.

On the other hand, the observations performed at the Pushchino radio telescope were carried out using a bandwidth of 4 MHz and the Japanese VLBI recording system, K5[5]. Only one frequency channel was acquired

---

[5]http://www2.nict.go.jp/w/w114/stsi/K5/index-e.html

with 8-bit resolution. Data were uploaded to their server and then transferred using FTP to the local server at Metsähovi.

The list of radio telescopes that have participated in the spacecraft observations is shown in Table 5.7.

Table 5.7. Summary of the main characteristics of several EVN radio telescopes: coordinates of the station, dish size (m) and SEFD (Jy) at X-band.

Station	Lat.	Long.	Alt (m)	ϕ(m)	SEFD
Effelsberg	50°31'29"	06°52'58"	300	100	20
Hartebeesthoek	−25°53'14"	27°41'05"	1415	26	700
Matera	40°38'58"	16°42'14"	543	20	3000
Medicina	44°31'14"	11°38'49"	57	32	320
Metsähovi	60°13'04"	24°23'25"	75	14	3200
Noto	36°42'34"	14°59'20"	143	32	770
Onsala	57°23'47"	11°55'39"	33	20	2000
Pushchino	37°37'53"	54°49'20"	33	22	1500
Warkworth	−36°26'05"	174°39'48"	100	12	3000
Wettzell	49°08'42"	12°52'03"	669	20	750
Yebes	40°31'27"	−03°05'22"	998	40	200

In addition to the standard VLBI equipment utilised for detecting the spacecraft signals, we designed new solutions to reduce the cost and simplify the hardware. The idea behind these developments was to have a generic solution for spacecraft tracking independent of the VLBI equipment. Two ideas were developed: a processing board based on FPGA and a multi-bit digitizer platform.

The first option was the iBOB FPGA-based board, developed at the UC Berkeley. More detailed information is available in Section 3.4. The iBOB was designed to digitize the analogue signal provided by two VLBA baseband converters, filter the signal, packetize the digital data using UDP packets, and send them via the 10 GbE connector. The design was built to record one frequency channel, dual polarization, a bandwidth of 8 or 16 MHz with 8-bit sampling. Data were streamed using the 10 Gbps CX4 cable to a Linux-based data storage system. The total data output was 256 or 512 Megabits per second.

The second method consisted of using the MAX1217[6] evaluation kit to

---

[6] http://www.maxim-ic.com/quick_view2.cfm/qv_pk/5130/t/al

sample two analogue signals up to 125 Msps with 12-bit resolution. The board features parallel-format LVDS outputs terminated on-board in addition to optionally powered 3.3 V PECL outputs. The Metsähovi VSIB board and other VSI-bus boards can be interfaced directly to the evaluation kit LVDS outputs. With one board it is possible to feed $12/16$-bit dual channel data onto the VSI bus. With two boards, 4-channel 8-bit data can be placed on the VSI bus.

Each board allows recording only one channel and two polarizations or two channels and one polarization with two different analogue-to-digital converters. It cannot be used for broadband recording as VLBI systems, unless several boards are used in parallel, which increases the complexity of the system. The developments were not fully compatible with VLBI correlation for phase-referencing. Roach DBE boards or dBBC could be a good solution for broadband recording and spacecraft tracking based on FPGA-devices.

5.3.2 Computational performance

In earlier spacecraft VLBI experiments fast results were not feasible. Several days were needed before the data obtained from one radio telescope was processed and the results were ready. If the observations involved several stations and broadband correlation for phase-referencing, the delay increased to several months. The broadband correlation is not the main subject of this thesis. The author expects that future correlators based on software clusters, FPGA or hybrid systems will improve the latency.

The sessions carry out a certain routine. The astronomical data are extracted from the recording DAS at the telescope, transferred over the Internet to the processing centre, processed with the on-purpose developed software for spacecraft detection and finally the results are post-analysed. New methods were taken into consideration to improve the processing and reduce the latency:

• Data are recorded into the PC-EVN system instead of the conventional Mark5A, whenever the stations have both recording systems. PC-EVN records the data using conventional Linux file system and therefore is easy and fast to read and transfer the data. When the station has only a Mark5A unit we use **fusemk5a** [117] to read and extract the scans. Fusemk5a uses the user-space file system to extract the observed scans

from the special disk modules developed by Conduant and copy data into any standard hard disk or to transfer via network anywhere.

- Tsunami-UDP is used as a standard transfer protocol for all the sessions. The transfers benefited from an improvement of 10 to 20 times compared to the basic FTP transfers. A slightly modified version of the Tsunami-UDP transfer protocol enables real-time data transfer. In order to stream real-time data the station must record the data with a PC-EVN. Data are captured with the PCI VSIB board and then streamed directly to the Internet. Data can be simultaneously stored into disk, as a backup mode.

- The **SWspec** was programmed to support multi-core operations. It enables to run several parallel threads for calculating the Fourier transform and the data overlapping. We have tested the multi-core mode in different architectures with excellent results. The multi-core results for **SWspec** and **SCtracker** is shown in Table 5.8.

- Finally, part of the data post-analysis is done at Metsähovi and so the processing latency has decreased. At the beginning, the results were sent back and forth between JIVE and Metsähovi. Nowadays, the phase-polynomial fit and the PLL are conducted by the author at Metsähovi. Furthermore, a real-time spectrometer was developed to verify and monitor the output spectra. The tool is extremely useful for fast-checking the correctness of the input settings and the coherency of the results.

Table 5.8. Software benchmark with system A (Dual-Core AMD opteron(tm) processor) and System B (Intel Quad-Core - i7 920 @ 2.66 GHz). The scan was 1140 s and 8-bit encoding.

Program	Cores	System A	System B
SWspec	1 core	2097 s	420 s
SWspec	2 core	1118 s	262 s
SWspec	4 core	723 s	193 s
SCtracker	1 core	12400 s	4635 s

The system A is a two-years old Dual-Core AMD opteron, with 8 GB of memory RAM and system B is a one-year old Intel Quad-Core i7 920, also with 8 GB of memory. The scan for the benchmarking was 1140 s long with 8-bit resolution. SWspec and SCtracker were used with 3.2 million DFT

points and 5 second integration time. SWspec was benchmarked using 1, 2 and 4 cores. SCtracker was tested only using 1 core, since the program is still limited to single core operations. The time latency of the principal tasks for spacecraft single-dish detection is shown in Table 5.9.

Table 5.9. Data processing latency for all steps required for the spacecraft narrow band detection. Two hours are required to analyse each scan. The results for the entire are usually obtained after 10 hours.

Task	Time elapsed	Percentage
Observation	$1140\,\text{s}$	$19.7\,\%$
Network transfer	$275 - 550\,\text{s}$	$4.7\,\%$
SWspec	$193\,\text{s}$	$3.3\,\%$
Polynomial fit	$10\,\text{s}$	$0.1\,\%$
SCtrack	$4150\,\text{s}$	$71.6\,\%$
PLL	$30\,\text{s}$	$0.3\,\%$
Total	$5768\,\text{s}$	$100\,\%$

Only the spacecraft narrow band processing is taken into account here. The particular processing times shown in Table 5.9 are the standard values obtained in VEX sessions. For this specific case $1140\,\text{s}$ scan, 1.6 million DFT points, $5\,\text{s}$ integration time and 2-bit data were used. The turnover for the scan data analysis was less than two hours.

As seen in the table, the SCtracker is the slowest process of the current spacecraft narrow band processing pipeline. New multi-core parallel support or GPU-based code should accelerate the processing performance. Both solutions have been evaluated and may be implemented in the near future. However, the broadband VLBI calibrator correlation is the bottleneck for spacecraft VLBI tracking. The current old existing hardware correlators are slowly being substituted with newer software correlators, DiFX [118] developed at Swinburne University and SFXC [109] developed at JIVE, or FPGA-based correlator, Uniboard[7] developed at JIVE or ROACH2[8] developed at UC, Berkeley.

5.3.3 Data analysis and interpretation

SCtrackAnalysis is a Matlab tool using a graphical user interface designed to analyse the results obtained with SWspec and SCtracker. Fur-

---

[7]http://www.radionet-eu.org/uniboard
[8]http://casper.berkeley.edu/wiki/ROACH2

thermore, SCtrackAnalysis enables implementing the phase polynomial fit and the digital PLL. The scripts can also be used independently as a verification tools. The graphical interface allows the user to perform all the data post-analysis from one menu. The program assumes that the user has knowledge about the observation set-up and the parameters of the processing. The SCtrackAnalysis software has been developed and is being maintained by the author.

The application reads spectral data in binary format (32-bit) with variable length, the extracted tone data in complex format (real 32 bits and imaginary 32 bits) and the apparent phase of the tone in ASCII format. The results can be plotted directly using the graphical interface or stored into files.

The input parameters for the application are fully configurable and they can be adjusted to the observing and/or processing mode used. The input settings to be defined by the user are in Table 5.10:

Table 5.10. Input settings to be defined in the graphical user interface.

Field definition	Default value
Number of DFT points for the spectra	$3.2 \cdot 10^6$
Number of scans to process	1
Bandwidth (MHz) of the channel	$8\,\mathrm{MHz}$
f_S min value	$3.4 \cdot 10^6$
f_S max value	$3.6 \cdot 10^6$
Order of the polynomial fit	6
Spectra calculated in SWspec	$1.4\,\mathrm{GB}$
Spectra calculated in SCtracker	$1.4\,\mathrm{GB}$
Narrow band tone	$35\,\mathrm{MB}$

The main functionalities of the software are:

- Previewing the time-integrated spectra generated by SWspec and SCtracker.

- Plotting the total aggregate spectra per the entire scan.

- Zooming the spectra around the spacecraft tone.

- Calculating the phase-polynomial coefficients for an m-order fit of frequency detections.

- Measuring the SNR level of the signal detection after calculating the spectra with SWspec and SCtracker.

- Verifying the phase extracted from the spacecraft signal.

- Checking the spectra in narrow-band of the spacecraft tone signal

- Running the PLL with the narrow band signal.

The scripts can work as a stand-alone application or with the GUI interface module. The tools were developed using Matlab m-code and are in constant development in order to improve and optimise the capabilities of the software. A screenshot of the Matlab graphical interface of the spacecraft tracking analysis is shown in Figure 5.6.
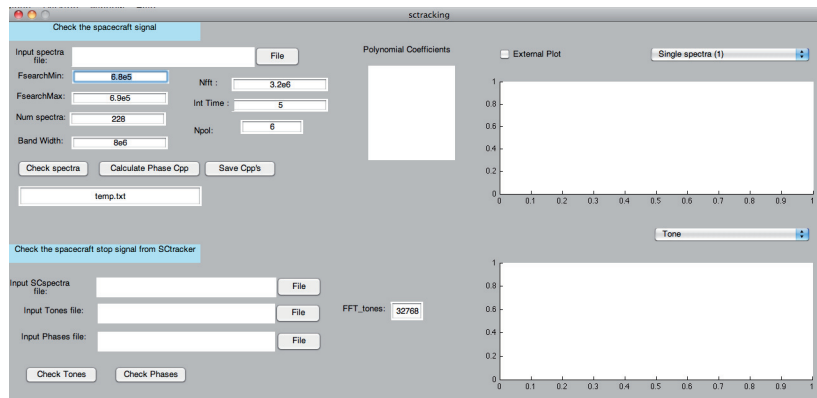
Figure 5.6. Screenshot of the Matlab GUI tools (SCtrackAnalysis) written by the author.

5.4 Results

5.4.1 Spacecraft signal detection with a single-dish

The observations of the spacecraft signal were conducted routinely during the period from 2009 until 2011 as a test-bench for signal detection and study of the phase scintillations caused by the solar wind. The interplanetary scintillations have been thoroughly studied using the data collected during these two years and are detailed in Chapter 6. The sessions consisted of observing the spacecraft signal, usually VEX, with a single radio telescope. The duration of the sessions varied from two to three hours and

were conducted almost every two weeks. The observations were conducted indistinctly with any of the EVN radio telescopes.

The broad range of available telescopes allowed us to test the observations and the processing software in several scenarios. Furthermore, the results of the phase fluctuations along propagation path are not biased by the receiving antenna. Most of the observations were scheduled just few days in advance, mainly depending of the availability on antenna time of the stations. The primary goals for spacecraft detection with single dish are to:

- Improve the software data processing pipeline.

- Improve data flow from the stations to correlator centre.

- Improve the planning and scheduling of the sessions.

- Improve the accuracy of the results of the data analysis.

- Study of the interplanetary scintillations.

This section presents a thorough analysis of one session that yielded good detection of the spacecraft signal. The walk trough shows the results of single-dish obtained at each stage of the spacecraft tracking software. Some of the other observations did not have as good results for several reasons. A couple of them are also presented here for completeness.

The v100830 session was observed on 2010.08.30 with the radio telescope of Onsala (Sweden). This was the second attempt to use the Swedish antenna to detect the spacecraft signal. The session started at 12:00 UTC and elapsed for 3 hours. The sky coordinates of the spacecraft at 12:00 UTC had a right ascension (RA) of 13h18m19.8s and declination (Dec) of -11d21'32.0". The spacecraft was at a distance of only 0.6 AU and solar elongation of 45.5°. Venus was located almost at the greatest-western elongation. Nine scans were recorded in total using simultaneously both Mark5A and PC-EVN systems. Data were transferred to Metsähovi over Internet using Tsunami-UDP once the observation was completed.

The first step on the processing pipeline is to use the SWspec to preview the spacecraft signal in the spectral domain. The time-integrated spectra are written into disk using output binary files with 32-bit resolution. This data can be visualised with any mathematical graphic software available in the market: Python, Matlab, Mathcad, Octave, among others. The results presented here were analysed using the **SCtrackAnalysis** tools.

A typical scheme of the recorded radio band spectra processed with the SWspec is shown in Figure 5.7. The spectra were processed using the bandwidth of $8\,\mathrm{MHz}$, 3.2 million points, integration time of 5 seconds and spectral resolution of $5\,\mathrm{Hz}$.
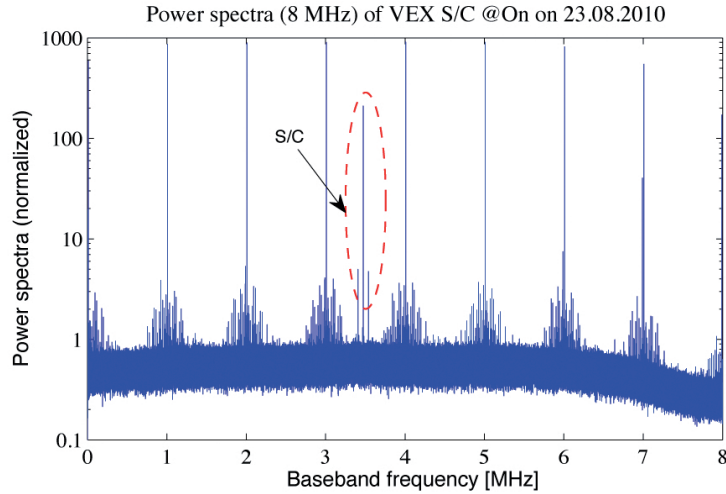
Figure 5.7. Wide band spectrum ($8\,\mathrm{MHz}$) observed on $2010.08.30$ at On. The high peaks are the PCal tones, the circle marks the S/C signal and the lower spurious are RFI. The relative spectral power is determined by the T_{sys}.

At first glance the main features seen in the spectrum are the PCal tones, the spacecraft carrier signal and sub-ranging tones, the receiver system and cosmic background noise and the undesired RFI spurious. The PCal tones, which are inserted at the beginning of the S/X receiver chain, are easy to distinguish since the peaks are repeated exactly at every Megahertz in the spectrum. The explicit frequency of the inserted PCal tone is set in the schedule of the observation. Thus, the frequency is well-known by the observer and the spurious are separated tens of kHz from the exact $1\,\mathrm{MHz}$ (i.e. $0.99\,\mathrm{MHz}$). These PCal tones can be extracted with the current software and they are useful for determining possible problems in the receiver or in the acquisition rack system.

The large peak located in the centre between the third and fourth MHz is the spacecraft signal. The power level of the spacecraft signal is just 10 times below the PCal tones and about 200 times superior than the temperature noise of the receiver at the resolution of $5\,\mathrm{Hz}$ in $5\,\mathrm{s}$. The two lower peaks next to the carrier line (a few kHz apart) belong to the sub-ranging tones emitted by the spacecraft. The comparison between the carrier line and the harmonics tones will be compared later with higher resolution.

All the undetermined frequency spikes are related to the RFI. The origin of the RFI can be associated to the S/X-band receiver system, external radio sources within the antenna beam or others outside of the beam and generated by Earth's sources. With high levels of RFI masking the spectrum, it is complicated to discriminate the spacecraft signal from the rest of spikes. The level of RFI in the spectrum is almost negligible and does not interfere with the analysis. These facts combined with strong detection of the spacecraft make this a good demonstration example.

Unfortunately, not all the observations yielded good and clean detection of the tone signal. Two cases were the spacecraft tone is difficult to discriminate from the RFI are illustrated in Figures 5.8 and 5.9.
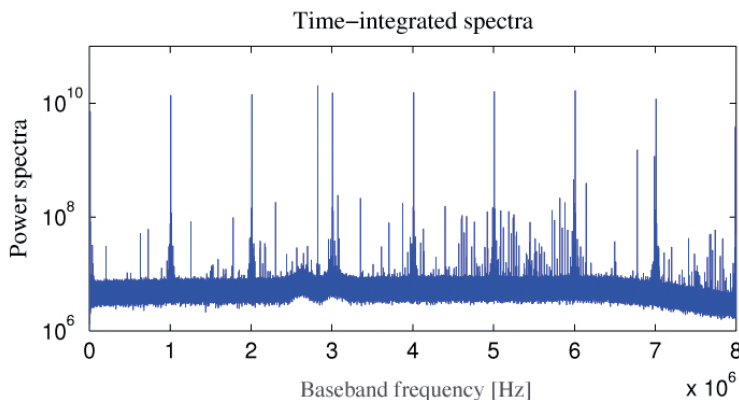
Figure 5.8. Wide band spectrum (16 MHz) masked with several RFI spikes. Some times it is difficult to discriminate the spacecraft tone from RFI. The session was observed on 2011.04.23 at Wz.

The first example shows a spectrum masked with high amount of RFI along the entire bandwidth. This scan was recorded at the radio telescope of Wettzell on 2011.04.23. The spacecraft signal is strong and outstands from the other peaks. However, it is difficult to discriminate it from the RFI spikes that are spread along the entire bandwidth. RFI in S and X-band is a permanent problem that just keeps increasing.

Figure 5.9 shows a reasonable RFI level, but the system noise temperature and performance of the observation were so weak that it is almost impossible to spot the signal. The session was observed on 2011.05.24 at Metsähovi. In addition to the typical extremely high system noise temperature, there were problems with the antenna pointing causing a bad detection of the signal. The spacecraft signal is centred at 2.85 MHz within the bandwidth. At first glance it is impossible to decide which is the cor-

rect tone. Hence, we need to take a closer look at each tone for the Doppler variation and discriminate the valid tone from pure RFI.
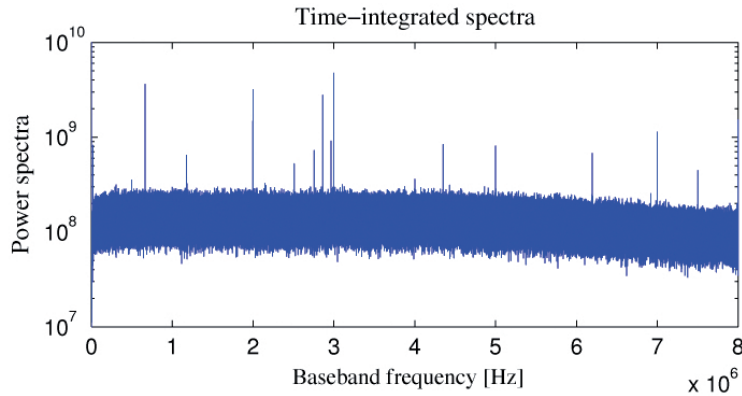
Figure 5.9. The spacecraft signal was so weak that was almost indistinguishable. There was a problem with pointing of the antenna and almost the signal was not detected. The session was observed on 2011.05.24 at Mh.

When the RFI is masking all the signal and the detection is weak, we need to evaluate the frequency detection of possible candidate tones along the whole observed scan and measure the coherency of the Doppler detection with the expected values in order to distinguish the spacecraft tone. The frequency of the received spacecraft tone shifts along the time, while the natural radio wave sources and other RFI keep constant. By repeating the VEX observations and estimating the predicted Doppler shift we are able to set certain frequency boundaries between which the spacecraft signal tone is most likely to be found.

To detect the carrier tone from a new spacecraft, it is important to know in advance the frequency of the transmission and the apparent arrival frequency of the signal at the antenna. However, sometimes a thoroughly scan of the wide band spectrum is still necessary for detecting the correct signal. In Figure 5.7 is seen a detection of the spacecraft signal was clear and did not require any extra fiddling.

The quality of the spacecraft detection is determined by measuring the SNR of the spacecraft with respect to the system noise temperature (T_{sys}). The SNR obtained on 2010.08.30 session after the first iteration of SWspec is shown in Figure 5.10. The detection of the VEX signal was clear with a mean SNR of 2125 units, relative to T_{sys}, at 5 Hz spectral resolution.

Best detections of the spacecraft are obviously achieved with the most sensitive antenna available. In our case, the top sensitive radio telescope

SNR detection of the tone at 5 Hz
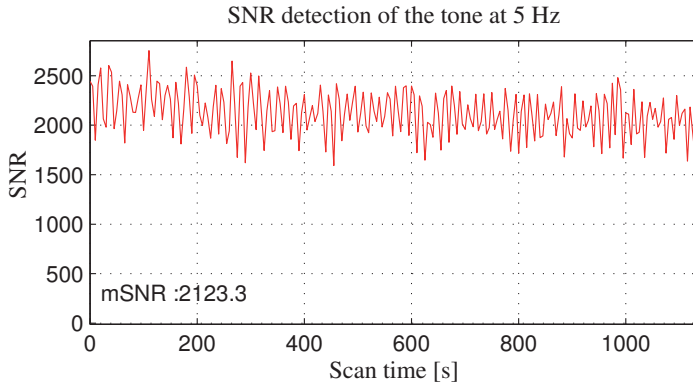
Figure 5.10. Good SNR detection of the VEX signal observed on 2010.08.30 at On. The SNR level after SWspec was approximately 2125.

was Yebes (40-m, Spain). The antenna was completed on 2007 and has one of the best SEFD ($200\,Jy$), acceptable RFI and low value of T_{sys}. Metsähovi is the least sensitive antenna used in our experiments. The SNR of Metsähovi is typically between 600 and 1000 at $5\,Hz$ resolution. The lowest sensitivity antenna still allows us to detect accurately the spacecraft signal as demonstrated along the past two years.

Doppler variation of the frequency detections is calculated from the averaged time-integrated series of spectra. The movement of the planet of which the spacecraft is orbiting, the own velocity and acceleration of the spacecraft, and also the rotation of the Earth are the causes for the Doppler shift. The Doppler shift measured from the averaged time-integrated spectra is shown in Figure 5.11. The 19-minute scan was observed on 2010.08.30 at Onsala.

Generally the Doppler shift ranges from several hundreds of Hz to $1\,kHz$ during one full 19-minute scan of VEX. The estimation of the Doppler shift is the next step on the processing pipeline and we approached it by building a model to compensate the effect. We use a phase-polynomial model of the Mth order to fit the Doppler variation with the constructed model. The best approximation for the VEX observations is a 6th order phase polynomial model. The topocentric frequency detections observed with SWspec of the second scan (12:20 UT) on 2010.08.30 is shown in Figure 5.12.

The frequency bin detections along the entire scan are shown in blue lines and the 6th order phase polynomial fit is shown with red-crosses. The total frequency variation for the full scan was $400\,Hz$ centred to a nominal tone frequency of $f_0 = 3.473295\,MHz$. These values correspond
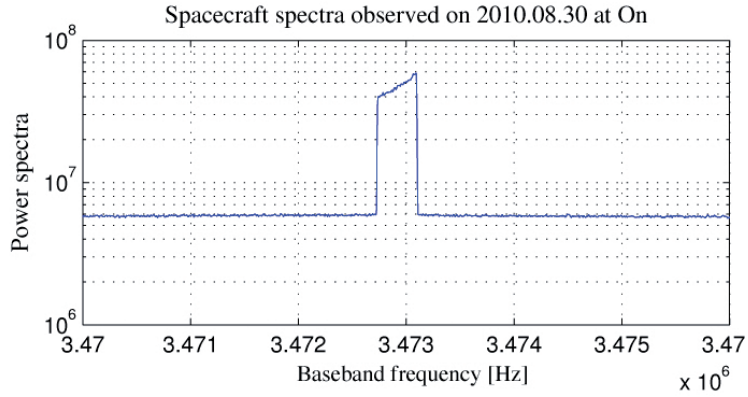
Figure 5.11. The averaged time-integrated spectra observed on 2010.08.30 at On. The Doppler shift allows distinguishing the S/C tone from RFI.
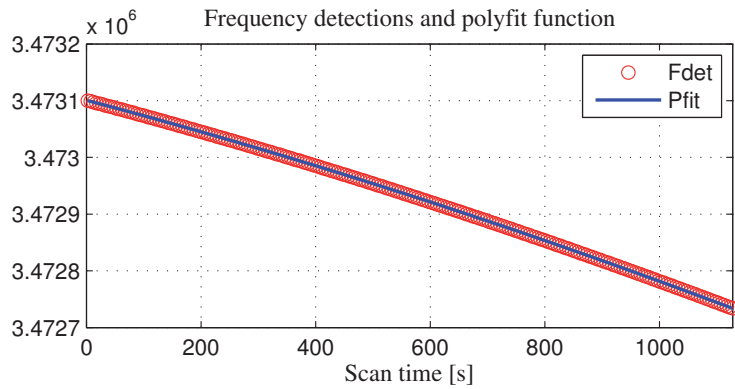
Figure 5.12. Topocentric frequency detection after the first iteration of SWspec. The total frequency variation is about $400\,\mathrm{Hz}$. 2nd scan of data observed on 2010.08.30 at On.

to the habitual range of values that we are working with. The residuals between the topocentric frequency detections and the phase polynomial fit is shown in Figure 5.13.

The goodness of the residual of the polynomial fit, the difference between topocentric frequency detections and the polynomial fit, is $36.6\,\mathrm{mHz}$ at $5\,\mathrm{Hz}$ resolution.

During a whole session, the Doppler frequency will vary approximately between 3 to $6\,\mathrm{kHz}$. The frequency detections for the 3-hour session is shown in Figure 5.14 (8 scans out of 9 were valid).

The Doppler shift for the session observed on 2010.08.30 was $5\,\mathrm{kHz}$. The session lasted three hours and we gathered 8 scans, instead of the usual 6. The relation frequency-time varies from the beginning of the session

107
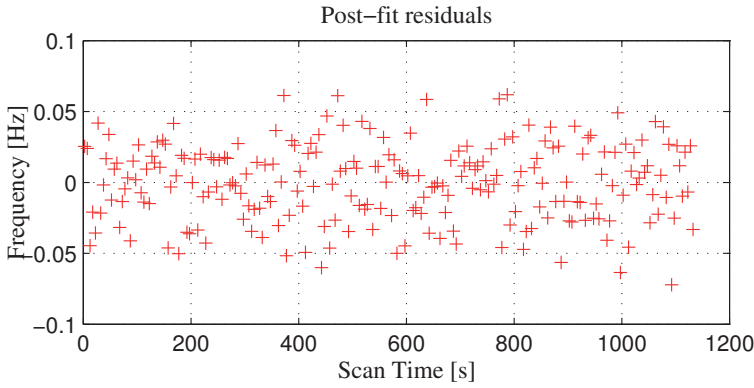
Figure 5.13. Frequency residuals between fit and frequency detections. The goodness of the fit is $36.6\,\text{mHz}$ at $5\,\text{Hz}$ resolution. 2nd scan of data observed on 2010.08.30 at On.
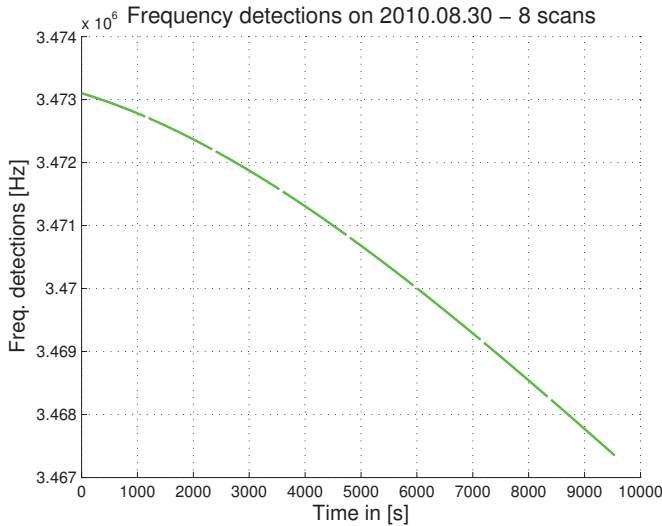
Figure 5.14. Frequency detections obtained from the 8 scans observed on 2010.08.30 at On. The Doppler shift ranges 0.5 to $1\,\text{kHz}$ for single scans and $6\,\text{kHz}$ for the full session.

towards the end. The orbit of the spacecraft and motion of the planet itself caused that. We always try to observe the spacecraft in the two-hour frame when the spacecraft is in the apogee respect the Earth.

The next step in the processing pipeline consists of running **SCtracker**. It uses the raw telescope data and the estimated phase polynomial coefficients. The SCtracker calculates the residual phase of the carrier tone, the complex signal in time-domain in narrow band of the tone and again the time-integrated spectra with the moving band stopped.

One way to analyse the quality of the phase stop is to zoom into the averaged time-integrated spectra. The zoomed spectra after SCtracker is shown in Figure 5.15.
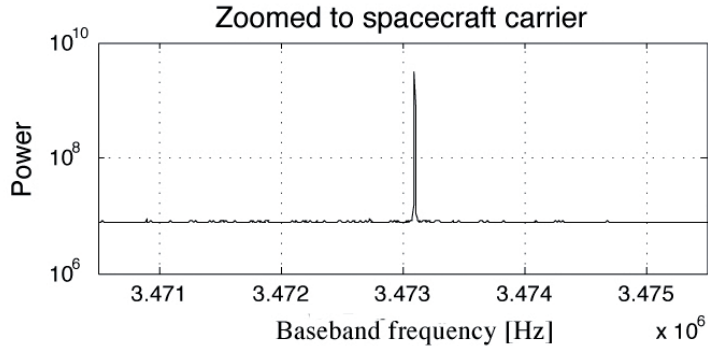
Figure 5.15. A zoom-in to time-integrated spectra looks like a single delta. The width of the tone is relative to the integration time. If the resultant tone spreads along 2 or more bins, the Doppler model is not good enough.

After SCtracker, the spectra shown in Figure 5.11 was converted to a single narrow peak. Before applying the phase correction, the spacecraft signal was split into several frequency bins, it looked like a pulse with a bandwidth of several hundreds of Hz. Next, the amplitude of the tone received was all accumulated into one single delta with a narrow band of only few Hz. The width of this tone was relative to the processing integration time and the amplitude of the signal received. If the tone was segmented along several bins, the Doppler compensation was not accurate enough and, therefore, the phase rotation failed to stop the spacecraft signal.

Another way to validate the quality of the phase stopping is to use the time-domain complex signal in the narrow band of the tone. The analysis of the tone in narrow band is more convenient than using the wide band data.

The tone files are several times smaller than the wide band spectra and the processing time is consequently much shorter. The filtered bandwidth of the tone is chosen in the initial settings of the SCtracker. By default the bandwidth is $2\,\mathrm{kHz}$ for VEX observations. To analyse the quality of the narrow band tone we use the third module of the software (PLL). The corresponding sampling rate is 4000 samples per second and we can use either 10.000 or 20.000 points. The new frequency resolution is 0.4 or $0.2\,\mathrm{Hz}$, respectively. The frequency resolution is $10\text{-}20$ times better than the last

iteration.

The detection of the tone in a $200\,\text{Hz}$ band, 4000 samples, 10 thousand FFT points and $0.4\,\text{Hz}$ resolution is shown in Figure 5.16.
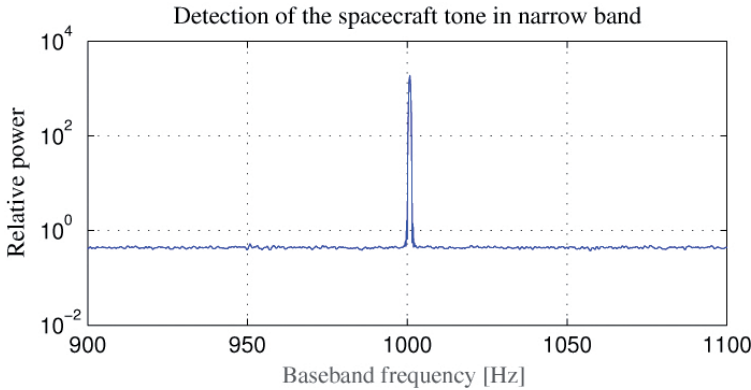
Figure 5.16. Detection of the spacecraft tone after analysing the time-domain complex data in narrow band. The filtered signal is sampled at a rate of $2\,\text{kHz}$ and 10000 points is used in the FFT (resolution of $0.4\,\text{Hz}$).

The figure assembles to the previous result with the wide band spectra seen in Figure 5.15. The SNR of the tone also improves after calculating the spectra at the new frequency resolution. The SNR of the tone detect on the 2nd scan is shown in Figure 5.17. The media of the SNR is 8000 at $0.4\,\text{Hz}$ resolution.
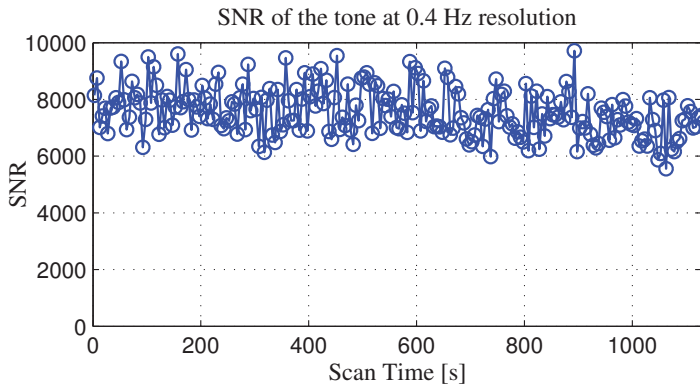
Figure 5.17. The level of the spacecraft tone SNR after analysing the narrow band output of SCtracker. The average ratio between the noise and spacecraft tone is 8000 at a frequency resolution of $0.4\,\text{Hz}$.

Taking a closer look to the new time-integrated spectra at $0.4\,\text{Hz}$ frequency resolution, the power spectra is distributed along an approximate bandwidth of $1.5\,\text{Hz}$ around the tone. This tone broadening of $1.5\,\text{Hz}$ is

equivalent to 5 to 7 bins of the spectra.

The next iteration on the PLL consists of correcting these detections by building a second phase polynomial fit. A 4th order phase polynomial fit is enough to correct the new Doppler variations. The topocentric frequency detections and the residual frequency are presented in Figure 5.18.
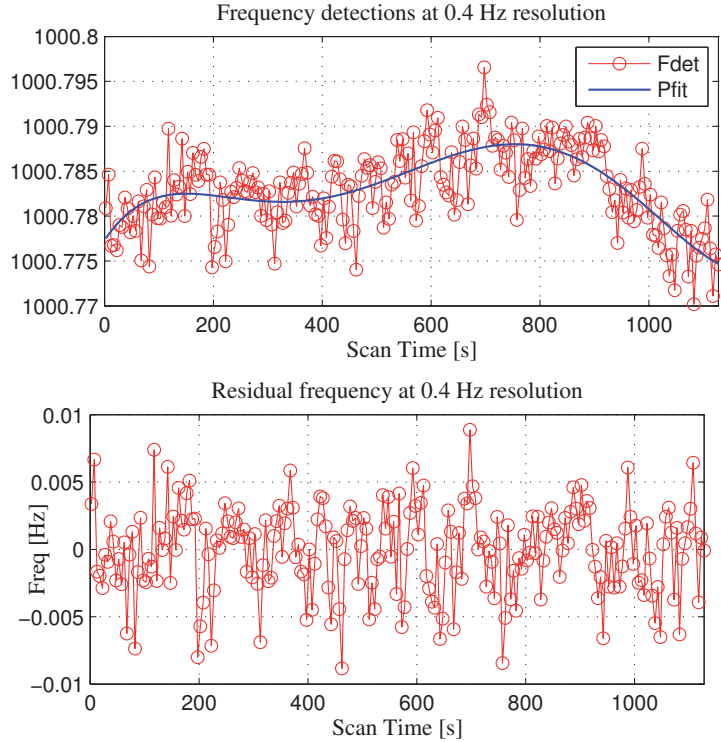
Figure 5.18. top: Topocentric frequency detections and phase polynomial model, using 2 kHz band and 0.4 Hz resolution. bottom: The residual frequency with a standard deviation of 4.1 mHz. Data observed on 2010.08.30 at On.

The frequency detections of the principal tone (in red) and the new phase polynomial fit (in blue) are shown in the upper panel. The scale in the y-axis is the relative frequency of the new filter around the tone. The scale of the x-axis is the scan duration in seconds. Residual frequency between the model and the detected frequency is shown in the lower panel.

As the analysis bandwidth has decreased in the order of 10 (from 5 to 0.4 Hz) the SNR has, therefore, increased by this factor. The accuracy of the frequency detection improves from 36 mHz (after SWspec) to 4.1 mHz (after SCtracker).

A comparison between the first and second set of polynomials is shown in Figure 5.19. The red crosses indicate the residual frequencies after the

first iteration. The blue crosses indicate the residual frequencies and the blue line the reconstructed model after the second iteration of polynomials. The case shown here was extracted from the session on 2011.10.17 at Wettzell radio telescope. In this case the standard deviation of the residuals were 16 and 3 mHz respectively. The resolution was approximately improved by a factor of five.
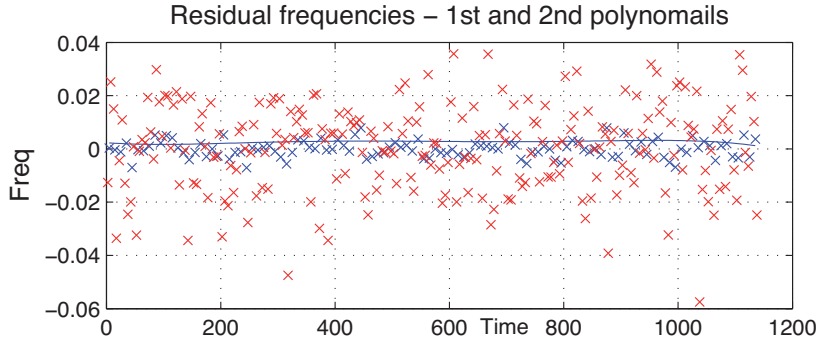
Figure 5.19. Residual frequencies after the first and second iteration of polynomials are indicted by red and blue crosses, respectively. The blue line represents the polynomial model after the second iteration.

The moving phase of the carrier tone is again extracted from the series of the time-integrated spectra using the new set of polynomial coefficients and the complex signal in time-domain. The phase stop also provides the tone filtered in a 20 Hz bandwidth. To calculate the spectra of the tone we use all the input samples to calculate the FFT, therefore the spectral resolution is relative time span of the scan ($df = 1/T_{span} =\sim 0.8$ mHz). The tone spectrum at 20 Hz bandwidth and 0.8 mHz resolution is shown in Figure 5.20

The power of the signal is dominant in a single frequency bin, but still split with the adjacent bins (each bin is 0.8 mHz wide). This is caused by an additional error introduced when applying the second phase correction. The signal can be cleaned by narrowing down again the frequency band. First, the frequency line of the tone is shifted towards the baseband. The tone is centred approximately at 10.5 Hz and the line is shifted to a frequency band of 5 Hz. The time domain pattern of the tone resembles to a sinusoidal wave with additional noise. The filtering gets rid of most of this noise. The Figure 5.21 shows the real and imaginary components of the tone after cleaning the noise.

The amplitude and phase of the signal can be extrapolated from the
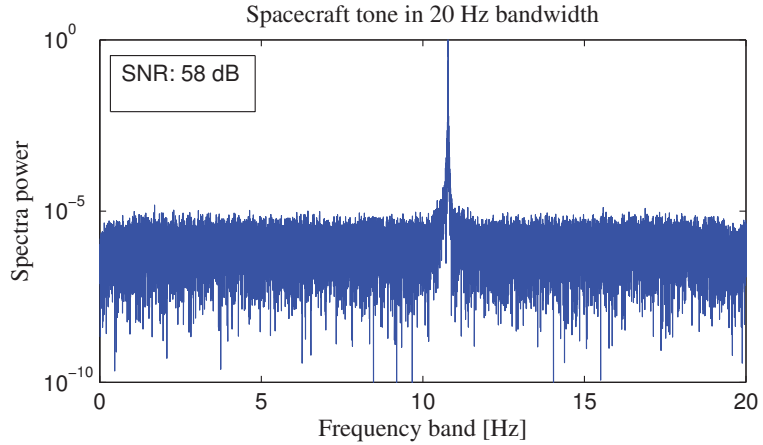
Figure 5.20. Narrow band spectra of the spacecraft tone detected on $2010.08.30$ at On after correcting the Doppler drift with the second set of polynomials. The resolution of the spectra is $0.8\,\text{mHz}$ and width bandwidth of $20\,\text{Hz}$.
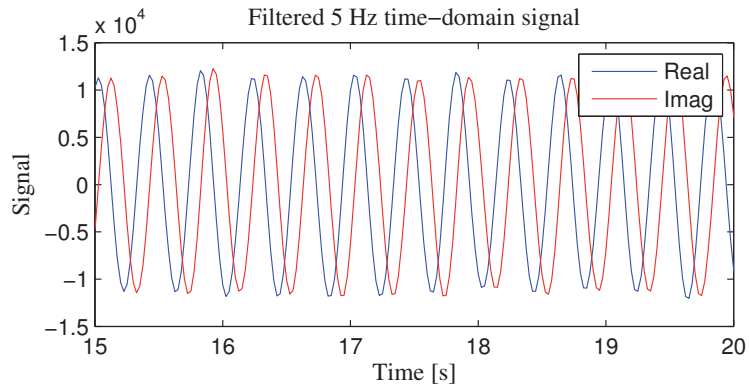
Figure 5.21. Real (in blue) and imaginary (in red) components of the spacecraft tone after down converting and filtering the signal at $5\,\text{Hz}$. The tone was observed on $2010.08.30$ at On.

time domain signal. The phase is wrapped over 2π cycles relative to the frequency of the target. The phase is de-wrapped and the frequency target for correcting the down-conversion of the signal is removed.

With the new values of the phase, a new fourth-order polynomial fit is calculated in order to clean the phase from noise-free errors. The difference between the measured phase and the polynomial fit leads to the residual phase. The extracted phase (in red) and the phase polynomial fit (in blue) of the second scan of session v100830 are shown in Figure 5.22.

The phase of the tone spectra is rotated with the third-order phase poly-
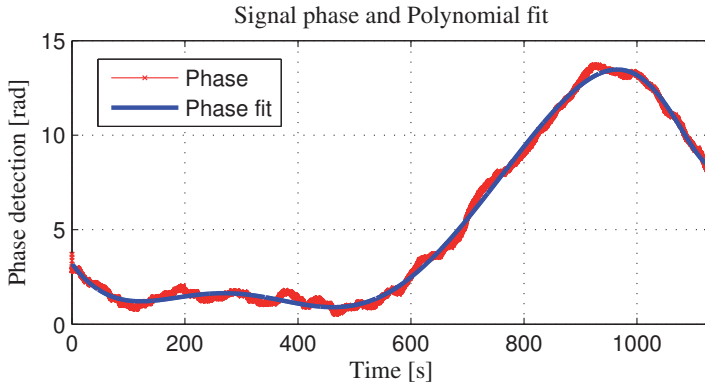
Figure 5.22. Extracted phase of the tone signal (in red) and the 4th order phase polynomial fit (in blue). The resolution is 0.8 mHz and a signal bandwidth of $5\,$Hz. The scan was observed on $2010.08.30$ at On.

nomial fit. Then the residual spectrum is concentrated into a single frequency bin as seen in Figure 5.23.
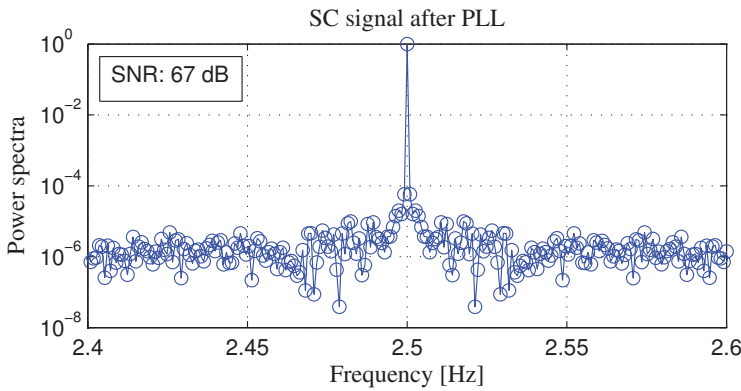
Figure 5.23. Closer look to the tone frequency bins after rotating its phase with the third phase polynomial fit. The new SNR observed on $2010.08.30$ at On is $67\,$dB.

The last step on the processing analysis consists on determining the residual phase from the difference between the phase polynomial model and the phase of the signal. The extracted residual phase of the second scan at $5\,$Hz bandwidth and resolution of $0.8\,$mHz is shown in Figure 5.24. The measured residual phase is dependent on the local H-maser clock of each station.

The quality of the signal phase detection basically depends on the stability of the USO of the spacecraft, the system noise temperature of the receiver (more specifically on the phase stability of its local oscillator), the atmospheric degradation and the interplanetary plasma scintillation.

Residual phase detected in 20 Hz band
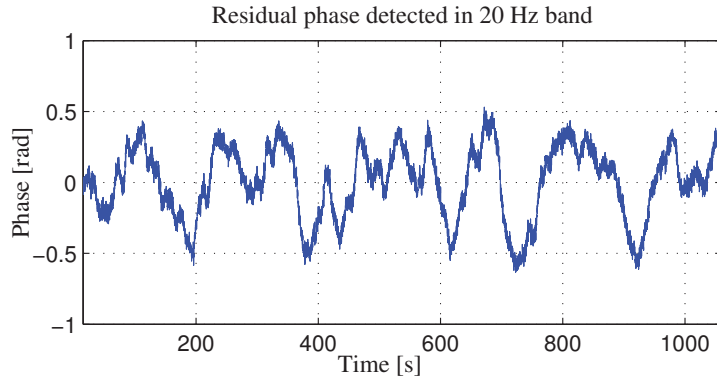
Figure 5.24. Residual phase extracted from the second scan observed on 2010.08.30 at On. The standard deviation of the residual phase is 0.26 radians.

Multi-station and multi-epoch observations enable discriminating the nature of these fluctuations on the residual phase. The implications of the solar wind in the residual phases in two different epochs observed with the same radio telescope are shown in Figure 5.25.
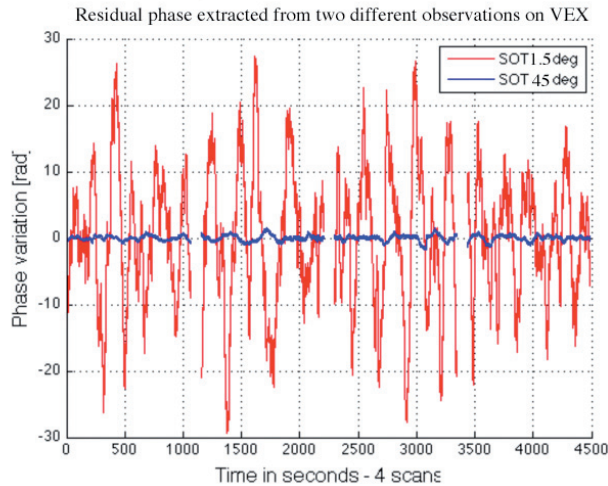
Figure 5.25. Phase fluctuations observed in two different experiments. In red, session conducted on 2010.01.16 with a SOT of $1.5°$ and , in blue, on 2010.08.23 with a SOT of $45°$. The phase fluctuations were 50 times higher in the first case.

The phase fluctuations were detected both at Metsähovi within 8 months of difference, on 2010.01.16 (in red) and on 2010.08.23 (in blue). The solar elongations were respectively $1.5°$, close to the major conjunction, and $45.5°$, close to the most western conjunction. The level of the phase fluctuations was 50 times larger for the earlier observation.

Spacecraft for station diagnostic tool

Spacecraft tracking offers useful opportunities as a powerful diagnostic tool beyond immediate applications for space and radio science. Indeed, evaluation of the spacecraft signal recorded at the telescope can be used to verify the general performance of a radio telescope. This section describes several errors discovered during our observations and the solutions to solve certain problems related to the VLBI station. It is also a guide to trouble-shoot typical errors that may occur in the observations.

One of the most common cause of errors during our sessions was due to bad pointing of the antenna. The wrong orientation of the antenna beam can either be caused by a problem with the pointing system of the antenna or by a wrong election of the schedule sky coordinates of the target.

For instance, the VEX spacecraft was observed for the first time with the radio telescope of Hartebeesthoek (South Africa) on 2011.03.25. Usually, the schedules for the sessions are created to be compatible with several antennas and therefore they use a generic reference station to determine the coordinates of the target in the sky. The reference antenna used is geographically located in the central Europe (Germany). This interpolation method was practical for all observations performed with the EVN telescopes so far. Unfortunately, this common reference station set-up cannot be applied for the antenna of Hartebeesthoek or others at similar locations. The distance between Hartebeesthoek station and the reference is too great to assume similar sky coordinates and, hence, the coordinates were slightly wrong and the pointing was not accurate for the 25-metre antenna. The SNR and frequency detections plots are shown in Figure 5.26.

When the data were analysed, the SNR detection showed a saw-tooth pattern. The SNR in normal conditions tends to keep constant during the entire scan. For this session the beginning of the scan had much lower detection of the spacecraft signal than at the end of. Furthermore, another peculiarity was found with the Doppler analysis. The usual trend is that the frequency drifts several kHz during the whole session. However, as seen in the last three scans, the Doppler only varies in order of magnitude of hundreds of Hz. As this session was conducted in parallel with other radio telescopes (Onsala, Pushchino and Metsähovi), it was easy to spot the different pattern for the SNR and the frequency detections for all the stations. The reason for this different Doppler behaviour was due to a broken LO at their S/X receiver.
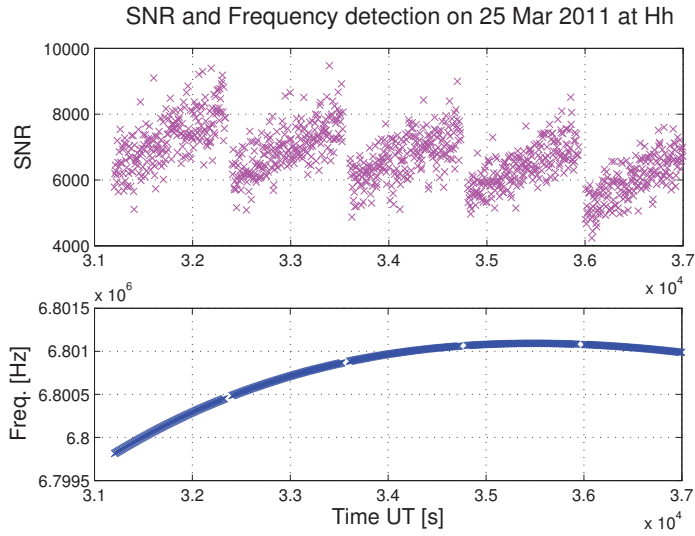
Figure 5.26. Wrong pointing of the antenna caused this saw-tooth pattern in the detected SNR. Doppler frequency drifts few hundred Hz during the full session due to a broken LO. Session observed on 2011.03.25 at Hh.

As mentioned, another source of error can be caused by the station itself as demonstrated in Figure 5.27. This session was observed at Metsähovi on 2011.05.04.

The origin of the problem can be related to wrong coordinates, problems with the antenna rotation gearings, bad-pointing model or wrong calibration procedures. On 2011.05.24 we loaded a calibration procedure before the session. The pointing model was not reset and the antenna used the new offset compensation based on the previous session. When the model is estimated in bad weather conditions the new pointing may be totally inaccurate. Hence, the antenna could barely track the spacecraft signal on that epoch. The SNR pattern was similar than the one showed in Figure 5.26, but the detection of the signal was so weak, the SNR was around 50 units, that it was extremely difficult to determine the correct tone from the spectra.

Another example of the importance of these observations in order to detect and track errors at the stations was seen with the Wettzell telescope on 2011.03.21. The residual phase revealed a strange modulation along the extracted phase. At first glance, we did not know what was the origin of this modulation. Whether it was related to the signal transmitted by the spacecraft itself or it was originated at the receiving station. The
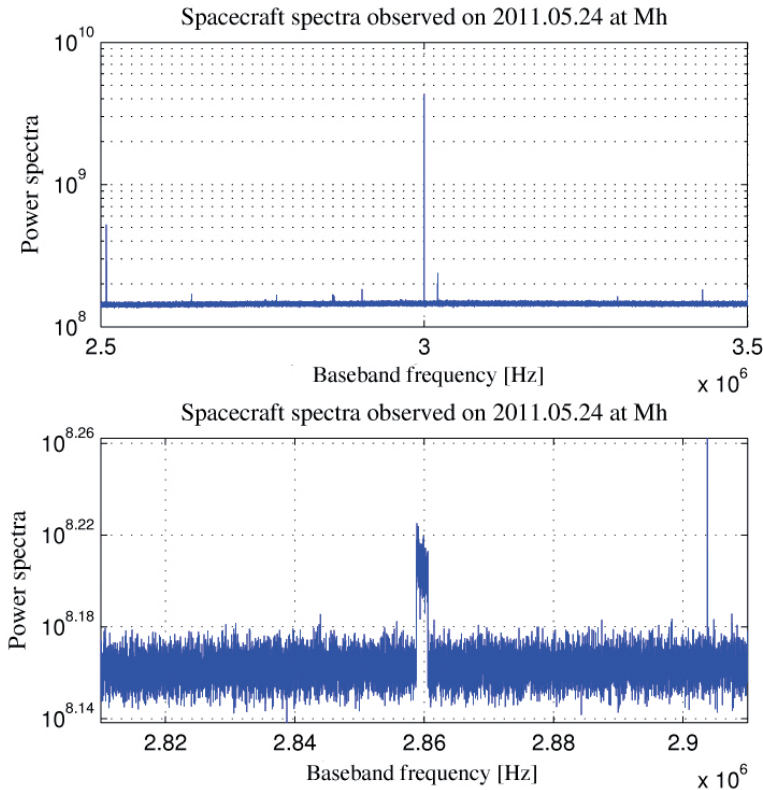
Figure 5.27. top: $8\,\mathrm{MHz}$ wideband spectra zoomed to $1\,\mathrm{MHz}$ band span. The spacecraft is centred at $2.8\,\mathrm{MHz}$ and is barely visible. bottom: Zoom to $10\,\mathrm{kHz}$ band with the weak S/C signal. The SNR observed on $2011.05.24$ at Mh was 50.

phase modulation, seen in Figure 5.28, had amplitude of 0.25 radians and a cycle frequency of $1\,\mathrm{Hz}$.

We could proceed in two different ways in order to verify the integrity of the spacecraft signal. The first method is to evaluate any of the PCal tones and demonstrate whether the tones are also affected by the same phase modulation. In that case, the origin of this modulation would be caused by an inside component of the receiver. The second method consists of conducting a multi-station observation, recording the same spacecraft signal with two different antennas and determining if the modulation is shown in the results of both stations or not. We performed both methods of analysis and concluded that the problem was caused inside the receiver, since PCal tones were also affected by the same modulation. The operators of the Wettzell radio telescope replaced the LO of the S/X receiver and the problem was solved for the later experiments.
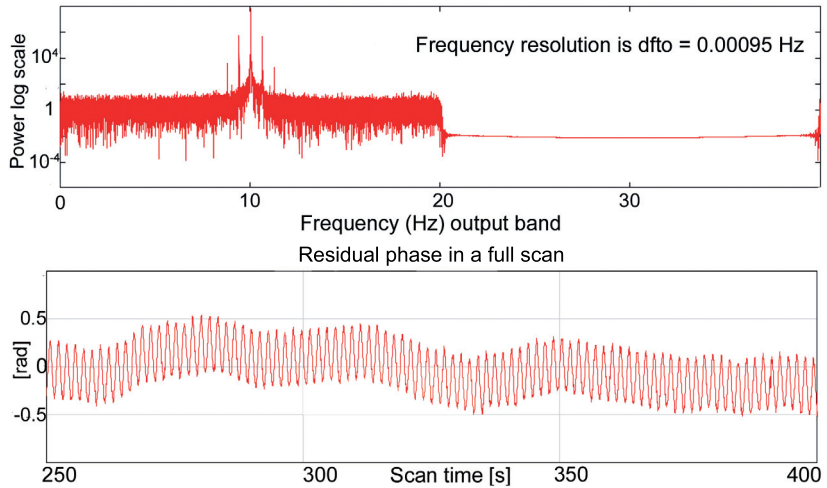
Figure 5.28. top: Narrow band signal (4 kHz) with the carrier tone at the middle of band, with several peaks around it. bottom: Extracted residual phase characterised by the phase modulation. The modulation had amplitude of 0.25 radians and a cycle of 1 Hz.

Other attempts to detect spacecraft

The 12-metre Warkworth VLBI antenna of the Auckland University of Technology, New Zealand, observed the JAXA's spacecraft Ikaros and Akatsuki on 2010.07.16 at X-band. Observational data were acquired with PC-EVN unit in 32 MHz band centred at a frequency of 8421.111 MHz. Observational data were electronically transferred to Metsähovi and processed using the software spectrometer. The transmitted signal from the JAXA spacecraft's Ikaros and Akatsuki has the pattern showed in Figure 5.29.
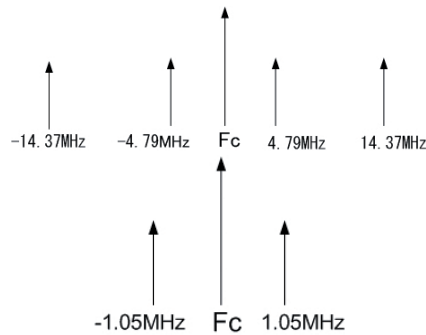
Figure 5.29. Carrier and sub-harmonic tones relative frequencies emitted by the Akatsuki and Ikaros spacecraft.

At the beginning, the data did not show any detection at the supposed arrival frequency. However, the scientists at New Zealand pointed out

a feature, similar than 3 peaks using a local spectrometer, at a sky frequency of 8.410079 GHz, which corresponds to a Doppler shift of $+4.6$ km/s with respect of the rest frequency of Akatsuki.

We took a deeper look into the data and found this feature in the spectral data. The satellite lines were separated by ± 16.4 and 16.5 kHz. It was also found that the major line experienced a Doppler acceleration of -0.37 Hz s^{-1} over 500 seconds time span. The possible detection of Akatsuki after post-lock detection of the carrier line is shown in Figure 5.30.
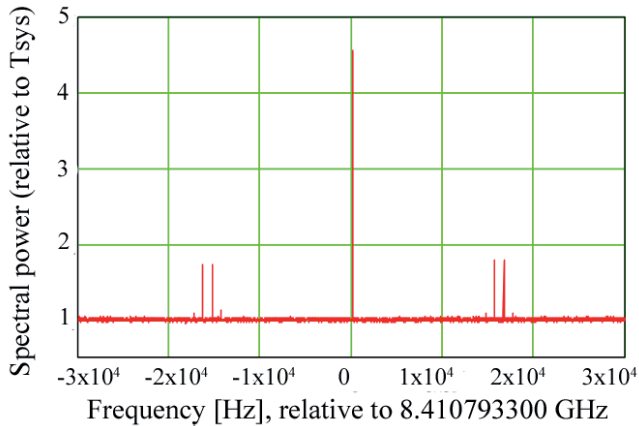
Figure 5.30. Post-lock detection, with acceleration of -0.37 Hz removed using also resolution of 10 Hz.

We also have attempted to detected other planetary spacecraft without too much success. One of the first attempts by the group aimed for the Ulysses spacecraft before its shut down. The team conducted few observations of the spacecraft with the Metsähovi telescope in the summer 2008. More recently, in 2011, we used the Effelsberg antenna to observe the beacon installed on the Mars Explorer Rover. In both cases, the data were processed at Metsähovi with the spacecraft tracking software. Unfortunately, neither of the cases reported successful detection of the spacecraft signals.

Detection of the sub-harmonic tones

Analysis of the 7th sub-harmonic tone relative to the VEX carrier line have been performed as a preliminary study of VLBI radio telescopes capabilities to detect the Phobos-Soil spacecraft. As mentioned in the Phobos-Soil mission general description, the spacecraft will be equipped with a low-power transmitter comparable to some sub-harmonics present in the

VEX tones. The 7th sub-carrier harmonic of VEX spacecraft has a power level of -30 dB with respect to the carrier and is separated by 7 MHz from the carrier. To simulate the Phobos-Soil detection we used the 14-m Metsähovi telescope, with rather high $T_{sys} \sim 100$ K at X-band. Signal of this -195 dBW per dish sub-carrier harmonic was successfully detected at 3 s integration and 0.15 Hz tracking bandwidth.

Stochastic phase noise of the detection was 0.4 radians in 3 seconds, and the Doppler noise had a level of 11 mHz in 3 seconds for a -35 dB tone and 3 mHz for the carrier. On global baselines, the 0.4 radian detection phase noise will correspond to positioning accuracy of ~ 40 meters at a distance of 1 AU, and Doppler noise will correspond to the 0.5 mm/s radial velocity error at a sampling time of 3 seconds. Results of this test are presented in Figure 5.31, the detection accuracy is mostly dominated by scintillations due to the interplanetary plasma and not by the system noise of the telescope at given power levels and observing conditions.
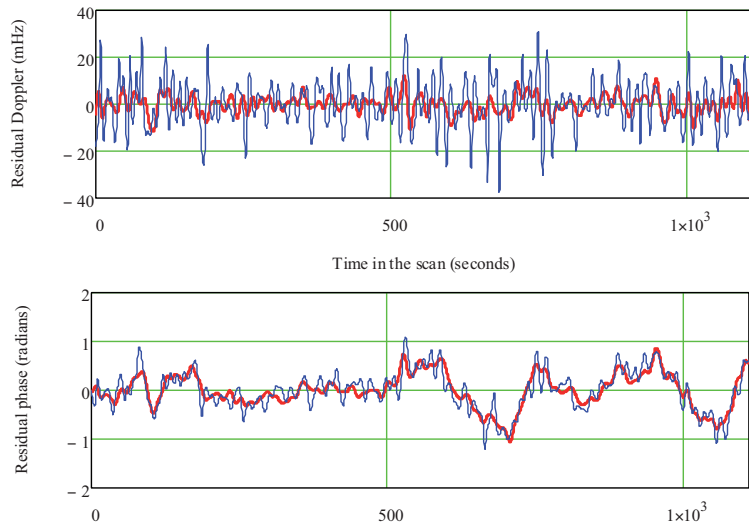
Figure 5.31. Residual phase and Doppler noise for the -165 dBW carrier line (red trace) and -195 dBW sub-carrier harmonic (blue trace) signals, as detect at Mh on 2011.03.25. We used a -30 dB sub-carrier harmonic from VEX as a test signal. The test mimics the expectation of the Phobos-Soil beacon.

The PRIDE team was supposed to face the challenge of detecting and estimating the state vectors of the Phobos-Soil probe and the robotic craft using the EVN radio telescopes in summer 2012. Detections of sub-carrier harmonics relative to the VEX carrier signal have demonstrated that our software could cope with the low constraints imposed by the Phobos-Soil X-band transmission channel. The detection of the signal was ensured

even with the smaller EVN radio telescope dishes, such as the Metsähovi radio telescope. Unfortunately, the planetary mission failed during its launch stage.

5.4.2 Spacecraft signal detection with multi-stations

Several sessions were performed using two or more EVN radio telescopes observing simultaneously the signal transmitted by the spacecraft. The configuration was similar to single-dish sessions and the scans were 19-minute long. In several occasions, a reference source was incorporated to the observations in order to have an absolute phase-reference and clock offset values between each station. Usually, the quasars were observed at the beginning and the end of the session.

Simultaneous multi-station observations using two or more radio telescopes allow us to compare the Doppler frequency and phase detections at each station. Thus, the carrier tone, the subsequent harmonics and its residual phase can be determined via different Fresnel channels. The Fresnel zone is defined as an area where any object can affect the strength and phase of the received signal, although they might not directly obscure the direct visual path. The first Fresnel zone is usually the spheroid space formed within the trajectory of the path. The maximum width of the Fresnel zone can be calculated as [119]:

$$r_f = 8.657 \cdot \sqrt{\frac{L}{f}} \qquad (5.13)$$

where r_f is the radius of the Fresnel zone in metres, L is the distance in kilometres between the radio telescope and the spacecraft and f the frequency of the transmission band in Hz.

Observing the spacecraft signal via different channels allows us to discriminate the independents errors caused by the interplanetary plasma, the troposphere and the atmosphere of the Earth. When the ground stations are widely separated it is possible to analyse the contribution of planetary plasma because the different Fresnel channels barely overlap. Fresnel channels observed for two different antennas with a baseline of $2000 \, \text{km}$ and at a distance of 10^{08} km at $0.66 \, \text{AU}$ are shown in Figure 5.32.

For instance, if we use a global baseline of $6000 \, \text{km}$ (antennas in Europe and America/China) at a distance of $1 \, \text{AU}$, like Venus or Mars, the Fresnel channels are well separated. Therefore, the phase fluctuations of the
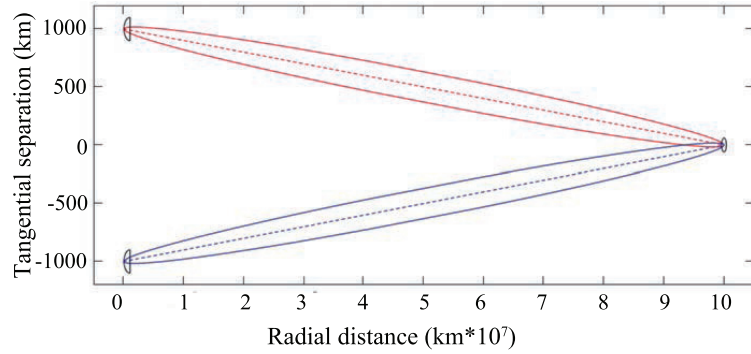
Figure 5.32. Signal propagation via two different Fresnel channels using two radio tele-
scopes spaced within $2000\,\mathrm{km}$ and at a distance $0.66\,\mathrm{AU}$. That mimics the
configuration of possible detection of any spacecraft at Mars or Venus.

signal detected by the Earth-based radio telescopes will be uncorrelated.
Fresnel channels partly overlap in distances closer to Mars; the overlap-
ping may exist along the first $30\,\mathrm{km}$. These small overlaps allow discrimi-
nating between interplanetary scintillations and scintillations near-Mars
or Venus atmosphere/plasma. That yields complementary in-situ mea-
surements of plasma environment of the planets.

The phases detected on a multi-station session observed on $2011.03.25$
with the telescopes of Metsähovi and Onsala and the phase difference are
shown in Figure 5.33. The standard deviation of the residual phase is at
the level of 187 milliradians.

Another example of multi-station session is shown in Figure 5.34. It was
observed on $2009.12.21$ with the radio telescopes of Wettzell and Yebes.
The session lasted two hours and consisted of six scans of 19-minute. We
did not include any quasar as a reference source to calibrate the phases of
both stations.

The phases from both stations are highly correlated. An arbitrary de-
lay to align both phases was added to plot the phases and improve read-
ability. The standard deviation of the residual phase is at the level of
210 milliradians. This observations was conducted at low solar elongation
and, that's, explains the high level of phase fluctuations.

5.4.3   VLBI tracking of spacecraft

Several VLBI and Doppler tracking observations of ESA Venus Express
and Mars Express spacecraft were conducted with EVN radio telescopes
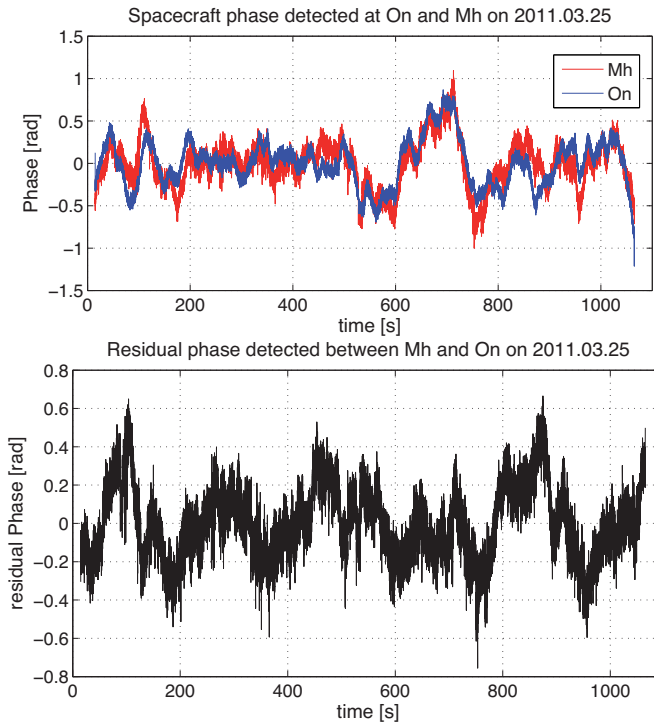
Figure 5.33. top: Comparison of the phases of the first scan detected with the On and Mh on 2011.03.25. bottom: Phase difference between On and Mh. The standard deviation of the residual is at the level of 0.188 rad.

in the period of 2009-11. The main objective was to test and improve the scheduling, data processing, pipeline analysis and to estimate an achievable accuracy of spacecraft tracking with different configurations of radio telescopes arrays. The VLBI experiments conducted are:

- **v091126**: four radio telescopes: Wettzell - Matera - Noto - Medicina on 2009.11.26.

- **m100303**: (MEX) three radio telescopes: Yebes - Wettzell - Metsähovi on 2010.03.03.

- **em081a**: five radio telescopes: Metsähovi - Medicina - Yebes - Onsala - Pushchino on 2010.08.23

- **em081b**: with four radio telescopes: Metsähovi - Medicina - Onsala - Pushchino on 2010.09.20.

- **em081c**: with ten radio telescopes: Metsähovi - Medicina - Noto - Matera - Wettzell - Yebes - Pushchino - Onsala - Hartebeesthoek - Badary - Zelenchukskaya - Saint Croix on 2011.03.28.
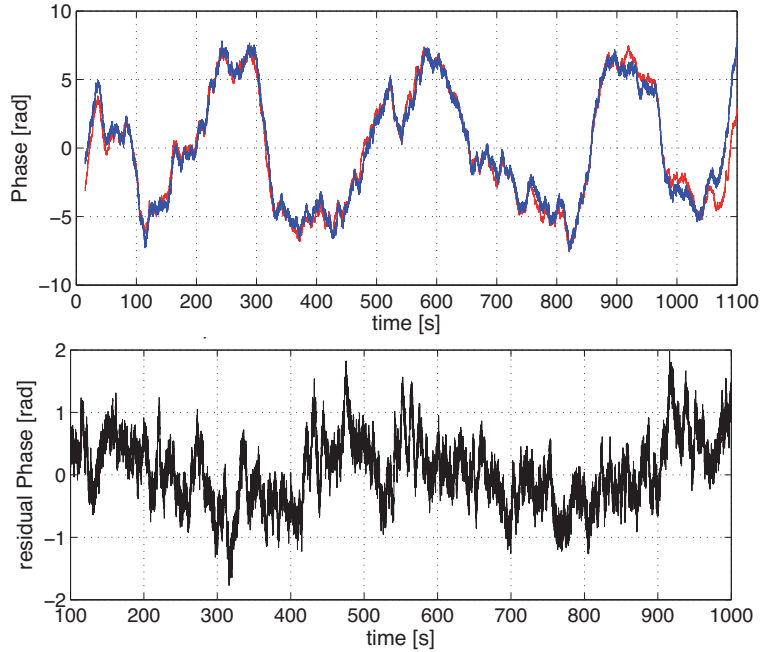
Figure 5.34. top: Phase detected with the radio telescopes of Wettzell (in red) and On-sala (in blue) on 2009.12.21. bottom: Residual phase for the first scan. The standard deviation of the residual is at the level of 210 millirad.

v091126 session

The v091126 experiment was conducted at X-band (8.4 GHz, λ3.5 cm) on 2009.11.26 using 4 radio telescopes: 20-m Wettzell (Germany), 32-m Medicina, 32-m Noto and 20-m Matera (Italy). At the time of observations, from 09:00 until 12:00 UTC, Venus had mean coordinates (RA/Dec J2000) of 15h23m13s $-17°36'45"$ and was at a solar elongation of 11 degrees and distance from Earth of 1.6 AU. Venus was approaching to the solar eclipse. The radio source J1507-1652 was used as a calibrator. The radio source has coordinates 15h07m04.7s $-16°52'30.3"$, a flux of ~ 1.0 Jy at X-band and an angular distance from target (Venus) of 3.9 degrees.

For the session we used 25 minutes nodding cycle, based on 19 minutes on VEX and four minutes on the calibrator. A one-minute gap was reserved for telescope re-pointing and checking the system temperature of the receiver. We gathered six scans with VEX data and seven shorter scans with the calibrator information. We used 4 wide channels, bandwidth of 16 MHz, 2-bit Nyquist sampling, for an aggregate data rate of 256 Mbps per station. Disks were shipped to JIVE using regular postal service and data were electronically transferred to Metsähovi. Data pro-

cessing was conducted in parallel at JIVE and Metsähovi. The baselines in the uv-coverage plain, with a maximum baseline of $670\,$km in the East-West direction (u) and $750\,$km in the North-South direction (v) are shown in Figure 5.35.
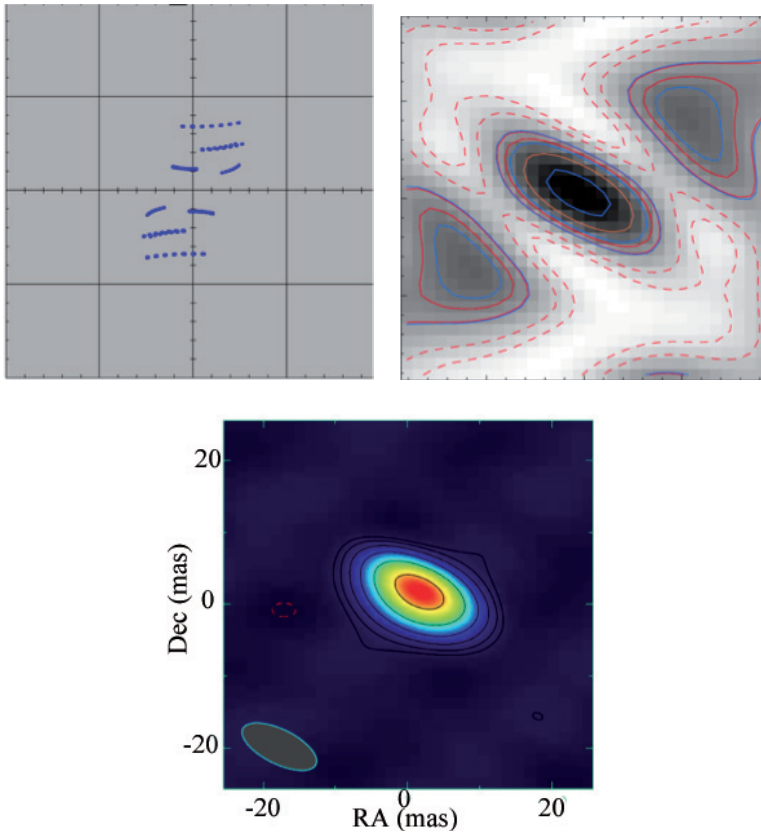
Figure 5.35. top-left: Baselines uv-coverage (in km), with the maximum baseline of 670 km in E-W direction (u) and 750 km in N-S direction (v). top-right: Synthesized beam with principal axis of 11.3 and $4.8\,$mas and position angle of $63°$. bottom: Reconstructed image of the calibrator source J1507-1652.

The upper-right panel shows the synthesized beam of the calibrator, their principal axis were 11.3 and 4.8 mas, respectively, and inclination of 63 degrees. The reconstructed image of the calibrator J1507-1652 using the correlator results and the Astronomical Image Processing System (AIPS) software [120] is shown in the lower panel.

The **residual delays** are obtained after fringe fitting of the calibrator data for all the baselines. The residual delays for J1507-1652 on v091126 are shown in Figure 5.36. Wettzell was used as a reference antenna for the analysis. The RMS post-linear fit for the baselines Wettzell-Matera, Wettzell-Medicina and Wettzell-Noto were 0.26 ns, 0.70 ns and 0.52 ns

respectively. Unfortunately, the RMS was larger than the X-band wave period (0.120 ns) and we could not use the calibrator results for phase-referencing. Low detection of the source, high system temperature of the receiver, adverse atmospheric conditions, short baselines or lack of a big dish as a main reference could be reasons for the poor quality of the observation.
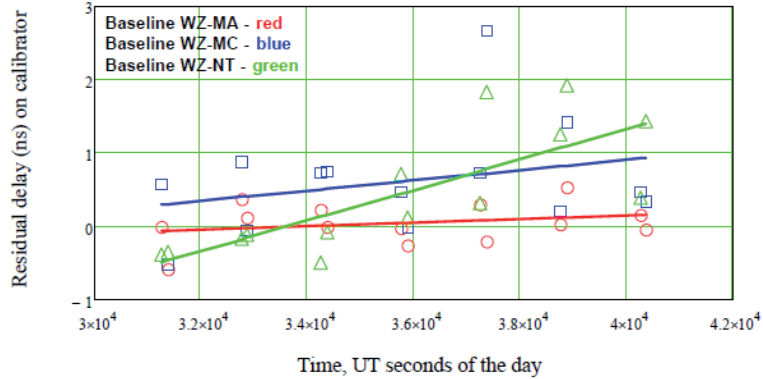
Figure 5.36. Residuals delays obtained from the calibrator source, J1507-1652, per each of the baseline. Values were significantly larger than X-band wave period.

The spacecraft detection of the carrier line frequency and phase were robust for all four radio telescopes. Indeed, the SNR of the tone was measured at the level of 10^{04} at $1\,\mathrm{Hz}$ resolution with Wettzell radio telescope. The detections with other antennas yielded lower SNR values. The typical residual phase and frequency of the carrier line in a $0.2\,\mathrm{Hz}$ $2.5\,\mathrm{s}$ sampling tracking band after the adaptive PLL are illustrated in Figure 5.37. The residuals show a phase noise RMS of 0.46 radians and frequency noise of $-6.4\,\mathrm{mHz}$ at $2.5\,\mathrm{s}$ sampling. We consider the interplanetary plasma scintillations to be the major contributor to the phase/frequency noise of the carrier line detections.

The topocentric detections of the phase and frequency of the spacecraft signal were reduced to the common phase centre (geocentre) for each station. For the reduction we used the predicted VLBI delays from station to geocentre, computed with the near-field model, which is fully compatible with the Consensus Model for far field VLBI computation, as explained in Section 5.2.7. We used the spacecraft state vectors provided by ESA to compute the VLBI delays on VEX in this session.

Because we could not apply a real phase-referencing to the spacecraft carrier differential phases on the baselines, we used the first order best
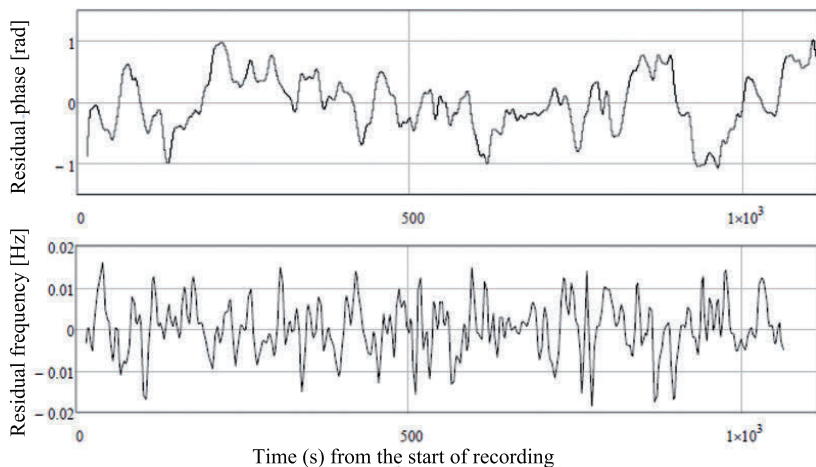
Figure 5.37. top: Residual phase [rad] and bottom: frequency [Hz] of the spacecraft carrier detection on 2009.11.26 at Wz. The other three radio telescopes yielded similar residual phase and frequency results.

fit to the a priori state vectors. The detected baseline phases, corrected for the system clock/clock offset rates using the calibration data and linear fit to a priori orbit are shown in Figure 5.38.
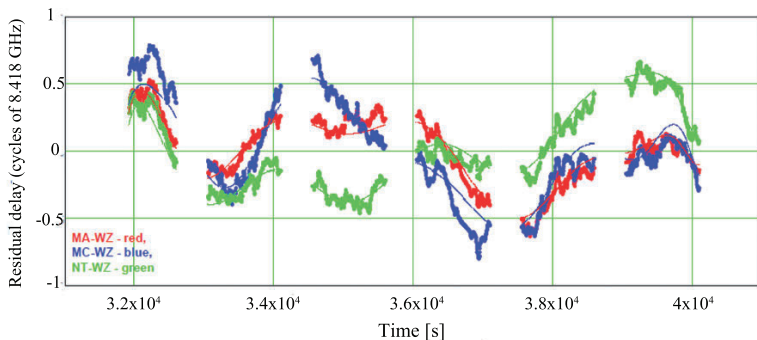
Figure 5.38. The residual delay for thee baselines (Ma-Wz in red, Mc-Wz in blue and Nt-Wz in green), after all the proper corrections are applied.

Further into the analysis pipeline, we varied the predicted delays by the spacecraft position offset along the lateral coordinates in geocentric frame. The results of the solution of the variance equation are shown in Figure 5.39.

Note, that the scatter plot (dRA/dDec) resembles the system beam in size and shape. As it is seen, the measured coordinates show a covariance due to not that good baseline coverage. First approximation to remove this covariance is to rotate coordinate frame to align its axis of the ellipse
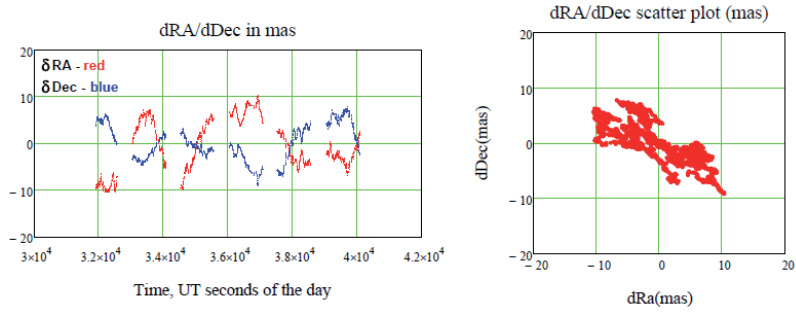
Figure 5.39. The observed lateral deviations dRA/dDec (mas) of the spacecraft position, projected to the plane of sky.

of the synthesised beam. The new aligned frame is known as the A/B frame. This new frame is defined according the preferences of the investigator. The new prime axis of the synthesized system beam are shown in Figure 5.40.
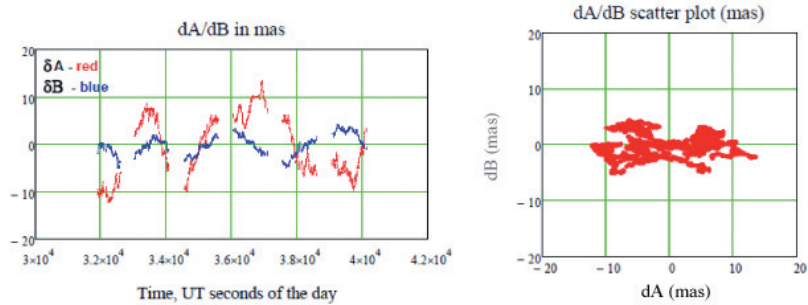
Figure 5.40. Observed lateral deviations dA/dB (mas) of the spacecraft position, projected to the plane of sky. The RMS of deviations is 6.4 mas and 2.0 mas for A and B axis correspondingly.

We note that the characteristic time of deviations is about 20-30 minutes, corresponding to the referencing nodding cycle of our observations. Shortening the nodding cycle can help to remove the long time trends caused by propagation effects and station clock instability. We also note that such accuracy can be achieved with a moderate VLBI array, corresponding to Central European part of EVN. Further improvement of spatial accuracy are possible by using larger VLBI arrays. Additional collecting area and increased number of the redundant baselines will also improve the calibration capability, thus providing a factor of 20 of improvement to what was demonstrated with four central European antennas, yielding $\sim$ 10-metre spacecraft coordinates measurement at a distance of ~ 2 AU.

m100303 - Phobos flyby by Mars Express

The m100303 experiment was observed at X and S-band (8.4 and 2.1 GHz, λ of 3.5 and 13.1 cm) on 2010.03.03 using three radio telescopes: Wettzell, Yebes and Metsähovi. The three radio telescopes successfully observed the Mars Express flyby to the Phobos Martian moon. The spacecraft signal was only detected in one of the two bands. At the time of the observations, from $18{:}00$ until $21{:}00$ UTC, Mars had mean coordinates of 08h15m05.5s - 23°51'23.4" and a solar elongation of 137 degrees and distance from Earth of 0.78 AU. We used the radio sources J0813+2435 and J0813+2542 with coordinates 08h13m47s - 24°35'05" and 08h13m03s - 25°42'11", respectively, as calibrators. The session was divided into 3 long scans of Mars Express 20, 49 and 20 minutes each. The calibrator scans were interleaved with the spacecraft data with a length of 5 and 10 minutes. The exact moment of the flyby occurred in the middle of the 49-minute scan.

The scans were too large to apply a coherent phase-referencing using the calibrator sources. Therefore, this step was skipped and the results were analysed in similar way as proceed with the v091126 session. The essential parameters for the network coverage (uv-plane) and system beam are shown in Figure 5.41. The longest baseline was Yebes-Metsähovi with a distance about 3000 km. The configuration provided a synthesized system beam width about 1.7 mas and major axes of 5.5 mas.
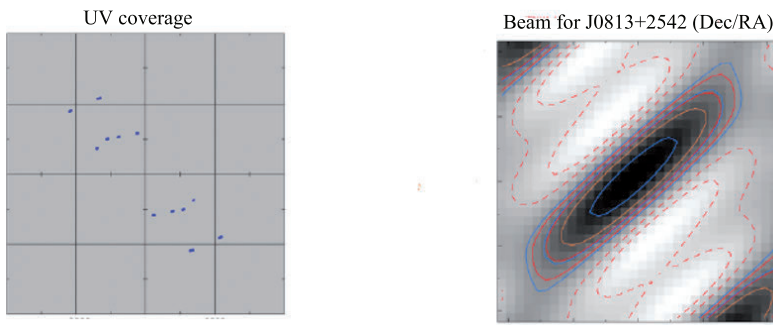
Figure 5.41. left: Baselines uv-coverage (in km), with the maximum baseline of 2000 km in E-W direction (u) and 3000 km in N-S direction (v). right: Synthesized system beam with principal axis of 1.7 and 5.5 mas and position angle of 45 degrees.

The spacecraft detection of the carrier line frequency and phase were robust for Metsähovi and Wettzell radio telescopes. Yebes antenna was the exception and had problems with the polarization feed of the S/X receiver.

The SNR of the tone signal was lower than expected. The level of the SNR were respectively $20 \cdot 10^{03}$, 600 and 800 for Wettzell, Yebes, and Metsähovi at a resolution of $0.4\,$Hz. The spectral power of the spacecraft tone relative and the residual frequency of the second scan observed at Wettzell is shown in Figure 5.42.
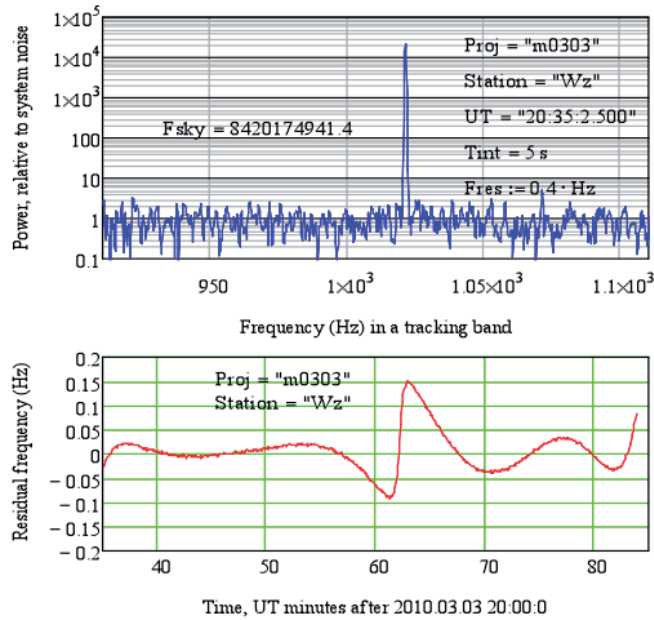
Figure 5.42. Detection of the spacecraft tone of MEX during the Phobos flyby on 2010.03.03. top: Spectral power detection with a SNR of $20 \cdot 10^{03}$. bottom: Residual frequency along the 49-minute of the second scan.

The residual phase extracted from the scan number 2 of Metsähovi and Wettzell and the pre-zoomed spacecraft phase noise are shown in Figure 5.43. The residual phase proofs a high-correlation between the data extracted from both stations.

The $90°$ bump in the middle of the scan is the closest point that Mars Express orbited in respect to the surface of Phobos. It corresponds to the change of the orbital position of the spacecraft (along the line of sight) due to the gravity field of Phobos. The phase noise of the Metsähovi data (in blue) is dominated by the system noise. The receiver T_{sys} was $80\,$K at the time of the observations. On the other hand, the phase noise of the Wettzell data (in red) is dominated by the scintillations on the interplanetary plasma. The receiver T_{sys} was $40\,$K. Combined system and scintillation noise in a $5\,$Hz tracking band is at the level of 0.10 radians for Metsähovi and 0.07 radians for Wettzell.
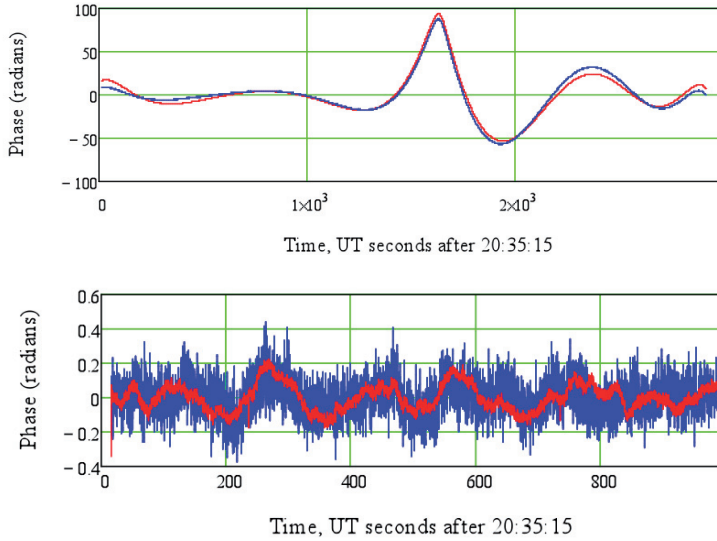
Figure 5.43. top: Phase detected at Mh and Wz. The $90°$ bump is caused by the gravity field of Phobos. bottom: Zoom into pre-event part of the scan to determine the phase noise. The phase noise of Mh (in blue) is dominated by the system noise ($T_{sys} = 80\,K$), and of Wz (in red), is dominated by the IPS ($T_{sys} = 40\,K$).

The observed frequency of the link MEX and Metsähovi according to the Doppler predictions with Phobos gravity OFF (in red) and with Phobos gravity ON (in blue) are shown in Figure 5.44. The data were processed using models including and excluding the Phobos gravity from our data set. Both *a priori* models were provided from ESA's range rate data. The lower panel shows the similar detections, which were shown in Figure 5.43, after removing the 3rd order polynomial from both data sets, using the Phobos gravity model.

We analysed the single 49-minute long scan centred at the flyby event time. No phase-referencing was performed during this analysis. However, results can be analysed in the same way as done for the v091126 experiment. Doppler detection stochastic noise at this experiment was at a level of 2-6 mHz at 2.5 second sampling rate. Phase detections were much more accurate than in the case of v091126, due to the apparent solar elongation of 137 degrees and proximity to Mars.

A first estimation of the MEX spacecraft position used the first priori orbit model from ESA database and rotation of the principal axis according to the synthesized beam. The estimation of the spacecraft position is shown in Figure 5.45. We could use only two of the antenna for estimating
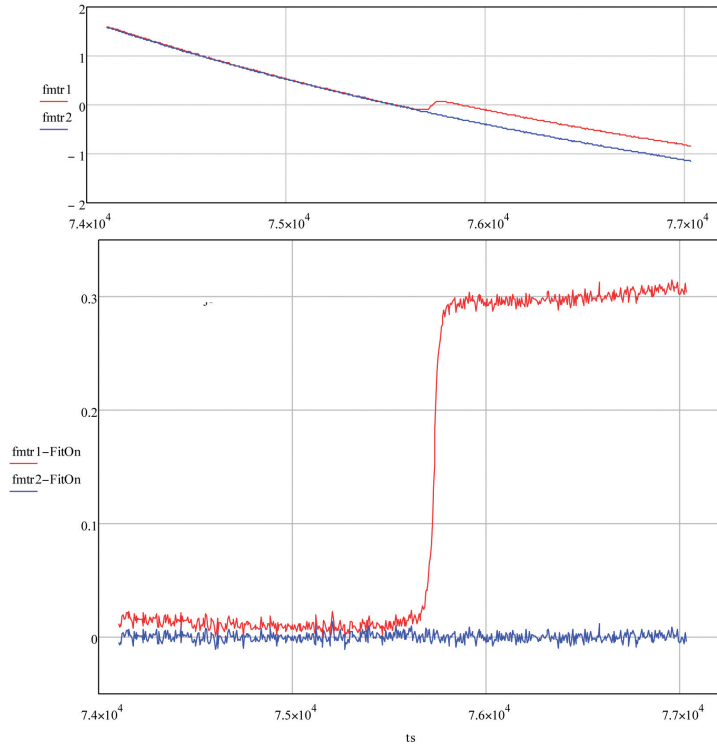
Figure 5.44. a) Frequency detection of the signal respect to Doppler predictions with Phobos gravity OFF (in red) and with Phobos gravity ON (in blue). b) Similar detections after a 3rd order polynomial fit for the blue line (Phobos gravity ON) was removed from both data sets.

the coordinates within the RA/Dec plane RMS of 2.7 mas and 0.5 along the major and minor axis of the system beam. At the apparent distance of 1.2 AU of Mars to Earth the RA/Dec plane corresponds to 2.4 km and 450 m.
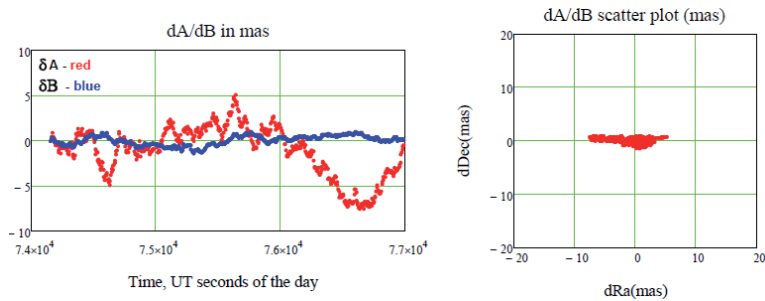
Figure 5.45. MEX position in the RA/Dec plane. The first priori orbit model was used and the axis were rotated according to the synthesized beam. The RMS' were at a level of 2.7 and 0.5 mas at a distance of 1.2 AU (2.4 km and 450 m).

With the current results, we simulated the effect on the data of using

3-minute nodding cycle with constant calibration instead of 20-minute scans. The new estimation of the position of the MEX spacecraft in the RA/Dec plane is shown in Figure 5.46.
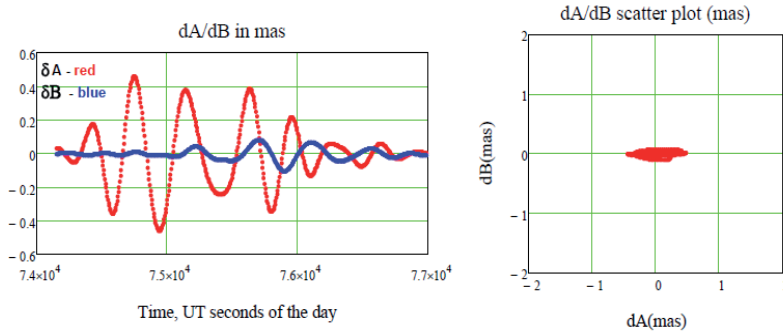
Figure 5.46. Expected A/B positioning residuals along the axis of the system beam simulating a 3 minutes nodding cycle and 60 s adaptive integration. Scatter of angular coordinates is 0.19 mas and 0.035 mas (1σ), or 170 m and 30 m in linear measure at the distance of 1.2 AU.

Expected excursions of the coordinates determination are at a level of 0.19 mas and 0.03 mas, or 170 m and 30 m correspondingly.

em081a - VEX session on 2010.08.23

The $em081(x)$ sessions were conducted in the framework of the EVN observations under the code $R10A007$. The sessions were partially funded by EVN and 20 observing hours were granted. The observations were considered as a Target of Opportunity. Therefore, the author was responsible in contacting the available radio telescopes and arrange the observing times. All the costs for shipping the disks to the correlator were supported by the EVN.

The $em081a$ session was conducted on 2010.08.23 from 11:50 until 15:10 UTC. The observations switched between Venus Express spacecraft and two calibrators sources, J1255-0804 and J1256-0547. We captured nine scans of VEX, four of J1255-0804 and twelve of J1256-0547 during the three-hours observation. The images from both calibrator sources at X-band are shown in Figure 5.47. The images were created with the AIPS VLBI software [120] for the calibration and with the Difmap tools [121] for the rendering of the images. The beam resolution of each reference source was 7.65 and 1.65 mas.

Five EVN radio telescopes participated in this experiment: Yebes (40-m, Spain), Onsala (20-m, Sweden), Metsähovi (14-m, Finland), Medicina
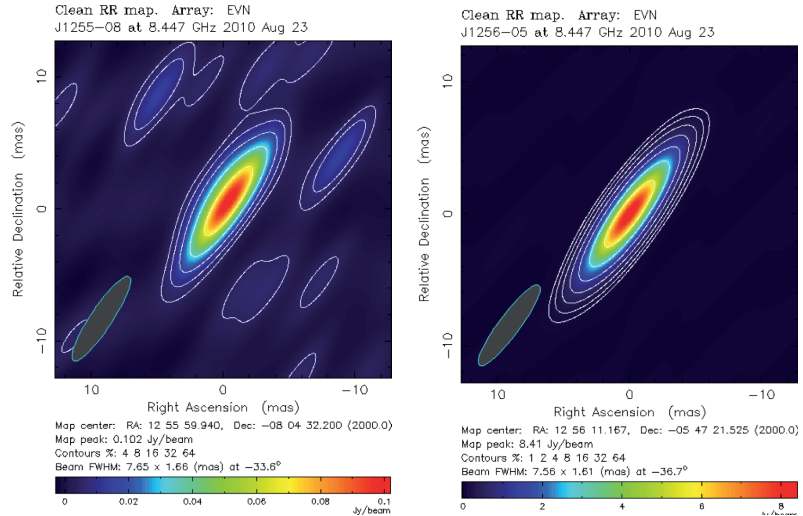
Figure 5.47. left: The radio image at X-band of the J1255-0804. right: Radio image at X-band of the calibrator J1256-0547.

(32-m, Italy) and Pushchino (20-m, Russia). All the stations alternated observing the spacecraft and the reference sources, excluding Pushchino that ran in single-dish mode observing only the spacecraft signal. More than 150 GB of data were recorded into disks at each station. The cable patching at the station of Onsala was not installed correctly and therefore the data were corrupted. Hence, we used only three of the antennas (Metsähovi, Medicina and Yebes) for the VLBI correlation and the phase-referencing. The narrow band spacecraft analysis included the data from Pushchino, despite the high level of phase noise.

The detection of the VEX spacecraft carrier signal with the Yebes antenna is shown in Figure 5.48. The dynamic range of the main tone is over 70 dB at a frequency resolution of 0.95 mHz.

The topocentric frequency detections from all the radio telescopes and the residual phase for the first scan observed at Yebes are embedded in the picture. The topocentric frequency detections at Metsähovi, Yebes, Medicina and Pushchino are seen with more detail in Figure 5.49.

Only five scans out of nine are presented in the plot. The Doppler shift per each 15-minute scan was approximately 1 kHz. The topocentric frequency detection differed between 3 to 9 kHz between the stations and the frequency-time pattern was similar for all of them. Pushchino was configured with 19-minute scans and, therefore, the start/stop times are different.
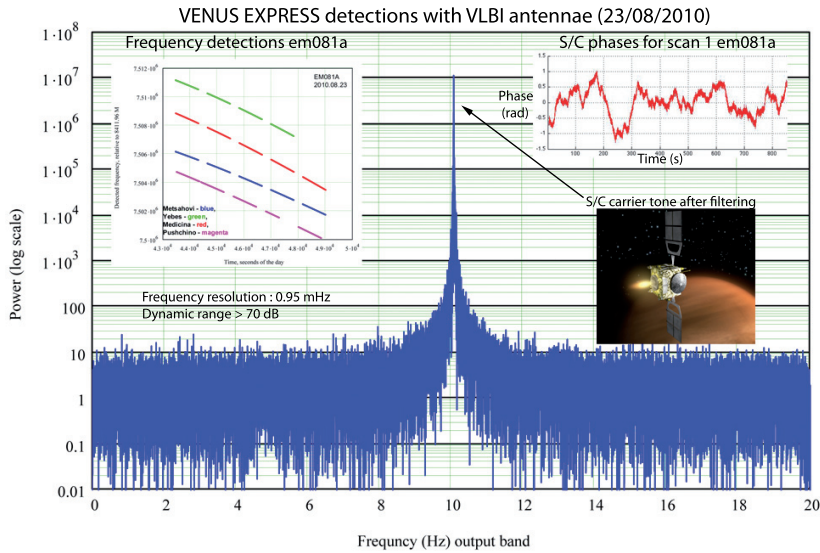
Figure 5.48. Detection of the VEX spacecraft carrier tone with the EVN radio telescopes on 2010.08.30. The dynamic range was over 70 dB. left-corner: Topocentric frequency detections per each antenna. right-corner: Residual phase from the first scan.
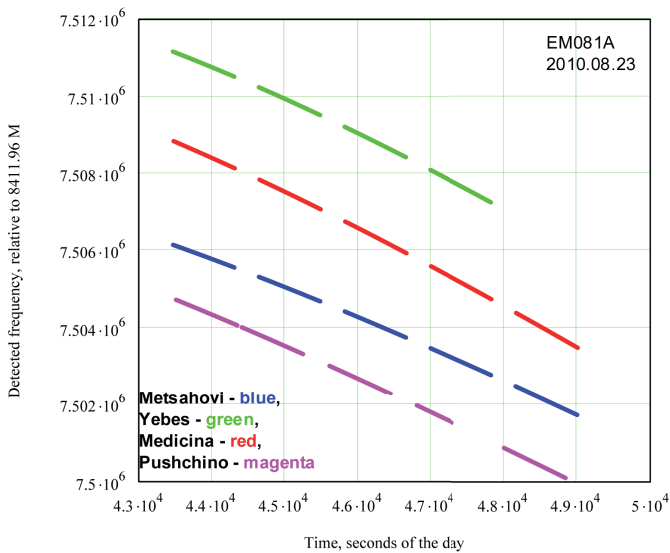
Figure 5.49. Frequency detections for five VEX scans with four radio telescopes (Mh, Mc, Wz, Pu) in the $em081a$ session. The Doppler shift is approximately equal to $1\,\text{kHz}$ per each 19-minute scan.

The residual phases extracted from the first scan of the $em081a$ session are shown in Figure 5.50. The scans were 15 minutes long, instead of the usual $1140\,\text{s}$. The residual phases extracted from Medicina, Yebes and

Metsähovi showed consistent cross-correlation. On the other hand, the phase detected at Pushchino was dominated by the system noise temperature. The phase stability of the S/X receiver is not so good and the results are not useful scintillation analysis or spacecraft tracking purposes.
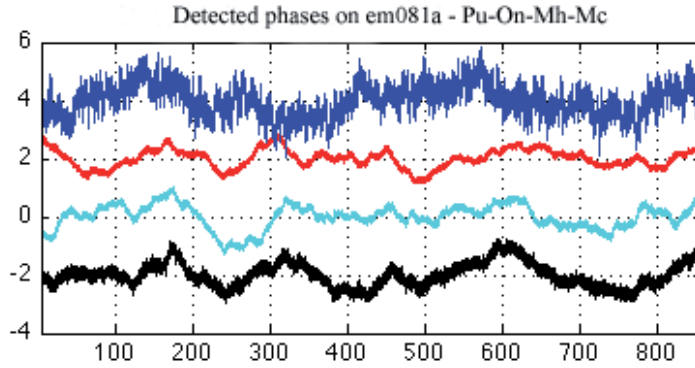
Figure 5.50. Phase fluctuation of 4 antennas (Pu, Mh, Mc, Ys) observed on 2010.08.23. The phase is shifted Pu (in blue) $+4$ rad, Ys (in red) $+2$ rad, Mh (in cyan) $+0$ rad and Mc (in black) -2 rad to improve the visualisation.

The phase fluctuations are partially correlated per each antenna as seen in the graph. The scintillation contribution to the phase is the same at each antenna for the uplink communications link. The difference on the phase detected is caused by the downlink propagation of the spacecraft signal towards the Earth. The phase fluctuations caused during the uplink of the trajectory can be compensated by calculating the average of all signals and subtracting it from each independent scan. The nodding cycle can also be optimised if this compensation is taken into account.
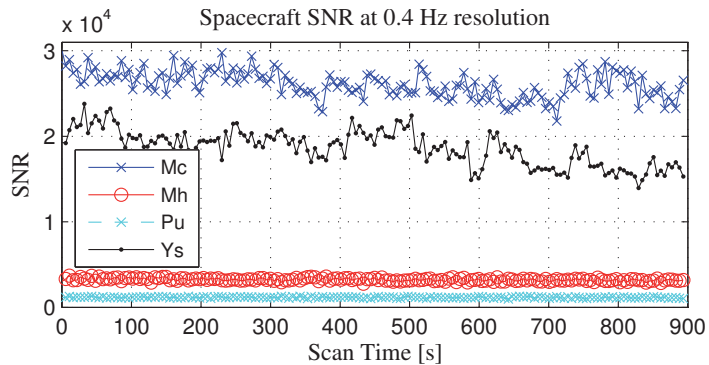
Figure 5.51. SNR of the spacecraft tone detected at Mc, Mh, Pu and Ys in 2 kHz bandwidth around the tone with 0.4 Hz resolution. The SNR were $2.6 \cdot 10^{04}$, $3.2 \cdot 10^{03}$, $1.1 \cdot 10^{03}$ and $1.8 \cdot 10^{04}$.

The SNR's at a 0.4 Hz resolution are compared in Figure 5.51. The SNR for Medicina (in blue), Metsähovi (in red), Pushchino (in cyan) and Yebes (in black) were respectively $2.6 \cdot 10^{04}$, $3.2 \cdot 10^{03}$, $1.1 \cdot 10^{03}$ and $1.8 \cdot 10^{04}$.

The correlation of the broadband data were performed with the MkIV hardware correlator. The Figure of the calibrators was shown in Figure 5.47. The poor results of the calibration and the long scans used for observing the spacecraft did not allow us to calculate the state vectors of the spacecraft.

em081b - VEX session on 2010.09.20

The $em081b$ session was conducted on 2010.09.20 from 11:00 to 14:00 UTC. The antennas alternate observing the VEX spacecraft and two calibrators sources, J1419-1928 and J1337-1257. We captured 16 scans of VEX data, 17 scans of the first reference source and two of the second. This time we reduced the length of the scans to five minutes, in order to apply phase-referencing. Four stations were supposed to participate in the experiment, Onsala, Medicina, Metsähovi and Yebes.

Yebes dropped out of the experiment at the last moment due to limited observing time. Furthermore, the stations of Onsala and Medicina had major problems during the session and the observations failed. The Metsähovi radio telescope was the only one to record the whole session without problems. However, the data were not valid for studying the interplanetary scintillations, because the scans were only 5-minute long. Furthermore, Pushchino observed VEX and recorded 19-minute scans, although, the scintillation analysis was not possible due to the excessive phase noise. So basically, the results of the session could not have been more unsatisfactory.

em081c - VLBI VEX session on 2011.03.28

The largest attempt to track a spacecraft with VLBI radio telescopes was organised in March 2011. The idea was to observe the VEX signal on 2011.03.25 with four radio telescopes as a pre-testing and perform the real spacecraft tracking on 2011.03.28. The original plan for $em081c$ included eleven radio telescopes from the EVN network and the NRAO VLBA station of Saint Croix. For the v110325 session, the telescopes observed the calibrator source at the beginning and at the end of the schedule, and five 19-minute scans between them. For the $em081c$ session, all the EVN radio telescopes were configured to observe alternatively the phase-reference source and the spacecraft signal with a nodding cycle of 4 minutes.

Metsähovi, Hartebeesthoek, Wettzell and Pushchino took part in the pre-session. Meanwhile, the $em081c$ was conducted with the radio telescopes of Metsähovi, Onsala, Matera, Medicina, Yebes, St. Croix, Zelenchukskaya, Hartebeesthoek, Svetloe and Pushchino. St. Croix station did only observe the calibrator source and Pushchino performed standard IPS sessions.

This VLBI session was a great challenges for the team, including the preparation of the schedules, synchronisation of the observations, transferring of the data from all stations and processing of the large amount of data. Furthermore, three new stations, without any experience of spacecraft tracking sessions were included in the schedule. The 14-metre dish of Fortaleza (Ft, Brazil) was supposed to take part in the session, but unfortunately were able due to major reparations on the antenna. The Brazilian radio telescope can introduce an incredible baseline inside our array of telescopes and it is expected to be operative soon.

The $em081c$ session was scheduled between 08:45 and 11:30 UTC, for a total duration of 2 hours and 45 minutes. The nodding cycles was 4-minute long with 20-seconds gap for re-pointing and antenna calibration. We collected 79 scans per station, divided between 38 of VEX and 41 of the calibrator sources. We used two different reference sources during the session: the J2211-1328 (39 scans) with coordinates RA=22h11m24.1s and Dec=$-1°52$'30.2" and the J2225-0457 (the first and the last) with coordinates RA=22h25m47.2s and Dec=$-04°57$'01.4". The VEX spacecraft had mean coordinates of RA=22h14m13s and Dec=$-11°41$'22". Venus was at a solar elongation of 36 degrees and at a distance of 1.23 AU at the time of the observations.

The v110325 session was carried out between 09:00 and 11:00 UTC on 2011.03.25. This observation was considered as a preparation for the following spacecraft tracking ($em081c$). The schedule included the same target (VEX) and the same calibrator (J2225-0547) in both cases. Seven scans were observed at each station: the first and last scans contained the calibrator data and the 100-minutes between had the spacecraft signal. Typical 19-minute scan were used in order to use the scans for interplanetary scintillations analysis. Coordinates and position of the spacecraft were similar to the previous mentioned.

The uv-plane of the VLBI array of eight radio telescopes for the two radio source calibrators and the VEX spacecraft is shown in Figure 5.52. Note,

that the image covers only 8 radio telescopes, instead of the 11 used in the session. Three radio telescopes joined the observations at the last moment and they were not included in the initial plan.
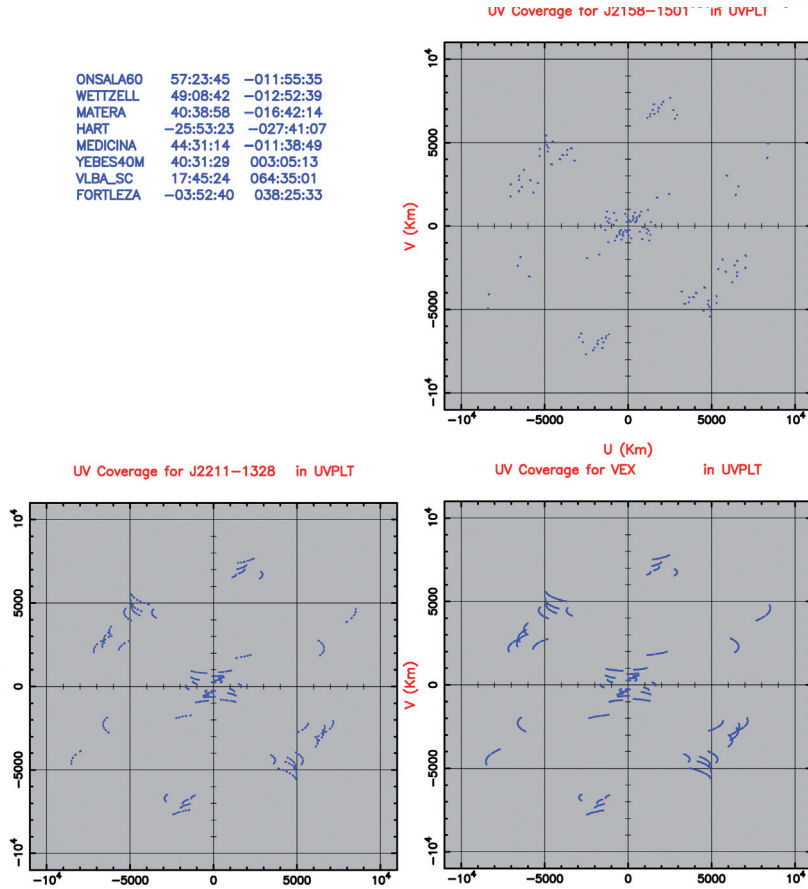
Figure 5.52. top-right: Coverage in the uv-plane (in km) for the source J2225-0457. bottom-left: J2211-1328. bottom-right: VEX. The uv-coverage was simulated with the $em081c$ session antennas. The max baselines were 8500 km in E-W direction and 7800 km in N-W.

The array of eight radio telescopes covers pretty well the uv-plane. The inner part of the map represents the coverage of the European antennas. The baselines shown in the most external part represents the addition of Russian, American, South-African and Brazilian antennas. The maximum baseline in the East-West direction is around 8500 km and 7800 km in the North-South direction.

The shape of the synthesized beam of the reference source J2225-0547 is illustrated in Figure 5.53. Note the granularity of the beam: the central core is ~ 1 mas wide and surrounded by side lobes with ~ 1 mas separa-

tion.
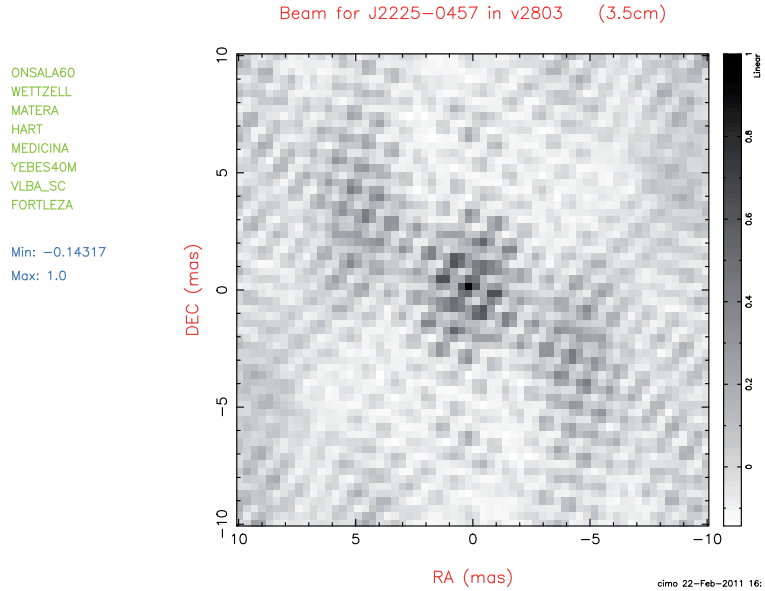
Figure 5.53. Synthesised beam for the reference source J2225-0457 in X-band ($\lambda 3.5$ cm). The simulation was made using the radio telescopes involved in the $em081c$ session.

Data were acquired using the standard Mark5A/B VLBI data acquisition systems. We used four 16 MHz wide band channels with 2-bit Nyquist sampling and data rate of 256 Mbps per station. The total amount of data per station was 270 GB for a total aggregate data of 2.4 TB. As some stations do not have a dedicate fibre connection to transfer the data, all the disk packs were shipped to JIVE for the correlation and processing. The spacecraft observations were separated from the other scans and analysed at Metsähovi, as usual.

The topocentric frequency measured on $2011.03.25$ for the four radio telescopes are shown in Figure 5.54. The Doppler detections show similar pattern between the Onsala, Metsähovi and Pushchino results; the Doppler frequency differs by several kHz between each station.

An excessive phase drift caused the different pattern observed on Hartebeesthoek from the local oscillator of the receiver. This broken LO caused instability on the frequency and the phase detected. A second problem occurred with Hartebeesthoek was due to the scheduling of the spacecraft coordinates. Similar sky coordinates than the rest of European radio telescopes were used. This approach resulted to be slightly inaccurate. Specific sky coordinates of the target at each telescope may be required. The
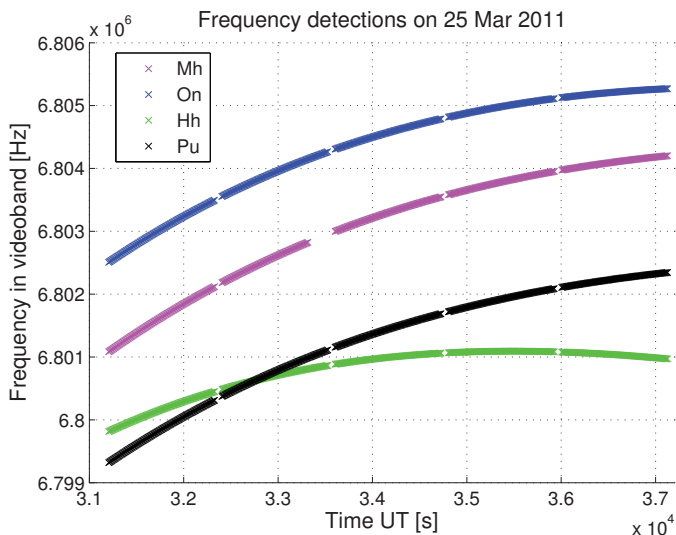
Figure 5.54. Topocentric frequency detections observed at On, Mh, Hh and Pu on the VEX session on 2011.03.25.

accuracy of the detection of the spacecraft signal benefits from this approach, but the complexity of the scheduling increases drastically.

The maximum variation in the Doppler frequency for the stations of Onsala, Metsähovi and Pushchino were $2.6\,\text{kHz}$ for the 100 minutes of spacecraft data. The Doppler variation was approximately $0.7\,\text{kHz}$ per each of the three first 19-minute scans. The Doppler barely shifted few hundred Hz for the last two scans. Probably the telescopes observed the spacecraft before it was occulted by Venus and, hence, the Doppler showed that pattern at the end of the session. For Hartebeesthoek, the frequency drift is only $1\,\text{kHz}$. An integration time of $5\,\text{s}$ and spectral resolution of $10\,\text{Hz}$ was used for the SWspec iteration.

The level of SNR after processing the data with the spacecraft tracking software is shown in Figure 5.55. The signal to noise ratio using the 20 thousand FFT points and spectral resolution of $0.2\,\text{Hz}$ has an average level of 10^{04}, $5.5 \cdot 10^{05}$, $2.5 \cdot 10^{05}$ and $1.3 \cdot 10^{05}$ at Metsähovi, Hartebeesthoek, Onsala and Pushchino, respectively.

The digital PLL narrows the signal to $20\,\text{Hz}$ band around the carrier line with a $0.2\,\text{Hz}$ spectral resolution and allows us to extract the phase of the signal. The Doppler frequency residuals from the VLBI radio telescopes at $20\,\text{Hz}$ are shown in Figure 5.56.

At this accuracy, we detected the problems with the local oscillator at
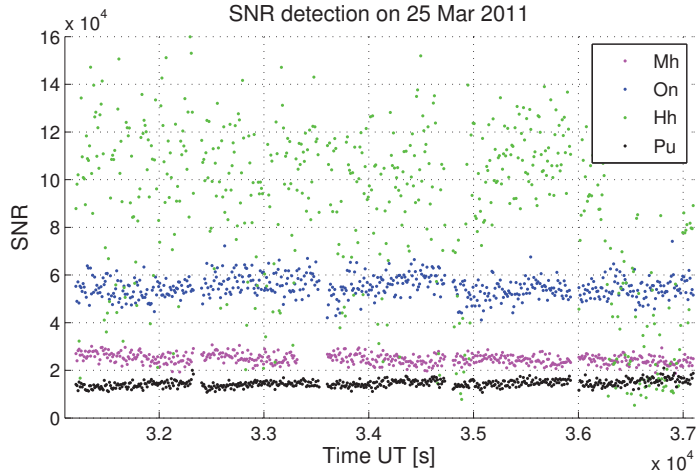
Figure 5.55. SNR detections observed at Mh, Hh, On and Pu on the VEX session on 2011.03.25. The mean SNR level were 10^{04}, $5.5 \cdot 10^{05}$, $2.5 \cdot 10^{05}$ and $1.3 \cdot 10^{05}$, respectively.
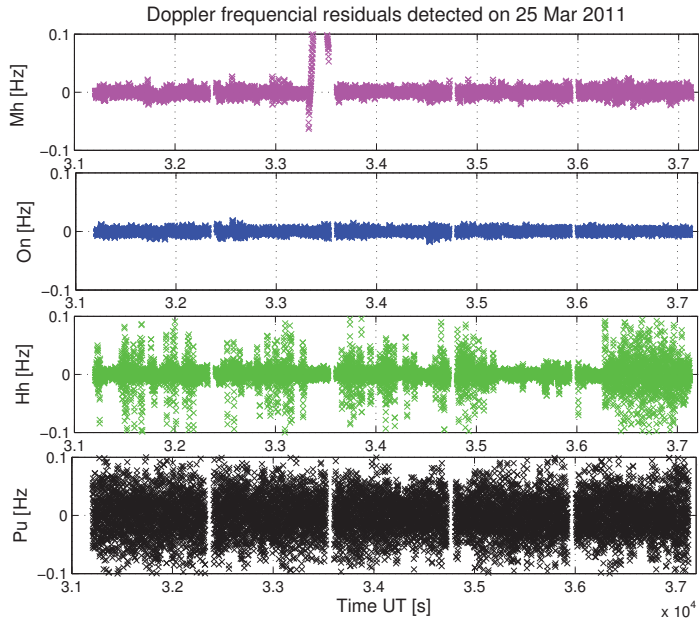
Figure 5.56. Doppler residuals detected at Mh (in magenta), On (in blue), Hh (in green) and Pu (in black) on the VEX session on 2011.03.25. Excessive high phase noise was presented in the last two antennas.

Pushchino and Hartebeesthoek, which caused an excessive variance of the measured Doppler residuals. Thus, the phase of the VEX signal on both stations was extracted but they were not useful for further analysis.

The level of the Doppler residual at Metsähovi and Onsala is much lower

than in the other two stations. The residual Doppler is within the $20\,\mathrm{mHz}$ boundaries. The residual phase extracted at Onsala and Metsähovi are shown in Figure 5.57.
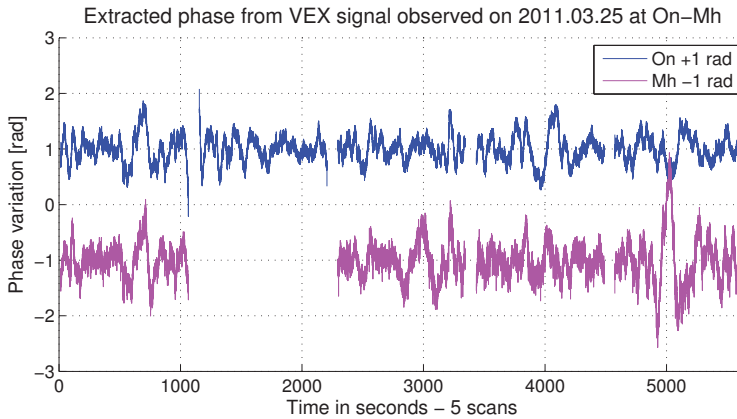
Figure 5.57. Phase detected at On and Mh on the VEX session on 2011.03.25. The second scan from Mh had corrupted data.

We added and subtracted $1\,\mathrm{rad}$ from each data set to improve the readability of the plot. The last scan observed with Metsähovi showed also a strong variation in the phase. The origin is undetermined, but probably caused by internal or external RFI. The post-analysis of the phase fluctuations can isolate and filter such undesired break-ins. The Doppler shift, SNR and residual phase values per each scan are stored to disk for further post-processing combined with the broadband correlation.

The broadband correlation of the calibrators was processed at JIVE using the SFXC correlator. The search for **fringes** and the **group delays** between the elements of the array used the standard global fringe fitting tools offered by the AIPS software [120]. The residual group delay estimates per baseline observed on 2011.03.25 are shown in Figure 5.58.

The fringe search values per several of the baselines observed on the $em081c$ session are shown in Table 5.11. The delay offset between the stations is shown in microseconds, and the delay rate in picoseconds/s.

The cross-correlation spectrum of the VEX signal (amplitude and phase) on the baseline Onsala Mh, as observed on 2011.03.25 is represented in Figure 5.59.

Most of the spectral power is concentrated in the $\sim 1\,\mathrm{MHz}$ region around the carrier line, but this frequency spread at such high SNR is enough to
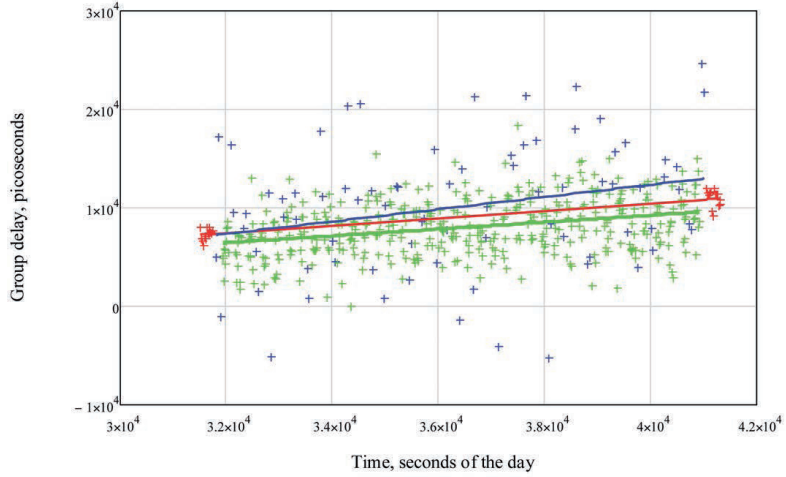
Figure 5.58. Residual group delay calculated in the v110325 session. Each color line represents the baselines On, Mh and Wz.

Table 5.11. Fringe search values per each of the different baselines. The columns indicate the delay offset (in microseconds), the delay dot (in ps/s) and the SNR.

Baseline	J2225-0457			J2211-1328		
	Delay	Delay Dot	SNR	Delay	Delay Dot	SNR
On-Wz	−0.405	0.204	545	−0.406	0.190	31
On-Mc	0.012	0.037	421	0.017	−0.013	18
On-Ys	10.37	−0.189	9	−7.445	0.064	7
On-Mh	0.010	−0.028	209	0.007	−0.141	12
Wz-Mc	0.417	−0.1694	563	0.415	−0.200	30
Wz-Ys	−15.63	0.286	8	6.747	0.520	6
Wz-Mh	0.415	−0.232	340	0.413	−0.217	18
Mc-Ys	−6.417	0.071	8	−6.879	−0.653	6
Mc-Mh	−0.001	−0.062	293	0.003	−0.126	12
Ys-Mh	−0.935	−0.016	8	13.147	−0.153	7

resolve the 2π ambiguity between the group delay detected by the broadband correlation with the SFXC and phase delay detected using the SC-tracker software.

The correlation of the calibrator source for each baseline provides the residual delays. To apply coherently the phase-referencing, the residual delays must be lower than the radio wave period at X-band, e.g. 0.120 ns. The measured residual delays and phases are then applied to detected
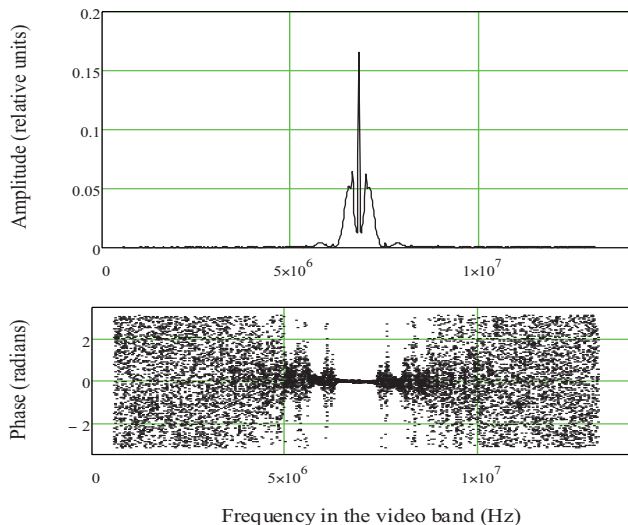
Figure 5.59. Cross-correlation spectrum (amplitude and phase) of the VEX signal on a baseline Onsala-Metsähovi observed on VEX 2011.03.25

residual phases of the target. Calibrated residual phases are used to re-cover the deviations of the lateral coordinates of the target with respect to *a-priory* ones.

Projection of the VEX spacecraft orbit around the planet on 2011.03.28 is shown in Figure 5.60. The spacecraft was observed during 3 hours, which corresponds to small fraction of its full orbit. The black boxes indicate the position of the spacecraft at the time of the observations.

Finally, the reconstructed position of the spacecraft within the Venus orbit observed on 2011.03.28 is shown in Figure 5.61. The plot shows the estimated offset position of the spacecraft using several of the available baselines. The red circles indicate the offset in meters in the East-West direction. The blue circles show the offset in meters in the North-South direction. The standard deviation is in the order of 100 meters for E-W and 1 km N-S direction.

The system beams are the reconstructed image of the VEX sky map at different times of the observations. The pixels in the images are 100 m wide. The whole image was 1 km wide, approximately 1.1 mas. Venus was at a distance to Earth equivalent to 1.23 AU.
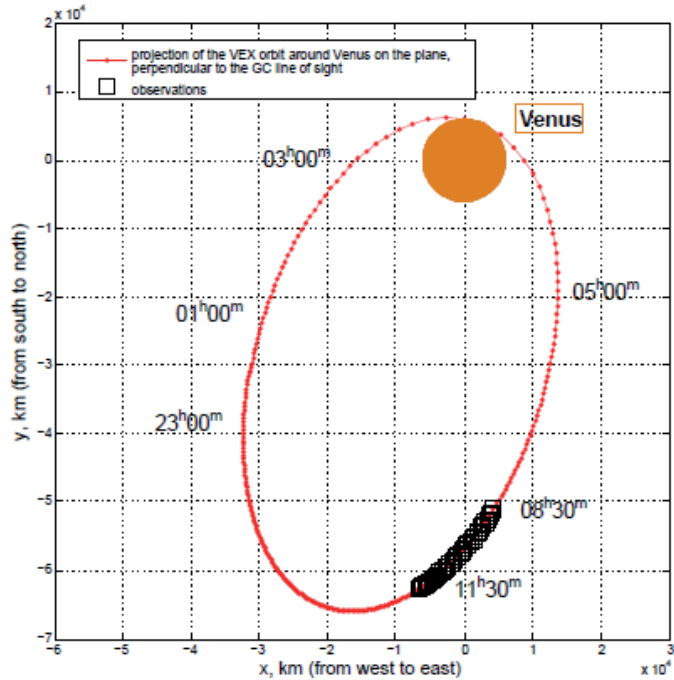
Figure 5.60. Image reconstruction of VEX detected on 2011.03.28. The three hours observation monitored a fraction of the spacecraft orbit around Venus.

5.4.4 VLBI Glonass observations

Global Navigation Satellites Systems (GNSS) are essential in our modern world for determining the coordinates of any location on the Earth with high accuracy. Currently, two operating systems are available: the American Global Positioning System (GPS) and the Russian GLObal NAvigation Satellite System (GLONASS). The GNSS systems are expanding with the recent launch of two satellites of the future European Galileo system. The GNSS coordinates are linked to the Conventional Terrestrial Reference Frame (CTRF) and in parallel the Celestial Reference Frame (CRF) is tied to the geodesy observations with the International VLBI Service for Geodesy and Astrometry[9]. The approach taken in this project aims to achieve the best link between both frames by observing and processing the signal transmitted by the GNSS satellites. The concept is based on the same technique used for planetary spacecraft tracking. The observations of the satellite radio signal and natural radio sources with VLBI will ensure the cross-correlation of the two frames.

[9]IVS web page: http://ivscc.gsfc.nasa.gov

147
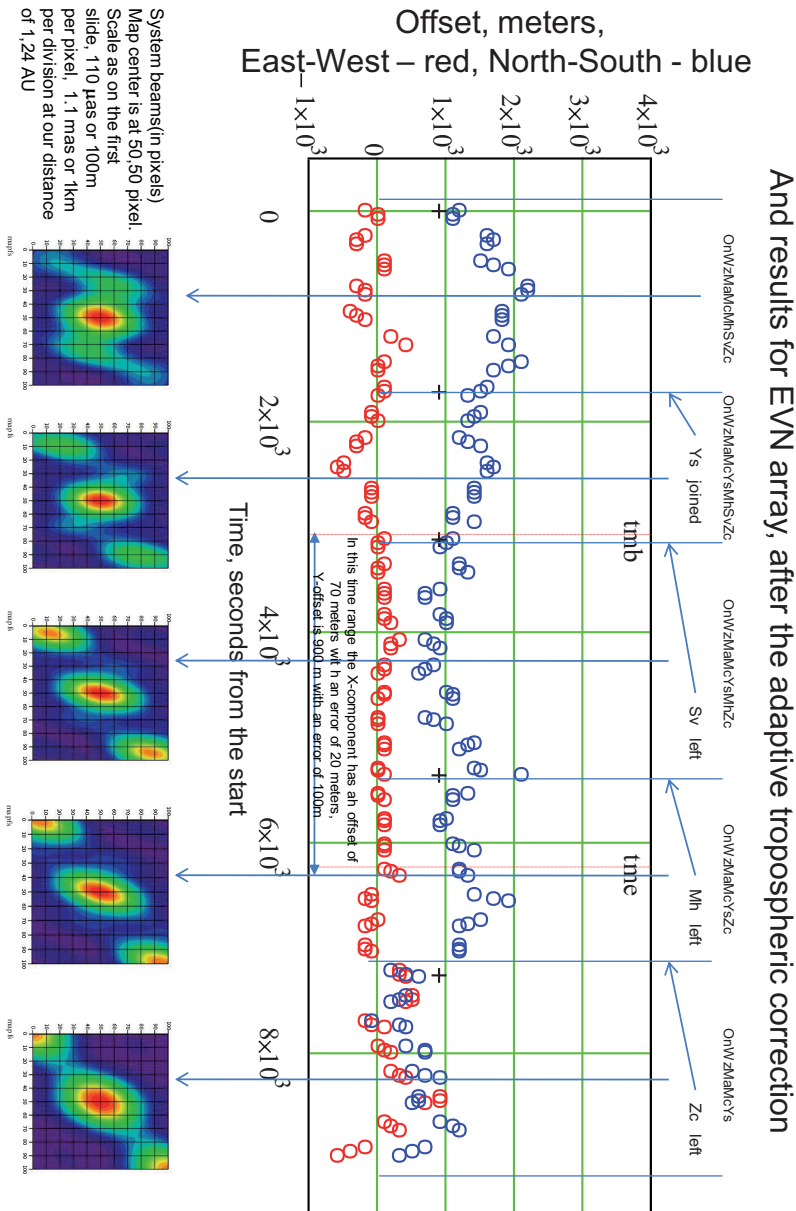
Figure 5.61. Spacecraft position reconstructed from the 2011.03.28 observations. The y-axis indicates the offset in meters for E-W (in red) and N-S directions (in blue). The system beams belong to the spacecraft position at several intervals of time.

Several tests have been conducted observing the signal transmitted by the GLONASS satellites using VLBI radio telescopes during 2010 [122, 123, 124]. So far, 3 European radio telescopes have participated in the sessions: Matera (Italy), Noto (Italy) and Onsala (Sweden). The GLONASS

radio signal is transmitted on L-band (1600 MHz). Unfortunately, the lack of L-band receiver excluded other stations to join these experiments, Metsähovi among others. The nature of such navigation systems signal is comparable to the planetary spacecraft ones. However, the power levels of the Earth satellites are several orders of magnitudes higher than in remote spacecraft.

During the observations the telescopes alternated targeting the satellites with natural radio sources. These are used for calibration and VLBI phase referencing. Similar to the geodetic VLBI observations, the time and phase delay of both natural and satellite sources are detected and correlated with widely spaced radio telescopes.

The goals of these experiments were to develop and test the scheduling, the acquisition of the data and the processing of the narrow band signal. Furthermore, it was expected to verify the full tracking pipeline, foreseeing the cross-correlation of the recorded data on the baseline Onsala Medicina. The involvement of the author in this project consisted of reusing the spacecraft multi-tone tracking software for satellites orbiting the Earth. For GNSS we had to take into consideration certain adjustments to ensure the optimal tracking of the satellites: higher power level, smaller Doppler frequency detections or shorter scans due to the fast re-pointing of the antenna.

Observations

During 2010, the team leaded by V. Tornatore conducted two different sessions, on $2010.06.28$ and $2010.08.16$, with the radio telescopes of Noto, Matera and Onsala. Only the data from the last two stations were processed. The goal was to observe several GLONASS satellites subsequently and a couple of reference radio sources. The sessions started observing the calibrator: 3C454.3 and 3C286. In June, the calibrators were observed for 2 minutes and The GLONASS satellites, PR10 and PR19 for 5 minutes, using 1-minute scan. In August, the scans of the calibrators were observed for 5 minutes and the PR13, PR11 and PR21 satellites for 15 minutes. In this case, we increased the length of all scans to simplify the processing and the analysis. Each radio telescope was re-pointed every 20 seconds to ensure correct tracking of the satellite orbit. This re-pointing affected with discontinuities on the tracking, thus producing some glitches every 20 seconds in the data residuals.

In June, we also used a fixed frequency on the receiver at 1570 MHz

for the entire session, while in August we used variable frequencies depending on each carrier signal of each observed satellite (1592.88, 1594.00 and 1696.25 MHz). The configuration of the session followed the usual set-up of the spacecraft tracking. We recorded two frequency channels, with a bandwidth of 16 MHz and both polarizations (RCP and LCP). Additional damping in both polarizations channels was required to attenuate the strong satellite signal and avoid saturation.

Signal processing of data recorded

Data processing was performed with the high-resolution software spectrometer (SWspec) and the spacecraft tone tracking software (SCtrack), presented in Section 5.2. For the spectra analysis we used $1.6 \cdot 10^6$ DFT points and integration time of 1 s for a spectral resolution of 20 Hz in the 16 MHz bandwidth. The spectra for the satellite PR19 observed with Onsala radio telescope is shown in Figure 5.62.
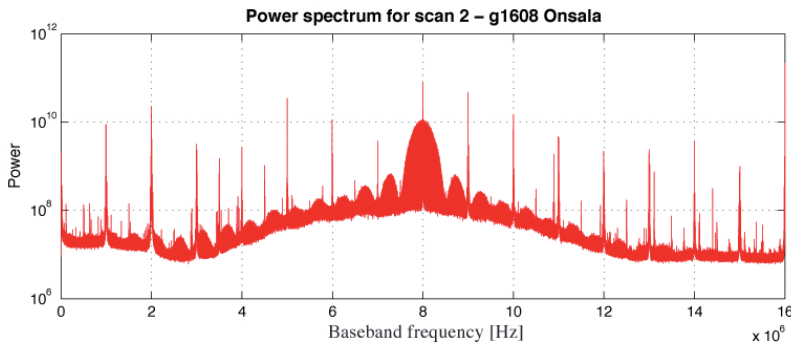
Figure 5.62. Spectrum of the GLONASS PR19 satellite observed at On on the 2010.08.16. For this preview, we used a spectral resolution of 100 Hz. The resolution was improved to 20 Hz for the data analysis.

A Doppler analysis on the same data set was also performed using a 4th-order phase stopping polynomial. The Figure 5.63 illustrates a zoom-view of the 2 kHz band around the carrier signal, after the adaptive stopping of the Doppler data.

One of the greatest problems in order to track the GLONASS signal is the fast orbit of the satellites and the need of constant re-pointing of the antenna. The consequences are seen in Figure 5.64, where a series of peaks repeating every 20 seconds are visible. These results were extracted from the session conduced on 2010.06.18 with the radio telescope of Onsala. For future sessions, it is recommended to implement the SatTrack software directly in the FS; this software has been developed [125] on pur-
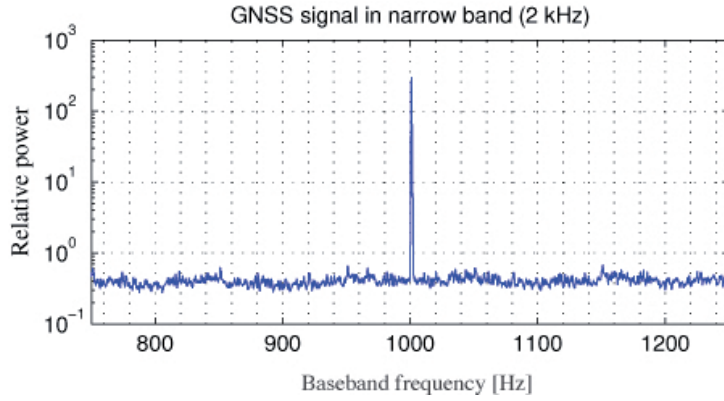
Figure 5.63. Spectrum of the narrow band tone after SCtracker. The GLONASS space-craft signal is correctly stopped into a $2\,$KHz band around the carrier with spectral resolution of $0.4\,$Hz.

pose for satellite tracking by astronomical antennas and could make the satellite tracking with VLBI antennas more feasible.
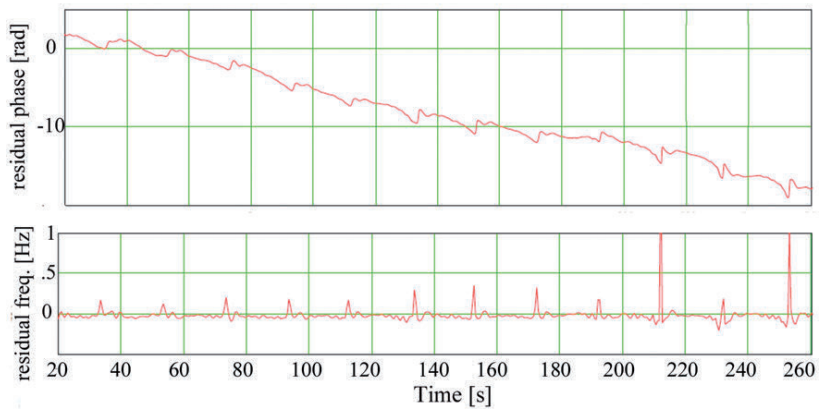
Figure 5.64. top: Post-PLL residual phase in the $1\,$Hz adaptive tracking band. bottom: Post-PLL residual frequency. The glitches are caused by the telescope re-pointing every 20 seconds.

After the PLL analysis and the correction of the glitches the phase of the radio signal is analysed. The phases from the 3 satellites (PR11, PR21, PR13) captured on $2010.08.16$ from the Medicina and Onsala antennas are shown in Figure 5.65. $+1\,$rad and $-1\,$rad have been added to the phase data of Medicina and Onsala respectively for convenience. The detection was successful on 5 out of 6 of the 15-minutes scans.

The phase scintillation on GNSS data was handled in the same way as with the interplanetary scintillations. The phase fluctuations are anal-ysed to determine the nature of such phenomena. The spectrum of the
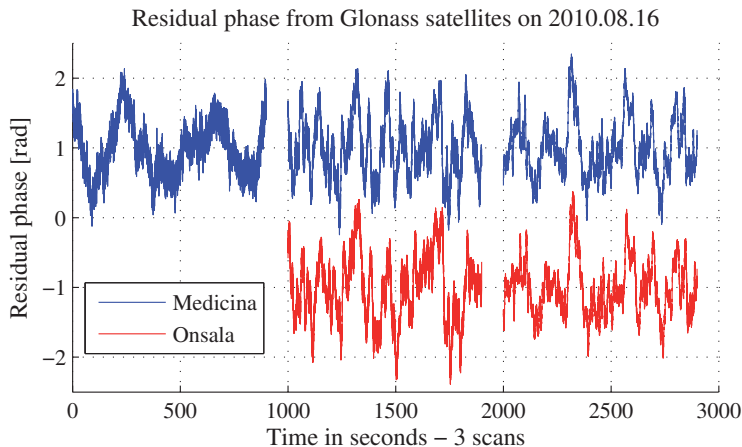
Figure 5.65. Phase fluctuations Mc and On for the three Glonass scans (PR11, PR19 and PR13) observed on 2010.08.16. These fluctuations are caused by the ionosphere and system noise.

phase fluctuations is seen in Figure 5.66. The fluctuations are characterised primarily by the ionospheric scintillations, the phase noise inserted by the satellite clock and the system noise temperature of the radio telescope. The plot highly reminds the shape of the interplanetary plasma fluctuations, although the slope of the ionospheric scintillation is more gentle than the one caused by the IPS. Furthermore, the internal clock of the satellite is not as precise as the USO installed in the spacecraft that causes an extra level of phase noise. The radio telescopes T_{sys} depend on the local receivers and are similar for Glonass and spacecraft observations.

Future on navigational satellite observations

Several tests have been conducted to detect and analyse the radio signals emitted by GLONASS satellites with VLBI antennas. These observations could open a new path for geodesy determination of positioning on Earth. The Doppler effect and intrinsic communications signal used to track satellites are detectable in the signal processing. The broadband correlation on the calibrator allow applying phase and timing delay from the CRF to the satellite results. Dual-frequency observations are recommended to improve ionospheric corrections.

A thorough analysis of the data captured on those two experiments lead to estimate the state vectors parameters in the order of 15 to 20 cm accuracy [123]. We would need to include coherent VLBI phase referencing
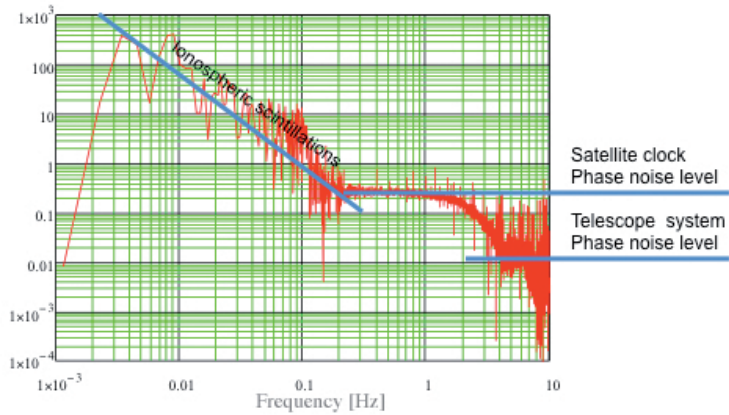
Figure 5.66. Phase scintillations in the GLONASS observations for PR-13 observed with the Onsala radio telescope. The main contributions are from: ionospheric scintillations, Glonass LO phase noise and receiver phase noise.

and more telescopes to improve the results. We expect that increasing the number of observing telescopes, the length of the baselines and the duration of observations will lead to a significant improvement on the accuracy of the GNSS ephemerides, currently to 5 cm. In a sense, these values are not accurate enough to use for geodesy purposes, specially now that VLBI2010 [126] is aiming to accuracy in the order of 1 mm. However, we are confident that the results of our observations will improve in near future.

New observations using a better configuration for the involved radio telescopes are planned for the following months. It is worth noting that the classical astronomical tools can contribute to space science too. In fact VLBI determination of GNSS state vector may also impact on the GNSS field leading to improved models and methods for orbitography.

5.5 Conclusions and discussion

The development of the multi-tone spacecraft tracking software was initiated by J. Wagner in 2008. The software is based on the software correlator developed by S. Pogrebenko and that has been successfully used in earlier spacecraft tracking experiments. During the following three years a lot of work has been done debugging the code, improving the performance, and adjusting the settings for different scenarios. All these tests helped to create a robust software package compatible with most of

the radio telescopes of the VLBI network and is adjustable to detect any spacecraft signal at any frequency band. The software runs on any Intel or AMD platform and can be ported to any environment. In fact, both SWspec and SCtracker have been installed and tested in the current computer cluster that was built to host the future software correlator (SFXC) at JIVE. The short-term plan is to move all the processing tasks from Metsähovi to JIVE.

The development of the software was always comprised in several environments and for different purposes. The project started by observing and detecting the signal emitted by a spacecraft in X-band with a single antenna. The number of possible spacecraft targets and the radio telescopes rapidly increase. The experiments were independent of the space agency, spacecraft coordinated by ESA, JAXA and NASA have been successfully detected, of the frequency of transmission, UHF, L-, S- and X-band transmission lines have been tested, or of the visibility time by the ground stations, European, African, Asian, American and Oceanic antennas have been used to detect the spacecraft signals. Even the geodesy community have been interested in this method to apply it for detecting satellites that are orbiting our planet. More sessions have been planned in order to incorporate similar satellite techniques in the routine VLBI sessions to improve the quality of the data.

PRIDE has been trusted by several space agencies to be included in their research plan for future deep space missions. The next big opportunity was supposed to arrive with Phobos-Soil. The work of the group will concentrate on observations of with VEX, MEX and Radio Astron. The Russian spacecraft launched to allow radio interferometry with a radio telescope in space. Meantime, observations of the VEX spacecraft will continue during this year aiming to complete the scintillation analysis on for the Venus orbit. Including data from other spacecraft in other locations can complement this scintillation analysis.

Acknowledgements

6. Interplanetary scintillation

6.1 Introduction

Four VLBI radio telescopes observed simultaneously the ESA Venus Express (VEX) spacecraft signal on 2009.11.26. The temporal evolution of the carrier line phases showed high level of fluctuations rather than steady behaviour. The residual phases also demonstrated high cross-correlation among the samples of each radio telescope. The phase variations are primarily caused by the phase stability of the receiver and transmitter equipment, and the propagation of the signal in the Earth's ionosphere and in the **interplanetary plasma**. Motivated by these **phase fluctuations**, a campaign to observe the spacecraft signal and its propagation at several solar elongations and several distances to the Earth was initiated. The campaign started at the ends of 2009 and have extended until the 2012. During these sessions the EVN radio telescopes tracked the signal of the spacecraft at X-band (8.4 GHz) continuously during 2 or 3 hours.

The structure of this chapter is organised as follows: a general overview of the **solar wind** and the **interplanetary scintillation** (IPS) is introduced in Sections 6.1.1 and 6.1.2. Special attention is given to the past and current studies for characterising the solar wind and the results obtained in this field by other research groups.

Secondly, the methodology, the characteristics of the participant radio telescopes and the results of the observations are summarised in Section 6.2. Furthermore, a description of the tools and software developed for the data processing is presented in Section 6.2.3. The data processing software is the same as used in the spacecraft tracking (for more references see Section 5.2). The phase fluctuations analysis software, developed integrally by the author, is described in Section 6.2.3.

Finally, the characterisation of the interplanetary plasma along the line of sight using the phase fluctuations of the spacecraft signal is presented in Section 6.3. In this section, essential parameters retrieved from these measurements, such as the phase scintillation index, bandwidth of scintillation or broadening of the spectra and their dependence on the solar elongation, distance to the target, celestial position of the spacecraft in the Solar System, solar activity index, and participant radio telescopes are discussed.

This study focuses on the measurements technique combined with the analysis of the phase fluctuations and the physical interpretation of the results. These results are complementary to the classical measurements of the IPS based on the power level fluctuations of natural radio sources. No other research group have studied the phase fluctuations of the spacecraft signal for such a long period.

6.1.1 The solar wind

The internal magnetic field of a planet produces a large magnetic structure known as **magnetosphere**. The largest magnetic structure in the Solar System is obviously generated by the Sun and is known as **heliosphere**. The size of the heliosphere is approximately 100 times larger than the Sun itself [12]. The solar wind is a supersonic plasma outflow, which expands continuously within the heliosphere, interacting with the **magnetic bubbles** of the structure. The first evidences of the solar wind were discovered by Biermann in 1951 [127] while observing a cometary ion tail propagating through the interplanetary plasma. The solar wind is formed in the surface of the Sun. The lines of the solar magnetic field open up to the free space through solar coronal holes. The solar particles are then thrown freely into the interplanetary space. The solar wind is composed almost proportionally with an equal mixture of protons and electrons, with a lower amount of heavier ions. Embedded in this plasma flow, there is a weak magnetic field known as the Interplanetary Magnetic Field (IMF). The intrinsic characteristics of the solar wind depend on several parameters: solar cycle, heliographic latitude, heliocentric distance and rotational period [86, 20].

The expansion of the solar wind is radially outwards and its each plasma particle has its own magnetic field. In result, the magnetic field of the solar wind follows an Archimedean spiral [128]. During the expansion of

the outflow in the heliosphere strong turbulences are generated, which affect its propagation. Such turbulences resemble the well known hydrodynamic turbulence described by Kolmogorov in 1941 [129]. It is commonly assumed that the acceleration of the solar wind is attributed to the heating of the coronal shell. However, the physical processes of such phenomena are not well understood and several models have been developed ever since [130].

The solar wind is classified as **fast** or **slow** wind depending on its propagation speed. Fast streams can speed up from 400 to 800 km s^{-1} with a low density of 3 particles per cm^{-3}. The fast winds are originated in the solar coronal holes and could last for several weeks. The slow winds have an average speed between 250 to 400 km s^{-1}, higher density of particles (10 per cm^{-3}) and their nature is related to helmet streamers near current sheet of the Sun [12].

Nowadays, several satellites monitor the apparent speed of the solar wind at a number of distances with respect to the Sun. For instance, the satellite Advanced Composition Explorer (ACE), launched by NASA in 1997, measures constantly the speed of the outflow from its position at the L1 Lagrange point (at an approximate distance of 1.5 million km from the Earth) [131]. The solar wind averaged speed is 468 km s^{-1} at the L1 Lagrange point. The estimated value for the solar wind speed at a distance equal to 1 AU is 375 km s^{-1} and the electron density is equal to 5 particles per cm^{-3} [132]. The electron density in the interplanetary medium follows a relation $\sim 1/r^2$ with respect to the Sun.

6.1.2 Interplanetary scintillation

The variations in the flux density of a radio wave propagating in the Solar System are associated with the IPS. The density variations within the solar wind cause the radio waves from any compact source to scintillate. For many years several studies have been conducted to proof solar wind effects through the heliosphere [133, 21, 134, 135]). More recently, the European Incoherent SCATter radar (EISCAT) conducted measurements of the IPS with Nordic antennas [136]. Data were acquired simultaneously with three antennas located at Tromsø (Norway), Kiruna (Sweden) and Sodankylä (Finland). The observations were performed at 928 and 1420 MHz in order to measure the intensity fluctuations of known celestial sources. The data acquired from all three antenna is cross-correlated

and, therefore, providing more information on solar wind streams along the line of sight [137].

The radio wave from any celestial source suffers from fluctuations on its amplitude and phase. The level of the scattering is categorized as **strong** or **weak** depending on the level of phase variations in the detected signal. If the RMS phase difference over the transverse scales equal to the Fresnel scale ($R_f = \sqrt{\lambda r/2\pi}$) are small ($\ll 1\,\text{rad}$) then the scattering level is weak. The diffraction model is built as a sum of the effects of a series of **thin screens** between the source and the receiver.

If the RMS phase variation introduced in the wave front is large ($\gg 1\,\text{rad}$) then the scattering is considered as strong. In this case, the scattered waves do not add up constructively and therefore the effect on the received power is small. However, if the phase variation is small ($\ll 1\,\text{rad}$), the scattered waves add constructively and the fluctuations on the power are larger [138]. The spacecraft is a point-like source, therefore, the analysis of the data assumes that the scintillation is produced by strong scattering [139]

The power fluctuations are usually characterised by two terms: the RMS **power scintillation variation** (σ_{Sc}) and the **scintillation index** (m). σ_{Sc} is the integral within the scintillation band of the power scintillation and the scintillation index is the ratio of the RMS variation in the power of the radio signal caused by the IPS. On the other hand, the work presented in this study is based on the analysis of the phase fluctuations and not the power. Therefore, the **phase scintillation index** (σ_φ) defines the level of phase fluctuations of the spacecraft signal and m is estimated using the slope of the spectral power density of the phase fluctuations. This analysis is described in Section 6.2.3.

6.2   Materials and methods

The PRIDE team started systematic observations of the ESA Venus Express spacecraft with VLBI radio telescopes in 2009. The goal of the observations was to analyse the phase fluctuations of the spacecraft signal due to the propagation in the interplanetary plasma. The target on this campaign was to study the evolution of these phase fluctuations during a full Venus synodic period (see Section 6.2.1). Venus was at the farthest position with respect to the Earth in January 2010, and again in August

2011. The observations, conducted between 2009.11.26 and 2011.10.17, covered the entire synodic period of Venus around the Sun.

For an optimal analysis of the phase fluctuations, the radio telescopes must observe the spacecraft signal continuously during several hours on each epoch, as it was explained in Section 2.2. The spatial wave number of plasma inhomogeneities (Δ_0) and the average of the solar wind speed (V_{wave}) are taken into account to estimate the optimal observing time span. Assuming rough values of $\Delta_0 = 3 \cdot 10^6$ km and $V_{wave} = 400$ km s^{-1}, the optimal duration of the spacecraft session should be around 3 hours [9]. The phase fluctuations are the result of an average variation of the phase along the propagation in solar wind and not instantaneous measurements of fast/slow winds.

Observing and recording the spacecraft signal continuously during three hours is inconvenient and definitely imprudent. Firstly, the spacecraft may not transmit a data stream continuously during the whole observed time, the recording of the signal may break at some point during the session, or the transmitted signal may contain some phase jitter. Several of the mentioned problems occurred during most of the sessions in one/two scans out of seven. If the data were recorded continuously in a single scan, the post-analysis should take care of removing unwanted segments of the original data. Consequently, the complexity and the time-consumption of the analysis would increase. Shorter scans make the detection and the analysis more straightforward. Secondly, the radio telescope at X-band needs re-pointing of the target coordinates approximately every 30 minutes (assuming that the distance from spacecraft to the Earth is approximately 1-2 AU). If the spacecraft is at larger distances, the re-pointing of the antenna is probably not required.

In addition to the re-pointing, the system may require frequent checks of the performance of the receiver and calibration of the antenna. These routines are automatically performed by the Field System [116]. The system noise temperature (T$_{sys}$) is measured using a noise diode built into the receiver. It is recommended to verify frequently the T$_{sys}$ during the session. High values of the receiver noise may indicate bad behaviour of the antenna or the system. The calibration procedures are performed every ten to twenty minutes. Following these three constraints, the sessions were scheduled between 2 to 3 hours, segmenting the scans into six to nine 19-minute length each.

During the post-processing, we measured the phase scintillation index

of each scan and then we calculated the average. In some sessions we recorded only 2-3 valid scans. In that case, the results were analysed and compared with other observations conducted around the same epoch. The results of those sessions have been included in the global analysis, but it was kept in mind that they could introduce some undesired bias to the data. So far the results have been coherent.

6.2.1 Earth and Venus orbits

Venus is the closest planet to the Earth and the second brightest planetary body after the moon. Venus is the most similar planet to Earth in sense of the core structure, body size and gravity field. The atmosphere is thick and dense with carbon dioxide and sulphuric acid clouds [86]. Thus, several space missions have been launched in order to study the composition of the atmosphere. Venus orbits the Sun at an average distance of 0.72 AU and the sidereal period is 225 days. The closest distance between Earth and Venus is called the **minor conjunction** and the planet is approximately at 0.3 AU (40 million km). The farthest point is known as the **superior conjunction** and is at 1.7 AU from the Earth. The simple model of the orbit of both bodies is shown in Figure 6.1.
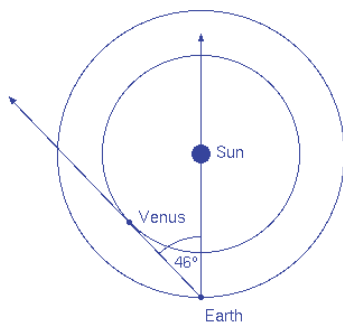
Figure 6.1. Orbits of Venus and Earth around the Sun. The angle between Earth-Venus-Sun is known as the solar elongation or Sun-Observer-Target (SOT).

The angle between the Sun and Venus viewed from the Earth is known as **solar elongation** or also Sun-Observer-Target (SOT). When the SOT equals to 0 degrees, the planet is located either in the superior or the minor conjunction. The **greatest elongation** is defined as the higher value of the solar elongation angle that a planet can achieve. For the case of Venus, this angle varies from $45°$ to $47°$. The synodic period is defined as the time interval that a planet reappears at the greatest elongation

in relation to the Sun and Earth. The Venus synodic period is 584 days. During our campaign, Venus crossed twice the superior conjunction: the first on 2010.01.02 and the second on 2011.08.15. The distances between Venus and Earth can be determined at any orbital position using simple trigonometry.

6.2.2   Set-up for the observations

The radio telescopes observed the VEX spacecraft during 2 or 3 hours. The epochs were carefully selected in order to combine the moment of maximum visibility of Venus and an active spacecraft radio communication link. As mentioned in Section 6.2, the sessions were divided into 19-minute scans to better understand the phase fluctuation of the signal.

We conducted almost 70 single-dish sessions and collected hundreds of hours of data between November 2009 and 2012. In the digital world, these sessions are equivalent to 5 TB (380 scans×17 GB scan) of raw data and 1 TB (380 scans×2 spectra×1.4 GB spectra) of processed spectra. The sessions were scheduled approximately every 2 weeks for a proper study of the phase scintillation with respect to the SOT angle. This ideal situation was not always possible due to the limited observing time at the radio telescopes.

The availability of the Metsähovi antenna and the S/X geodetic receiver is relatively limited. Several scientific projects are sharing the amount of antenna time. The time to change the receiver is another setback. Metsähovi focal point has room for only one receiver. Almost half a day is required to swap the receiver in use. Therefore, it is not practical to conduct a three-hour session just for one day. All our VEX sessions were conducted in conjunction with the regular IVS geodetic sessions [1], since we were able to use the telescope before and after their observations. The opportunities to observe were limited to 7 or 8 times per year.

However, we were able to raise the interest of several institutes and radio telescopes around Europe on this project. Most of this work is based on the results provided by the Metsähovi radio telescope, though, the valuable participation of all the other telescopes boosted enormously the scientific impact of this research. The list of the participant radio telescopes and the total amount of hours of observations is shown in Table 6.1. The

---

[1]http://ivscc.gsfc.nasa.gov/program/index.html

author was responsible for conducting the observations at Metsähovi and the data processing from all the radio telescopes.

Table 6.1. Summary of the radio telescopes used in the IPS analysis. Radio telescope, diameter of the dish and SEFD.

Station	Country	Dish (meters)	SEFD (Jy)
Metsähovi	FI	14	3200
Wettzell	GE	20	750
Yebes	SP	40	200
Medicina	IT	32	320
Matera	IT	20	3000
Noto	IT	32	770
Onsala	SW	20	2000
Pushchino	RU	22	1500
Hartebeeshoek	SA	22	700

We gathered almost 80 observations during these two years thanks to the cooperation of the participant stations. Statistically this means an average of one session every two weeks. However, no observations were conducted during the winter 2010. All sessions are listed in Table 6.2. The schedules for the sessions were provided by JIVE. We contacted directly the director of the station or the responsible person of the antenna operations for the scheduling of the sessions. In most of the cases, the other radio telescopes allowed us to observe once a month.

The number of scans observed at each station is summarised in the histogram of Figure 6.2. From the 380 scans, almost half were observed with Metsähovi (150). Wettzell was the second most used radio telescope with almost 100 scans. The other stations averaged between 20-40 scans each.

VLBI has a wide research community and several science groups coexist around the world (see Section 2.3.3). Therefore, not all the radio telescopes have the same data acquisition systems and the data is not always stored in the same format. The S/X receivers, the frequency bands, the baseband samplers, the data formatters and the recording systems are sometimes different among the radio telescopes. The first observations were mainly tests to obtain individual information of the specific hardware. They also helped to correct failures and errors both in the observation and in the data analysis. We improved significantly all the steps

Table 6.2. VEX sessions conducted between 2009 and 2012. The columns indicate epoch, station, start time, number of scans, scan duration [s], azimuth, elevation, solar elongation and distance to target.

Epoch	Sta	Time	Sc	d(s)	RA	Elev	SOT(°)	AU
27/08/09	Mh	08:00	6	1140	08 11 15.9	+19 48 00	33.41	1.30
28/08/09	Mh	07:00	6	1140	08 16 02.8	+19 35 59	33.19	1.30
13/10/09	Mc	10:00	7	1140	11 54 56.0	+02 10 18	22.15	1.54
13/10/09	Ma	10:00	7	1140	11 54 56.0	+02 10 18	22.15	1.54
04/11/09	Wz	10:00	1	1140	13 36 12.1	-08 27 08	16.68	1.61
16/11/09	Wz	08:30	3	1140	14 33 13.1	-13 45 11	13.72	1.64
17/11/09	Mh	08:30	7	1140	14 38 06.0	-14 09 58	13.47	1.64
18/11/09	Mh	08:30	6	1140	14 43 00.1	-14 34 23	13.20	1.65
20/11/09	Mh	08:30	5	1140	14 52 55.8	-15 22 27	12.73	1.65
26/11/09	Mc	08:45	5	1140	15 23 02.8	-17 36 02	11.24	1.66
26/11/09	Ma	08:45	4	1140	15 23 02.8	-17 36 02	11.24	1.66
26/11/09	Nt	08:45	6	1140	15 23 02.8	-17 36 02	11.24	1.66
26/11/09	Wz	08:45	5	1140	15 23 02.8	-17 36 02	11.24	1.66
14/12/09	Wz	10:20	4	1140	16 57 37.4	-22 24 13	6.82	1.69
15/12/09	Ys	09:40	5	1140	17 02 55.3	-22 34 43	6.58	1.69
21/12/09	Ys	10:00	6	1140	17 35 36.4	-23 20 29	5.14	1.70
21/12/09	Wz	10:00	6	1140	17 35 36.4	-23 20 29	5.14	1.70
04/01/10	Wz	10:00	3	1140	18 52 28.7	-23 27 29	1.87	1.70
16/01/10	Mh	09:00	4	1140	19 57 23.7	-21 41 12	1.45	1.71
17/01/10	Mh	09:00	3	1140	20 02 43.2	-21 27 55	1.65	1.71
18/01/10	Mh	09:00	4	1140	20 08 01.7	-21 13 59	1.86	1.71
25/01/10	Wz	10:00	6	1140	20 44 43.8	-19 19 36	3.45	1.70
25/01/10	Ys	10:00	2	1140	20 44 43.8	-19 19 36	3.45	1.70
01/02/10	Mc	10:00	6	1140	21 20 21.1	-16 56 59	5.09	1.70
02/02/10	Mh	10:00	2	1140	21 25 38.0	-16 33 27	5.34	1.70
04/02/10	Mh	10:00	6	1140	21 35 18.4	-15 48 44	5.80	1.70
11/02/10	Pu	10:00	2	1000	22 09 30.2	-12 54 45	7.46	1.69
12/02/10	Ys	10:00	7	1140	22 14 18.9	-12 28 23	7.70	1.69
16/02/10	Wz	11:00	7	1140	22 33 34.4	-10 38 38	8.66	1.68
25/02/10	Ys	11:00	5	1140	23 15 34.5	-06 18 59	10.81	1.67
26/02/10	Ys	11:00	5	1140	23 20 14.5	-05 48 44	11.05	1.67
01/03/10	Mh	14:00	1	1140	23 34 30.0	-04 14 58	11.80	1.66
02/03/10	Mh	13:00	1	1140	23 38 52.6	-03 45 58	12.03	1.66
04/03/10	Mh	09:00	2	1140	23 47 14.0	-02 49 51	12.47	1.66
21/03/10	Wz	10:30	6	1140	01 50 31.0	+10 47 37	19.04	1.58
17/05/10	Mh	12:00	6	1140	05 45 54.3	+24 50 58	30.49	1.37
18/05/10	Mh	12:00	10	1140	05 50 58.2	+24 54 25	30.71	1.37
03/07/10	Mh	11:00	5	1140	09 39 37.7	+15 47 48	40.67	1.05
04/07/10	Mh	11:00	5	1140	09 44 02.8	+15 23 38	40.85	1.05

Epoch	Sta	Time	Sc	d(s)	RA	Elev	SOT(°)	AU
06/07/10	Mh	11:00	18	1140	09 52 51.7	+14 33 53	41.22	1.03
23/08/10	Ys	12:00	5	840	12 55 49.1	-08 13 27	45.94	0.65
23/08/10	Mh	12:00	5	840	12 55 49.1	-08 13 27	45.94	0.65
23/08/10	Mc	12:00	5	840	12 55 49.1	-08 13 27	45.94	0.65
23/08/10	Pu	12:00	5	840	12 55 49.1	-08 13 27	45.94	0.65
30/08/10	On	12:00	8	1140	13 18 19.8	-11 21 32	45.53	0.60
23/09/10	Mh	12:00	4	1140	14 19 44.6	-20 03 50	39.43	0.42
21/03/11	Wz	09:00	6	1140	21 40 52.7	-14 15 30	37.48	1.19
22/03/11	Mh	09:00	5	1140	21 45 38.8	-13 54 48	37.28	1.19
25/03/11	Mh	08:40	4	1140	21 59 40.9	-12 51 14	36.66	1.21
25/03/11	On	08:40	5	1140	21 59 42.9	-12 51 05	36.66	1.21
25/03/11	Hh	08:40	0	1140	21 59 42.9	-12 51 05	36.66	1.21
26/03/11	Mh	09:00	6	1140	22 04 27.9	-12 28 42	36.45	1.22
26/03/11	Wz	09:00	6	1140	22 04 27.9	-12 28 42	36.45	1.22
27/03/11	Mh	08:00	10	1140	22 08 56.7	-12 07 12	36.25	1.23
27/03/11	Wz	08:00	7	1140	22 08 56.7	-12 07 12	36.25	1.23
31/03/11	On	08:00	0	1140	22 12 00.4	-12 00 03	36.05	1.25
18/04/11	Hh	09:00	6	1140	23 49 24.2	-02 44 39	31.40	1.36
18/04/11	Wz	09:00	6	1140	23 49 24.2	-02 44 39	31.40	1.36
21/04/11	Hh	09:00	5	1140	00 02 53.0	-01 21 22	30.70	1.38
21/04/11	Hh	09:00	5	1140	00 02 53.0	-01 21 22	30.70	1.38
23/04/11	Hh	09:00	6	1140	00 11 45.4	-00 26 02	30.24	1.39
23/04/11	Hh	09:00	6	1140	00 11 45.4	-00 26 02	30.24	1.39
03/05/11	Mh	09:20	5	1140	00 56 33.1	04 14 03	27.85	1.44
24/05/11	Mh	08:00	7	1140	02 32 41.7	13 25 57	22.65	1.44
26/05/11	Mh	09:00	3	1140	02 42 02.1	14 12 34	22.18	1.55
26/05/11	Hh	09:00	2	1140	02 42 02.1	14 12 34	22.18	1.55
26/05/11	Wz	09:00	3	1140	02 42 02.1	14 12 34	22.18	1.55
17/10/11	Wz	10:00	5	1140	14 30 44.1	-14 28 16	16.48	1.62
14/11/11	Wz	10:00	9	1140	16 53 37.8	-23 23 52	23.31	1.52
14/11/11	On	11:00	4	1140	16 53 37.8	-23 23 52	23.31	1.52
14/11/11	Mh	11:00	4	1140	16 53 37.8	-23 23 52	23.31	1.52
15/11/11	Mh	09:00	-	1140	17 51 40.8	-21 20 52	23.31	1.51

in the processing pipeline, from planning until results. Nowadays, most of the processes are almost automated, and the amount of errors are reduced.

The RF signal is filtered down to $8\,$MHz bandwidth, divided into four channels, 2-bit encoding for a total aggregate data sampling of $128\,$Mbps using the MarkIV formatter. Most of the participant telescopes used the standard Mark5A VLBI data acquisition system [33] or the PC-EVN [59]. Pushchino was the only station to observe one single channel with a band of $8\,$MHz and 8-bit precision. The Russian station samples and records
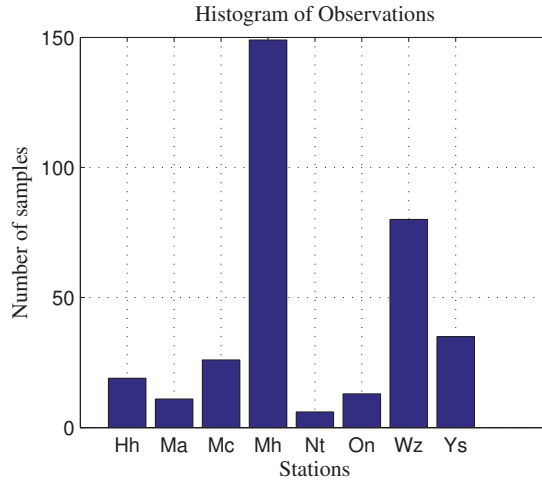
Figure 6.2. Number of scans collected during the VEX sessions per each radio telescopes. We gathered 380 scans during the last two years.

the data with the Japanese K5 system [140].

The data acquired at the telescopes were immediately transferred to the Metsähovi servers once the session was completed. Right now the processing grid consists of three computers that share the load of storing the large files into their RAID systems and performing the computational tasks. Furthermore, all the results have been uploaded to our public server[2]. The results are easily accessible worldwide and the operators are able to check the performance of their respective radio telescopes almost in real-time.

6.2.3   Data processing and analysis

The data processing starts by executing sequentially the three spacecraft tracking programs: the SWspec, the SCtracker and the digital PLL. This exclusive kit of software was already described in Section 5.4.1. The output bandwidth of the signal can be narrowed down as precise as required by interactively computing the spectra, detecting the carrier tone and post-filtering it.

SWspec processes a $8\,$MHz bandwidth channel using $3.2\,$million points for the FFT, integration time of 5 seconds and spectral resolution of $5\,$Hz. For VEX, the Doppler frequency variation is approximately $1\,$Hz every second, which means $1\,$kHz during the entire 19-minute scan. Therefore,

---

[2]http://abidal.metsahovi.fi/spectra/

a spectral resolution of $5\,\text{Hz}$ and 5 s is a good choice for detecting the spacecraft tone. If the tone is detected with a good SNR, in the order of 30 to $40\,\text{dB}$, the Doppler detection accuracy is in the order of $30\,\text{mHz}$.

SCtracker compensates the Doppler variation and locks the output signal around the carrier line. The initial bandwidth of $8\,\text{MHz}$ is filtered to the desired output bandwidth. For VEX, the signal band after the phase polynomial fit is set to $2\,\text{kHz}$, with a frequency change rate of $100\,\text{mHz}$ in 300 s.

The digital Phase-Locked-Loop (PLL) runs highly accurate iterations of the steps previously performed with SWspec and SCtracker. The spectra are computed on the $2\,\text{kHz}$ bandwidth, using typically 20 thousand FFT points with a spectral resolution of $0.2\,\text{Hz}$. The accuracy of the detected Doppler frequency depends of the SNR of the signal. For instance, the accuracy of sensitive antennas, such as Wettzell, Onsala and Medicina, is at the level of $1\text{-}2\,\text{mHz}$; Metsähovi and Hartebeeshoek at $3\text{-}5\,\text{mHz}$, and Pushchino at $10\,\text{mHz}$ at a spectral resolution of $0.2\,\text{Hz}$. The newly-generated phase polynomials track the main tone, lock it and narrow it down to the output bandwidth of $20\,\text{Hz}$. The output bandwidth is tunable and depends on the needs of the user. The final band is also determined by the statistical properties of the temporal behaviour of the phases. A bandwidth of $20\,\text{Hz}$ is enough for IPS studies. Such a narrow band allows us to discriminate the contribution of the system noise and plasma scintillation on the signal phase. A bandwidth of 5 or $1\,\text{Hz}$ will be required for precise tracking of spacecraft orbit.

The analysis of the phase fluctuations caused by the solar wind uses the data extracted from the spacecraft signal in a bandwidth of $20\,\text{Hz}$. The spectral power density is computed to characterise and differentiate the fluctuations on the phase due to the scintillation and the system noise. We perform a windowing and smoothing of the data with a cosine or cosine square window in order to calculate spectral power density. These spectra are computed per each of the 19-minute scan and then averaged. The resultant phase power spectrum characterises the fluctuations along the 2-hour session. If the session contains large amount of scans, i.e. larger than 10, the analysis is usually separated in two blocks. Although, almost no differences with the two parts were found in such cases.

The frequency boundaries that distinguish between the scintillation and the system noise band were decided by careful visual inspection. The

boundaries are mainly dependent on the level of the phase fluctuations of the signal. Typical limits of the scintillation and system noise bands were between $3\,$mHz and $3.003\,$Hz, and 6 and $9\,$Hz, respectively. We use the same bandwidth of $3\,$Hz in both cases for convenience.

Special considerations need to be taken into account when the position of the spacecraft is at a solar elongation near $0\,$degrees. In this case, the scintillation band extends to several Hz, since the phase is mainly dominated by the strong scintillation. The scintillation band of the spectrum shown in the upper plot of Figure 6.5 was set between $3\,$mHz and $10\,$Hz. The system noise also requires to be analysed using a wider bandwidth than usual. However, that is not possible if the tone is extracted with the typical $20\,$Hz bandwidth, therefore, the digital PLL is configured so that the output bandwidth is $100\,$Hz. The system noise is then evaluated using a bandwidth between 40 and $70\,$Hz. The standard deviation of the noise (σ_N) injected by the system in the phase is expressed in units of rad^2/Hz. The σ_N depends on the performance and sensitivity of each radio telescope and usually ranges from 10^{-03} to $10^{-05}\,$rad^2/Hz.

From the averaged phase power spectrum in logarithmic scale, we estimate the first-order polynomial (see Equation 6.1) fit to characterise the slope of the fluctuations. The linear fit is calculated exclusively within the part of the scintillation band, in which the spectrum follows a near-Kolmogorov slope. The lower limit depends on the length of the scan. If the scan contains 19 minute of data, the optimal lower boundary is $3\,$mHz ($\Delta T = 1/1140 \sim 1\,$mHz). The upper limit depends on the level noise and interplanetary scintillation. Therefore, the boundary is usually set after a first visual inspection. By default, the upper limit is set to $0.3\,$Hz.

$$L_\phi = a + m \cdot L_f \tag{6.1}$$

where L_ϕ is the average-windowed phase power spectrum, L_f the frequency in logarithm scale and m is the slope of the scintillation. The goodness of the approximation is verified by calculating the difference between the linear fit and phase power spectrum:

$$error = \frac{stdev(L_\phi - Fit)}{\max(L_f) - \min(L_f)} \tag{6.2}$$

where Fit is the linear fit, $\max(L_f)$ and $\min(L_f)$ are the boundaries of the slope. We tend to accept an error below 10%.

The **phase scintillation index** (σ_φ) is defined as the standard deviation of the signal phase within the scintillation band:

$$\sigma_\varphi = stdev(\phi_{Sc}) \qquad (6.3)$$

where ϕ_{Sc} is the phase fluctuations of the scan within the scintillation band. To calculate the coefficients (σ_φ) per each of the scans, first the linear fit is removed from the spectral power density, and then the data are filtered in order to isolate the contribution of the IPS. The standard deviation is then estimated from the resultant filtered phases.

6.3 Results

The spacecraft signal phases are stored in files after every VEX tracking session. The phases are saved in regular text format with 32-bit precision. Each file contains a column per each valid 1140-second scan, 34000 samples each yielding a time resolution of 33 milliseconds. Several examples of the residual phase obtained during the two years campaign are presented here to illustrate the variety of handled data. The first two examples of phase fluctuations at different level are shown in Figure 6.3.

The phase fluctuations were detected on two epochs separated by nearly 8 months. The y-axis scale in both images is the same to emphasise the difference between high and low levels of scintillations. The upper plot showed the results from the session observed on 2010.01.16 with the Metsähovi radio telescope. The spacecraft was at solar elongation of $1.5°$ and at a distance of 1.71 AU at the time of observations. The standard deviation of the phase fluctuations was 9.47 radians. Due to the high level of the fluctuations, the default band boundaries were increased to: 0.003 and 10 Hz for the scintillation band, and 40 and 70 Hz for the system noise band.

The lower panel in Figure 6.3 shows the results observed with the Onsala radio telescope on 2010.10.30. The target was at a solar elongation of $45.5°$ and at a distance of 0.6 AU. The standard deviation of the phase fluctuations was only 0.26 radians. Standard scintillation and system noise boundaries were used for the post-analysis. The levels of the fluctuations were 50 times lower than previously detected in January.

The phase fluctuations detected at Wettzell on 2011.04.18 are shown in Figure 6.4. The phases are primarily masked by strong level of RFI.
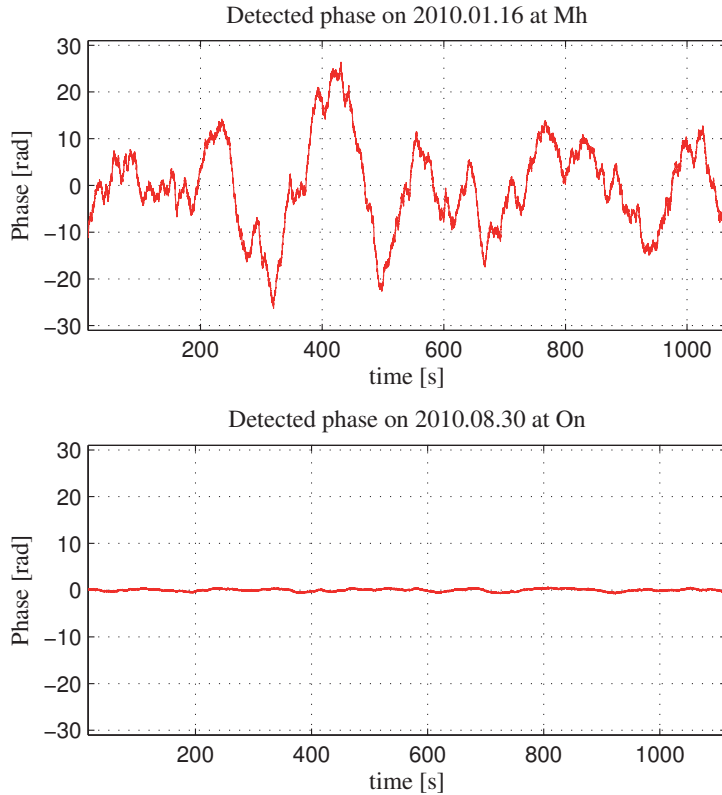
Figure 6.3. top: The level of phase fluctuations observed on 2010.01.16 at Metsähovi was high (SOT $\sim$ 1.5°). bottom: The fluctuations were about 50 times weaker when observed on 2010.10.30 at Onsala (SOT $\sim$ 45.5°).

Deeper into the analysis of this feature, we realised that it followed a certain sinusoidal pattern with a resonant oscillation frequency at 0.6 Hz. The RFI was caused by jitter noise originated at the local oscillator of the receiver. Replacing this component in the receiver solved the problem. This kind of RFI, with a known resonant frequency, is easy to filter away in the post-analysis for scintillation purposes.

The residual phases obtained in a multi-station session were compared in the Figure 5.50. The **em081a** session (see Section 5.4.3) was conducted using four VLBI radio telescopes on 2010.08.23: Yebes, Metsähovi, Medicina and Pushchino. Each scan was 15-minute long, slightly shorter than typical IPS scans. The phases detected with the three first stations were consistent and clean of RFI. Unfortunately, the noise dominated the data from Pushchino and the data were not useful for IPS analysis. To improve the visibility of the figure, we added $+4$ rad (Pushchino, in blue), $+2$ rad (Yebes, in red), 0 rad (Metsähovi, in cyan) and -2 rad (Medicina, in black).

Detected phase on 2011.04.18 at Wz
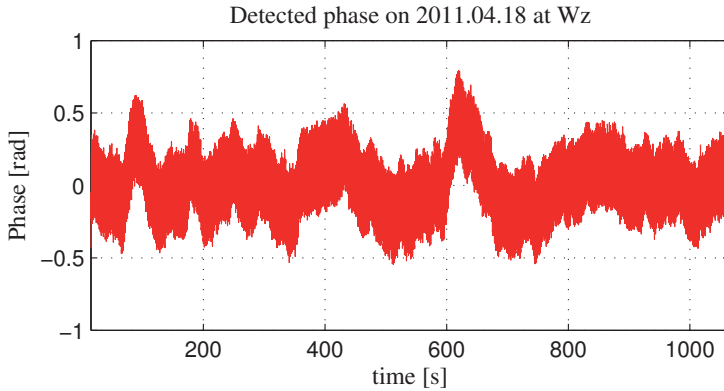
Figure 6.4. The phase fluctuations are masked by RFI. The session was observed on 2011.04.18 at Wz.

The phases showed consistent cross-correlation among the three other antennas. The data were partly correlated since the interplanetary media contribution was the same for the transmission up-link (Earth-to-spacecraft). The radio signal from the spacecraft took different paths, known as Fresnel channels, before arriving to each antenna on Earth. The phase difference detected at each radio telescope was caused exclusively by the IPS contribution in the down-link (spacecraft-to-Earth).

Sessions conducted simultaneously with multiple radio telescopes allow us to get precise information of the shared up-link. This contribution can then be cancelled from the detected phase at each telescope by subtracting from each scan the average phases from all stations. This procedure is crucial to adjust the optimal nodding cycle for the VLBI phase-referencing (see Section 5.3).

In order to characterise the level of the fluctuations, the spectral power density of the phases is computed per each scan. Several examples of the phase power spectra are shown in Figures 6.5 and 6.6. The examples in Figure 6.5 show a comparison of data acquired at different epochs by two antennas. We show the data from two different antennas in order to demonstrate that the scintillation analysis is not biased by the telescopes themselves. The phase power spectrum is an average of all spectra power density from each 19-minute scan observed on the same epoch. The behaviour of the spectra can be modelled by a first-order approximation in logarithmic scale. In the plots, the spectra is shown in blue and the linear-fits for the IPS and system noise in red.

The spectra shown in the upper plot were detected with the Metsähovi
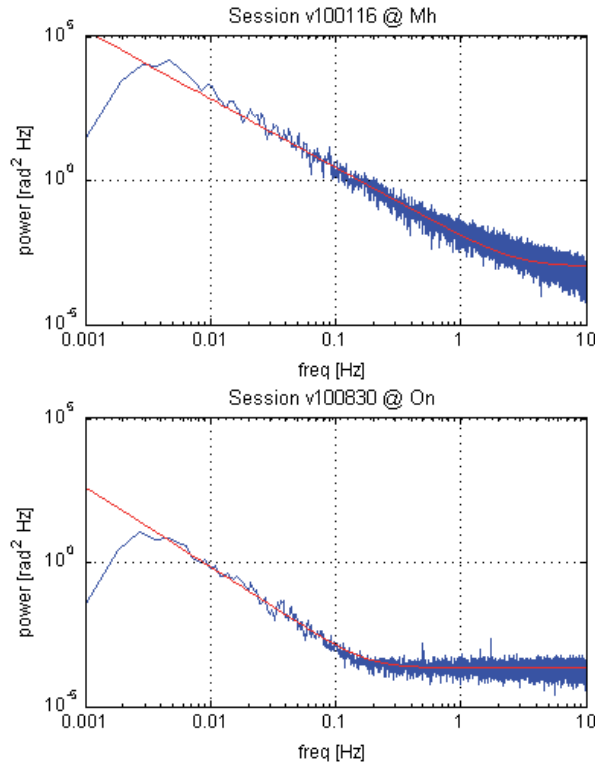
Figure 6.5. top: High-level of the phase fluctuations observed on 2010.01.16 at Mh. bottom: Low level of phase fluctuations observed on 2010.09.30 at On.

antenna on 2010.01.16. The spacecraft was at a solar elongation of $1.5°$ and at a distance of $1.7\,\mathrm{AU}$ at the time of observations. The planet was almost eclipsed by the Sun and therefore the radio waves propagated along a region extremely close to the hot star.

The effect of the solar wind on the radio waves is maximised at low SOT, since the spacecraft signal crosses the more dense region of the interplanetary plasma near the surface of the Sun. The phase fluctuations are 30 to 50 times larger than at wider angles. The spectral peak of the phase scintillation is at $8294\,\mathrm{rad^2/Hz}$.

The lower plot in Figure 6.5 illustrates the phase fluctuations when the spacecraft is located at a large solar elongation. We conducted this session on 2010.09.30 with the Onsala antenna. Venus was at a solar elongation of $45.5°$ and at a distance of $0.6\,\mathrm{AU}$. The peak of the phase scintillation spectrum had a density power of $8\,\mathrm{rad^2/Hz}$. Nine months elapsed between the two sessions displayed. The spectral peak was thousand times weaker than the first analysis. These examples were the same as presented in

Figure 6.3. The spacecraft radio waves were barely affected by the solar wind when the spacecraft was at the maximum solar elongation, (for Venus is $47°$).
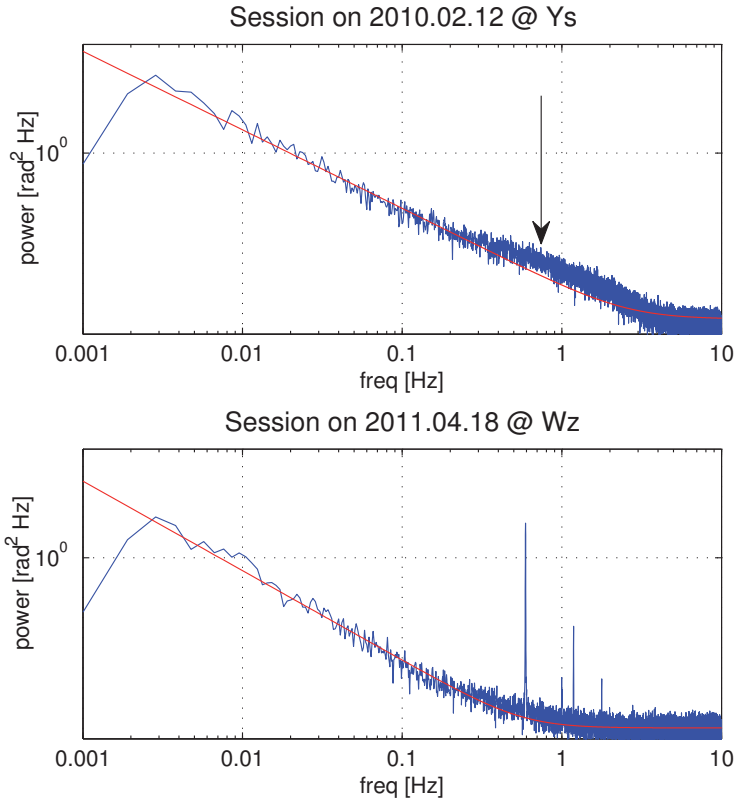
Figure 6.6. top: Strange $1\,\mathrm{Hz}$ bump that appears in the fluctuations spectra observed on 2010.02.12 at Ys. bottom: The phase was masked by RFI centred at $0.6\,\mathrm{Hz}$ frequency observed on 2011.04.18 at Wz.

An unexpected feature can be seen in the phase power spectrum in the upper panel of Figure 6.6. The session was conducted on 2010.02.12 at Yebes. This **bump** appeared in the phase spectra of several sessions. This bump was centred at a frequency of $1.5\,\mathrm{Hz}$ and had an approximate bandwidth of $2\,\mathrm{Hz}$. The data were smoothed with a Hann window to reduce the noise and show the bump clearer. The range of the spectral powers of the bump was 10 to 100 times bigger than the system noise. The origin of this bump is still uncertain. However, our hypothesis focus on intrinsic problems on the electronics: the cryogenic cooling pump (with a resonant cycle of $1.5\,\mathrm{Hz}$), jitter related to the Hydrogen-maser signal or any other component within the receiver.

The lower plot of Figure 6.6 shows a strong interference noise in the

phase power spectrum. The residual phase of this experiment (2011.04.18 at Wettzell) was already presented in the upper panel of Figure 6.4. The RFI is clearly identifiable in the spectral domain with a singular peak at the frequency of 0.6 Hz. A broken local oscillator in the S/X receiver added the extra noise in the phase. Simultaneous multi-station observations confirmed that the error could be caused by the spacecraft radio signal itself.

The spectral power density is well represented by a near Kolmogorov spectrum [129]. That is why, the power phase spectrum are also known as Kolmogorov spectrum. The Kolmogorov slope is in the order of $k^{-5/3}$. The phase power spectrum is approximated using a first-polynomial fit in logarithmic scale. The criteria to select the boundaries of the scintillation slope were described in Section 6.2.3. The upper limit depends on the amount scintillation and the system noise. The author determined the best upper limit in each case by visual inspection of the spectrum. This upper boundary can range from 0.1 Hz (see Figure 6.5 lower plot) to several Hz (see Figure 6.5 upper plot). The slope of the phase power spectrum were stored for further post-analysis after each session.

Scintillation slope

We compared the slope of the phase power spectra extracted from all the sessions during the last two years of observations. The Figure 6.7 shows the scintillation slope as a function of time. Each red circle denotes a value of the slope and they are sorted in the chronological order of the observations (x-axis). The blue lines represent the standard deviations of the samples.

Most the scintillation slope values within the scintillation band are comprised between -2.8 and -2.0. The arithmetic mean of the slope samples is equal to -2.418 and with a standard deviation of 0.25. Moreover, in most of the cases the slope values are within the range of -2.18 and -2.67.

The scintillation slope values can also be interpreted as a function of the solar elongation at the time of the observations. The solar elongation provides a more intuitive way to relate the position of the planets and the trajectory of the radio waves in the Solar System before arriving to Earth. The slope of the phase power spectrum with respect to the solar elongation is illustrated in Figure 6.8.
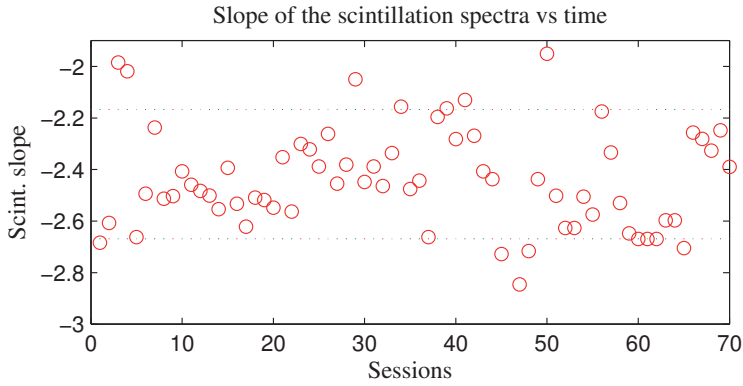
Figure 6.7. Slopes of the phase power spectra with respect to the sessions, sorted in chronological order. The mean value of the scintillation slope was -2.418 and a standard deviation of 0.25.
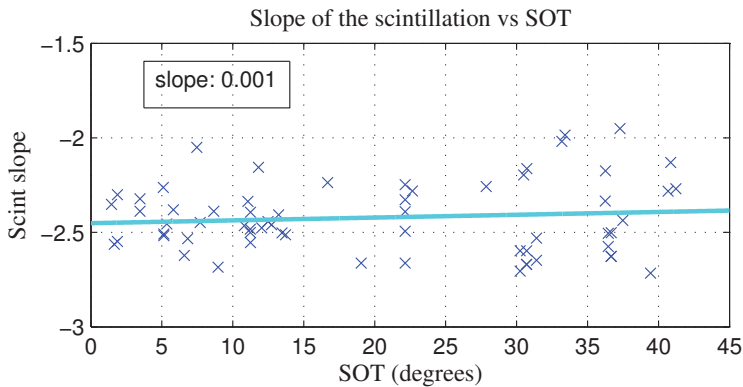
Figure 6.8. Slopes of the phase scintillation spectra as a function of the solar elongation. The linear fit, which characterises all the scattered samples, has a slope equal to 0.001.

A first-order polynomial approximation was used to evaluated the scintillation spectra slope as a function of the solar elongation. The linear fit between 0 to 45 degrees was completely flat (~ 0.001). Based on the data analysed, we can state that the slope of the phase fluctuations spectrum does not depend on the solar elongation or the scale of the variations. The slope values were coherent and consistent along all the research, independently on the solar elongation and distance to Earth at the time of the observations.

The standard deviation of the slope values seems much greater at larger solar elongations. These samples are seen at the top-right corner in Figure 6.8 with slope values near -2. The possible explanations for this high

dispersion at large solar elongations were narrowed down to two possibilities. The first consideration is that the results and the accuracy of the detected phases may be biased by the ground-based telescope. The size of the parabolic dish and its sensitivity is usually different on each EVN antenna. Our VEX observations were conducted with a broad range of radio telescopes. Therefore, the results were analysed at different ecliptic latitudes, dish-sizes, system temperature of the receivers, and signal processing hardware. This range of scenarios were all taken into account for our study.

The second possibility is related to the propagation media. The interplanetary plasma presents higher inhomogeneity at farther distances to the Sun than at closer ones. The inhomogeneity of the plasma causes random variations of the phase on the radio waves. Therefore, the dispersion of the scintillation slopes may be higher when the spacecraft is located at a wide solar elongation.

In order to investigate the effect of the radio telescopes in our data, the scintillation results were separated based on the antenna used. The number of samples was large enough for comparison but not for definitive conclusions. Furthermore, most of the radio telescopes had data only from two or three sessions. Therefore, the scintillation slope results were categorized according to the amount of observations carried out and the performance of the antennas. The first group included the data acquired at Metsähovi. The second group arranged the data acquired with sensitive antennas and with sufficient amount of samples. The last group combined the data from the rest of stations. The slope values of the phase power spectra as a function of the solar elongation taking into account the radio telescope used are shown in Figure 6.9. The scintillation slopes are marked in red for Metsähovi; in blue for Yebes, Wettzell and Onsala; and in black for the other stations.

Metsähovi encompassed almost half of the data observed. 35% of the observations were conducted with Yebes, Wettzell and Onsala radio telescopes. The rest of stations contributed with the last 15% of the sessions.

The scintillation slope for Metsähovi have a tendency to be larger at wider solar elongation. The linear fit that characterises its samples has a slope of 0.005. Inversely, the slope values for the second group tend to decrease at larger SOT angles. The linear fit for this group has a slope of -0.005 and a standard deviation of 0.3. One possible cause of this
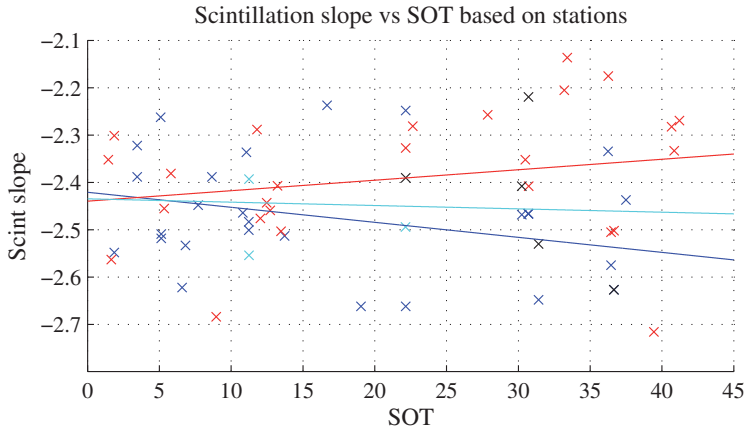
Figure 6.9. Slopes of the scintillation spectra as a function of the solar elongation, distributing the samples between three major groups: Mh (in red); Ys, Wz and On (in blue); and the rest of antennas (in black).

high scattering on Metsähovi data is that the antenna always observed at much lower elevations than other antennas. This could be then related to the effect of the auroral oval of the Earth. Due to the limited amount of samples we do not dare to make any statements whether the high dispersion is related to the antenna. Additional observations near the maximum solar elongation will allow us to determine this phenomena.

The second cause of the high dispersion could be caused by the propagation media. We decided to investigate it using two different methods: observing VEX with more than one antenna on the same epoch and using the same antenna in several consecutive epochs. This close examination was useful for Metsähovi, since at several epochs the results showed higher slope values than expected.

Two slightly different examples are highlighted here. Metsähovi and Wettzell observed simultaneously the VEX spacecraft on 2011.03.27 for a couple of hours. The phase scintillation measured from the six recorded scans had a mean slope of -2.175 and -2.334, respectively. The spectral peak of the power density at $3\,\mathrm{mHz}$ was approximately $2\,\mathrm{rad}^2/\mathrm{Hz}$ in both cases. However, the scintillation band was larger at Wettzell than at Metsähovi, being the main difference the level of system noise of the receivers. The system noise for Metsähovi and Wettzell was $0.15 \cdot 10^{-04}$ and $0.11 \cdot 10^{-04}\ \mathrm{rad}^2/\mathrm{Hz}$, correspondingly. Thus, the difference between their scintillation slopes is associated to the higher system noise of Metsähovi.

The other method consisted of comparing the results obtained with the

same antenna for two consecutive days. The Metsähovi radio telescope observed the VEX spacecraft consecutively on 2011.03.26 and 2011.03.27. The atmospheric conditions were good on both days with just few scattered clouds. The system noise on the 26th was $0.09 \cdot 10^{-04}$ rad^2/Hz and slightly worst on the following day, $0.15 \cdot 10^{-04}$ rad^2/Hz. The scintillation slopes were -2.505 and -2.175, respectively. Apparently, similar observing conditions provided different noise on the system and different slope on the scintillation.

Phase scintillation index

The phase scintillation index (σ_φ) is estimated from the temporal evolution of the phase of the signal in each 19-minute scan. The signal is filtered to eliminate part of the injected noise by the receiver system. The scintillation band, as described in Section 6.2.3, is by default between 3 mHz to 3.003 Hz. The standard deviation is then evaluated from the filtered phases.

The scintillation slope defined the phase power spectrum for the whole session. Instead, the σ_φ values are retrieved from each 19-minute scans. Usually, six σ_φ values are retrieved from each session. These indexes helped to characterise the level of fluctuations caused by the solar wind. The σ_φ were usually consistent during the entire session. The results obtained during the last 2 years of observations are plotted in Figure 6.10.
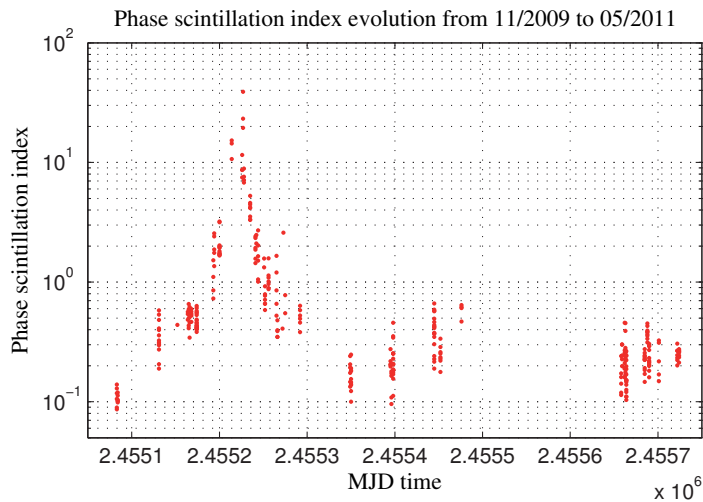
Figure 6.10. σ_φ retrieved from each scan during the two years of observations. σ_φ directly depends of the solar elongation.

At a first glance, we note a direct dependency of the σ_φ with the orbit of Venus around the Sun. As mentioned before, one of the goals of the project was to cover a full Venusian synodic period. It started at the beginning of 2010 and ended at the ends of summer 2011. The peak occurred approximately on the 2455200 MJD time (January 2010). This relationship is highlighted when the σ_φ are plotted as a function of the solar elongation, as shown in Figure 6.11.
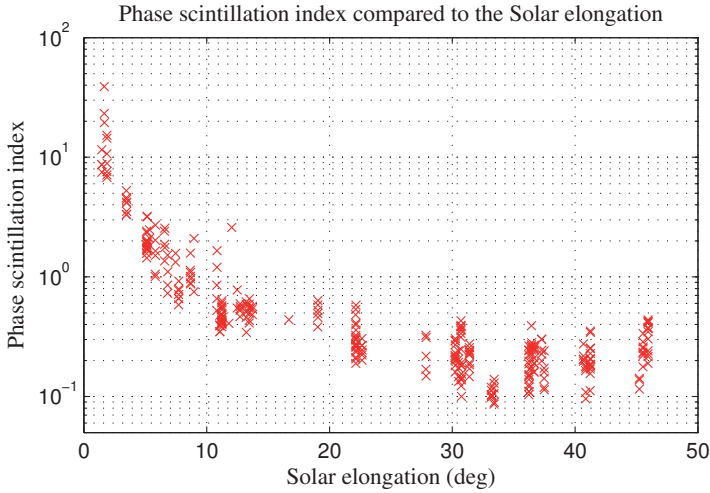
Figure 6.11. Phase scintillation index with respect to the solar elongation. Data include observations from the last two years.

The peak of the σ_φ occurs when the spacecraft is at a solar elongation near 0 degrees and the indexes value drastically increase. That is expected because the spacecraft radio waves propagate through regions close to the Sun, where the interaction between the transmitted signal and the interplanetary plasma is maximised. When the spacecraft is at the maximum solar elongation, in the case of Venus $46.5°$, the σ_φ values are around 0.10. The rest of the samples are distributed following approximately an inverse logarithmic curve. The relation between the σ_φ and the electron content in the solar wind can be extrapolated from Figure 6.11.

Next step was to determine the relation between the phase scintillation index and the theoretic plasma density along the line of sight. The best approximation was to superimpose the σ_φ and the Total Electron Content (TEC) with respect to the distance to the target and the solar elongation.

The electron density is inversely proportional to the square distance with respect to the Sun, and can be estimated as a function of the trajec-

tory. Thus, the TEC can be simulated as a function of the solar elongation. The electron density of the interplanetary plasma can be simplified to (see Section 2.2.2):

$$n(r) = n_0 \cdot \left(\frac{r_0}{r}\right)^2 \; [m^{-3}] \tag{6.4}$$

where $n(r)$ is the electron density at any point (x,y) in the interplanetary medium, r is the distance from that point with respect to the Sun, n_0 is the nominal electron density at a distance r_0. For convenience, the n_0 is approximated to 5 electrons cm^{-3} at a distance equal to 1 AU [141]. The electron density is usually expressed in particles m^{-3}.

The TEC along the path spacecraft-Earth can be estimated as the integral of the electron density for all the points in the trajectory:

$$TEC = \frac{1}{tecu} \int_0^{VEX} n(r(l)) \cdot dl \tag{6.5}$$

where $tecu$ is the electron content unit (10^{16} electrons/m^2) and $n(r(l))$ is the electron density of any point in the path length with respect to the Sun. The simulated TEC for a spacecraft transmitting from Venus or Mars to the Earth is seen in Figure 6.12.
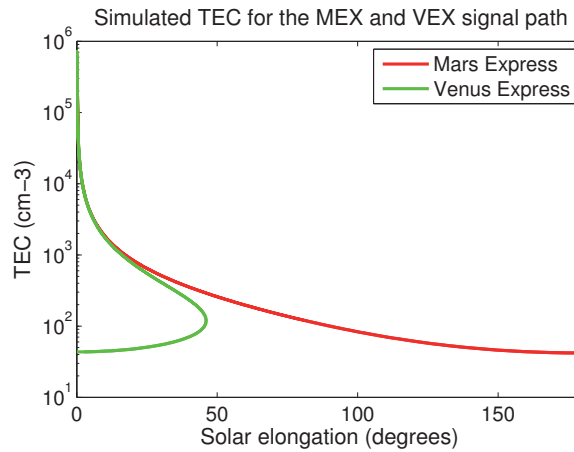
Figure 6.12. The simulated Total Electron Content with respect of the SOT for a spacecraft signal transmitted from Venus or Mars.

The illustration shows the simulated values of TEC at any orbital point along the orbit of both planets and the Earth around the Sun. Mars has been included in the plot, since the team is interested to conduct similar IPS studies from spacecraft orbiting the red planet. In the case of Venus,

the minimum value of the TEC is obtained when Venus is located at minor conjunction (between the Sun and the Earth). The distance from Venus to Earth is 0.28 AU and 0.72 AU towards the Sun. The TEC at the minor conjunction point is approximately 43.50 electrons cm^{-3}. On the other hand, near the major conjunction, the distance to the Earth is 1.72 AU and the electron content average is $7.16 \cdot 10^{05}$ electrons cm^{-3}. In the case of Mars, at the minor conjunction the distance betweens the planet and the Earth and the Sun are 0.6 AU and 1.6 AU, respectively. The TEC corresponds to 41.9 and $4.85 \cdot 10^{05}$ electrons cm^{-3} when is at the minor and major conjunctions.

The Figure 6.11 resembles to the simulated TEC for Venus shown in Figure 6.12. Hence, our aim was to superimpose the phase scintillation index with the simulated values of the TEC as a function of the solar elongation. The projection of the measured σ_φ coefficients and the simulated TEC is shown in Figure 6.13. All σ_φ values have been normalised ($\times 2000$) to match the curves. The TEC values are shown, in cyan, a certain margin offset was added (1.5 times), in dark blue, to account for errors and variations in the TEC.
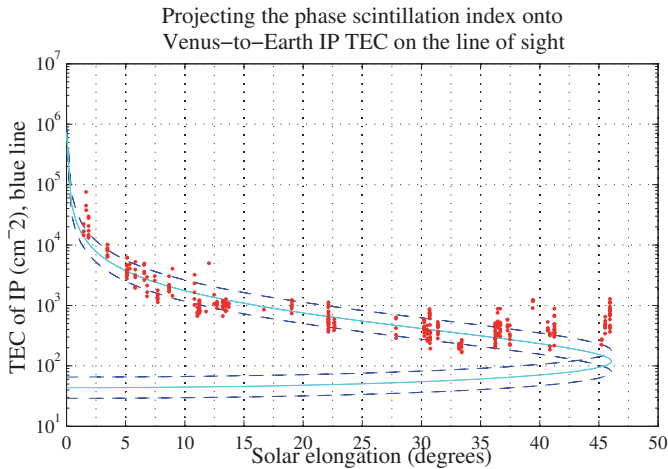
Figure 6.13. Superimposition of the σ_φ and the simulated TEC (cyan) along the line of sight Venus - Earth. In dark blue, the TEC line has been multiplied by ± 1.5. The σ_φ values have been normalised to match with the TEC.

The standard deviation of the difference between the simulated TEC and the σ_φ is 0.3. At this point, we think that the main contributor to the dispersion at wide solar elongations is the ionosphere. At closer distances of Venus with respect the Sun, the contribution of the ionosphere and interplanetary plasma are similar. We calculated the estimated TEC

of the ionosphere along the line of sight, according to procedure described at [10]. The TEC for the ionosphere was added to the TEC of the propagation path in the Solar System:

$$TEC_T = TEC_{ip} + TEC_{ion} \qquad (6.6)$$

The standard deviation of the difference between the simulated TEC and the σ_φ, including the contribution of the ionosphere, is now 0.281. The improvement by taking into account the ionosphere TEC is about 6.38%.

Another method to look the σ_φ with respect of the Sun is in logarithmic scale, as shown in the upper panel of Figure 6.14.
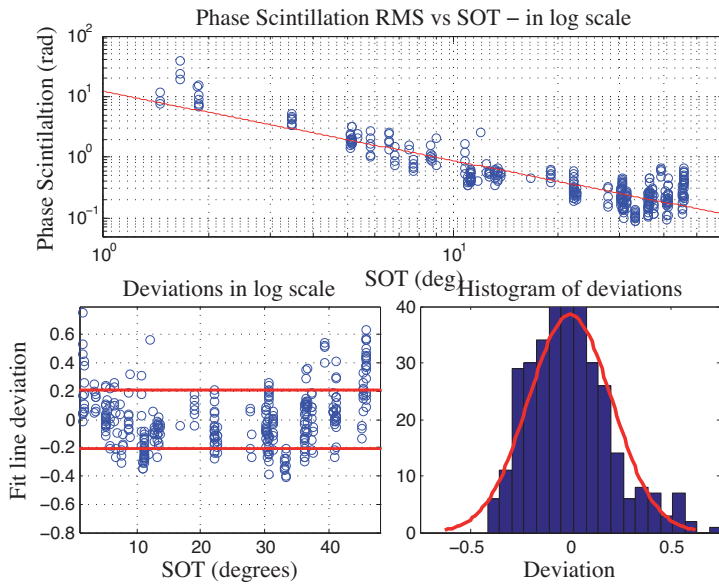
Figure 6.14. top: Phase scintillation RMS with respect to the SOT in the logarithmic scale. The slope of the linear fit is -1.135. bottom-left: Deviations of the samples. bottom-right: Histogram of the deviations.

The σ_φ can be approximated by a first-order linear fit with a slope equal to -1.135. The σ_φ peak at a solar elongation close to 0 is $12\,\mathrm{rad}^2/\mathrm{Hz}$. The bottom-left panel in Figure 6.14 shows the deviation of the samples from the linear fit in logarithm scale. The deviation of the samples with respect to the linear fit is ± 0.2. The samples that show higher dispersion were observed either at low or high solar elongations. The bottom-right panel in Figure 6.14 shows the histogram of the deviations. Most of the samples are included in the 0.2 boundaries and the histogram of deviations resembles a Gaussian distribution.

IPS study applied to coherent VLBI phase-referencing

This chapter has covered the effect of the solar wind on the propagation of a spacecraft radio signal in the Solar System. This study has shown the relation between the phase scintillation index and the Total Electron Content as a function of the solar elongation and the distance with respect to the Earth. The study has been conducted using a spacecraft at the Venus orbit. The role of this analysis is extremely important for future approaches of better determination of the state vectors of a spacecraft. Indeed, the optimal nodding cycle required for tracking spacecraft using VLBI phase-referencing can be estimated from the study presented here at any solar elongation.

The amount of phase scintillation is calculated by integrating the Kolmogorov spectrum within certain predefined frequency boundaries:

$$\Omega_{Sc} = \left[\int_{f_0}^{f_{max}} D(f_0) \cdot \left(\frac{f}{f_0} \right)^m \delta f \right]^{1/2} \tag{6.7}$$

where m is the slope of the spectrum, $D(f_0)$ is the spectral power density at f_0, f_0 and f_{max} are the lower and higher frequencies boundaries. The higher limit is known beforehand and depends on the amount of scintillation at certain solar elongation and on the system noise of the radio telescope. The lower limit also depends primarily on the duration of the scans for phase-referencing (nodding cycle):

$$f_0 = \frac{1}{\tau} \tag{6.8}$$

where τ is the duration of the scan. Therefore, the nodding cycle for phase referencing is selected in order to accept a reasonable amount of scintillation in the signal and a relative fast switching between the reference source and the target. Three phase scintillation spectra are compared in Figure 6.15.

It shows the 3 Kolmogorov spectra observed at Wettzell on 2010.01.25, 2010.03.31 and 2011.10.17. The area between the boundaries (f_{max} and f_0) indicates the amount of phase scintillation in each session. The frequency edges have been selected in order to have the same amount of scintillation in each case. The principal parameters of this phase scintillation analysis are summarised in Table 6.3.
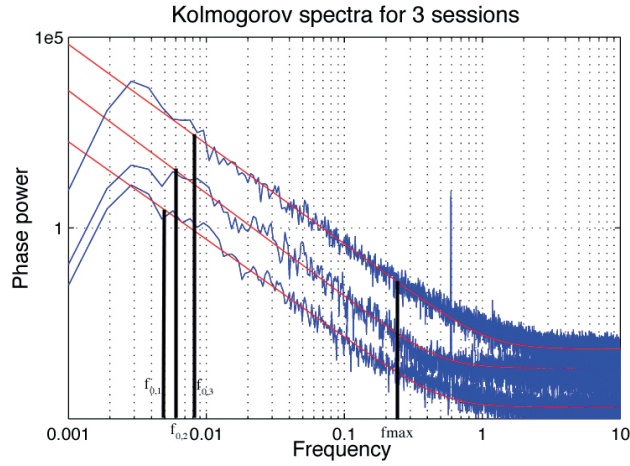
Figure 6.15. Three Kolmogorov spectra observed at Wz. The spectra were correspondingly observed on 2010.01.25, 2010.03.31 and 2011.11.17. Note the different amount phase scintillation in each spectrum.

Table 6.3. Properties of the phase scintillation spectra. The observations were carried out at Wettzell on 2010.01.25, 2010.03.31 and 2011.10.17.

Parameter	2010.01.25	2010.03.31	2011.10.17
Spectra slope	-2.32	-2.60	-2.29
RMS phase scint. [rad$^2\cdot$Hz]	3.72	0.38	0.31
System noise [rad$^2\cdot$Hz]	$0.46\cdot10^{-4}$	$0.19\cdot10^{-4}$	$0.27\cdot10^{-4}$
Freq$_{max}$ [Hz]	0.40	0.40	0.40

By selecting a certain amount of tolerable scintillation in our data, we can predict the optimal nodding cycle for any epoch depending on the solar elongation. The case showed in Figure 6.15 is an hypothetical example. In this case, the nodding cycle would vary between 100 and 200 s, for the best and worst case, respectively.

6.3.1 Kolmogorov simulation

The results in Section 6.3 demonstrated that the phase fluctuations spectra of the spacecraft signal followed a near-Kolmogorov behaviour. In this section a Kolmogorov turbulence model is simulated in order to compare the results with the ones obtained from the interplanetary plasma medium. For this simulation we construct a partial map of the solar wind filled by heterogeneous **bubbles**. The structure for the interplanetary medium is illustrated in Figure 6.16.
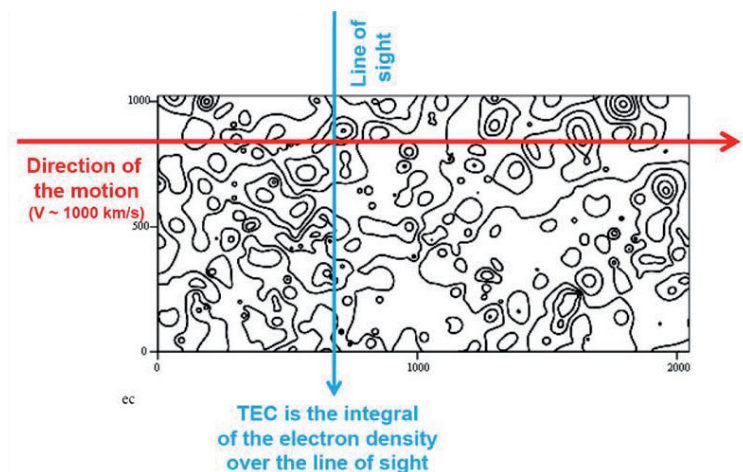
Figure 6.16. Distribution of the electron content in the solar wind region. The region assumes 100 km pixels. A number of fluctuation bubbles with certain statistical properties have been placed onto the grid.

The simulation represents a map of the distribution of the electron content with an area of 1024×2048 pixels of the sky. The pixel size is arbitrarily set to $100\,\mathrm{km}$, which corresponds to the size of the Fresnel channel. To represent the electron content, a number of fluctuation bubbles with certain statistical properties were placed onto the grid.

The x-axis represents the direction of propagation of the solar wind and the y-axis is the direction of propagation of the spacecraft radio wave. We assume that the spacecraft signal propagates in the direction y-axis downwards and the solar wind is moving radially outwards (left-to-right). The average speed of the solar wind is approximately $1000\,\mathrm{km\ s^{-1}}$ [131]. The TEC is measured as the integral of the electron density along the line of sight.

For the distribution of the electron content, we generate a multi-bubble model that fills the propagation medium of the spacecraft signal. We assume a multi-modal Gaussian distribution based on bubble statistics in order to approximate the system to the Kolmogorov statistics. The simulation intends to ensemble bubbles with a Kolmogorov distribution with different sizes assuming that a Kolmogorov ensemble can be approximated by the sum of several Gaussian ensembles.

The positions of the bubbles in the grid are uniformly distributed, with a variable radius and several peak density. The electron density distribution within a bubble follows a Gaussian distribution. For each distribution component we can play with the number of bubbles (Nb) in the pipe, the

radius of the bubble (r_b) in km, the coordinates (x_b) and (y_b) in km on the map and the amplitude (A_b) of an electron content (in units cm^{-3}).

The distribution of the bubbles follows a Kolmogorov distribution ($k = -5/3$) as shown in Figure 6.17. The bubbles distribution was built calculating the histogram of the samples (bins).
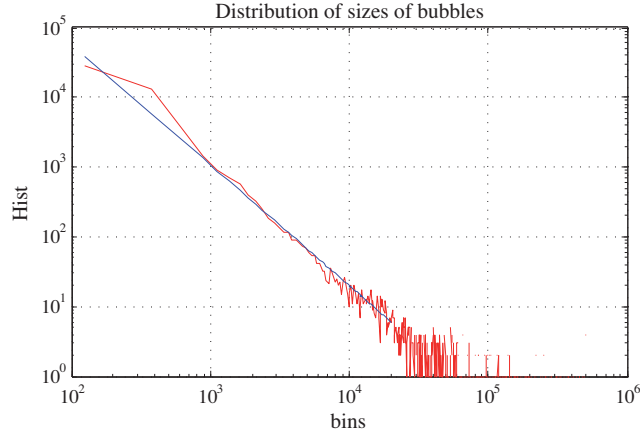
Figure 6.17. Kolmogorov distribution of the bubbles in the region simulated.

Using this distribution, we estimate the TEC for the line of sight as:

$$TEC = \frac{\sqrt{2\pi}}{tecu} \cdot \sum_{jb} \left[A_b \cdot r_b \cdot exp \left(\frac{-(x_b - x)^2}{2 \cdot (r_b)^2} \right) \right] \tag{6.9}$$

the TEC is measured in km cm^{-3}. The TEC values are converted into phase scintillation indexes and the power phase spectrum is evaluated as in the observations. The phase power spectrum is shown in Figure 6.18.

This simulation mimics well with the results achieved with the VEX observations. This simulation presents a slope equal to -3.138. The simulated power phase spectrum has a slightly steeper slope than the results collected from the observations. For a more precise simulation the grid should be as large as the distance between the Earth and the spacecraft.

6.4 Conclusions and discussion

In this chapter, the interplanetary scintillation retrieved from the spacecraft phase fluctuations were presented. Such long-term investigation of the phase fluctuations of the spacecraft signal is unique and unprecedented. A model that directly estimates the phase scintillation index and
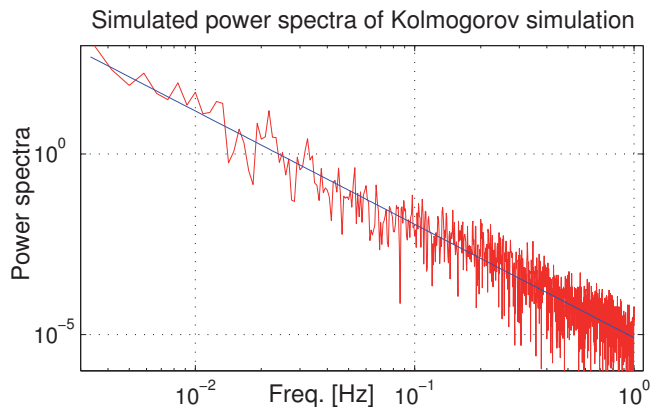
Figure 6.18. Spectral power density for a Kolmogorov distributed medium. The slope of the phase scintillation was -3.138.

the Total Electron Content as a function of the solar elongation and distance to the Earth was built.

VLBI tracking of planetary spacecraft missions may benefit from the results presented in this chapter. Spacecraft state vectors estimates with VLBI phase-referencing requires, among others, an optimal nodding cycle between the spacecraft and the reference source. The nodding cycle is optimised according to the amount of phase fluctuations. The phase scintillation depend on several parameters that are not easily quantifiable (solar activity, turbulence of the media), and on intrinsic parameters that are constrained by the observations (solar elongation, distance to the target, radio telescope). The last three have been widely studied here and the amount of fluctuations at any epoch can be anticipated. The estimate of the scintillation index helps for an optimal selection of the nodding cycling for VLBI tracking observations.

Finally, the phase of the radio waves are affected by the interplanetary medium during the propagation of the signal in directions, up- and downlinks. The phases detected simultaneously with multiple radio telescopes are partly correlated, since the contribution of the solar wind is the same for all phases for the uplink. Thus, the differences between the phases are caused exclusively by the downlink. Observing with VLBI and multi-station mode allow us to correct the scintillation caused in the uplink and the nodding cycle for phase-referencing depends only on the downlink. It would be desirable to conduct a similar study using spacecraft as Mars Express in view of future deep space missions.

7. Conclusions and future work

This thesis presents a new method to investigate several physical phenomena in our Solar System using VLBI radio telescopes. The idea is to use the existing 14-metre dish telescope and the VLBI data acquisition system to observe spectral signatures of planetary elements, cosmic radio sources and planetary spacecraft. Five scientific projects lay the foundation for this work and demonstrate the multiple uses of the software, hardware and firmware developed during the last years.

The first three cases focus on studying the spectral signatures of the planets and satellites of the Solar System. Observations of Saturn, Venus and Mars at several radio frequency bands and with the on-purpose software spectrometer were included. The water maser search in the Kronian system was the project that successfully demonstrated water evidence in one of the moons of Saturn. The search for carbon-chain molecules and lightning storms did not reveal any significant detection. However, they served to improve the capabilities of the processing software and improved the methodology of the observations.

After the development of the on-purpose multi-tone spacecraft tracking software, routine sessions observing several planetary spacecraft were initiated. During this time a lot of work has been conducted to debug the processing pipeline and to adjust the settings for different scenarios of spacecraft tracking. All these tests have helped to create a robust software package that is compatible with most of the radio telescopes in the VLBI network and that is adjustable to detect any spacecraft signal at any radio frequency. Several space agencies have included our techniques in their research plan for future deep missions. The original plan was to conduct precise VLBI tracking and Doppler noise estimates of Phobos-Soil mission in summer 2012. Unfortunately, the mission failed moments after its launch.

The narrow band spacecraft software works as a stand-alone application to determine amplitude and phase information of the spacecraft signal. We plan to integrate these tools into the new software correlator developed at JIVE. It will improve the automation of the processes and the quality and quickness to obtain the results.

Estimation of the spacecraft state vectors using VLBI phase-referencing requires an optimal nodding cycle between the spacecraft and the reference source. The rule of thumb for this nodding cycle is the faster the better. However, it is conditioned by the slewing speed and sensitivity of the antenna, the system noise temperature, the ionosphere and the interplanetary scintillations. The phase scintillations limit the determination of the state vectors and therefore this thorough study of phase scintillation index as a function of solar elongation and distance to the target will benefit the next spacecraft tracking sessions.

Furthermore, this unique long-term research of the phase scintillations has contributed to build a model of the scintillation index and the Total Electron Content as function of the position of Venus. Previous analyses of the scintillation index were based on amplitude scintillation rather than phase scintillation. We presented an innovative method using the stable and well-known radio signal of spacecraft. Meantime, observations of VEX and MEX spacecraft will continue during 2012 aiming to complement the interplanetary scintillations analysis from Venus and Mars.

Bibliography

[1] D. J. E. Ingram. *Radio and microwave spectroscopy*. Published by Wiley, 1978.

[2] G. W. Chantry, editor. *Modern aspects of microwave spectroscopy*. Published by Academic Press, a subsidiary of Harcourt Brace Jovanovich, New York, 1979.

[3] S. Montebugnoli, C. Bortolotti, S. Buttaccio, A. Cattani, N. D'Amico, G. Grueff, A. Maccaferri, G. Maccaferri, A. Orfei, M. Roma, G. Tuccari, and M. Tugnoli. A new high resolution digital spectrometer for radioastronomy applications. *Review of Scientific Instruments*, 67:365–370, February 1996.

[4] V. Strelnitski. Masers, lasers and the interstellar medium. *Astrophysics and Space Science*, 252:279–287, 1997.

[5] H. Weaver, D. R. W. Williams, N. H. Dieter, and W. T. Lum. Observations of a strong unidentified microwave line and of emission from the OH molecule. *Nature*, 208:29–31, October 1965.

[6] K. Rohlfs and T. L. Wilson. *Tools of radio astronomy*. 4th rev. Berlin: Springer, 2004.

[7] S. J. Franke and C. H. Liu. Observations and modeling of multi-frequency VHF and GHz scintillations in the equatorial region. *J. Geophys. Res.*, 88:7075–7085, September 1983.

[8] S. J. Franke, C. H. Liu, and J. P. McClure. Interpretation and modeling of quasiperiodic diffraction patterns observed in equatorial VHF scintillation due to plasma bubbles. *J. Geophys. Res.*, 89:10891–10902, December 1984.

[9] O. I. Yakovlev. *Space radio science*. translated from the Russian by Nikolai and Olga Golovchenko. London ; New York, NY: Taylor & Francis, Earth Space Institute book series; v. 8, 2002.

[10] D. A. Duev, S. V. Pogrebenko, and G. Molera Calvés. A tropospheric signal delay model for radio astronomical observations. *Astronomy Reports*, 55:1008–1015, 2011.

[11] M. A. Kolosov and A. V. Shabel'Nikov. Refraction of electromagnetic waves in the atmospheres of the Earth, Venus and Mars. *Moscow Izdatel Sovetskoe Radio*, 1976.

[12] D. J. Mullan. *Physics of the Sun: A first course*. published by Chapman and Hall/CRC, 2009.

[13] K. Saito, A. I. Poland, and R. H. Munro. A study of the background corona near solar minimum. *Solar Phys.*, 55:121–134, November 1977.

[14] J. V. Hollweg. Solar coronal effects on pulsar signals. *Nature*, 220:771–772, November 1968.

[15] S. J. Goldstein and D. D. Meisel. Observations of the Crab pulsar during an occultation by the solar corona. *Nature*, 224:349–350, October 1969.

[16] D. O. Muhleman, P. B. Esposito, and J. D. Anderson. The electron density profile of the outer corona and the interplanetary medium from Mariner-6 and Mariner-7 time-delay measurements. *Astrophys. J.*, 211:943–957, February 1977.

[17] C. M. Ho, D. D. Morabito, and R. Woo. Solar corona effects on angle of arrival fluctuations for microwave telecommunication links during superior solar conjunction. *Radio Science*, 43:2003, March 2008.

[18] N. A. Lotova and A. A. Rukhadze. The nature of the irregular structure of the interplanetary plasma. *Soviet Astronomy*, 12:271, October 1968.

[19] R. Buckley. Fluctuations in the interplanetary plasma. *Planetary Space Science*, 19:421, May 1971.

[20] R. Bruno and V. Carbone. The solar wind as a turbulence laboratory. *Living Reviews in Solar Physics*, September 2005.

[21] W. A. Coles. Interplanetary scintillation. *Space Sci. Rev.*, 21:411–425, February 1978.

[22] R. Woo. Multifrequency techniques for studying interplanetary scintillations. *Astrophys. J.*, 201:238–248, October 1975.

[23] R. Woo, F.-C. Yang, K. W. Yip, and W. B. Kendall. Measurements of large-scale density fluctuations in the solar wind using dual-frequency phase scintillations. *Astrophys. J.*, 210:568–574, December 1976.

[24] R. Woo and J. W. Armstrong. Spacecraft radio scattering observations of the power spectrum of electron density fluctuations in the solar wind. *J. Geophys. Res.*, 84:7288–7296, December 1979.

[25] M. A. Kolosov, A. V. Sokolov, and O. I. Yakovlev. Investigation of radiowave propagation in the solar system. *IEEE Transactions on Antennas and Propagation*, 27:18–22, 1979.

[26] M. Ryle, F. G. Smith, and B. Elsmore. A preliminary survey of the radio stars in the Northern Hemisphere. *Monthly Notices of the RAS*, 110:508, 1950.

[27] T. Cornwell. Imaging Concepts. In J. A. Zensus, P. J. Diamond, & P. J. Napier, editor, *Very Long Baseline Interferometry and the VLBA*, volume 82 of *Astronomical Society of the Pacific Conference Series*, page 39, 1995.

[28] R. F. Burke and F. Graham-Smith. *An introduction to radio astronomy. Cambridge U Press,*, volume 117. October 1997.

[29] A. R. Thompson. Fundamentals of radio interferometry. In G. B. Taylor, C. L. Carilli, & R. A. Perley, editor, *Synthesis imaging in radio astronomy II*, volume 180 of *Astronomical Society of the Pacific Conference Series*, page 11, 1999.

[30] R. N. Bracewell. Radio interferometry of discrete sources. *Proc. IRE*, pages 97–105, 1958.

[31] J. M. Wrobel and R. C. Walker. Sensitivity. In G. B. Taylor, C. L. Carilli, & R. A. Perley, editor, *Synthesis imaging in radio astronomy II*, volume 180 of *Astronomical Society of the Pacific Conference Series*, page 171, 1999.

[32] M. Felli and R. E. Spencer. *Very Long Baseline Interferometry - techniques and applications*, volume 99. Kluwer Ac. Pub., 1989.

[33] A. R. Whitney. Mark 5 Disc-Based Gbps VLBI Data System. In *International VLBI Service for Geodesy and Astrometry: General Meeting Proceedings*, page 132, May 2002.

[34] J. Ritakari and A. Mujunen. Gbit/s VLBI and eVLBI with Off-The-Shelf Components. In N. R. Vandenberg & K. D. Baver, editor, *International VLBI Service for Geodesy and Astrometry 2004 General Meeting Proceedings*, page 182, June 2004.

[35] J. F. Wagner. Eight Gbps streaming between two VLBI radio telescopes. Presented at 7th International e-VLBI Workshop, Shanghai, China, 2008.

[36] EXPReS project. Home page. http://www.expres-eu.org, 2010. [Online; accessed 19-July-2011].

[37] NEXPReS project. Home page. http://www.nexpres.eu, 2012. [Online; accessed 19-July-2011].

[38] S. Matsuzaka, S. Kurihara, M. Sekido, T. Hobiger, R. Haas, J. Ritakari, and Wagner J. Ultra rapid dUT1 experiments on Japan-Fennoscandian baselines - application to 24-hour session. In *Proceedings of the 6th IVS General Meeting, Hobart, Australia*, pages 143–14, 2010.

[39] R. Haas, M. Sekido, T. Hobiger, T. Kondo, S. Kurihara, D. Tanimoto, K. Kokado, J. Wagner, J. Ritakari, and Mujunen A. Ultra-rapid dut1-observations with e-vlbi. *Artificial Satellites*, 45(2):75–79, 2010.

[40] Wikipedia. Time corretion dUT1. http://en.wikipedia.org/wiki/DUT1. [Online; accessed August 2011].

[41] The 24 hours experiment of e-VLBI in 2009. http://www.expres-eu.org/iya2009/. [Online; Accessed August 2011].

[42] The 100 hours of radio astronomy session in 2009. http://www.100hoursofastronomy.org/. [Online; accessed August 2011].

[43] G. Tuccari. DBBC - a wide band Digital Base Band Converter. In N. R. Vandenberg & K. D. Baver, editor, *International VLBI Service for Geodesy and Astrometry 2004 General Meeting Proceedings*, page 234, June 2004.

[44] G. Tuccari, W. Alef, A. Bertarini, S. Buttaccio, D. Graham, G. Nicotra, A. Roy, and M. Wunderlich. DBBC development status. In A. Finkelstein & D. Behrend, editor, *Measuring the Future, Proceedings of the Fifth IVS, held in St. Petersburg, Russia, ISBN 978-5-02-025332-2*, page 376, July 2008.

[45] NRAO. ROACH Digital Back End (RDBE). `http://www.vlba.nrao.edu/astro/obstatus/current/`, 2011. [Online; accessed August 2011].

[46] H. Takeuchi, M. Kimura, J. Nakajima, T. Kondo, Y. Koyama, R. Ichikawa, M. Sekido, and E. Kawai. Development of a 4 Gbps multifunctional Very Long Baseline Interferometry Data Acquisition System. *Publications of the ASP*, 118:1739–1748, December 2006.

[47] M. Sekido, N. Kawaguchi, Y. Koyama, M. Kimura, T. Kondo, H. Takiguchi, T. Hobiger, K. Takefuji, T. Ikeda, S. Shimojo, T. Oyama, H. Harai, T. Hara, Y. Kono, S. Kurihara, K. Kokado, D. Tanimoto, K. Nozawa, H. Takeuchi, H. Uose, K. Fujisawa, and H. Takaba. e-VLBI Activities in Japan. Presented at 8th International e-VLBI Workshop, 2009.

[48] VLBI Standard Interface. `http://www.vlbi.org/vsi/`. [Online; Accessed September 2011].

[49] A. R. Whitney, M. Kettenis, C. Phillips, and M. Sekido. VLBI Data Interchange Format. In G. Bourda, P. Charlot, & A. Collioud, editor, 19th *European VLBI for Geodesy and Astrometry Working Meeting*, pages 156–160, September 2009.

[50] C. Phillips. e-VLBI scientific benefits. `ftp://ftp.atnf.csiro.au/`. [Online; Accessed May 2011].

[51] G. Molera Calvés, J. Wagner, J. Ritakari, and A. Mujunen. European 4 Gbps VLBI and e-VLBI. Presented at 8th International e-VLBI Workshop, 2009.

[52] J. Wagner. Tsunami UDP Protocol. `http://tsunami-udp.sourceforge.net/`. [Online; Accessed September 2011].

[53] J. Wagner and G. Molera Calvés. Set of software tools for VLBI and e-VLBI purposes. `http://www.metsahovi.fi/en/vlbi/`, 2009. [Online; Accessed August 2011].

[54] J. Wagner and G. Molera Calvés. Metsähovi 10 Gbit/s e-VLBI data aquisition documents. `http://www.metsahovi.fi/en/vlbi/10gbps`, 2010. [Online; Accessed August 2011].

[55] A. Mujunen and J. Ritakari. Using VSIB test software. `http://www.metsahovi.fi/en/vlbi/boards/`, 2004. [Online; Accessed August 2010].

[56] Filesystems comparison on Debian Etch - Debian Administrator. `http://www.debian-administration.org/articles/388`, 2006. [Online; Accessed August 2011].

[57] Wikipedia. Redundant Array of Independent Disks (RAID). `http://en.wikipedia.org/wiki/RAID`. [Online; Accessed March 2011].

[58] J. Ritakari. Funet network rate more than 8 Gbps, Metsähovi Radio Observatory sets world record. http://www.csc.fi/english/csc/news/news/funet_metsahovi, 2008. [Online; Accessed August 2011].

[59] S. Parsley, S. Pogrebenko, A. Mujunen, and J. Ritakari. PCEVN. In Y. C. Minh, editor, *Astronomical Society of the Pacific Conference Series*, volume 306, page 145, 2003.

[60] C. Ruszczyk. Mark 5C software development program. In A. Finkelstein & D. Behrend, editor, *Measuring the Future, Proceedings of the Fifth IVS, held in St. Petersburg. ISBN 978-5-02-025332-2*, page 395, July 2008.

[61] G. Molera Calvés. Comparing frequency synthesizer boards for iBOB designs. http://www.metsahovi.fi/en/vlbi/ibob/CompareSynth.pdf, 2007. [Online: Accessed August 2011].

[62] CASPER wiki. Reconfigurable Open Architecture Computing Hardware. http://casper.berkeley.edu/wiki/ROACH, 2010. [Online: Accessed July 2011].

[63] Square Kilometre Array (SKA) official web page. http://www.ska.ac.za/newsletter/print.php. [Online: Accessed July 2011].

[64] J. Wagner, G. Molera, and M. Uunila. High bandwidth data acquisition and network streaming in VLBI. In Franco Davoli, Norbert Meyer, Roberto Pugliese, and Sandro Zappatore, editors, *Proceedings of the Instrumenting the Grid (InGrid) Workshop*, pages 363–374. Springer US ISBN: 978-1-4419-5597-5, 2010.

[65] CASPER wiki. A 1 GHz - 1024 channel wideband spectrometer. http://casper.berkeley.edu/wiki/, 2009. [Online: Accessed July 2011].

[66] D. E. Gary, Z. Liu, and G. M. Nita. A wideband spectrometer with RFI detection. *Publications of the ASP*, 122:560–572, May 2010.

[67] 10 GbE tutorial for FPGA boards. http://casper.berkeley.edu/wiki/Tutorial$_$10GbE, 2009. [Online: Accessed July 2011].

[68] J. Wagner. iBob wideband IF streaming and VDIF utilities. http://www.metsahovi.fi/en/vlbi/ibob/ibobSampler, 2009. [Online: Accessed August 2011].

[69] S. V. Pogrebenko, L. I. Gurvits, M. Elitzur, C. B. Cosmovici, I. M. Avruch, S. Montebugnoli, E. Salerno, S. Pluchino, G. Maccaferri, A. Mujunen, J. Ritakari, J. Wagner, G. Molera, and M. Uunila. Water masers in the Saturnian system. *A & A*, 494:L1–L4, February 2009.

[70] C. Ruf, N. O. Renno, J. F. Kok, E. Bandelier, M. J. Sander, S. Gross, L. Skjerve, and B. Cantor. Emission of non-thermal microwave radiation by a Martian dust storm. *Geophys. Res. Lett.*, 36:13202, July 2009.

[71] G. Molera Calves, S. V. Pogrebenko, J. Wagner, G. Cimo, L. I. Gurvits, M. Perez-Ayúcar, M. Paetzold, T. Morley, P. de Vicente, and G. Kronschanbl. VLBI and Doppler tracking of the VEX and MEX spacecraft and future Martian missions. Presented at European Planetary Science Congress, September 2010.

[72] G. M. Nita, D. E. Gary, Z. Liu, G. J. Hurford, and S. M. White. Radio Frequency Interference excision using spectral-domain statistics. *Publications of the ASP*, 119:805–827, July 2007.

[73] D. R. Williams. Planetary Fact Sheet. NASA Archives, 2006. [Online: Retrieved August 2011].

[74] C. J. Hansen, L. Esposito, A. I. F. Stewart, J. Colwell, A. Hendrix, W. Pryor, D. Shemansky, and R. West. Enceladus' water vapor plume. *Science*, 311:1422–1425, March 2006.

[75] S. V. Pogrebenko. First results of the First EVN VLBI Practice Run on the Smart-1. Presented at Cassini PSG meeting, Nantes, France, June 2006.

[76] J. Wagner and G. Molera Calvés. Evaluation of new high-performance spectrometer and spacecraft tracking software. 2008.

[77] S. V. Pogrebenko, J Wagner, and G et al. Molera Calv'es. Software spectrometer developments at Metsahovi Radio Observatory and JIVE. Presented at 7th Radionet Engineering Forum, Bonn Digital Backend Implementation: Software vs Hardware, NA4-EN-SU-020, June 2008.

[78] T. L. Wilson, K. Rohlfs, and S. Hüttemeister. *Tools of radio astronomy*. Published by Springer-Verlag, Berlin, Germany. ISBN 978-3-540-85121-9, 2009.

[79] J. D. Giorgini, D. K. Yeomans, and A. B. Chamberlin. Ephemeris database. `http://ssd.jpl.nasa.gov/horizons.cgi`, 1996.

[80] Online cosmic sources database for radio astronomy (SIMBAD). `http://simbad.u-strasbg.fr/simbad/`. [Online; Accessed July 2009].

[81] M. S. Reid. *Low-Noise Systems in the Deep Space Network*. Published by John Wiley & Sons, Inc, Hoboken, NJ USA. ISBN 978-0-470-40228-3., 2008.

[82] J. Wagner and G. Molera Calvés. Instructions set-up for the software spectrometer and test data. `http://www.metsahovi.fi/en/vlbi/spec/swspectrometer`, 2008. [Online; Accessed August 2011].

[83] J. Wagner. CellSpe-Tasklib: source code and user guide of the Software Spectrometer. `http://cellspe-tasklib.sourceforge.net/`, 2008. [Online; Accessed September 2011].

[84] S. V. et al. Pogrebenko. VLBI tracking of the Huygens probe in the atmosphere of Titan. Presented at the International Workshop of Planetary Probe Atmospheric Entry and Descent Trajectory Analysis and Science, Portugal, October 2003.

[85] E. E. Lekht. Total-flux variability of the H_2O maser emission in W75N. *Astronomy Letters*, 20:395–397, May 1994.

[86] I. de Pater and J. J. Lissauer. *Planetary sciences*. pp. 544. ISBN 0521482194 Cambridge University Press, December 2001.

[87] N. Kaifu, H. Suzuki, M. Ohishi, T. Miyaji, I. Ishikawa, T. Kasuga, M. Morimoto, and S. Saito. Detection of intense unidentified lines in TMC-1. *Astrophys. J.l*, 317:L111–L114, June 1987.

[88] Y. Hirahara, H. Suzuki, S. Yamamoto, K. Kawaguchi, N. Kaifu, M. Ohishi, S. Takano, S.-I. Ishikawa, and A. Masuda. Mapping observations of sulfur-containing carbon-chain molecules in Taurus Molecular Cloud 1 (TMC-1). *Astrophys. J.*, 394:539–551, August 1992.

[89] N. O. Renno, A. Wong, S. K. Atreya, I. de Pater, and M. Roos-Serote. Electrical discharges and broadband radio emission by Martian dust devils and dust storms. *AGU Fall Meeting Abstracts*, page C459, December 2003.

[90] N. O. Renno and J. F. Kok. *Electrical activity and dust lifting on Earth, Mars, and beyond*, page 419. 2008.

[91] C. S. Ruf, S. M. Gross, and S. Misra. RFI detection and mitigation for microwave radiometry with an agile digital detector. *IEEE Transactions on Geoscience and Remote Sensing*, 44:694–706, March 2006.

[92] Wikipedia. Spectral Kurtosis. http://en.wikipedia.org/wiki/Kurtosis. [Online; Accessed August 2011].

[93] R. D. de Roo, S. . Misra, and C. S. Ruf. Sensitivity of the Kurtosis statistic as a detector of pulsed sinusoidal RFI. *IEEE Transactions on Geoscience and Remote Sensing*, 45:1938–1946, July 2007.

[94] R. A. Preston, C. E. Hildebrand, G. H. Purcell, J. Ellis, C. T. Stelzried, S. G. Finley, R. Z. Sagdeev, V. M. Linkin, V. V. Kerzhanovich, V. I. Altunin, L. R. Kogan, V. I. Kostenko, L. I. Matveenko, S. V. Pogrebenko, I. A. Strukov, E. L. Akim, Y. N. Alexandrov, N. A. Armand, R. N. Bakitko, A. S. Vyshlov, A. F. Bogomolov, Y. N. Gorchankov, A. S. Selivanov, N. M. Ivanov, V. F. Tichonov, J. E. Blamont, L. Boloh, G. Laurans, A. Boischot, F. Biraud, A. Ortega-Molina, C. Rosolen, and G. Petit. Determination of Venus winds by ground-based radio tracking of the VEGA balloons. *Science*, 231:1414–1416, March 1986.

[95] J.-P. Lebreton, O. Witasse, C. Sollazzo, T. Blancquaert, P. Couzin, A.-M. Schipper, J. B. Jones, D. L. Matson, L. I. Gurvits, D. H. Atkinson, B. Kazeminejad, and M. Pérez-Ayúcar. An overview of the descent and landing of the Huygens probe on Titan. *Nature*, 438:758–764, December 2005.

[96] M. K. Bird, M. Allison, S. W. Asmar, D. H. Atkinson, I. M. Avruch, R. Dutta-Roy, Y. Dzierma, P. Edenhofer, W. M. Folkner, L. I. Gurvits, D. V. Johnston, D. Plettemeier, S. V. Pogrebenko, R. A. Preston, and G. L. Tyler. The vertical profile of winds on Titan. *Nature*, 438:800–802, December 2005.

[97] D. L. Jones, E. Fomalont, V. Dhawan, Jon Romney, W. M. Folkner, G. Lanyi, J. Border, and R. A. Jacobson. Very long baseline array astrometric observations of the cassini spacecraft at saturn. *The Astronomical Journal*, 141(2):29, 2011.

[98] H. Takeuchi, S. Horiuchi, C. Phillips, P. Edwards, J. McCallum, S. Ellingsen, J. Dickey, R. Ichikawa, K. Takefuji, T. Yamaguchi, S. Kurihara, B. Ichikawa, M. Yoshikawa, A. Tomiki, H. Sawada, and P. Jinsong. VLBI tracking of the solar sail mission IKAROS. Presented at XXXth URSI General Assembly and Scientific Symposium, August 2011.

[99] G. Molera Calvés, J. Wagner, S. V. Pogrebenko, L. I. Gurvits, G. Cimo, M. Perez Ayucar, G. Maccaferri, P. de Vicente, G. Kronschnabl, F. Schilliro, G. Colucci, and A. Smirnov. Venus Express spacecraft observations with EVN radio telescopes. Presented at Interplanetary Probe Workshop (IPPW-7), Barcelona, Spain, June 2010.

[100] C. L. Thornton and J. S Border. Radiometric Tracking Techniques for Deep-Space Navigation. Deep Space Communication Series, JPL Publication, 2000.

[101] A. J. Beasley and J. E. Conway. VLBI Phase-Referencing. In J. A. Zensus, P. J. Diamond, & P. J. Napier, editor, *Very Long Baseline Interferometry and the VLBA*, volume 82 of *Astronomical Society of the Pacific Conference Series*, page 327, 1995.

[102] S. W. Asmar. Characteristic trends of ultrastable oscillators for radio science Experiments. *Telecommunications and Data Acquisition Progress Report*, 129:1–5, January 1997.

[103] S. Remus. An introduction to the radio science experiments. `www.rssd.esa.int/SD/ESACFACULTY/docs/seminars/291009_Remus.pdf`, 2009. [ESA's lecture talk].

[104] A. Whitney, M. Kettenis, C. Phillips, and M. Sekido. VLBI Data Interchange Format (VDIF). Presented at 8th International e-VLBI Workshop, 2009.

[105] W. Brisken. C libraries for reading Mark IV formatted data. `http://www.nrao.edu`. [Online; Accessed February 2010].

[106] Wikipedia. Hann Window function. `http://en.wikipedia.org/wiki/Hann_function`. [Online: Accessed September 2011].

[107] J. Wagner, S. V. Pogrebenko, and G. Molera Calvés. Phase Calibration extraction, 2011. in preparation.

[108] S. V. Pogrebenko, J. Wagner, and G. Molera Calves. Evaluation of new high performance spectrometer and spacecraft tracking software. Presented at 8th FP6 Radionet workshop, Yebes, 2008.

[109] M. Kettenis, A. Keimpema, D. Small, and D. Marchal. e-VLBI with the SFXC correlator. Presented at 8th International e-VLBI Workshop, 2009.

[110] K. A. Kempeima, D. A. Duev, S. V. Pogrebenko, and G. Molera Calvés. Spacecraft tracking with the SFXC software correlator. Presented at URSI-Benelux, ESTEC, The Netherlands, June 2011.

[111] D. D. McCarthy and G. Petit. *IERS Conventions (2003)*. IERS Technical Note 32 at the IERS Convention, 2003.

[112] M. Sekido and T. Fukushima. A VLBI delay model for radio sources at a finite distance. *Journal of Geodesy*, 80:137–149, June 2006.

[113] Wikipedia. Method of numerical iteration of Newton and Raphson. `http://en.wikipedia.org/wiki/Newton_method`. [Online; Accessed August 2011].

[114] J. Boehm and H. Schuh. Vienna mapping functions in VLBI analyses. *Geophys. Res. Lett.*, 31:1603, January 2004.

[115] R. C. Walker. The SCHED user manual. NRAO user guide. [Online; Accessed October 2011].

[116] E. Himwich. MarkIV Field System documentation. `http://lupus.gsfc.nasa.gov/fsdoc/fshome.html`, 1997. [Online user guide; Accessed August 2011].

[117] J. Wagner. User space file system for Conduant StreamStor, Sourceforge source code. `http://fusemk5a.sourceforge.net/`, 2008.

[118] A. T. Deller, S. J. Tingay, M. Bailes, and C. West. DiFX: A Software Correlator for Very Long Baseline Interferometry using multiprocessor computing environments. *Proceedings of the ASP*, 119:318–336, March 2007.

[119] C. Haslett. *Essentials of radio wave propagation*. Cambridge University Press, New York, NY, USA, 1st edition, 2008.

[120] The AIPS cookbook developed at NRAO. `http://www.aips.nrao.edu/cook.html`. [Online; Accessed August 2011].

[121] CalTech VLBI analysis program. `http://www.astro.caltech.edu/~tjp/citvlb/vlbhelp/citvlb.html`. [Online; Accessed August 2011].

[122] V. Tornatore, R. Haas, G. Maccaferri, S. Casey, S. V. Pogrebenko, Molera G., and Duev D. Tracking of GLONASS satellites by VLBI radio telescopes. Presented at 5th ESA Workshop on Tracking, Telemetry and Command Systems for Space Application, 2010.

[123] V. Tornatore, R. Haas, S. Casey, S. V. Pogrebenko, Molera Calvés G., Duev D., and Keimpema A. Single baseline GLONASS observations with VLBI: preliminary results. Presented at PoS of the 20th EVGA Meeting and 12th Analysis Workshop MPIFR, Bonn, March 2011.

[124] V. Tornatore, R. Haas, S. Casey, S. V. Pogrebenko, Molera Calvés G., and Duev D. Determination of GLONASS satellite coordinates with respect to natural radio sources using the VLBI technique: preliminary results. Presented at 5th ESA Workshop on Tracking, PoS of Telemetry and Command Systems for Space Application, 2011.

[125] M. Moya Espinosa and R. Haas. SatTRACK - A Satellite Tracking Module for the VLBI Field System. In *Proc. 18th European VLBI for Geodesy and Astrometry Working Meeting, Tech. Univ. Wien*, pages 53–58, 2007.

[126] A. Niell. VLBI2010 Demonstrator Project. *AGU Fall Meeting Abstracts*, December 2008.

[127] L. Biermann. Kometenschweife und solare Korpusku-larstrahlung. *Zeitschrift fuer Astrophysik*, 29:274, 1951.

[128] A. J. Hundhausen, A. L. Stanger, and S. A. Serbicki. Mass and energy contents of coronal mass ejections: SMM results from 1980 and 1984-1988. In *Solar Dynamic Phenomena and Solar Wind Consequences, the Third SOHO Workshop*, volume 373 of *ESA Special Publication*, page 409, December 1994.

[129] A. Kolmogorov. The local structure of turbulence in incompressible viscous fluid for very large Reynolds' Numbers. *Akademiia Nauk SSSR Doklady*, 30:301–305, 1941.

[130] S. R. Cranmer. The solar corona and the solar wind. In *Lecture talk at the Phillips Academy, Andover, Massachusetts*, April 2011.

[131] Official Advanced Composition Explorer (ACE) web site. `http://www.srl.caltech.edu/ACE/`. [Online; Accessed on August 2011].

[132] L. A. McFadden, P. R. Weissman, and T. V. Johnson. *Encyclopedia of the Solar System, Second Edition*. Academic Press of Elsevier, 2007.

[133] A. Hewish, P. F. Scott, and D. Wills. Interplanetary scintillation of small diameter radio sources. *Nature*, 203:1214–1217, September 1964.

[134] A. R. Breen, W. A. Coles, R. R. Grall, M. T. Klinglesmith, J. Markkanen, P. J. Moran, B. Tegid, and P. J. S. Williams. EISCAT measurements of the solar wind. *Annales Geophysicae*, 14:1235–1245, December 1996.

[135] A. Canals, A. R. Breen, L. Ofman, P. J. Moran, and R. A. Fallows. Estimating random transverse velocities in the fast solar wind from EISCAT Interplanetary Scintillation measurements. *Annales Geophysicae*, 20:1265–1277, September 2002.

[136] R. A. Fallows, A. R. Breen, M. M. Bisi, R. A. Jones, and G. Wannberg. Dual-frequency interplanetary scintillation observations of the solar wind. *Geophys. Res. Lett.*, 33:11106, June 2006.

[137] M. M. Bisi, R. A. Fallows, A. R. Breen, S. Rifai Habbal, and R. A. Jones. Large-scale structure of the fast solar wind. *Journal of Geophysical Research (Space Physics)*, 112:6101, June 2007.

[138] L. T. Little and A. Hewish. Interplanetary scintillation and its relation to the angular structure of radio sources. *Monthly Notices of the RAS*, 134:221, 1966.

[139] R. Narayan. The physics of pulsar scintillation. *Royal Society of London Philosophical Transactions Series A*, 341:151–165, October 1992.

[140] Y. Koyama, H. Osaki, and T. Kondo. Results of test e-VLBI experiments with the K5 VLBI system. Presented at Breaking through the magnetic media barrier with fibre-optic networks, Proceedings of the 2nd e-VLBI Workshop, 2003.

[141] W. I. Axford. Observations of the Interplanetary Plasma. *Space Sci. Rev.*, 8:331–365, July 1968.

Only a tiny fraction of the universe has been studied even though the possibilities are unlimited given the current technologies, the resources and the time. To optimise the use of resources, the Metsähovi radio telescope and the existing VLBI processing equipment were exploited to study a broad variety of space phenomena. This thesis emphasizes two fundamental aspects of radio astronomy: radio spectroscopy of celestial bodies and radio science studies with planetary spacecraft in the Solar System. The research made use of the 14-metre radio telescope of the Metsähovi radio observatory and of other VLBI antennae to conduct regular observations of planets and planetary spacecraft. The work included the development of new VLBI hardware systems, processing and analysis software, and improvement of the observations pipeline.

BUSINESS +
ECONOMY

ART +
DESIGN +
ARCHITECTURE

SCIENCE +
TECHNOLOGY

CROSSOVER

DOCTORAL
DISSERTATIONS